A study of nuclear quantum effects in hydrogen bond symmetrization via the Quantum Thermal Bath

Yael Bronstein

THÈSE DE DOCTORAT
DE L'UNIVERSITÉ PIERRE ET MARIE CURIE

Spécialité : Physique

École doctorale : Physique et Chimie des Matériaux

réalisée

à l'Institut des NanoSciences de Paris

présentée par

Yael Bronstein

pour obtenir le grade de :

DOCTEUR DE L'UNIVERSITÉ PIERRE ET MARIE CURIE

Sujet de la thèse :

A study of nuclear quantum effects in hydrogen bond symmetrization via the Quantum Thermal Bath

soutenue le 26 septembre 2016

devant le jury composé de :

M.	Jean-Louis Barrat	Examinateur
Mme	Magali Benoit	Rapporteure
M.	Michele Ceotto	Rapporteur
M.	Daniel Borgis	Examinateur
M.	José Teixeira	Examinateur
M.	Fabio Finocchi	Directeur de thèse
M.	Philippe Depondt	Co-directeur de thèse - Membre invité

Abstract

In the recent past, increasing interest has risen for nuclear quantum effects (NQE), especially in hydrogen-containing systems. Indeed, NQE such as proton tunneling and zero-point energy often play a crucial role in the properties of these materials, even at room temperature. The standard methods to simulate NQE are based on path integrals. An interesting alternative to these methods is the Quantum Thermal Bath (QTB) [1]: this method is based on a Langevin equation where the classical degrees of freedom are coupled to an ensemble of quantum harmonic oscillators. While in the classical Langevin equation, the random force consists in a white noise and fulfills the classical fluctuation-dissipation theorem, in the QTB approach, the random force fulfills the quantum fluctuation-dissipation theorem [2]. We show through simple models that the QTB is a viable approach to take into account NQE, even, to some extent, in anharmonic systems [3]. Hence, the QTB enables realistic simulations of complex condensed-phase systems, generating static and dynamic information, such as pair correlation functions and vibrational spectra, which can be directly confronted with experimental results. We show that the QTB method is particularly successful in the study of the symmetrization of hydrogen bonds in several systems. Indeed, the difficulty resides in the identification of a precise transition pressure since the phase transition is often blurred by quantum or thermal fluctuations. It can depend on the oxygen-oxygen distance, as in high-pressure ice [4], but it can be affected by the electric field induced by ionic impurities [5] or by the inherent asymmetric environment of the hydrogen bonds, as in the delta phase of AlOOH [6]. Moreover, by comparing results from QTB and standard ab initio molecular dynamics, we are also able to disentangle the respective roles of NQE and thermal fluctuations in these phase transitions.

Résumé

L'étude des effets quantiques nucléaires et de leurs conséquences suscite de plus en plus d'intérêt, en particulier dans les matériaux comportant de l'hydrogène. En effet, les effets quantiques, tels que l'effet tunnel ou l'énergie de point zéro, ont souvent un impact important sur les propriétés de ces matériaux, et peuvent être présents même à température ambiante. Actuellement, les méthodes les plus courantes qui permettent de faire des simulations numériques en tenant compte des effets quantiques nucléaires sont basées sur le formalisme des intégrales de chemin. Le bain thermique quantique (ou QTB) [1] constitue quant à lui une alternative intéressante à ces méthodes: il repose sur le principe que les degrés de liberté classiques du système obéissent à une équation de Langevin par laquelle ils sont couplés à un ensemble d'oscillateurs harmoniques quantiques. Dans le cas de l'équation de Langevin classique, la force aléatoire est constituée d'un bruit blanc afin que le système respecte le théorème de fluctuation-dissipation classique; au contraire, dans l'approche du QTB, la force aléatoire est telle que la version quantique du même théorème est vérifiée [2]. On montrera à l'aide de modèles relativement simples que le QTB constitue une approche valide et efficace pour tenir compte des effets quantiques nucléaires dans des systèmes avec des degrés variés d'anharmonicité [3]. Ainsi, grâce au QTB, on peut réaliser des simulations de systèmes complexes et obtenir des informations sur leurs propriétés structurales et dynamiques, telles que des fonctions de corrélation de paires ou des spectres vibrationnels, qui peuvent à leur tour être confrontés directement aux résultats expérimentaux. Nous montrerons que la méthode du QTB est particulièrement adaptée pour l'étude de la symétrisation de liaisons hydrogènes dans différents systèmes. En effet, identifier de manière précise une pression de transition est relativement difficile car la transition est souvent brouillée par des fluctuations quantiques et thermiques. La pression de symétrisation peut également dépendre de la distance entre deux oxygènes voisins, comme c'est le cas dans la transition VII-X de la glace [4], mais elle peut aussi être impactée par le champ électrique induit par des impuretés ioniques [5] ou par l'asymétrie de l'environement atomique de la liaison hydrogène, ainsi que nous l'avons établi dans la phase δ de AlOOH [6]. De plus, en comparant les résultats des simulations de dynamique moléculaires ab initio standards et à ceux de simulations QTB, nous pouvons distinguer les rôles respectifs des effets quantiques nucléaires et des fluctuations thermiques dans ces différentes transitions de phases.

Thanks - Remerciements

A la fin de ces trois années de doctorat, je voudrais prendre un moment pour remercier toutes les personnes qui ont rendu ce projet possible. Il m'est bien sur impossible de toutes les nommer et je m'excuse de ne pouvoir être exhaustive sur ce point.

Tout d'abord, j'ai une pensée particulière pour mes deux directeurs de thèse, Philippe Depondt et Fabio Finocchi. Lors de mon arrivée, ils proposaient un sujet de recherche qui parlait de simulations et de physique quantique – c'est ce que j'en ai compris à ce moment-là, mais leur enthousiasme m'a suffit pour me lancer dans l'aventure. Je leur serai toujours reconnaissante de m'avoir encadrée, aidée, soutenue, dirigée, conseillée pendant ces années. Chacun à leur manière, ils ont toujours été disponibles pour répondre aux questions, pour prendre un café, pour discuter de tous les sujets. Ils m'ont considéré comme l'une de leurs collègues et m'ont permis de mûrir et de devenir autonome. Je ne pourrais pas imaginer de meilleurs encadrants pour réaliser ma thèse et je garderai toujours en moi la rencontre de deux personnes avec de grandes qualités scientifiques mais surtout humaines.

Je souhaiterai également remercier tous les collègues avec qui j'ai eu l'occasion de travailler et de discuter : Marco Saitta, sans qui je ne me serais jamais intéressée au sujet sans fin de la glace, Hichem Dammak et Marc Hayoun, pour nos discussions (et chocolats chauds) sur les problèmes (et les avantages) du QTB. Je remercie aussi mes rapporteurs, Magali Benoit et Michele Ceotto, qui ont accepté de relire ma thèse, ainsi que les autres membres du jury, Jean-Louis Barrat, Daniel Borgis et José Teixeira, pour les discussions et approfondissements qui ont été très constructifs.

Je tiens également à remercier particulièrement Fabien Brieuc avec qui j'ai énormément travaillé pour le développement du QTB, et qui a toujours été là même aux pires moments de déprime dus à un code qui refusait de coopérer. Merci à tous les collègues de l'INSP et de l'IMPMC avec qui j'ai travaillé et en particulier aux membres de l'équipe Oxydes pour m'avoir accueillie au sein de l'équipe. Merci aux doctorants du labo, pour nos discussions sur tout et n'importe quoi, qui m'ont permis de relâcher la pression et de relativiser.

Je termine en remerciant ma famille et mes amis, qui m'ont soutenu tout du long. Merci Christelle, Olivier, Pascal et tant d'autres pour m'avoir aidé/supporté/encouragé (rayer la mention inutile) pendant ces années. Et pour finir, je ne trouve pas de mots suffisants pour exprimer toute ma gratitude envers Rémi-Louis, qui a toujours été là.

Contents

Introduction

Nuclear quantum effects (NQE) arise when a nucleus cannot be described through classical mechanics but obeys the laws of quantum mechanics instead. The consequences thereof are many, unexpected, and sometimes by no means negligible. From a simulation point of view, NQE are a challenge but progress is being steadily made. The situation is now that, given enough computation time, many problems and thus many different systems, can be addressed. In this thesis, our objective is to study NQE in real systems through an efficient and pragmatic approach.

NQE can impact the behavior of condensed matter systems and affect properties such as thermal expansion, proton diffusion or specific heat. When NQE are present, two conflicting effects occur: spatial delocalization due to quantum mechanics on the one hand and confinement due to the atomic environment on the other. This is especially true for light atoms, such as hydrogen, where the nucleus is simply a proton. As an illustration of its quantum delocalization, the thermal wavelength of a "free" proton is of the order of 1 Å at room temperature i.e. the same order of magnitude as interatomic distances in hydrogen-containing systems. This can have many implications since hydrogen is ubiquitous and can be found in various systems, from the interior of stars and gaseous planets to water [7] and biological matter [8]. For example, the fact that the melting point of heavy water (D_2O and T_2O) is higher than that of light water (H_2O) is due to NQE and is one of the isotope effects in water [9, 10]. Other consequences of NQE are the quantum ferroelectric behavior of KH_2PO_4 (KDP) [11] or the formation of many different ice phases under pressure [12]. Hence, the study of the consequences of quantum effects has been the focus of intense research in the recent years, both experimentally and theoretically.

The main difficulty resides in the simulation of NQE. Molecular dynamics (MD) is an efficient tool to study the structural and dynamical properties of condensed matter systems and has been widely used; however, it relies on Newton's equations of motion for the nuclei and thus treats them as classical particles. Simulating a system containing quantum particles is problematic because of the well-known wave-particle duality: while MD takes care of the "particle" aspect of a quantum nucleus, the "wave" aspect is much more complicated and requires more complex and computationally heavy methods. As an example, let us consider a simple water molecule: the zero-point energy in the two O-H stretching vibrations and in the bending vibration is more than twenty times larger than the thermal energy at room temperature (k_BT). Within the quantum mechanics framework, this energy is "bounded" to the internal vibrations of the molecule; however, if the system were treated classically by means of a standard MD simulation, then equipartition of this energy would occur meaning that it would be shared equally among all the degrees of freedom of the molecule, which would in turn cause the water to boil [13] ! Usually, simulations treat the water molecule as a rigid molecule that can rotate but whose internal degrees of freedom cannot vibrate. This allows for a correct description of the properties of water in many cases but fails in others, such as proton transfer reactions for exam-

ple. Indeed, these reactions imply complex processes, based on the original von Grotthuss process [14], where the O-H bonds must be able to break and reform.

Therefore, a lot of effort is being made to develop various approaches and techniques to simulate efficiently quantum effects in condensed matter. Among them, the Quantum Thermal Bath (QTB) method [1] simulates NQE by introducing a stochastic motion of the nuclei, as in a standard Langevin equation. The difference in the QTB method is that both thermal and quantum fluctuations are included in the stochastic force, in contrast with standard Langevin dynamics where only the thermal energy is considered. This allows us to treat protons as quantum particles within MD simulations with the same computational cost as standard MD. Hence, we can address systems with a typical size accessible by density functional theory-based calculations i.e. a few hundred atoms and for time lengths up to 30 ps. This enables us to compute both structural properties and vibrational spectra, that can be compared to experimental data. Furthermore, QTB simulations also allow us to develop simple models i.e. with few degrees of freedom, that capture the essence of the studied physical phenomenon and provide a clear description of the mechanisms underlying it.

In the following, we will first describe in detail how the QTB works and what its advantages are with respect to other existing methods, such as path integral molecular dynamics (chapters 1 and 2). By adopting a pragmatic viewpoint, we will then use the QTB in a straigthforward manner to analyze the behavior of hydrogen bonds under pressure, since we expect the quantum nature of protons to play a role in their evolution. The most common model that describes a proton in a hydrogen bond is a double well potential as a function of a reaction coordinate that settles the (strong) iono-covalent bond either with an oxygen on one side or the other. We will confront this picture to real cases, such as the VII-X transition in high-pressure ice. In particular, the VII-X transition will allow us to describe the mechanism behind a "quantum-driven" phase transition (chapter 3). The double-well picture is however challenged in more complex materials; we will show that NQE can disappear in the presence of impurities e.g. in salty ices, and that, more generally, the atomic environment can massively modify the behavior of protons under pressure (chapter 4). Therefore, by considering different systems in which the balance between quantum delocalization and atomic confinement varies, we will illustrate the complexity of protons' properties in materials. In parallel to the use of the QTB on several systems, we will also conduct a critical analysis of the method by using simple models in order to define its limitations and its field of applicability; in particular, we will discuss one of the main pitfalls of the QTB, namely the zero-point energy leakage (chapter 5). This will allow us to identify the pros and cons of the QTB and develop practical guidelines to use this method when studying NQE.

Chapter 1

State of the art

Contents

1.1 Introduction

In this chapter, we will present some of the methods that are available today for simulating quantum effects in condensed matter systems. This presentation is clearly not exhaustive; rather, it aims at providing a quick overview that will be useful when the pros and cons of the Quantum Thermal Bath method will be discussed. Numerical simulations have become a staple in condensed matter studies; in particular, molecular dynamics (MD), which was introduced by Alder and Wainwright in the 1960s [15], is one of the most widely used theoretical tool nowadays. It allows to describe statistical mechanical systems by computing the time evolution of the atomic motion i.e. the atomic trajectories. However, when tackling the motion of hydrogen nuclei, we are confronted with many difficulties arising from quantum mechanics. While standard MD is very satisfactory when dealing with classical nuclei, it is, strictly speaking, only valid above the Debye temperature. Several reviews about the development of methods including quantum mechanics in MD simulations already exist, and can be found in references [13, 16–19]. First, we will briefly present the reference method for treating nuclear quantum effects within MD simulations, namely path integral molecular dynamics (PIMD) (section 1.2). Indeed, since PIMD is an exact method that yields the structural properties of a quantum system, we will compare our own simulation results, obtained via an approximate method - the Quantum Thermal Bath (QTB), to PIMD results whenever they are available. Then, we will discuss methods that are designed to provide access to the time-correlation functions of the system (section 1.3). Indeed, if we are interested in the dynamical properties of the system, path integral based methods such as centroid molecular dynamics [20–25] or ring polymer molecular dynamics [26, 27] are necessary and they can become quite demanding computationally. Hence, approximate methods are needed to study more complex minerals and many semiclassical approaches have been developed in the recent years in particular in order to compute time

correlation functions. Since the QTB method falls into this category, we will make a rapid overview of the most used semiclassical method, namely initial value representation. Thus, we will attempt in this chapter to explain the context in which the QTB method was introduced in order to understand how it relates to other methods aiming at treating nuclear quantum effects. This will allow us to better understand the advantages and drawbacks of the QTB with respect to other available approaches (see chapters 2 and 5).

1.2 Path integral molecular dynamics

Within Feynman's path integral formalism [28], the canonical partition function writes:

$$Q = \int \mathrm{d}x_1 \int_{x_1}^{x_1} \mathrm{e}^{-S[x(\tau)]}\, \mathcal{D}x(\tau) \tag{1.2.1}$$

where the integration is over all paths $x(\tau)$ in imaginary time τ starting and ending at x_1 i.e. $x(0) = x(\hbar\beta) = x_1$ where $\beta = (k_B T)^{-1}$ is the inverse temperature. S is the Euclidian action and writes:

$$S[x(\tau)] = \int_0^{\hbar\beta} \mathcal{H}(x(\tau))\, \mathrm{d}\tau \tag{1.2.2}$$

where $\mathcal{H}$ is the Hamiltonian which is composed of a kinetic part and of the potential $V(x)$. If we discretize the imaginary time τ so that $\tau = n\hbar\beta/P$, $n = 0, P$ and P being an integer, then $x(\tau)$ can be approximated by a series of straight lines between each time step. The partition function in equation (1.2.1) can thus be rewritten as:

$$Q_P = \left(\frac{mP}{2\pi\hbar^2\beta}\right)^{P/2} \int \mathrm{d}x_1 \ldots \int \mathrm{d}x_P\, \mathrm{e}^{-\beta V_P(x_1,\ldots,x_P)} \tag{1.2.3}$$

with

$$V_P(x_1,\ldots,x_P) = \frac{mP}{2\hbar^2\beta^2} \sum_{n=1}^{P} (x_n - x_{n+1})^2 + \frac{1}{P} \sum_{n=1}^{P} V(x_n). \tag{1.2.4}$$

Here, we have considered periodic boundary conditions i.e. $x_{P+1} = x_1$. Now, the partition function in equation (1.2.3) also corresponds to the configurational partition function of a system consisting of P classical particles with the potential V_P. Hence, there is an isomorphism between the quantum system (with potential V) and a cyclic chain of P classical particles (see Figure 1.2.1). In this chain, each particle, also called a bead, interacts with its two nearest neighbors via a harmonic potential with a force constant $mP/\hbar^2\beta^2$ and is trapped in the potential V/P. This isomorphism is in principle exact only when the number of beads P is infinite i.e.

$$Q = \lim_{P\to\infty} Q_P. \tag{1.2.5}$$

In practice, the classical isomorphism in equation (1.2.3) is valid if the potential $V(x)$ does not vary much with respect to the bond length fluctuations of the classical beads, which can be attained for large but finite P. If we consider a free chain (i.e. without any external potential), then the root mean square of the bond lengths is proportional to $\sqrt{\hbar^2\beta/mP}$. If σ is the characteristic length scale over which the potential $V(x)$ varies significantly then, we need to set:

$$\sigma \gg \sqrt{\frac{\hbar^2\beta}{mP}} \Leftrightarrow P \gg \frac{\hbar^2\beta}{m\sigma^2}. \tag{1.2.6}$$

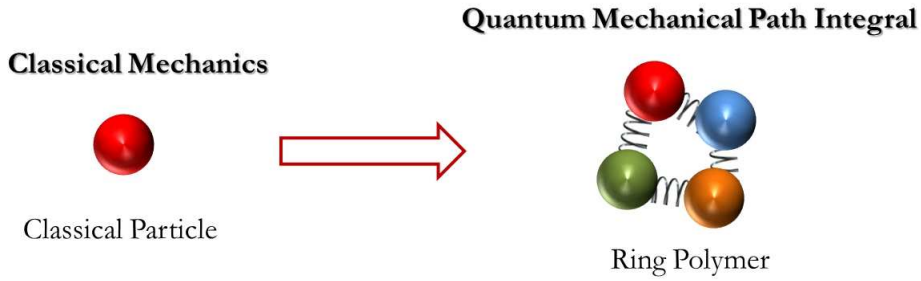

Figure 1.2.1: A depiction of the isomorphism between a quantum mechanical particle and a classical ring polymer within the path integral framework. Reference: http://web.stanford.edu/group/markland/research.html

Hence, when the temperature decreases i.e. $\beta \to \infty$, P must be very large. On the other hand, at relatively high temperatures, P can be finite. In path integral based simulations, one usually determines the value for P for which the relevant thermodynamic quantities of the system are converged. In the following paragraph, we will show how this formalism can be adapted for MD simulations.

Indeed, Parrinello and Rahman suggested in 1984 to use molecular dynamics in order to evaluate the path integrals [29]. Indeed, equation (1.2.3) can be rewritten in the following form:

$$Q_P = \int \mathrm{d}p_1 \ldots \int \mathrm{d}p_P \int \mathrm{d}x_1 \ldots \mathrm{d}x_P \, \mathrm{e}^{-\beta \mathcal{H}_{\text{eff}}} \tag{1.2.7}$$

where

$$\mathcal{H}_{\text{eff}} = \sum_{j=1}^{P} \frac{p_j^2}{2m'} + V_P(x_1, \ldots, x_P). \tag{1.2.8}$$

By properly choosing m', one can recover equation (1.2.3). The effective Hamiltonian $\mathcal{H}_{\text{eff}}$ then yields the classical equations of motion:

$$\dot{x}_j = \frac{\partial \mathcal{H}_{\text{eff}}}{\partial p_j}, \quad \dot{p}_j = -\frac{\partial \mathcal{H}_{\text{eff}}}{\partial x_j}. \tag{1.2.9}$$

Hence, starting from an initial configuration $(p_1, \ldots, p_P, x_1, \ldots, x_P)$, one integrates the equations of motion and then averages the thermodynamic properties over the trajectories. In the following, we will compare our results to PIMD calculations, when available, in order to validate our simulations (see sections 3.3.2 and 5.3.2). One should note that the trajectories computed within PIMD do not represent the real dynamics of the quantum system because they are just a mean to evaluate statistical averages. Equilibrium properties can be computed from these trajectories but, in order to calculate real-time correlation functions, one needs to resort to more complex methods.

1.3 Time correlation functions with nuclear quantum effects

In many instances, one is interested in time-correlation functions of the system. Indeed, many interesting quantities concerning the dynamics of complex systems can be expressed in terms of time-correlation functions [30], such as:

$$C_{AB}(t) = \mathrm{Tr}\left[\rho_0 AB(t)\right] \tag{1.3.1}$$

where A and B are quantum operators, ρ_0 is the equilibrium density operator,

$$\rho_0 = \frac{\mathrm{e}^{-\beta H}}{Z}, \tag{1.3.2}$$

$Z = \mathrm{Tr}\left[\mathrm{e}^{-\beta H}\right]$ is the quantum partition function and H the Hamiltonian of the system containing N particles. The time-dependent operator $B(t)$ can be written as:

$$B(t) = \mathrm{e}^{iHt/\hbar} B \mathrm{e}^{-iHt/\hbar}. \tag{1.3.3}$$

For example, if both A and B are the dipole moment operators, then the Fourier transform of $C_{AA}(t)$ is the absorption spectrum; another example is if A is the velocity of a given particle, then the time integral of $C_{AA}(t)$ yields the diffusion coefficient.

1.3.1 Time correlation functions via path-integrals

While PIMD is a powerful technique to compute equilibrium properties (see section 1.2), it cannot yield directly information about the dynamics of the system. In order to compute real time-correlation functions, one needs to resort to more complex methods, such as centroid molecular dynamics [20–25] or ring polymer molecular dynamics [26,27], and both of these methods can be quite demanding computationally for large or complex systems.

Centroid molecular dynamics The idea of centroid molecular dynamics (CMD) [20–25] is to consider the centroids of the paths as classical phase space variables. In this formalism, the centroid phase space "quasi-density" operator is:

$$\phi_c(x_c, p_c) = \frac{\hbar}{2\pi} \int \mathrm{d}\zeta \int \mathrm{d}\eta \, \mathrm{e}^{i\zeta(x-x_c)+i\eta(p-p_c)-\beta\mathcal{H}} \tag{1.3.4}$$

where x_c and p_c are the position and the momentum of the centroid respectively, x and p are the position and momentum quantum operators, and $\mathcal{H}$ is the Hamiltonian. By definition, the centroid distribution function is given by:

$$\rho_c(x_c, p_c) = \mathrm{Tr}\left[\phi_c(x_c, p_c)\right] = \mathrm{e}^{-\beta p_c^2/2m} \mathrm{e}^{-\beta V_c(x_c)} \tag{1.3.5}$$

where $V(x_c)$ is the centroid potential. The quantum partition function is then given by:

$$Z = \frac{1}{2\pi\hbar} \int \mathrm{d}x_c \int \mathrm{d}p_c \, \rho_c(x_c, p_c) \tag{1.3.6}$$

and the average value of any operator A is:

$$\langle A \rangle = \frac{1}{2\pi\hbar Z} \int \mathrm{d}x_c \int \mathrm{d}p_c \, \rho_c(x_c, p_c) A_c(x_c, p_c; t) \tag{1.3.7}$$

where

$$A_c(x_c, p_c; t) = \mathrm{Tr}\left[\delta_c(x_c, p_c; t) A\right] \tag{1.3.8}$$

and δ_c is the normalized "quasi-density" operator:

$$\delta_c(x_c, p_c; t) = \frac{\mathrm{e}^{-iHt/\hbar} \phi_c(x_c, p_c) \mathrm{e}^{iHt/\hbar}}{\rho_c(x_c, p_c)}. \tag{1.3.9}$$

In this framework, the equations of motion of the centroid are:

$$p_c(t) = m\dot{x}_c(t) = \mathrm{Tr}\left[\delta_c(x_c, p_c; t) p\right], \quad \dot{p}_c(t) = F_c(t) = \mathrm{Tr}\left[\delta_c(x_c, p_c; t) F\right] \tag{1.3.10}$$

where F is the force operator. In the CMD approach, the following approximation is made on the "quasi-density" operator:

$$\delta_c(x_c, p_c; t) \approx \delta_c(x_c(t), p_c(t)) \tag{1.3.11}$$

Using equations (1.3.10) with this approximation, the centroid correlation functions become approximations for the true quantum correlation functions. However, equation (1.3.11) is true only at $t = 0$ and in the case of a free particle or a particle in a harmonic potential. It is also verified in the high-temperature limit. Finally, the centroid potential $V_c(x_c)$ can be written as a centroid constrained imaginary time path integral averaged over all closed imaginary time paths:

$$V_c(x_c) = -\frac{1}{\beta}\ln\left[\sqrt{\frac{2\pi\hbar^2\beta}{m}}\oint \mathcal{D}x(\tau)\,\delta(x_c - x_0)\mathrm{e}^{-S[x(\tau)]}\right] \tag{1.3.12}$$

where S is the Euclidian action and

$$x_0 = \frac{1}{\hbar\beta}\int_0^{\hbar\beta} x(\tau)\,\mathrm{d}\tau \tag{1.3.13}$$

is the centroid of the path $x(\tau)$. The force F_c is then just $-\mathrm{d}V_c/\mathrm{d}x_c$. Using the same formalism as for PIMD, the integral $\oint \mathcal{D}x(\tau)\ldots$ can be replaced by a configurational integral over P particles, with cyclic boundary conditions (see equation (1.2.3)). In this representation, the centroid coordinates become:

$$x_c = \frac{1}{P}\sum_{j=1}^{P} x_j, \quad p_c = \frac{1}{P}\sum_{j=1}^{P} p_j. \tag{1.3.14}$$

After having evaluated V_c in equation (1.3.12) via PIMD for instance, x_c and p_c are propagated in real time using the equations of motion (1.3.10). The centroid correlation function is then:

$$\langle B_c(0)A_c(t)\rangle = \frac{1}{(2\pi\hbar)^P Z}\int \mathrm{d}p_c \int \mathrm{d}x_1 \ldots \int \mathrm{d}x_P\, \mathrm{e}^{-\beta p_c^2/2m + V_P} B_c A_c[x_c(t), p_c(t)] \tag{1.3.15}$$

where V_P is the potential in equation (1.2.4). Thus, CMD simulations require one to evaluate V_c at each time step of the trajectory. However, computing V_c in equation (1.3.12) implies many PIMD steps. Approximations exist, such as adiabatic decoupling, that allows to separate the non-centroid modes from the centroid's motion and therefore speed up the calculation [23, 31–33]. Hence, CMD can be quite demanding computationally and is out of reach for large and complex systems. In reference [18], Witt and coworkers investigate the performance of path-integral based methods and in particular, of CMD on several systems (diatomic and polyatomic molecules): they found that CMD works relatively well at high temperature but also displays some problems at low temperature.

Ring-polymer molecular dynamics More recently, Craig and Manolopoulos presented a new method to compute time-correlation functions based on path integrals, namely ring-polymer molecular dynamics (RPMD) [26]. In their formalism, the mass m' of the fictitious classical particles (see the effective Hamiltonian in equation (1.2.8)) is taken to be m/P. Hence, the centroid has a mass m, as in CMD. As in PIMD, one then propagates the equations of motion in real time. The force on the centroid is given by:

$$F_c = -\frac{1}{P}\sum_{j=1}^{P}\frac{\partial V(x_j)}{\partial x_j} \tag{1.3.16}$$

and after propagation to a time t, the following RPMD time-correlation function is computed:

$$\langle B(0)A(t)\rangle = \frac{1}{(2\pi\hbar)^P Z}\int \mathrm{d}x_1 \ldots \int \mathrm{d}x_P \int \mathrm{d}p_1 \ldots \mathrm{d}p_P \, \mathrm{e}^{-\beta\mathcal{H}_{\mathrm{eff}}} B_P(0)A_P(t) \tag{1.3.17}$$

where

$$A_P(t) = \frac{1}{P}\sum_{j=1}^{P} A[x_j(t)], \quad B_P(0) = \frac{1}{P}\sum_{j=1}^{P} B[x_j(0)]. \tag{1.3.18}$$

The RPMD correlation function is equal to the CMD correlation function in equation (1.3.15) at $t = 0$ and if the operators A and B are linear functions of position and momentum. In this case, the RPMD correlation function is a good approximation to the real physical time correlation function. One should note however that $x_c(t)$ and $p_c(t)$ are propagated using the instantaneous centroid potential in RPMD whereas in CMD, they were propagated using the average centroid potential of mean force. Hence, RPMD is less computationally expensive than CMD and can be seen as an approximation to CMD. It has been shown to give reasonable results in different cases [34–38], but as for now, no rigorous derivation of RPMD has yet been provided. Witt and coworkers [18] also studied the performance of RPMD and compared it to CMD: in particular, they found that the chain frequencies that arise from the intrinsic dynamics of the ring polymers can interfere with the physical frequencies of the system leading to non-physical peaks in the vibrational spectrum, especially at low temperature.

1.3.2 Approximate methods: semiclassical approaches

Wavefunction-based methods

We have shown just above that path-integral based methods are the reference methods to incorporate nuclear quantum effects, in a rigorous way, into MD simulations. However, as explained in the previous section, PIMD can be quite demanding computationally, especially at low temperature or for large and complex systems. Moreover, extracting dynamical properties from path-integral based simulations is not straightforward: CMD and RPMD methods aim at providing quantum time correlation functions but are subject to other problems as pointed out in reference [18]. Other fully quantum calculations exist but are similarly out of reach for large and complex systems; however, these exact methods are being used more and more often for simple chemical reactions [39] and provide benchmark results to which more approximate methods can be compared. For instance, Makri and coworkers [40, 41] developed an approach based on path-integrals and applied on models of molecular systems i.e. only a few relevant degrees of freedom describe the main properties of the system and are being coupled to the environment via a bath of harmonic oscillators. Another Hamiltonian-based approach, namely the time-dependent Hartree method [42, 43], has been applied to systems with about ten degrees of freedom. Here, we will show a few ideas to describe real-time dynamical processes while taking into account the quantum nature of nuclei, through approximate methods.

Semiclassical theory and initial value representation

Many of the approximate or semiclassical approaches described in the literature are "mixed quantum-classical" methods i.e. one or two degrees of freedom are treated quantum mechanically while the rest of the degrees of freedom are treated via the classical equations of motion. The main problem resides in the coupling between the quantum degrees of

freedom and the classical ones. Some of the existing methods are based on a wave packet approach. Indeed, the wave packet approach is in principle exact if all the degrees of freedom of the system are considered, as explained in the previous paragraph. This is often not attainable for systems with more than just a few degrees of freedom. However, if one can separate the classical from the quantum degrees of freedom, one could in principle use an exact approach for the quantum degrees of freedom. In particular, the self-consistent field theory introduced by Bowman and coworkers [44,45] aims at finding the wavefunction as a self-consistent solution to a given model Hamiltonian. By doing so, they are able to reproduce the coupled vibrational motion of polyatomic molecules. Similar methods exist that are based on an expansion of the wavefunction in terms of $\hbar$ or that approximate the wave packets as variational Gaussians [46–48] and exploit the correspondence between the classical and quantum dynamics of a Gaussian wave function in a harmonic potential. These methods have been successful in the study of various clusters (e.g. solid and liquid neon [47]); however, they scale poorly with the system size and have thus been applied only to small molecules or clusters so far.

In the following, we will focus on a particular semiclassical method, namely initial value representation (IVR), developed by Miller and coworkers along the last 40 years [49–55]. Semiclassical (SC) theory dates back to the late 1950s and 1960s when Ford and Wheeler described quantum effects in elastic scattering using the WKB approximation within the Schrödinger equation [56]. Their work was confirmed a few years later when Bernstein showed that all the quantum effects in elastic scattering could indeed be described within the SC theory [57]. SC theory was then extended to inelastic and reactive scattering processes in the 1970s [49,58–60], and allowed to describe quantum effects such as tunneling and interference within classical MD simulations. IVR then represents the first step towards a practical way of carrying out SC calculations on complex systems by introducing a Monte Carlo average over the initial conditions of classical trajectories.

The idea behind the semiclassical initial value representation (SC-IVR) method is to approximate the time evolution operator, $\mathrm{e}^{iHt/\hbar}$, by a phase space average over the initial conditions of classical trajectories [13,17,49,55,58]. In particular, in the original formulation of IVR of Van Vleck [61], the time evolution operator can be written as:

$$\mathrm{e}^{iHt/\hbar} = \int \mathrm{d}\mathbf{p}_0 \int \mathrm{d}\mathbf{q}_0 \sqrt{\frac{M_{qp}}{(2i\pi\hbar)^{3N}}} \mathrm{e}^{iS(\mathbf{p}_0,\mathbf{q}_0)/\hbar} |\mathbf{q}_t\rangle\langle\mathbf{q}_0| \tag{1.3.19}$$

where $(\mathbf{p}_0, \mathbf{q}_0)$ are the set of initial conditions for the momentum and coordinate operators. $(\mathbf{p}_t, \mathbf{q}_t)$ is the phase space point at time t and S is the classical action along the trajectory. Finally, M_{qp} is the determinant of the Jacobian matrix relating the final coordinate $\mathbf{q}_t$ to the initial momentum $\mathbf{p}_0$:

$$M_{qp} = \mathrm{Det}\left[\frac{\partial \mathbf{q}_t}{\partial \mathbf{p}_0}\right]. \tag{1.3.20}$$

Within this approximation, the expression for the correlation function in equation (1.3.1) becomes:

$$C_{AB}(t) = \int \mathrm{d}\mathbf{p}_0 \mathrm{d}\mathbf{p}'_0 \mathrm{d}\mathbf{q}_0 \mathrm{d}\mathbf{q}'_0 \sqrt{\frac{M_{qp} M'_{qp}}{(2i\pi\hbar)^{3N}}} \mathrm{e}^{-iS(\mathbf{p}_0,\mathbf{q}_0)/\hbar + iS(\mathbf{p}'_0,\mathbf{q}'_0)/\hbar} \langle\mathbf{q}'_0|A_\beta|\mathbf{q}_0\rangle\langle\mathbf{q}_t|B|\mathbf{q}'_t\rangle \tag{1.3.21}$$

where we have rewritten $A_\beta \equiv \rho_0 A$. The first bottleneck in the method is the need to perform a double phase space average at the initial time $t = 0$ and at any time $t \neq 0$. A second and even more challenging problem resides in the evaluation of the exponential terms which exhibit an oscillatory character that is difficult to tackle. This "phase problem"

is crucial because it is the phase of the integrand in equation (1.3.21) which carries all the quantum coherence information. Many techniques have been developed to solve these issues.

Here we will present one of the simplest method which was introduced by Miller and coworkers [62,63] and is called the "linearization approximation". The idea is to consider, rather drastically, that the dominant terms in this double phase space average come from trajectories that are close to each other. This approximation, however, has been shown to yield very good results in many different cases e.g. the description of tunneling in a one-dimensional potential which matches very well with benchmark results from fully quantum mechanical calculations [13]. Hence, if one considers the following variables:

$$\overline{\mathbf{p}}_0 = \frac{\mathbf{p}_0 + \mathbf{p}_0'}{2}, \quad \overline{\mathbf{q}}_0 = \frac{\mathbf{q}_0 + \mathbf{q}_0'}{2} \tag{1.3.22}$$

$$\Delta\mathbf{p}_0 = \mathbf{p}_0 - \mathbf{p}_0', \quad \Delta\mathbf{q}_0 = \mathbf{q}_0 - \mathbf{q}_0' \tag{1.3.23}$$

i.e. the sum and the difference of the two sets of initial conditions, then one can expand the terms in equation (1.3.21) to the first order in $\Delta\mathbf{p}_0$ and $\Delta\mathbf{q}_0$. The integrals over $\Delta\mathbf{p}_0$ and $\Delta\mathbf{q}_0$ then become Fourier integrals since the phase of the integrand is linear. This is true only if the phase is almost constant. This yields the following linearized time-correlation function or LSC-IVR:

$$C_{AB}^{\text{LSC-IVR}}(t) \simeq \int \mathrm{d}\mathbf{p}_0 \int \mathrm{d}\mathbf{q}_0 A_\beta^{(w)}(\mathbf{p}_0, \mathbf{q}_0) B^{(w)}(\mathbf{p}_t, \mathbf{q}_t) \tag{1.3.24}$$

and is also called the "classical Wigner model" for the correlation function (we have replaced $(\overline{\mathbf{p}}_0, \overline{\mathbf{q}}_0)$ by $(\mathbf{p}_0, \mathbf{q}_0)$). $A_\beta^{(w)}$ and $B^{(w)}$ are the Wigner functions of the corresponding operators i.e.

$$O^{(w)}(\mathbf{p}, \mathbf{q}) = (2i\pi\hbar)^{-3N} \int \mathrm{d}(\Delta\mathbf{q}) \langle \mathbf{q} - \frac{\Delta\mathbf{q}}{2} | O | \mathbf{q} + \frac{\Delta\mathbf{q}}{2} \rangle \tag{1.3.25}$$

for each operator A_β and B.[1] In practice, $C_{AB}^{\text{LSC-IVR}}(t)$ necessitates only one phase space average and has the form of a classical correlation function except that the classical functions have been replaced with Wigner functions. Usually, calculating the Wigner function of B is relatively straightforward, in particular if B is simply a function of the coordinates i.e. a local operator. On the contrary, computing $A_\beta^{(w)}$ is more complex because of the presence of the Boltzmann operator, $\mathrm{e}^{-\beta H}$. A rigorous way to treat the Boltzmann operator is via Feynman's path integrals but is rather tedious. Hence, various approaches have been proposed, such as the harmonic approximation which works well at temperatures that are not too low [63]. The local harmonic approximation [65–67] and the thermal Gaussian approximations (TGA) [68,69], have also been developed and are less drastic. For instance, in the TGA approach, the Boltzmann operator is approximated by a multidimensional Gaussian which implies the different gradients of the potential. Other formulations of the SC-IVR method exist, such as the Herman-Kluk approach [70], also called *coherent state IVR*, which yields the "forward-backward" approximation to the SC-IVR [71,72] but they display the same problems as the approach described here. These various methods have been applied to several systems, such as anharmonic oscillators and Lennard-Jones fluids [73] where the velocity autocorrelation functions have been computed. They have also been mixed with other methods such as the PIMD formalism or Liouville dynamics [74,75].

[1] We note that the classical Wigner model has been obtained before through various formulations [64,65].

1.4 Conclusion

In this chapter, we described the reference method to include NQE into molecular dynamics simulations, namely PIMD. It is an exact method based on an isomorphism between a quantum particle and a chain of classical beads. PIMD thus yields exact results when the number of beads is sufficiently large. However, the number of beads increases as temperature decreases making low-temperature simulations quite heavy computationally. Moreover, PIMD yields structural properties of the system but not dynamical properties. To compute real time correlation functions, approximate methods such as CMD or RPMD are needed and are much more computationally demanding than PIMD simulations. Thus, path integral methods have several advantages: they are exact when the number of beads is large enough and they can be massively parallelized. However, they are problematic for complex or large systems or when computer resources are limited. We then showed that over the last 40 years, many developments have been made in semiclassical methods. While fully quantum calculations, such as the wave packet-based approaches, are out of reach for systems with more than a few degrees of freedom, approximate methods have been proposed. In particular, one of the most used formalism, IVR, relies on an average over the initial conditions of classical trajectories and is still being improved today. Hence, the need for efficient methods that are able to simulate large and complex systems and that can give access to time correlation functions is quite important. In the following chapter, we will present another approximate method - namely the Quantum Thermal Bath (QTB) - that has been developed recently by Dammak and coworkers [1]. The idea of coupling the system to a bath of oscillators was already discussed in the 1980s [76] and has been used to calculate thermal transport properties and heat capacities [77–79]. Hence, methods based on a Langevin equation of motion for the nuclear degrees of freedom, where the random force which is generally a white noise in classical MD is a colored noise, have been proposed in the last years. This quantum random force is chosen such that its power spectrum is in accordance with the quantum fluctuation-dissipation theorem [2,80]. In 2009, two different schemes combining quantum thermal baths with MD simulations were published. While the formalism presented by Ceriotti and coworkers [81] relies on a generalized Langevin equation, we will use in the following manuscript the QTB proposed by Dammak and coworkers [1]. We will see that, compared to path integral methods, the QTB is much less demanding computationally: running QTB molecular dynamics simulations presents no additional cost compared to standard MD. While it is not an exact method, one can easily run QTB and classical simulations simultaneously and thus determine whether nuclear quantum effects are important in the system or not.

Chapter 2

The Quantum Thermal Bath

Contents

2.1 The Langevin equation

2.1.1 Brownian motion and the Langevin equation

In 1827, Brown discovered the irregular and incessant motion of pollen particles suspended in water [82]. In 1905, Einstein gave the first theoretical explanation for this phenomenon, which in turn, led to the fundamentals of the atomic theory. His theory however lacked the notion of inertia for the particles [83]. Hence, in 1908, Langevin proposed a more elaborate model for Brownian motion which is defined as the erratic motion of a "heavy" particle in a fluid consisting of much "lighter" particles [84].

Langevin introduced two forces in order to describe the effect of the fluid on the particle: a friction force, characterized by a friction coefficient γ, and a random force $\mathbf{R}$

which represents the incessant collisions between our particle and the particles constituting the fluid. If no external force is applied on the particle, its equation of motion is given by

$$m\frac{\mathrm{d}\mathbf{v}}{\mathrm{d}t}(t) = -m\gamma\mathbf{v}(t) + \mathbf{R}(t) \tag{2.1.1}$$

where m is the mass of particle and $\mathbf{v}$ its velocity.

Several assumptions are then made on the random force $\mathbf{R}(t)$. First, the fluid (also called the bath) is considered to be in a stationary state; in most cases, the bath will be considered in thermodynamic equilibrium. Hence, the random force $\mathbf{R}(t)$ is stationary, meaning that the two following conditions are satisfied:

1. its mean value is zero:
$$\langle \mathbf{R}(t) \rangle = 0 \tag{2.1.2}$$
This assumption is necessary so that the mean value of the particle velocity is zero, as should be the case in the absence of any external force.

2. its time-correlation function is infinitely short-ranged:
$$\langle R_i(t) R_j(t') \rangle = 2Dm^2\delta(t-t')\delta_{ij}, \quad i,j = x,y,z \tag{2.1.3}$$
where $D \in \mathbb{R}$ is a constant; we anticipate that D is the diffusion constant of the particle, as we will discuss it later. This means that, for two different times t and t', $R_i(t)$ and $R_j(t')$ are independent random variables. This arises from the fact that the correlation time of the random force is of the order of the time between two collisions in the fluid, which can be assumed to be very short compared to the other characteristic times of the system.

The random force is most often a Gaussian white noise. For simplicity, we consider in the following paragraph one degree of freedom (the generalization to three dimensions is straightforward). We solve equation (2.1.1) for a given initial condition $v(t=0) = v_0$. We obtain

$$v(t) = v_0 \mathrm{e}^{-\gamma t} + \frac{1}{m}\int_0^t R(s)\mathrm{e}^{-\gamma(t-s)}\,\mathrm{d}s, \tag{2.1.4}$$

and, averaging over time, we get

$$\langle v(t) \rangle = v_0 \mathrm{e}^{-\gamma t}. \tag{2.1.5}$$

Hence, the average velocity decreases exponentially with time, due to the friction term, and the relaxation time is of the order of γ^{-1}. Furthermore, the variance $\sigma_v^2(t)$ of the velocity is given by

$$\sigma_v^2(t) = \langle v(t)^2 \rangle - \langle v(t) \rangle^2 = \frac{D}{\gamma}\left(1 - \mathrm{e}^{-2\gamma t}\right) \tag{2.1.6}$$

Equation (2.1.6) shows that at time $t = 0$, the variance is equal to zero as expected (the velocity at time $t = 0$ is known with certainty). For times shorter than the relaxation time, i.e. $t \ll \gamma^{-1}$, the variance increases linearly with time:

$$\sigma_v^2(t) \sim 2Dt. \tag{2.1.7}$$

This is characteristic of a diffusion phenomenon for the velocity, where D is the diffusion coefficient. Finally, in the long-time limit, we get

$$\sigma_v^2(t) \sim \frac{D}{\gamma} \tag{2.1.8}$$

which means that the variance has saturated. Equation (2.1.8) indicates that in the long-time limit, the fluctuations of the velocity are independent of time. The mean value of the energy of the particle is then

$$\langle E \rangle = \frac{1}{2} m \langle v(t)^2 \rangle = \frac{mD}{2\gamma}. \tag{2.1.9}$$

Thus, the particle is in equilibrium with the bath. If we now assume that the bath is in thermodynamic equilibrium, then the equipartition theorem states that

$$\langle E \rangle = \frac{1}{2} k_B T \tag{2.1.10}$$

which in turn leads to the following relation between the random force, i.e. the fluctuations, and the friction, i.e. the dissipation:

$$mD = \gamma k_B T. \tag{2.1.11}$$

We note in passing that equation (2.1.11) is equivalent to the Einstein relation for the diffusion constant [83]. Using the definition of D given in equation (2.1.3), equation (2.1.11) can also be rewritten in the form

$$\gamma = \frac{1}{m k_B T} \int_0^\infty \langle R(t) R(t+\tau) \rangle \, \mathrm{d}\tau. \tag{2.1.12}$$

This expression can also be derived in the framework of the classical fluctuation-dissipation theorem [85] as we show in the following.

2.1.2 The classical fluctuation-dissipation theorem

If we consider equation (2.1.1) (in one dimension) in Fourier space, where the Fourier transform of a function $f(t)$ is given by

$$\tilde{f}(\omega) = \frac{1}{2\pi} \int_{-\infty}^{\infty} f(t) \mathrm{e}^{i\omega t} \, \mathrm{d}t, \tag{2.1.13}$$

we obtain the following relation between the Fourier components of the velocity and the random force:

$$\tilde{v}(\omega) = \frac{1}{m} \frac{1}{\gamma - i\omega} \tilde{R}(\omega). \tag{2.1.14}$$

We now define the spectral densities of the random force and the velocity as

$$S_R(\omega) = \langle |\tilde{R}(\omega)|^2 \rangle \tag{2.1.15}$$

$$S_v(\omega) = \langle |\tilde{v}(\omega)|^2 \rangle \tag{2.1.16}$$

Equation (2.1.14) thus rewrites in the following form

$$S_v(\omega) = \frac{1}{m^2} \frac{1}{\gamma^2 + \omega^2} S_R(\omega). \tag{2.1.17}$$

This means that the spectral density of the velocity is the product of the spectral density of the random force by a Lorentzian function of width γ.

In the case of a white noise, the spectral density is independent of the frequency, i.e. $S_R(\omega) \equiv S_R$. The Wiener-Khintchine theorem states that the autocorrelation function is the inverse Fourier transform of the spectral density i.e.

$$\langle R(t) R(t') \rangle = \int_{-\infty}^{\infty} S_R \, \mathrm{e}^{-i\omega t} \, \mathrm{d}\omega = 2\pi S_R \, \delta(t - t'). \tag{2.1.18}$$

Using equation (2.1.3), we obtain

$$S_R = \frac{Dm^2}{\pi}. \tag{2.1.19}$$

The combination of the Wiener-Khintchine theorem for the velocity and equation (2.1.17) yields:

$$\langle v(t)v(0)\rangle = \frac{\pi S_R}{\gamma m^2} \mathrm{e}^{-\gamma|t|}. \tag{2.1.20}$$

Assuming the bath is in thermodynamic equilibrium, we have $\langle v(0)^2\rangle = k_B T/m$; thus,

$$\gamma = \frac{\pi S_R}{m k_B T}. \tag{2.1.21}$$

Since $S_R = S_R(\omega = 0)$, we get:

$$\gamma = \frac{1}{2mk_BT} \int_{-\infty}^{\infty} \langle R(t)R(t+\tau)\rangle \, \mathrm{d}\tau \tag{2.1.22}$$

which is also the classical fluctuation-dissipation theorem (as in equation (2.1.12)).

2.1.3 The quantum fluctuation-dissipation theorem

The classical fluctuation-dissipation theorem just described (section 2.1.2) relies on the equipartition of energy i.e. each degree of freedom has an energy proportional to the temperature. From a quantum point of view, in addition to the thermal energy, we expect the energy of a vibrational mode to be proportional to its frequency ω (since its zero-point energy is $\hbar\omega/2$). The quantum version of the fluctuation-dissipation can be derived through linear response theory [2]. We consider an unperturbed system described by the Hamiltonian $H_0(\{q_i\}, \{p_i\})$, where q_i are the coordinates and p_i the momenta. In the presence of a perturbation, the Hamiltonian of the system becomes

$$H(t) = H_0(\{q_i\}, \{p_i\}) + V(t)Q(\{q_i\}, \{p_i\}) \tag{2.1.23}$$

where Q is a function of the coordinates and momenta and V is a function of time which corresponds to the magnitude of the perturbation. Q is a generic operator for the system. Its time-derivative $\dot{Q}$ is the response of the system to the external perturbation; without any loss of generality, we assume that $\langle \dot{Q} \rangle = 0$ if $V = 0$. The wavefunction Ψ of the system thus obeys the following time-dependent Schrödinger equation:

$$i\hbar \frac{\partial \Psi}{\partial t} = H\Psi = H_0\Psi + V(t)Q\Psi \tag{2.1.24}$$

We denote $\{\Psi_j\}$ the eigenfunctions of the unperturbed Hamiltonian so that

$$H_0\Psi_j = E_j\Psi_j, \quad j = 1, N. \tag{2.1.25}$$

Hence, Ψ can be written in the form of a linear combination of the eigenfunctions $\{\Psi_j\}$:

$$\Psi = \sum_j c_j(t)\Psi_j \tag{2.1.26}$$

where the c_j are functions of time. Equation (2.1.24) thus becomes

$$i\hbar \sum_j \frac{\mathrm{d}c_j}{\mathrm{d}t}(t)\Psi_j = \sum_j c_j(t)E_j\Psi_j + \sum_j V(t)c_j(t)Q\Psi_j \tag{2.1.27}$$

leading to a set of first-order differential equations for the coefficients $c_j(t)$:

$$i\hbar\frac{\mathrm{d}c_j}{\mathrm{d}t}(t) = E_j c_j(t) + V(t)\sum_k \langle\Psi_k|Q|\Psi_j\rangle c_k(t) \tag{2.1.28}$$

If we now assume that the applied perturbation varies sinusoidally with time, i.e. $V(t) = V_0 \sin\omega t$ then we can use the standard time-dependent perturbation theory. If we consider that the energy levels of the system are densely distributed, the transition probability density from an initial state with energy E_i to a final state with energy $E_i + \hbar\omega$ is (see Appendix 2.A for more details):

$$P_{if} = \frac{\pi V_0^2}{2\hbar}\left[|\langle E_i + \hbar\omega|Q|E_i\rangle|^2\rho\left(E_i + \hbar\omega\right) + |\langle E_i - \hbar\omega|Q|E_i\rangle|^2\rho\left(E_i - \hbar\omega\right)\right] \tag{2.1.29}$$

where we denote $|E_i\rangle \equiv \Psi_i$. $\rho(E)$ indicates the energy density so that the number of states that have an energy between E and $E + \delta E$ is $\rho(E)\delta E$. Each transition from state Ψ_i to a state with energy $E_i + \hbar\omega$ is accompanied by the absorption of an energy $\hbar\omega$, and inversely, each transition to a state with energy $E_i - \hbar\omega$ is accompanied by the emission of $\hbar\omega$. Hence, the rate of absorption of energy is $\hbar\omega P_{if}$ i.e.

$$R_{\text{absorption}} = \frac{\pi V_0^2\omega}{2}\left[|\langle E_i + \hbar\omega|Q|E_i\rangle|^2\rho\left(E_i + \hbar\omega\right) - |\langle E_i - \hbar\omega|Q|E_i\rangle|^2\rho\left(E_i - \hbar\omega\right)\right]. \tag{2.1.30}$$

In order to predict the behavior of a real thermodynamic system, one must average over all possible initial states, weighted by the Boltzmann factor $f(E_i) \propto \exp\left(-E_i/k_BT\right)$. The power dissipation is then:

$$P = \sum_i R_{\text{absorption}} f(E_i) \tag{2.1.31}$$

$$\simeq \frac{\pi V_0^2\omega}{2}\int_0^\infty \rho(E)f(E)\left[|\langle E + \hbar\omega|Q|E\rangle|^2\rho\left(E + \hbar\omega\right) - |\langle E - \hbar\omega|Q|E\rangle|^2\rho\left(E - \hbar\omega\right)\right]\mathrm{d}E \tag{2.1.32}$$

We see that the power dissipation is quadratic in the perturbation. We can then define an impedance $z(\omega)$ which is the ratio of the force V to the response $\dot{Q}$. The instantaneous power dissipation is thus $V\dot{Q}r(\omega)/|z|$ where $r(\omega)$ is the real part of $z(\omega)$ (the resistance), and the average power is

$$P = \frac{V_0^2 r(\omega)}{2|z(\omega)|^2}. \tag{2.1.33}$$

Hence:

$$\frac{r}{|z|^2} = \pi\omega\int_0^\infty \rho(E)f(E)\left[|\langle E + \hbar\omega|Q|E\rangle|^2\rho\left(E + \hbar\omega\right) - |\langle E - \hbar\omega|Q|E\rangle|^2\rho\left(E - \hbar\omega\right)\right]\mathrm{d}E \tag{2.1.34}$$

We now consider the system without any external perturbation. We expect that the system will exhibit spontaneous fluctuations (i.e. $\dot{Q}(t) \neq 0$ at a given time t), that we may associate with a spontaneously fluctuating force ($V(t)$). If the system is in the eigenstate Ψ_n, then $\langle E_n|\dot{Q}|E_n\rangle = 0$ due to the hermitian property of the Hamiltonian H_0. The mean

square fluctuation of $\dot{Q}$ is thus given by

$$\begin{aligned}\langle E_n|\dot{Q}^2|E_n\rangle &= \sum_k \langle E_n|\dot{Q}|E_k\rangle\langle E_k|\dot{Q}|E_n\rangle \\ &= \frac{1}{\hbar^2}\sum_k \langle E_n|H_0Q - QH_0|E_k\rangle\langle E_k|H_0Q - QH_0|E_n\rangle \\ &= \frac{1}{\hbar^2}\sum_k (E_n - E_k)^2|\langle E_k|Q|E_n\rangle|^2.\end{aligned}$$

We introduce the frequency $\omega = |E_n - E_k|/\hbar$, and we obtain:

$$\begin{aligned}\langle E_n|\dot{Q}^2|E_n\rangle &= \frac{1}{\hbar^2}\int_0^\infty (\hbar\omega)^2|\langle E_n + \hbar\omega|Q|E_n\rangle|^2\rho(E_n + \hbar\omega)\hbar\mathrm{d}\omega \\ &+ \frac{1}{\hbar^2}\int_0^\infty (\hbar\omega)^2|\langle E_n - \hbar\omega|Q|E_n\rangle|^2\rho(E_n - \hbar\omega)\hbar\mathrm{d}\omega \\ &= \int_0^\infty \hbar\omega^2\left[|\langle E_n + \hbar\omega|Q|E_n\rangle|^2\rho(E_n + \hbar\omega) + |\langle E_n - \hbar\omega|Q|E_n\rangle|^2\rho(E_n - \hbar\omega)\right]\mathrm{d}\omega.\end{aligned}$$

We now sum over all eigenstates, correctly weighted by $f(E_n)$:

$$\langle\dot{Q}^2\rangle = \int_0^\infty \hbar\omega^2\left[\int_0^\infty \rho(E)f(E)\left[|\langle E + \hbar\omega|Q|E\rangle|^2\rho(E + \hbar\omega) + |\langle E - \hbar\omega|Q|E\rangle|^2\rho(E - \hbar\omega)\right]\mathrm{d}E\right].\mathrm{d}\omega$$

Thus, we obtain

$$\begin{aligned}\langle V^2\rangle = \int_0^\infty |Z|^2\hbar\omega^2\Bigg[\int_0^\infty \rho(E)f(E)\Big[&|\langle E + \hbar\omega|Q|E\rangle|^2\rho(E + \hbar\omega) \\ &+ |\langle E - \hbar\omega|Q|E\rangle|^2\rho(E - \hbar\omega)\Big]\mathrm{d}E\Bigg]\mathrm{d}\omega.\end{aligned} \tag{2.1.35}$$

Both quantities $r/|z|^2$ (equation (2.1.34) - which is related to the power dissipation) and $\langle V^2\rangle$ (equation (2.1.35) - which is the mean square value of the spontaneous fluctuating force in the absence of any external perturbation) involve the following integrals:

$$I_\pm = \int_0^\infty \rho(E)f(E)\left[|\langle E + \hbar\omega|Q|E\rangle|^2\rho(E + \hbar\omega) \pm |\langle E - \hbar\omega|Q|E\rangle|^2\rho(E - \hbar\omega)\right]\mathrm{d}E. \tag{2.1.36}$$

The integral runs over positive energies E i.e. on energies higher than the ground-state energy which is assumed to be 0. Hence, $\rho(E) = 0$ for $E < 0$ since there are no states with an energy lower than the ground-state energy and $\rho(E - \hbar\omega) = 0$ for $E < \hbar\omega$. Hence:

$$\begin{aligned}I_- &= \int_0^\infty \rho(E)f(E)|\langle E + \hbar\omega|Q|E\rangle|^2\rho(E + \hbar\omega)\mathrm{d}E \\ &- \int_0^\infty \rho(E)f(E)|\langle E - \hbar\omega|Q|E\rangle|^2\rho(E - \hbar\omega)\mathrm{d}E \\ &= \int_0^\infty \rho(E)f(E)|\langle E + \hbar\omega|Q|E\rangle|^2\rho(E + \hbar\omega)\mathrm{d}E \\ &- \int_0^\infty \rho(E + \hbar\omega)f(E + \hbar\omega)|\langle E|Q|E + \hbar\omega\rangle|^2\rho(E)\mathrm{d}E \\ &= \int_0^\infty \rho(E)|\langle E + \hbar\omega|Q|E\rangle|^2\rho(E + \hbar\omega)\left(f(E) - f(E + \hbar\omega)\right)\mathrm{d}E.\end{aligned}$$

Since $f(E + \hbar\omega)/f(E) = \exp(-\hbar\omega/k_BT)$, we obtain:

$$I_- = \left(1 - \mathrm{e}^{-\hbar\omega/k_BT}\right)\int_0^\infty \rho(E)f(E)|\langle E + \hbar\omega|Q|E\rangle|^2\rho(E + \hbar\omega)\mathrm{d}E \tag{2.1.37}$$

Similarly:

$$I_+ = \left(1 + \mathrm{e}^{-\hbar\omega/k_BT}\right) \int_0^\infty \rho(E) f(E) |\langle E + \hbar\omega | Q | E \rangle|^2 \rho(E + \hbar\omega) \mathrm{d}E \tag{2.1.38}$$

Thus:

$$\frac{R}{|Z|^2} = \pi\omega I_- \tag{2.1.39}$$

$$\langle V^2 \rangle = \int_0^\infty |Z|^2 \hbar\omega^2 I_+ \tag{2.1.40}$$

This yields directly the following relation between the fluctuations $\langle V^2 \rangle$ and the energy dissipation R:

$$\langle V^2 \rangle = \frac{2}{\pi} \int_0^\infty R(\omega) E(\omega, T) \mathrm{d}\omega \tag{2.1.41}$$

where

$$E(\omega, T) = \hbar\omega \left[\frac{1}{2} + \frac{1}{\exp\left(\hbar\omega / k_B T\right) - 1} \right]. \tag{2.1.42}$$

Formally, $E(\omega, T)$ is the mean energy of a harmonic oscillator of frequency ω at temperature T. At high temperatures, i.e. $k_BT \gg \hbar\omega$, we recover the classical equipartition value $E(\omega, T) \approx k_BT$.

2.2 Formalism of the Quantum Thermal Bath

2.2.1 The equations of motion

The Quantum Thermal Bath (QTB) applied to molecular dynamics (MD), was introduced by Dammak and coworkers in 2009 [1]. The idea is to use a Langevin equation for the motion of the nuclei similar to equation (2.1.1). Hence, for each particle of mass m and position $\mathbf{r}$, the equation of motion is

$$m \frac{\mathrm{d}^2\mathbf{r}}{\mathrm{d}t^2}(t) = \mathbf{f}(\mathbf{r}) - m\gamma \frac{\mathrm{d}\mathbf{r}}{\mathrm{d}t}(t) + \mathbf{R}(t) \tag{2.2.1}$$

where $\mathbf{f}$ is the internal force acting on the nucleus and given by the other nuclei and electrons in the system[1], γ is a friction coefficient and $\mathbf{R}$ is a random force.

When the particle is *classical*, the random force consists in a white noise, which simulates the thermal fluctuations of the system (see section 2.1.1). In this case, its spectral density is related to the friction coefficient by

$$S_R^{(\mathrm{class})}(\omega) \equiv \langle |\tilde{R}_i^{(\mathrm{class})}|^2 \rangle(\omega) = 2m\gamma k_B T, \quad i = x, y, z \tag{2.2.2}$$

In this framework, which we will denote by "standard Langevin MD", the energy equipartition theorem holds and each degree of freedom has the same mean energy. The frequency of each vibration mode does not affect its energy; hence $S_R^{(\mathrm{class})}$ does not depend on ω (see Figure 2.2.1).

The idea behind the QTB method is to replace the white noise by a "colored-noise", which depends on the frequency. In order for the quantum fluctuation-dissipation theorem

[1] Within the Born-Oppenheimer approximation - see appendix 2.B.2, $\mathbf{f} = -\nabla_{\mathbf{r}} E_{\mathrm{tot}}\left(\{\mathbf{r}_i\}, \{\mathbf{R}_j\}\right)$ where E_{tot} is the total (internal) potential energy of the system.

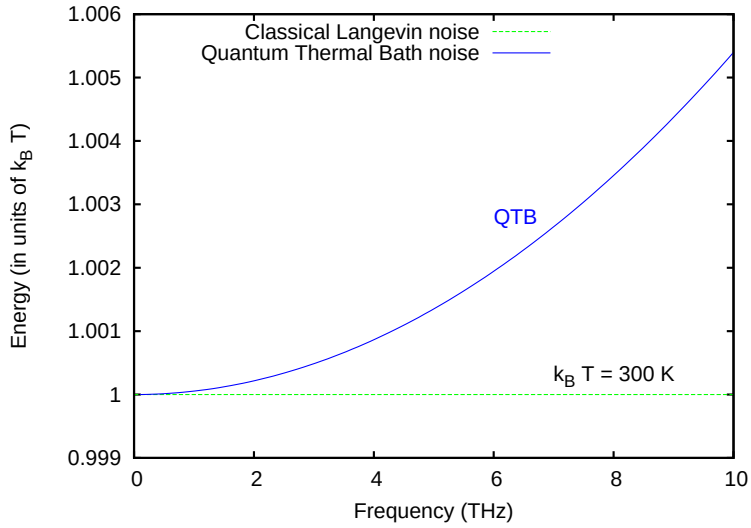

Figure 2.2.1: Spectral density of the random force in standard Langevin molecular dynamics (classical) and in QTB molecular dynamics.

to be verified (equation (2.1.41)), the spectral density of the random force in the QTB framework is given by the following equation:

$$S_R^{(\mathrm{QTB})}(\omega) \equiv \langle |\tilde{R}_i^{(\mathrm{QTB})}|^2 \rangle(\omega) = 2m\gamma\hbar|\omega| \left[\frac{1}{2} + \frac{1}{\exp\left(\hbar|\omega|/k_BT\right) - 1}\right]. \tag{2.2.3}$$

In this case, the random force simulates both the thermal and the quantum fluctuations of the system. In contrast with the classical white noise, which tends to zero at low temperature i.e. when $k_BT \to 0$, the QTB random force does not vanish since :

$$\lim_{T\to 0} S_R^{(\mathrm{QTB})}(\omega) = 2m\gamma\frac{\hbar|\omega|}{2}. \tag{2.2.4}$$

This term corresponds to the residual motion at $T = 0$ due to the zero-point energy of the system (see Figure 2.2.1). On the other hand, at high temperatures, i.e. when $k_BT \gg \hbar\omega$, the QTB random force is similar to the classical white noise:

$$\lim_{T\to\infty} S_R^{(\mathrm{QTB})}(\omega) = 2m\gamma k_BT = S_R^{(\mathrm{class})}. \tag{2.2.5}$$

The QTB method thus requires no previous knowledge of the frequencies of the system, and is completely general (there are no fitting parameters). In practice, the random forces are generated at the beginning of the simulation and then read throughout the simulation, at each time step. Therefore, QTB MD presents no additional computational cost compared to standard Langevin MD.

2.2.2 The case of a harmonic oscillator

In the case of a harmonic oscillator, the QTB formalism is exact since the quantum fluctuation-dissipation theorem holds in the linear regime. We consider a one-dimensional harmonic oscillator of frequency ω_0. The equation of motion (2.2.1) can be rewritten in the following form:

$$m\ddot{x} = -m\omega_0^2 x - m\gamma\dot{x} + \sqrt{2m\gamma}\theta \tag{2.2.6}$$

where the random force has been rewritten in the form $R(t) = \sqrt{2m\gamma}\theta(t)$. In Fourier space, we obtain:

$$-m\omega^2\tilde{x} = -m\omega_0^2\tilde{x} - im\gamma\omega\tilde{x} + \sqrt{2m\gamma}\tilde{\theta}. \tag{2.2.7}$$

$\tilde{x}(\omega)$ is the Fourier transform of $x(t)$ and is:

$$\tilde{x}(\omega) = \frac{\sqrt{2\gamma}}{m}\frac{\tilde{\theta}(\omega)}{\omega_0^2 - \omega^2 + i\gamma\omega} \tag{2.2.8}$$

The mean energy of the oscillator with position $\tilde{x}$ and velocity $\tilde{v} = i\omega\tilde{x}$ is then given by

$$E = \int_{-\infty}^{+\infty} \left[\frac{1}{2}m\omega_0^2|\tilde{x}(\omega)|^2 + \frac{1}{2}m|\tilde{v}(\omega)|^2\right] \frac{\mathrm{d}\omega}{2\pi} \tag{2.2.9}$$

Hence:

$$E = \int_{-\infty}^{+\infty} \frac{\gamma(\omega^2 + \omega_0^2)}{(\omega_0^2 - \omega^2)^2 + \gamma^2\omega^2}|\tilde{\theta}(\omega)|^2 \frac{\mathrm{d}\omega}{2\pi} \tag{2.2.10}$$

Classical harmonic oscillator In the classical case, θ is a white noise and we have: $|\tilde{\theta}(\omega)|^2 = k_BT$. Hence, the energy of the oscillator is:

$$E = \frac{\gamma k_BT}{2\pi}\int_{-\infty}^{+\infty} \frac{\omega^2 + \omega_0^2}{(\omega_0^2 - \omega^2)^2 + \gamma^2\omega^2}\,\mathrm{d}\omega \tag{2.2.11}$$

We then use the residue theorem which gives:

$$E = \frac{\gamma k_BT}{2\pi}2\pi i\sum \mathrm{Res} \tag{2.2.12}$$

where Res are the residues of the integrand. The poles of the integrand obey the following equation:

$$(\omega_0^2 - \omega^2)^2 + \gamma^2\omega^2 = \left(\omega_0^2 - \omega^2 + i\gamma\omega\right)\left(\omega_0^2 - \omega^2 - i\gamma\omega\right) = 0 \tag{2.2.13}$$

Thus, the integrand has four poles given by:

$$\omega_1 = \frac{i\gamma}{2} + \Omega, \quad \omega_2 = \frac{i\gamma}{2} - \Omega, \quad \omega_3 = -\frac{i\gamma}{2} + \Omega, \quad \omega_4 = -\frac{i\gamma}{2} - \Omega \tag{2.2.14}$$

where $\Omega = \sqrt{\omega_0^2 - \gamma^2/4}$ if $\gamma < 2\omega_0$ and $\Omega = i\sqrt{\gamma^2/4 - \omega_0^2}$ otherwise. Hence, two poles have a positive imaginary part and the two others have a negative imaginary part. The residue of a function f at point a is $\mathrm{Res}(f, a) = \lim_{x\to a}(x - a)f(x)$, hence, the energy of the classical harmonic oscillator is:

$$E = \frac{\gamma k_BT}{2\pi}2\pi i\left[\mathrm{Res}(\omega_1) + \mathrm{Res}(\omega_2)\right] \tag{2.2.15}$$

and, whether $\gamma - 2\omega_0$ is positive or negative, we obtain:

$$E^{(\mathrm{class})} = k_BT \tag{2.2.16}$$

which is simply the thermal energy. As expected, the energy is independent of the friction coefficient γ and the frequency ω_0.

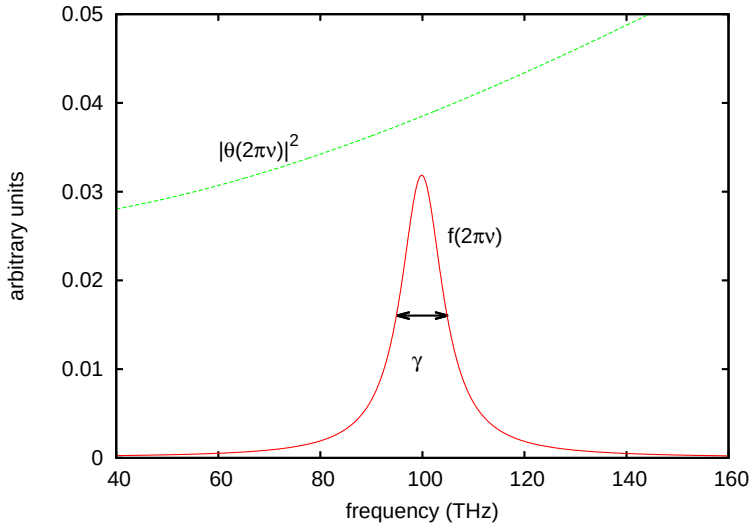

Figure 2.2.2: The two parts of the integrand of the energy integral in equation (2.2.10): $f(2\pi\nu) \equiv f(\omega) = \frac{1}{2\pi}\frac{\gamma(\omega^2+\omega_0^2)}{(\omega_0^2-\omega^2)^2+\gamma^2\omega^2}$ and $|\tilde{\theta}(\omega)|^2$ is given in equation (2.2.17). Here, $T = 300$ K, $\nu_0 = 100$ THz and $\gamma = 10$ THz.

Quantum harmonic oscillator For a quantum harmonic oscillator, the noise $\tilde{\theta}$ depends on the frequency ω. If we choose

$$|\tilde{\theta}(\omega)|^2 = \hbar|\omega|\left[\frac{1}{2} + \frac{1}{\exp(\hbar|\omega|/k_BT) - 1}\right], \tag{2.2.17}$$

then the integral in equation (2.2.10) diverges for large values of ω for any finite value of γ. Indeed, the integrand behaves as $1/|\omega|$ for large values of ω, as pointed out by Barrat and coworkers [86]. This comes from the fact the QTB includes fluctuations for all frequencies, even for arbitrary high frequencies, which are not expected to be present in a real system. Hence, we introduce a cutoff frequency Ω_{cut} in the generation of the QTB so that the noise has a finite frequency support $[-\Omega_{\text{cut}}, \Omega_{\text{cut}}]$. This is easily justified if Ω_{cut} is larger than any physical frequency contained in the system. In particular, the integrand in equation (2.2.10) consists in a function centered around ω_0 with a width γ multiplied by $|\tilde{\theta}(\omega)|^2$ (see Figure 2.2.2): the integrand is therefore still centered in ω_0 but is no longer symmetric (its tail for $|\omega| > \omega_0$ is longer than for $|\omega| < \omega_0$). Hence, we can choose any value for Ω_{cut} that is larger than $\omega_0 + \gamma$ for example i.e. Ω_{cut} larger than the tail of the integrand. In this case, for large values of $|\omega|$, we have:

$$\frac{\gamma(\omega^2+\omega_0^2)}{(\omega_0^2-\omega^2)^2+\gamma^2\omega^2}|\tilde{\theta}(\omega)|^2 \sim \frac{\gamma\hbar}{|\omega|} \tag{2.2.18}$$

and thus the divergent part of the integral is proportional to $\hbar\gamma\ln(\Omega_{\text{cut}})$. For a given value of Ω_{cut}, one should then choose γ small enough that this term is negligible compared to the energy. Then, if γ is small enough, we simply obtain:

$$E^{(\text{quant})} \approx |\tilde{\theta}(\omega_0)|^2 \tag{2.2.19}$$

and the energy of the oscillator is simply the zero-point energy and the Bose-Einstein distribution. However, the accuracy of the energy typically depends on the friction coefficient γ. The top panel in Figure 2.2.3 shows the influence of γ on the total energy given by

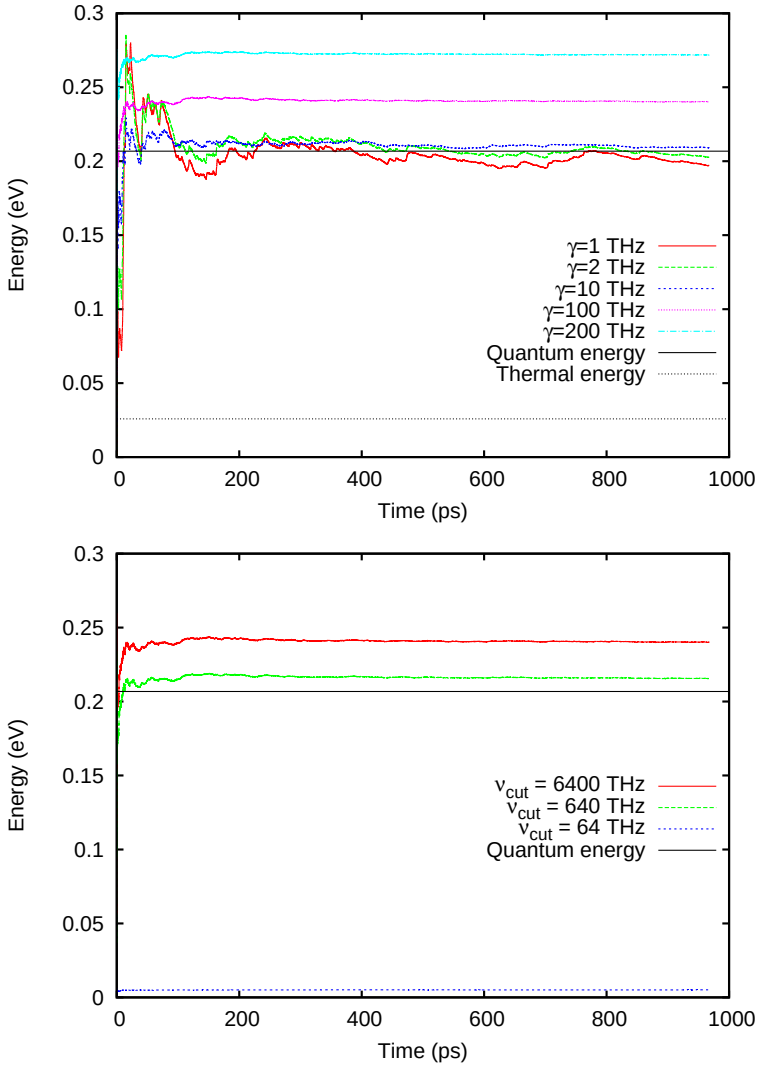

Figure 2.2.3: Time evolution of the total energy of a harmonic oscillator ($\nu_0 = 100$ THz) given by the QTB using different friction coefficients γ (top panel) or different cutoff frequencies $\nu_{\text{cut}} \equiv \Omega_{\text{cut}}/2\pi$ (lower panel). The exact quantum energy as well as the thermal energy $k_B T$ are also indicated ($T = 300$ K, $\nu_{\text{cut}} = 6400$ THz in the top panel and $\gamma = 100$ THz in the lower panel).

QTB for a harmonic oscillator. As expected, for γ small enough, the energy given by QTB coincides with the exact quantum energy. However, if γ is too large (e.g. $\gamma \simeq \omega_0/2\pi$), the energy increases and reaches non-physical values. The correct energy can be recovered for large values of γ only if Ω_{cut} is decreased (see lower panel in Figure 2.2.3). However, if Ω_{cut} becomes too low i.e. too close to the frequency ω_0, then the relation in equation (2.2.19) is no longer true and the QTB method fails to give the correct energy.

The top panel in Figure 2.2.4 shows the probability distributions obtained via classical Langevin dynamics and via QTB at room temperature in a harmonic oscillator. We can clearly see that the QTB yields the correct quantum distribution (that we can obtain by numerically solving the exact Schrödinger equation). We can also compare the spectral density obtained via QTB to the exact result (lower panel in Figure 2.2.4): $|\tilde{x}(\omega)|^2/|\theta(\omega)|^2$ is not be dependent on the type of noise chosen and both classical Langevin dynamics and QTB provide the correct spectral density (the exact expression is derived from equation (2.2.8)).

2.3 Technical details

2.3.1 Implementation of QTB in Quantum Espresso

We compute the random force $R_{i\alpha}(t)$ for each degree of freedom (i, α) (where i is the atom index and α is the Cartesian coordinate) using a numerical technique designed to generate Gaussian-distributed stochastic variables with a prescribed correlation function [87, 88]. For a time interval $[0, t_{\max}]$, with time step $\delta t = t_{\max}/(N-1)$, the corresponding frequencies are $\nu_n = n/t_{\max}$, with $n \in [0, N/2]$. For each degree of freedom (i, α) and for each frequency ν_n, two independent random numbers are generated, ξ_1 and ξ_2, so that the Fourier transform of the random noise is:

$$\tilde{R}_{i\alpha} = \sqrt{\frac{t_{\max}}{2}} \sqrt{2 m_i \gamma |\theta(\omega_n, T)|^2}\, (\xi_1 + i\xi_2) \tag{2.3.1}$$

where $\theta(\omega, T)$ is defined by equation (2.2.17) and m_i is the mass of atom i. We then perform an inverse Fourier transform to get the random force in real time space, for each time step and each degree of freedom of the MD simulation. We also want to avoid the collective motion of the system. Therefore, we replace $R_{i\alpha}$ by $R_{i\alpha} - m_i \sum_j R_{j\alpha} / \sum_j m_j$.

Quantum Espresso [89] is an ensemble of open-source computer codes for electronic structure calculations based on density functional theory (DFT), plane waves and pseudopotentials (see Appendix 2.B). Molecular dynamics algorithms based on the Born-Oppenheimer approximation are available in the PWscf package. The basic structure of this package is shown in a schematic way in Figure 2.3.1. The main program manages the input and output and at each time step, calls the programs `electrons.f90` and `move_ions.f90`. The first one computes the interatomic forces using DFT for a certain set of atomic positions at time t. The second program generates the new set of atomic positions at time $t+\delta t$. The different MD algorithms are implemented in the `dynamics_module.f90` program, which is where we added two new subroutines: `langevin_classical_md` and `langevin_qtb_md` corresponding to the numerical integration of the equations of motion (2.2.1) with a white noise and with a colored noise obeying equation (2.2.3) respectively.

The integration algorithm consists in a modified Verlet algorithm or "velocity-verlet", described in Reference [90]. For the sake of simplicity, we show how this algorithm works in the following paragraph for one degree of freedom x. If this degree of freedom is simply submitted to an internal force $f(x)$ which depends only on the position $x(t)$ then the

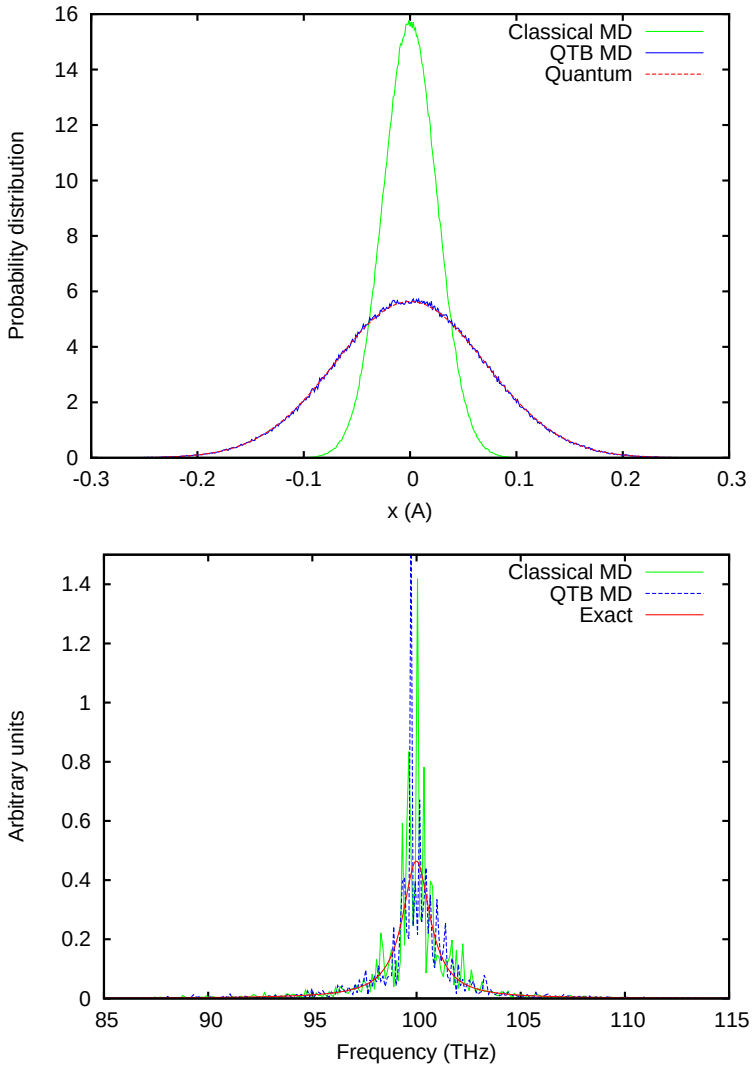

Figure 2.2.4: Top panel: Probability distribution in a harmonic oscillator ($\nu_0 = 100$ THz, $T = 300$ K) obtained via classical Langevin dynamics (in green), via QTB (in blue) and via the numerical solution of the Schrödinger equation (in red). We chose a friction coefficient $\gamma = 10$ THz and a cutoff frequency $\nu_{\text{cut}} = 6400$ THz approximately. Lower panel: Spectra ($|\tilde{x}(\omega)|^2$ / $\left|\tilde{\theta}(\omega)\right|^2$) obtained via classical Langevin dynamics (in green), QTB (in blue) compared to the exact result (in red - see equation (2.2.8)). *The QTB and classical spectra have been filtered to avoid any non-physical high-frequency noise.*

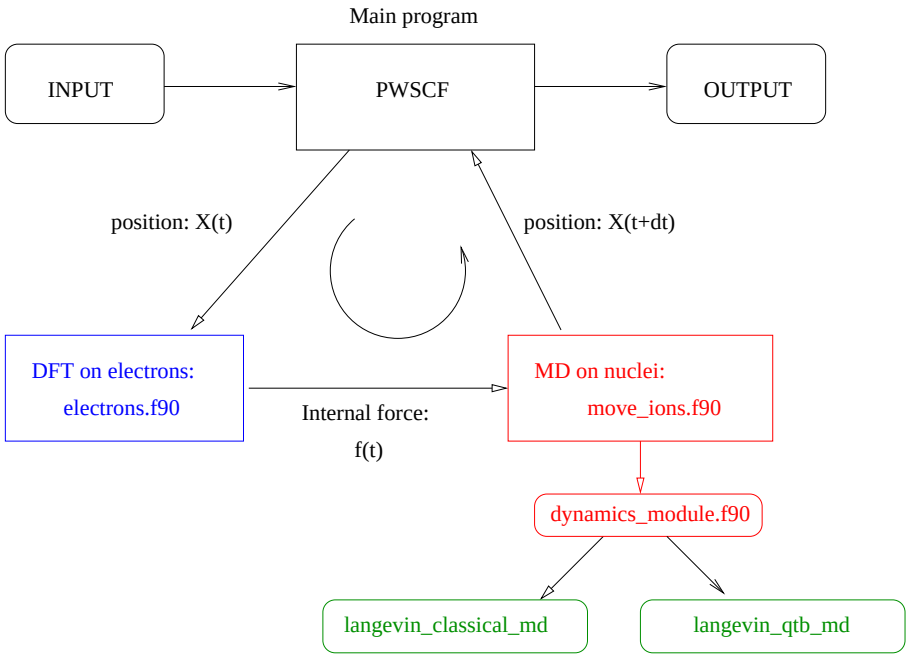

Figure 2.3.1: Schematic description of the PWscf package in the Quantum Espresso code [89].

velocity at a half time step $(t + \mathrm{d}t)$ is given by (see Figure 2.3.2):

$$v\left(t + \frac{\mathrm{d}t}{2}\right) = v(t) + \frac{\mathrm{d}t}{2} \cdot \frac{f(x(t))}{m} \tag{2.3.2}$$

The position and the velocity at time $t + \mathrm{d}t$ are then

$$x(t + \mathrm{d}t) = x(t) + \mathrm{d}t \cdot v\left(t + \frac{\mathrm{d}t}{2}\right) \tag{2.3.3}$$

$$v(t + \mathrm{d}t) = v\left(t + \frac{\mathrm{d}t}{2}\right) + \frac{\mathrm{d}t}{2} \cdot \frac{f(x(t + \mathrm{d}t))}{m} \tag{2.3.4}$$

In our case, there are two additional forces, the random force $R(t)$ and the friction term, $-m\gamma v(t)$. Hence, the first step of the algorithm becomes:

$$v\left(t + \frac{\mathrm{d}t}{2}\right) = \left[1 - \gamma\frac{\mathrm{d}t}{2}\right] v(t) + \frac{\mathrm{d}t}{2} \cdot \frac{f(x(t)) + R(t)}{m} \tag{2.3.5}$$

Then, we obtain at $t + \mathrm{d}t$:

$$x(t + \mathrm{d}t) = x(t) + \mathrm{d}t \cdot v\left(t + \frac{\mathrm{d}t}{2}\right) \tag{2.3.6}$$

$$v(t + \mathrm{d}t) = \left[v\left(t + \frac{\mathrm{d}t}{2}\right) + \frac{\mathrm{d}t}{2} \cdot \frac{f(x(t + \mathrm{d}t)) + R(t + \mathrm{d}t)}{m}\right] \left(1 + \gamma\frac{\mathrm{d}t}{2}\right)^{-1} \tag{2.3.7}$$

Therefore, the algorithm consists in three steps: from the knowledge of the position and the velocity at time t, one can first compute the internal force $f(x(t))$ and the intermediate velocity at time $t + \mathrm{d}t/2$; then, one computes the new position and the new force at time $t+\mathrm{d}t$; finally, one computes the velocity at time $t+\mathrm{d}t$. We note in passing that, within the "velocity-verlet" algorithm, the velocities are accurate up to $(\mathrm{d}t/2)^3$, while the positions

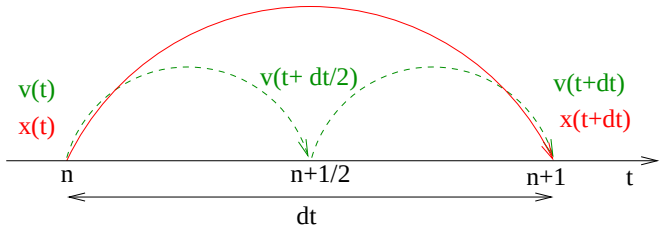

Figure 2.3.2: Schematic representation of the modified Verlet integration algorithm [90] used to solve the Langevin equation of motion (2.2.1) in Quantum Espresso [89].

are accurate up to $(\mathrm{d}t)^4$ as in the standard Verlet algorithm. Finally, one should note that the PWscf package of Quantum Espresso uses Rydberg atomic units, which are recalled in Appendix 2.C. In practice, to run a QTB or a classical Langevin dynamics simulation within Quantum Espresso, the input file should contain the following parameters:

Name	Type	Value
calculation	*character*	`'md'`
nstep	*integer*	number of time steps; nstep+1 should be a power of 2
ion_dynamics	*character*	`'langevin_classical'` or `'langevin_qtb'`
langevin_friction	*real*	friction coefficient in THz
cutoff_freq_qtb	*real*	cutoff frequency in THz.

2.3.2 Vibrational spectra from QTB trajectories

In both Langevin and QTB molecular dynamics, we can compute the vibrational spectrum of the system directly from the atomic trajectories, via a simple Fourier Transform of the atomic autocorrelation function [91].

Incoherent spectrum In the following manuscript, whenever it is not specified, the spectrum is the *incoherent* vibrational spectrum:

$$I_{\mathrm{incoh}}(\omega) = \frac{1}{N}\sum_{k=1}^{N}\left|\tilde{C}_{vv}^{(k)}(\omega)\right|^2 \tag{2.3.8}$$

where N is the number of atoms in the system and $\tilde{C}_{vv}^{(k)}(\omega)$ is the Fourier Transform of the velocity-velocity autocorrelation function of atom k:

$$\tilde{C}_{vv}^{(k)}(\omega) \propto \int_{-\infty}^{+\infty} \langle v_k(t)v_k(t+\tau)\rangle \mathrm{e}^{-i\omega\tau}\,\mathrm{d}\tau \tag{2.3.9}$$

where v_k is the velocity of atom k and $\langle\cdot\rangle$ indicates the average over time. We note in passing that $I_{\mathrm{incoh}}(\omega)$ can also be obtained via the Fourier Transform of the atomic positions as well (the only difference is a multiplication by ω^2). Equation (2.3.8) yields the *complete* vibrational spectrum. However, the intensities of the computed spectrum are not directly related to the infrared spectrum because we neglect the calculation of dynamical charges entering the infrared matrix element. Nevertheless, we can compare the positions of the peaks in the computed vibrational spectrum to the frequencies obtained via infrared or Raman spectroscopy. The computed spectrum can also be filtered if we

are interested in some particular vibration modes. For example, if we are interested in the oxygen-hydrogen stretching mode, one can compute directly:

$$I(\omega) \propto \sum_{k=1}^{N_H} \left| \int \mathrm{d_{OH}}(t) \mathrm{e}^{-i\omega t} \mathrm{d}t \right|^2 \tag{2.3.10}$$

where the sum runs over all hydrogen atoms in the system and $\mathrm{d_{OH}}$ is the distance between a hydrogen and its nearest oxygen. $I(\omega)$ will thus contain all information concerning the vibrations of the O-H segment. In a more general way, if we are interested in a particular vibrational mode, we can define the associated vector $\mathbf{w}_p$, which has $3N$ components and N is the total number of atoms in the system. The spectrum associated to this vibration is then obtained via the Fourier Transform of the scalar product of $\mathbf{w}_p$ and $\mathbf{\Delta r} = \mathbf{r} - \overline{\mathbf{r}}$ where $\mathbf{r}$ is a $3N$-components vector containing the positions of the N atoms and $\overline{\mathbf{r}}$ is its time average:

$$I_p(\omega) \propto \left| \int \mathbf{w}_p \cdot \mathbf{\Delta r}(t) \mathrm{e}^{-i\omega t} \, \mathrm{d}t \right|^2 \tag{2.3.11}$$

This method has the advantage of yielding relatively precise information about the peaks in the vibrational spectrum rendering their interpretation easier. However, it requires the knowledge of the nature of the vibrations (i.e. the vector $\mathbf{w}_p$) beforehand. The vectors $\mathbf{w}_p$ can be accessed via dynamical matrix calculations for instance. Indeed, we assume that if the *nature* of the vibration remains relatively similar in the harmonic approximation and in the anharmonic system, then the same eigenvector can be used. This kind of interpretation needs to be confirmed by confronting the computed results to experimental data for example. Other methods have also been developed to extract effective normal modes from MD simulations, but are for now limited to molecular systems [92].

Coherent spectrum In equation (2.3.8), the incoherent spectrum is given by a sum over the square modulus of each individual autocorrelation function. On the other hand, the *coherent* vibrational spectrum is given by [91]:

$$I_{\mathrm{coh}}(\omega) = \left| \frac{1}{N} \sum_{k=1}^{N} \tilde{C}_{vv}^{(k)}(\omega) \right|^2 . \tag{2.3.12}$$

If the atomic vibrations are not in phase and basically independent from each other, then $I_{\mathrm{coh}} \ll I_{\mathrm{incoh}}$. However, the analysis of the coherent spectrum allows to determine whether there are any collective motions of the atoms in the system. Figure 2.3.3 shows the difference between the coherent and the incoherent spectra in the case of high-pressure ice (see also chapter 3). Below a critical pressure (approximately 70 GPa), there is no collective motion of hydrogen atoms in ice (corresponding to phase VII). However, above this critical pressure, there are coherent vibrations of the hydrogen atoms, corresponding to the phase X of ice. These different characteristics can also be seen via the real-time velocity autocorrelation function, shown in Figure 2.3.4. In phase VII, at approximately 50 GPa, the autocorrelation function simply displays an exponential damping. On the contrary, at higher pressures in phase X, oscillations appear which indicate coherent vibrations of protons in this phase.

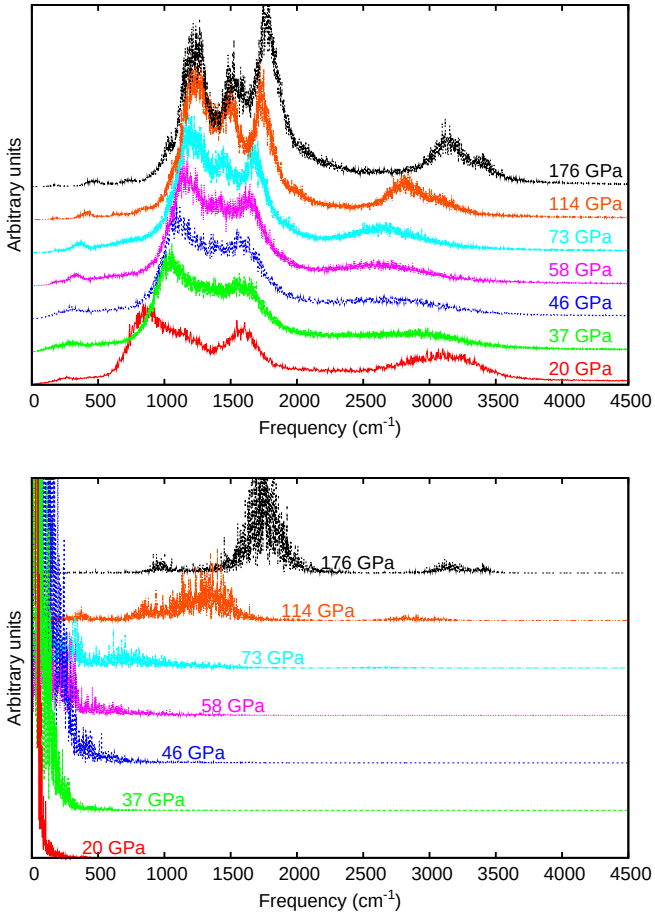

Figure 2.3.3: Incoherent (top panel) and coherent (lower panel) spectra of hydrogen atoms in high-pressure ice VII and ice X for different pressures computed from QTB simulations (from Supplemental Material of reference [5]).

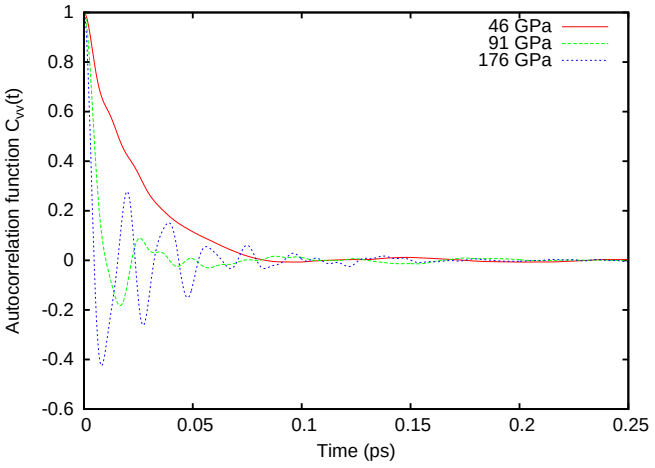

Figure 2.3.4: Hydrogen velocity autocorrelation function $C_{vv}(t)$ in high-pressure ice for different pressures computed from QTB simulations (from Supplemental Material of reference [5]).

Appendix

2.A Perturbation theory

In section 2.1.3, we showed that the coefficient $c_j(t)$ obey the set of equations (2.1.28). Without any perturbation, these equations become:

$$\frac{\mathrm{d}c_j^{(0)}}{\mathrm{d}t}(t) + \frac{i}{\hbar}E_j c_j^{(0)}(t) = 0 \tag{2.A.1}$$

which can be solved directly:

$$c_j^{(0)}(t) = a_j \mathrm{e}^{-iE_j t/\hbar} \tag{2.A.2}$$

where $a_j = c_j^{(0)}(t=0)$ are constants. If we now substitute $c_j(t) = a_j(t)\mathrm{e}^{-iE_j t/\hbar}$ into equation (2.1.28) in the presence of a perturbation, we get the following equation for the coefficients $a_j(t)$:

$$i\hbar\frac{\mathrm{d}a_j}{\mathrm{d}t}(t) = V(t)\sum_k \langle\Psi_k|Q|\Psi_j\rangle a_k(t)\mathrm{e}^{-i(E_k-E_j)t/\hbar} \tag{2.A.3}$$

Since $V(t) = V_0 \sin\omega t$ is considered a perturbation, we can decompose a_j in powers of V_0, i.e.

$$a_j(t) = \sum_k V_0^k a_j^{(k)}(t) \tag{2.A.4}$$

Hence, equation (2.A.3) becomes at the first orders:

$$i\hbar\frac{\mathrm{d}a_j^{(0)}}{\mathrm{d}t}(t) = 0 \tag{2.A.5}$$

$$i\hbar\frac{\mathrm{d}a_j^{(1)}}{\mathrm{d}t}(t) = \sin\omega t\sum_k \langle\Psi_k|Q|\Psi_j\rangle a_k^{(0)}(t)\mathrm{e}^{-i(E_k-E_j)t/\hbar} \tag{2.A.6}$$

Now, if we assume that at time $t=0$, the system Ψ is an initial state Ψ_i, then

$$c_j(t=0) = a_j(t=0) = \delta_{ij}, \quad j = 1, N \tag{2.A.7}$$

$$\Rightarrow \begin{cases} a_j^{(0)} = \delta_{ij}, & j = 1, N \\ a_j^{(k>0)}(t=0) = 0, & j = 1, N \end{cases} \tag{2.A.8}$$

And finally, equation (2.A.6) becomes

$$i\hbar\frac{\mathrm{d}a_j^{(1)}}{\mathrm{d}t} = \sin\omega t\,\langle\Psi_i|Q|\Psi_j\rangle\mathrm{e}^{-i(E_i-E_j)t/\hbar} \tag{2.A.9}$$

$$\Rightarrow a_j^{(1)}(t) = -\frac{i}{\hbar}\langle\Psi_i|Q|\Psi_j\rangle\int_0^t \sin\omega t'\,\mathrm{e}^{-i(E_i-E_j)t'/\hbar}\,\mathrm{d}t' \tag{2.A.10}$$

By definition, the transition probability from state Ψ_i to a final state Ψ_f is

$$P_{if}(t) = |\langle\Psi_f|\Psi\rangle|^2 = |a_f(t)|^2 \tag{2.A.11}$$

Thus, at first order in the perturbation, we get:

$$P_{if}(t) = |a_f^{(0)} + V_0 a_f^{(1)}(t)|^2 \tag{2.A.12}$$

$$= V_0^2 |a_f^{(1)}(t)|^2 \quad \text{if the final state is different from the initial state.} \tag{2.A.13}$$

Then,

$$P_{if}(t) = \frac{V_0^2}{\hbar^2} |\langle\Psi_f|Q|\Psi_i\rangle|^2 \left| \int_0^t \sin\omega t' \, \mathrm{e}^{-i(E_i - E_f)t'/\hbar} \, \mathrm{d}t' \right|^2 \tag{2.A.14}$$

$$= \frac{V_0^2}{4\hbar^2} |\langle\Psi_f|Q|\Psi_i\rangle|^2 \, |A_+ + A_-|^2 \tag{2.A.15}$$

where

$$A_+ = \frac{\mathrm{e}^{i(\omega_{fi}+\omega)t} - 1}{\omega_{fi} + \omega} \tag{2.A.16}$$

$$A_- = \frac{\mathrm{e}^{i(\omega_{fi}-\omega)t} - 1}{\omega_{fi} - \omega} \tag{2.A.17}$$

are the antiresonant and resonant terms and

$$\omega_{fi} = \frac{E_f - E_i}{\hbar} \tag{2.A.18}$$

If $\omega_{fi} > 0$ i.e. $E_f > E_i$, then the system has *absorbed* energy; on the other hand, if $\omega_{fi} < 0$, then the system has *emitted* energy. In the case of absorption, for ω near ω_{fi}, the term A_- is dominant while in the case of emission, A_+ is dominant. If we consider the two processes, we can consider that:

$$P_{if}(t) = \frac{V_0^2}{2\hbar^2} |\langle\Psi_f|Q|\Psi_i\rangle|^2 \left[|A_-|^2 + |A_+|^2 \right] \tag{2.A.19}$$

This allows us to recover the Fermi golden rule:

$$P_{if}(t) = \frac{\pi V_0^2 t}{2\hbar^2} |\langle\Psi_f|Q|\Psi_i\rangle|^2 \left[\delta\left(\omega_{fi} - \omega\right) + \delta\left(\omega_{fi} + \omega\right) \right] \tag{2.A.20}$$

If we now consider that the energy levels of the system are densely distributed, with an energy density ρ, then

$$P_{if}(t) = \int_{E_f - \mathrm{d}E}^{E_f + \mathrm{d}E} \rho(E') P_{if'} \, \mathrm{d}E' \tag{2.A.21}$$

where $P_{if'}$ is given by equation (2.A.20). By definition, we have

$$\delta(\omega_{f'i} \pm \omega) \equiv \delta(E' - E_i \pm \hbar\omega) \tag{2.A.22}$$

and we obtain, for the probability per unit of time $P_{if} \equiv \mathrm{d}P_{if}(t)/\mathrm{d}t$:

$$P_{if} = \frac{\pi V_0^2}{2\hbar} \left[|\langle E_i + \hbar\omega|Q|E_i\rangle|^2 \rho\left(E_i + \hbar\omega\right) + |\langle E_i - \hbar\omega|Q|E_i\rangle|^2 \rho\left(E_i - \hbar\omega\right) \right] \tag{2.A.23}$$

2.B Density Functional Theory

2.B.1 Introduction

In order to describe interactions between atoms, different methods are available. Empirical interatomic potentials, such as the Lennard-Jones potential, are usually fitted to reproduce some measured physical property. These potentials are however limited by their restricted applicability (their transferability to other systems than the one they have been designed for or other physical quantities is relatively low) and by the accuracy of their parametrization. Moreover, the chemical complexity of different types of bonding in a material is generally not attainable via empirical potentials which do not treat explicitly the electronic interactions. Indeed, all electronic properties of a system are also out of reach of empirical potentials. Hence, *ab initio* methods i.e. methods that do not require any a priori knowledge of the chemical bonding properties or any other experimental input, are quite appealing since they attempt to solve the Schrödinger equation for the electrons and the nuclei of the system.

2.B.2 Born-Oppenheimer approximation

The full wave function of the system $\Phi(\{\mathbf{r}_i\},\{\mathbf{R}_I\})$ obeys the following Schrödinger equation:

$$H_{\text{tot}}\Phi(\{\mathbf{r}_i\},\{\mathbf{R}_I\}) = \epsilon\,\Phi(\{\mathbf{r}_i\},\{\mathbf{R}_I\}) \tag{2.B.1}$$

where $\{\mathbf{r}_i\}$ and $\{\mathbf{R}_I\}$) are the scalar coordinates of the electrons and the nuclei respectively and ϵ is the energy of the system. The total Hamiltonian is given by:

$$H_{\text{tot}} = H_{\text{elec}} + K_N + V_N \tag{2.B.2}$$

where H_{elec} is the many-body electronic Hamiltonian, K_N the kinetic energy of the nuclei and V_N the Coulomb interaction between the nuclei:

$$H_{\text{elec}} = \sum_{i=1}^{N}\left[-\frac{\hbar^2\nabla_i^2}{2m} + V_{\text{ext}}(\mathbf{r}_i)\right] + \sum_{i<j}\frac{e^2}{|\mathbf{r}_i-\mathbf{r}_j|} \tag{2.B.3}$$

$$K_N = \sum_{I=1}^{N_N} -\frac{\hbar^2\nabla_I^2}{2M_I} \tag{2.B.4}$$

$$V_N = \sum_{I<J}\frac{Z_I Z_J e^2}{|\mathbf{R}_I-\mathbf{R}_J|} \tag{2.B.5}$$

with V_{ext} the external potential that depends on the parameters $\{\mathbf{R}_I\}$ (if all electronic interactions are taken into account, it corresponds to the Coulomb interaction between the nuclei and the electrons), N and N_N the total numbers of electrons and nuclei respectively, Z_I and M_I the atomic number and mass of the nuclei, m the mass of an electron. Solving equation (2.B.1) is completely out of reach, hence, we need to simplify the problem. The Born-Oppenheimer approximation consists in a separation of the electronic and nuclear parts of the wave function:

$$\Phi(\{\mathbf{r}_i\},\{\mathbf{R}_I\}) \approx \chi(\{\mathbf{R}_I\}) \times \Psi(\{\mathbf{r}_i\}) \tag{2.B.6}$$

where $\Psi(\{\mathbf{r}_i\})$ is now the solution to the electronic Hamiltonian H_{elec} (equation (2.B.4)) for a given configuration i.e. for fixed nuclear positions: $H_{\text{elec}}\Psi = E_{\text{elec}}\Psi$. The total energy E_{tot} is thus a function of $\{\mathbf{R}_I\}$ and

$$E_{\text{tot}}(\{\mathbf{R}_I\}) = V_N + E_{\text{elec}} \tag{2.B.7}$$

where V_N is the interaction between the nuclei and E_{elec} is the electronic energy (of the electronic ground-state). This approximation is valid in the limit where the electronic degrees of freedom vary on much smaller time scale than the nuclear degrees of freedom. Moreover, recent works have shown that such a factorization can be written exactly for any system, even in the presence of strong coupling between the electronic and the nuclear degrees of freedom [93–95]. Then, injecting equation (2.B.6) into the Schrödinger equation (2.B.1), we obtain:

$$[K_N + V_N + \epsilon]\,\chi + \Gamma = \epsilon\chi \tag{2.B.8}$$

where we used the normalization of Ψ i.e. $\langle\Psi|\Psi\rangle = 1$ and

$$\Gamma = -\sum_{I=1}^{N_N} \frac{\hbar^2}{2M_I}\left[\langle\Psi|\nabla_I^2|\Psi\rangle + 2\langle\Psi|\nabla_I|\Psi\rangle\nabla_I\right]\chi \tag{2.B.9}$$

The second approximation within the Born-Oppenheimer framework is to neglect Γ in equation (2.B.8). Indeed, if the momenta of the electrons and of the nuclei are of the same order of magnitude [96], then the ratio of the corresponding kinetic energies is of the order of the ratio of the masses, m/M_I. Hence, χ obeys a Schrödinger equation with potential energy $V_N + E$. The first term is simply the Coulomb interaction between the nuclei while the second term, called the "potential energy surface", comes from the electronic Hamiltonian. Therefore, solving equation (2.B.1) can be done in two steps within the Born-Oppenheimer approximation: first, one solves the electronic problem (equation (2.B.4)) for fixed nuclei positions thus obtaining the energy $\epsilon(\{\mathbf{R}_I\})$; then, one solves the Schrödinger equation for the nuclear part (equation (2.B.8)) neglecting Γ. Hence, if one minimizes $V_N + E$ where E is the electronic ground-state for one configuration, then one finds the atomic equilibrium positions. The Born-Oppenheimer approximation also allows to decouple the dynamics of the electrons and the nuclei: for each new atomic configuration during the molecular dynamics simulation, one can compute the electronic ground-state and the corresponding forces (see following sections for more details).

2.B.3 Density Functional Theory

In principle, one should solve the full Schrödinger equation for the system i.e. finding the complete many-body wave function. Even if one is interested only in the electronic wave function $\Psi(\{\mathbf{r}_i\})$ (see section 2.B.2) where $\mathbf{r}_i$ are the spatial coordinates of the N electrons, Ψ has $3N$ variables. As an example, lets consider a simple benzene molecule C_6H_6 which has 42 electrons. Hence, Ψ is defined in a Cartesian space of dimension $3N = 126$. To find the ground-state of the system, one needs to minimize the energy and thus minimize the matrix element $\langle\Psi|H|\Psi\rangle$, where H is the Hamiltonian. If we choose a discrete mesh to represent Ψ in space with 50 points, then the determination of any matrix element requires 50^{126} operations, which is unattainable with even the most powerful current computers.

One of the first solution to this problem was suggested by Hartree and Fock who considered that Ψ could be written as a determinant of N one-particle wave function ϕ_i i.e. $\Psi = \text{Det}(\phi_1, \ldots, \phi_N)$. Therefore, the problem consists in solving N coupled one-particle equations instead of the full N-electron wave function, which is much easier from a computational point of view. A further step is to consider a physical quantity, different from the wave function, that defines the system uniquely. The idea behind the density functional theory or DFT, is to use the electronic density, which we will briefly describe in the following paragraph.

The energy of the system is $E[\Psi] = \langle\Psi|H|\Psi\rangle$ (we consider the wave function to be normalized) and E_0 the ground-state energy is a functional of the external potential V_{ext}.

The electron density (considering electrons as indistinguishable particles) is defined as:

$$n(\mathbf{r}) = \langle \Psi | \sum_{i=1}^{N} \delta(\mathbf{r} - \mathbf{r}_i) | \Psi \rangle \tag{2.B.10}$$

where $\delta(\mathbf{r})$ is the Dirac delta function. Obviously, if one knows the Hamiltonian and the corresponding wave function Ψ, one can compute the electron density. However, in 1964, Hohemberg and Kohn showed that the reverse is also true through two theorems [97]. First, two different Hamiltonians cannot have the same ground-state electron density (if we consider non-degenerate ground-states) i.e. the ground-state energy is a functional of the electron density, $E_0 = E[n]$. Second, the energy $E[n]$ is minimal when $n(\mathbf{r})$ is indeed the ground-state density. These two theorems are easily proved and are valid for systems with a fixed number of electrons. Hence, if one knows the energy functional $E[n]$, then one needs only to minimize it to find the ground-state electron density, without any knowledge of the wave function. The problem is now to find the actual form of the energy functional $E[n]$ and its construction is a fundamental part of the DFT. Different energy functionals exist and while their form usually implies several approximations, they also perform differently depending on the system.

One of the easiest energy functional is the Thomas-Fermi-Hartree functional, $E^{\mathrm{TFH}}[n]$. The Hamiltonian in equation (2.B.4) consists in three terms: the kinetic operator, the external potential and the Coulomb potential. The energy corresponding to the external potential can be written as:

$$E_{\mathrm{ext}}[n] = \int V_{\mathrm{ext}}(\mathbf{r}) n(\mathbf{r}) \, \mathrm{d}\mathbf{r}. \tag{2.B.11}$$

If we consider the electrons as classical charges, instead of quantum particles, then the Coulomb potential can be approximated by the Hartree functional that writes:

$$E_H = \frac{e^2}{2} \iint \frac{n(\mathbf{r}) n(\mathbf{r}')}{|\mathbf{r} - \mathbf{r}'|} \, \mathrm{d}\mathbf{r}\mathrm{d}\mathbf{r}'. \tag{2.B.12}$$

In doing so, we also include the electron self-interaction, corresponding to the terms $i = j$ in equation (2.B.4), which should not appear in $U[n]$. Finally, the kinetic energy is written as:

$$K[n] \approx C \int [n(\mathbf{r})]^{5/3} \, \mathrm{d}\mathbf{r}. \tag{2.B.13}$$

This equation comes from the expression of the kinetic energy of a non-interacting homogeneous electron gas. The Thomas-Fermi-Hartree functional has many drawbacks and very often yields results different from experiments; however, it is a first attempt at an expression for the energy functional.

In order to go beyond this simple energy functional, we introduce $K_s[n]$, the kinetic energy of a virtual system consisting of non-interacting electrons but that has the exact same electron density as the real system. Therefore, we can write the exact energy functional as:

$$E[n] = K_s[n] + E_{\mathrm{ext}}[n] + E_H[n] + E_{\mathrm{xc}}[n] \tag{2.B.14}$$

where $E_{\mathrm{ext}}[n]$ is the external potential energy (equation (2.B.11)), $E_H[n]$ is the Hartree functional (equation (2.B.12)) and $E_{\mathrm{xc}}[n]$, called the "exchange-correlation energy functional" contains all the other terms. The variational equation for the energy functional becomes:

$$\frac{\delta E[n]}{\delta n(\mathbf{r})} = \frac{\delta K_s[n]}{\delta n(\mathbf{r})} + V_{\mathrm{ext}}(\mathbf{r}) + e^2 \int \frac{n(\mathbf{r}')}{|\mathbf{r} - \mathbf{r}'|} \, \mathrm{d}\mathbf{r}' + \frac{\delta E_{\mathrm{xc}}[n]}{\delta n(\mathbf{r})} = \mu \tag{2.B.15}$$

where μ is the Lagrange multiplier associated with the conservation of the number of electrons. In 1965, Kohn and Sham introduced the idea that for any system of interacting electrons, one could find a virtual system of non-interacting electrons with the exact same electron density [98]. For this virtual system, the variational equation is:

$$\frac{\delta E[n]}{\delta n(\mathbf{r})} = \frac{\delta K_s[n]}{\delta n(\mathbf{r})} + V_{1\mathrm{p}}(\mathbf{r}) = \mu \tag{2.B.16}$$

where $V_{1\mathrm{p}}$ is an effective potential. From equations (2.B.15) and (2.B.16), we get:

$$V_{1\mathrm{p}}(\mathbf{r}) = V_{\mathrm{ext}}(\mathbf{r}) + e^2 \int \frac{n(\mathbf{r}')}{|\mathbf{r} - \mathbf{r}'|}\,\mathrm{d}\mathbf{r}' + V_{\mathrm{xc}}(\mathbf{r}) \tag{2.B.17}$$

where $V_{\mathrm{xc}}(\mathbf{r}) = \delta E_{\mathrm{xc}}[n]/\delta n(\mathbf{r})$ is called the "exchange-correlation potential". One can then solve the N one-electron Schrödinger equations in order to find the one-particle wave functions ψ_i:

$$\left[-\frac{\hbar^2\nabla^2}{2m} + V_{1\mathrm{p}}(\mathbf{r})\right]\psi_i(\mathbf{r}) = \epsilon_i\psi_i(\mathbf{r}). \tag{2.B.18}$$

Then, if the potential $V_{1\mathrm{p}}$ obeys equation (2.B.17), then the electron density is then given by:

$$n(\mathbf{r}) = \sum_{i=1}^{N} f_i|\psi_i|^2 \tag{2.B.19}$$

where f_i are the occupation factors. Equations (2.B.18) and (2.B.19) are called the Kohn-Sham equations: they are non-linear (since $V_{1\mathrm{p}}$ depends on the density) but can be solved self-consistently. In passing, we note that the eigenvalues ϵ_i and eigenfunctions ψ_i do not have any physical meaning and in most cases, do not represent the actual eigenvalues of the real system.

2.B.4 The exchange-correlation functional

The exchange-correlation energy functional $E_{\mathrm{xc}}[n]$ has been introduced as the difference between the unknown energy functional $E[n]$ and the sum of several known terms (see equation (2.B.14)). In practice, $E_{\mathrm{xc}}[n]$ takes into account the electronic quantum effects, exchange and correlation, and compensates the electronic self-interaction introduced by the Hartree functional. Several approximations exist for the actual dependence of $E_{\mathrm{xc}}[n]$ on the density.

First, the local density approximation (LDA) is one of the simplest approximation to $E_{\mathrm{xc}}[n]$ and is based on the construction of the exchange and correlation for the homogeneous electron gas (HEG) [98]:

$$E_{\mathrm{xc}}^{(\mathrm{HEG})}(n) = V\frac{N}{V}e_{\mathrm{xc}}^{(\mathrm{HEG})}(n) \tag{2.B.20}$$

where $e_{\mathrm{xc}}^{(\mathrm{HEG})}$ is the exchange-correlation energy per electron in the HEG and n is the mean density in space. Within the LDA, this expression is generalized to densities that are not constant in space by assuming the same functional dependence:

$$E_{\mathrm{xc}}^{(\mathrm{LDA})}[n] = \int e_{\mathrm{xc}}^{(\mathrm{HEG})}(n(\mathbf{r}))n(\mathbf{r})\,\mathrm{d}\mathbf{r}. \tag{2.B.21}$$

The LDA functional works quite well in many systems; this is mainly due to error compensations (typically, the exchange energy is overestimated and the correlation energy is

underestimated). However, the LDA also has some drawbacks that are well known: in particular, the cohesive energies are too high within LDA, meaning that the electrons are not enough localized in space. Furthermore, long-range effects, such as van der Waals interactions, are missing due to the local nature of the LDA. Therefore, LDA poorly describes hydrogen bonds, which we are interested in in this manuscript.

Another approximation to the exchange-correlation functional is the generalized gradient approximation (GGA). It attempts to describe the electron density variations in space in terms of its gradient ∇n:

$$E_{\text{xc}}^{(\text{GGA})}[n] = E_{\text{xc}}^{(\text{LDA})}[n] + \int e_{\text{xc}}^{(\text{GGA})}(n(\mathbf{r}), \nabla n(\mathbf{r}))\, \mathrm{d}\mathbf{r} \tag{2.B.22}$$

There are many different ways to write the function $e_{\text{xc}}^{(GGA)}$. Among them, the functionals presented by Perdew and coworkers in 1996 [99] have an analytical, but complex, form. GGA functionals perform well in many systems; however, contrary to LDA, they tend to overestimate bond lengths and underestimate cohesive energies. Finally, even though they do not account for long-range effects, they usually provide a good description of hydrogen bonds, which is why we use GGA in most of our *ab initio* calculations.

In order to solve the Kohn-Sham equations ((2.B.18) and (2.B.19)), one usually expands the one-electron orbitals on a basis of set composed of known functions: these functions can be localized in space such as atomic orbitals or gaussians, or they can be delocalized such as plane waves. Some methods also use both localized and delocalized functions. Here, we will use a basis of plane waves, as implemented in the PWscf package of the Quantum Espresso code [89]. In order to speed up the calculations and in particular, reduce the number of electronic orbitals that need to be solved, we resort to pseudo-potentials. The idea relies on a separation of core electrons and valence electrons. In a first approximation, one can consider the core electrons as inert and only the valence or outer electrons are responsible for the chemical properties of the system, namely the formation of bonds. Hence, we can replace the all-electron orbital by a smoothly-varying wave function that describes the valence electrons (and therefore the bonding properties) while the core electrons are replaced by a pseudo-potential. Hence, the number of Kohn-Sham orbitals needed is reduced and the rapid oscillations of the valence orbitals near the nucleus are also avoided.

2.B.5 Density Functional Perturbation Theory

In many cases, e.g. when we are interested in the dynamics of the system, we need the electronic forces acting on the ions. We might also want to calculate lattice dynamics and atomic vibrations. Hence, we show here how to access these information via a perturbative expansion of the energy.

The atomic forces $\mathbf{F}_I$ are the first derivatives of the potential energy $V_N + E$ (see section 2.B.2) with respect to the nuclei positions $\{\mathbf{R}_I\}$, where V_N is the Coulomb interaction between the nuclei and E is the energy coming from the electronic Hamiltonian:

$$\mathbf{F}_I = -\nabla_I \left[V_N(\{\mathbf{R}_I\}) + E(\{\mathbf{R}_I\})\right] \tag{2.B.23}$$

This method requires that one knows the exact dependence of the energy E on the atomic positions, which is not feasible for systems containing more than a few atoms. However, if one considers that E is actually a functional of the density n then, since $\int n(\mathbf{r})\mathrm{d}\mathbf{r} = N$, the total derivative of $E[n]$ is simply its partial derivative. Hence, from (2.B.14) and (2.B.11),

we obtain:

$$\mathbf{F}_I = -\frac{\partial E_{\text{ext}} + \partial V_N}{\partial \mathbf{R}_I} = -Z_I e^2 \int \frac{\mathbf{r} - \mathbf{R}_I}{|\mathbf{r} - \mathbf{R}_I|^3} n(\mathbf{r})\, \mathrm{d}\mathbf{r} + \sum_{J \neq I} Z_I Z_J e^2 \frac{\mathbf{R}_J - \mathbf{R}_I}{|\mathbf{R}_J - \mathbf{R}_I|^3} \tag{2.B.24}$$

The forces can thus be computed at the same time as the energy, where n is the ground-state density.

For small atomic displacements, the potential energy of the nuclei, $E_p = V_N + E$ can be expanded in terms of the displacements $\mathbf{u}_I = \mathbf{R}_I - \mathbf{R}_I^{(\text{eq})}$ where $\mathbf{R}_I^{(\text{eq})}$ is the equilibrium position of atom I:

$$E_p = E_p^{(\text{eq})} + \sum_{I,\alpha} \underbrace{\left.\frac{\partial E_p}{\partial R_{I,\alpha}}\right|_{\text{eq}}}_{=0 \text{ by definition}} u_{I,\alpha} + \frac{1}{2} \sum_{I,J,\alpha,\beta} \left.\frac{\partial^2 E_p}{\partial R_{I,\alpha} R_{J,\beta}}\right|_{\text{eq}} u_{I,\alpha} u_{J,\beta} \tag{2.B.25}$$

where α, β indicate the Cartesian coordinates. In the harmonic approximation, all terms of order higher than 2 are neglected. In this case, we can define an interatomic force constant matrix C so that the force acting on atom I due to the displacement $\mathbf{u}_I$ is:

$$F_{I,\alpha} = -\sum_{J,\beta} C_{I,\alpha,J,\beta} u_{J,\beta} \tag{2.B.26}$$

and

$$C_{I,\alpha,J,\beta} = \left.\frac{\partial^2 E_p}{\partial R_{I,\alpha} R_{J,\beta}}\right|_{\text{eq}} \tag{2.B.27}$$

The displacements $\mathbf{u}_I$ then correspond to harmonic oscillators: $u_{I,\alpha}(t) = u_{I,\alpha}^{(0)}/\sqrt{M_I}\exp(i\omega t)$. Injecting this expression into the equation of motion for the atom I, we obtain that the frequencies ω must obey the following equation:

$$\text{Det}\left[\frac{C_{I,\alpha,J,\beta}}{\sqrt{M_I M_J}} - \omega^2 \delta_{I,\alpha,J,\beta}\right] = 0 \tag{2.B.28}$$

where δ is the identity matrix. Hence, by diagonalizing the matrix $C/\sqrt{M_I M_J}$, one can obtain the eigenfrequencies ω and the corresponding amplitude and direction of the atomic vibration motion. The main difficulty now resides in determining the interatomic force constant matrix. One of the main straightforward method is to simply displace each atom individually from its equilibrium position and is called the "frozen phonon" method. In the case of a periodic crystal, the formalism is a little bit more complicated [100]. Indeed, C only depends on the interatomic distances: hence, displacing the origin of the coordinates by a lattice vector translation should not yield any modification in C. Therefore, one can get all the vibrational properties of the system simply through the unit cell. Usually, we introduce the dynamical matrix, which is the Fourier transform of the interatomic force constant matrix:

$$D_{I,\alpha,J,\beta}(\mathbf{q}) = \sum_{\mathbf{K}} C_{I,\mathbf{0},\alpha,J,\mathbf{K},\beta} \mathrm{e}^{i\mathbf{K}\cdot\mathbf{q}} \tag{2.B.29}$$

where $\mathbf{K}$ are the lattice vectors. By diagonalizing the dynamical matrix D, we get the phonon dispersion relation i.e. $\omega(\mathbf{q})$ inside the Brillouin zone.

2.C The jungle of atomic units

The PWscf package of Quantum Espresso [89] uses Rydberg atomic units, while in most other cases, standard atomic units (or Hartree units) are used. Here, we briefly describe both sets. First, we choose:

$$\text{Rydberg:} \quad \hbar \equiv 2m \equiv \frac{e^2}{2} \equiv 1 \tag{2.C.1}$$

$$\text{Hartree:} \quad \hbar \equiv m \equiv e \equiv 1 \tag{2.C.2}$$

where m and e are the mass and the charge of an electron respectively. Therefore, the unit of angular momentum is $\hbar$, the unit of mass is m in Hartree units and $2m$ in Rydberg units and the unit of charge is e in Hartree units and $e/\sqrt{2}$ in Rydberg units. Then, we can define all other units :

- the unit of length is the Bohr radius in both unit systems:

$$a_0 = \frac{\hbar^2}{me^2} = 1 \approx 0.529177\,\text{Å} \tag{2.C.3}$$

- the Rydberg energy is half the Hartree energy:

$$E_{\text{Ryd}} = \frac{e^2}{2a_0} = 1 \approx 13.6\,\text{eV} \tag{2.C.4}$$

$$E_{\text{Har}} = \frac{e^2}{2a_0} = 1 \approx 27.2\,\text{eV} \tag{2.C.5}$$

- time is defined as the ratio between an angular momentum and an energy:

$$t_{\text{Ryd}} = \frac{\hbar}{E_{\text{Ryd}}} = 1 \approx 4.84 \cdot 10^{-5}\,\text{ps} \qquad f_{\text{Ryd}} = \frac{1}{t_{\text{Ryd}}} = 1 \approx 2.07 \cdot 10^{4}\,\text{THz} \tag{2.C.6}$$

$$t_{\text{Har}} = \frac{\hbar}{E_{\text{Har}}} = 1 \approx 2.42 \cdot 10^{-5}\,\text{ps} \qquad f_{\text{Har}} = \frac{1}{t_{\text{Har}}} = 1 \approx 4.13 \cdot 10^{4}\,\text{THz} \tag{2.C.7}$$

Another useful physical constant is the Boltzmann constant: $k_B = 8.617 \cdot 10^{-5}\,\text{eV.K}^{-1}$. The mass of a proton is equal to 1836.15 in Hartree units and 918.08 in Rydberg units.

Chapter 3

Nuclear quantum effects on the hydrogen bond symmetrization

Contents

3.1 Introduction

3.1.1 An introduction to hydrogen bonds

Hydrogen bonds are ubiquitous in physics, chemistry or biology. They are one of the most important components of life, as they occur in many biological structures such as DNA and of course water. Hydrogen bonds are weaker than covalent bonds but stronger than standard dipole-dipole interactions. Their strength is usually of about an order of magnitude smaller than that of covalent bonds. For example, in ordinary ice Ih, the energies of the covalent and hydrogen bonds are 4.8 and 0.29 eV respectively [101]. Hence, they can contribute to the properties of the system, since they may be broken or reformed by thermal fluctuations. Moreover, although it is clear that electronic properties are

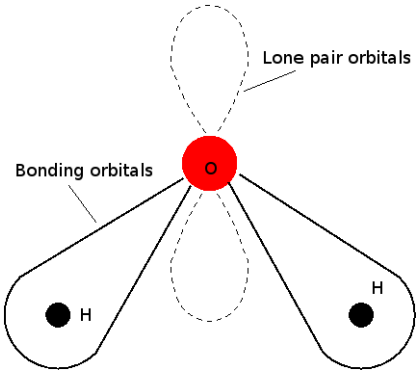

Figure 3.1.1: Schematic representation of a water molecule with its two bonding and two lone-pair orbitals. O indicates the oxygen atom, H indicates the hydrogen atoms.

essential to the description of hydrogen-bonded systems, the protons also play a major role, e.g. in the electrical properties of ice [102].

A hydrogen bond can be defined as "an attractive interaction between a hydrogen atom from a molecule or a molecular fragment X-H in which X is more electronegative than H, and an atom or a group of atoms in the same or a different molecule, in which there is evidence of bond formation" [103]. Thus, we can write the hydrogen bond in the form:

$$\mathrm{RX} - \mathrm{H} \cdots \mathrm{X'R'}$$

where X is considered the hydrogen-bond *donor*, while X' is the hydrogen-bond *acceptor*. Usually, the acceptor is an electron-rich region e.g. a lone pair of X'. A hydrogen bond is then formed via electrostatic forces and tiny charge transfer between the donor X and the acceptor X'. Indeed, when attached to the electronegative donor X, the hydrogen acquires a positive charge while the acceptor X' has, for example, at least one lone pair. The positive charge of the hydrogen is then attracted to this lone pair, forming a hydrogen bond. This is illustrated in more details in the following paragraph.

A hydrogen atom consists in a positive nucleus and a single electron which, in its lowest energy state, is in the first (1s) shell i.e. is characterized by an s-type atomic orbital. An oxygen atom has eight electrons: two fill the first shell $(1s)^2$, two are in the s orbital of the second shell $(2s)^2$, and four are in the p orbital of the second shell $(2p)^4$. Hence, to form a water molecule, each hydrogen shares an electron pair with the p orbital of an oxygen. Therefore, the first shell of the hydrogen is filled by two electrons, while the second shell of the oxygen is filled by eight electrons when bonded to two hydrogens. The bonds formed by these shared electron pairs are *covalent* bonds.[1] However, since oxygen is more electronegative than hydrogen, it will tend to exert a greater force on the shared electron than hydrogen. This results in the electron spending more time in the outer shell of the oxygen than that of the hydrogen. This in turn leads to a negatively charged oxygen and a positively charged hydrogen. Consequently, an attractive electrostatic force exists between hydrogen and oxygen atoms. A schematic picture of a water molecule is shown in Figure 3.1.1. Of the ten electrons constituting the system, two are in the first shell (1s) of the oxygen nucleus, two pairs of electrons form the *bonding* orbitals between each hydrogen and the oxygen, and the remaining two pairs of electrons form the *lone-pair* orbitals.

[1] As these bonds usually consist of an ionic contribution - as proved by the negative charge on the electronegative atom - they should be called *iono-covalent*. For the sake of simplicity, they are simply denoted as *covalent* in the following.

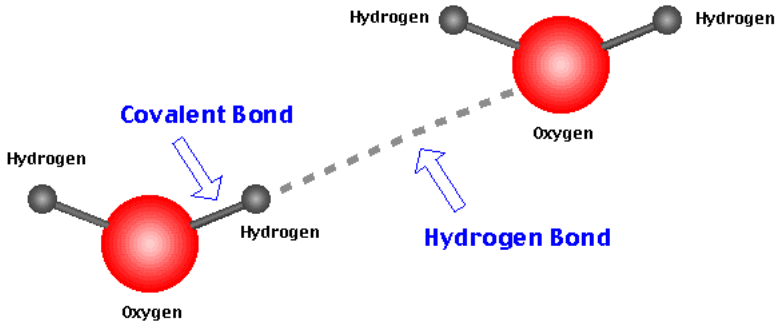

Figure 3.1.2: Schematic representation of the hydrogen bond between two water molecules.

The attraction between the lone-pair orbitals of the oxygen and a hydrogen atom (from a different water molecule for example) consists in a hydrogen bond (see Figure 3.1.2). Hence, each water molecule can form two hydrogen bonds involving hydrogen atoms from neighboring water molecules. These two hydrogen bonds and the two covalent O-H bonds typically arrange themselves in a tetrahedral geometry, as is the case in ordinary ice.

The exact nature of hydrogen bonds has been extensively studied by Pauling who predicted that they display characteristics of both covalent and ionic bonds [104]. The electrostatic description given above consists in the classical, ionic, aspect of hydrogen bonding. The intrinsic covalent and quantum nature of hydrogen bonds has been confirmed recently by Compton measurements on ice [105], where a purely electrostatic (classical) treatment of water molecules did not reproduce the phase coherence of the electronic wave function (only a fully quantum modelization of the electrons using density functional theory was able to reproduce the features of the Compton profile anisotropy). In order to characterize the hydrogen bonds between two water molecules, we can visualize the electronic density as given by the density functional theory (see Appendix 2.B) and shown in the left panel of Figure 3.1.3. As expected, the maximum of the density is located on the oxygen and the O-H covalent bond can be considered as a single entity. Since we will be interested in the symmetrization of hydrogen bonds, we also computed the electronic density in a symmetric configuration i.e. where the H nucleus is located at the O-O midpoint (see right panel of Figure 3.1.3): the electronic density displays a local maximum centered on the hydrogen nucleus. This means that the O-H bonds in this configuration are no longer covalent. We will now present several theoretical descriptions of hydrogen bonds and more precisely, of the behavior of the protons in those bonds.

3.1.2 A theoretical description of hydrogen bonds

In order to describe the properties of hydrogen bonds, a standard mean field picture for the potential felt by the protons can be useful. This mean field potential most probably depends on various parameters and especially on the atomic environment of the hydrogen bond. However, the standard picture is to consider only the influence of the distance between the hydrogen-bond donor and acceptor, X-X'. In the case of ice, this would be the oxygen-oxygen interatomic distance.

When the X-X' distance is large, the proton is covalently bonded to X and forms a longer, weaker, hydrogen bond with X'. This is the case in several ordered phases of ice, such as ice Ih or VIII, where the oxygen-oxygen distances are approximately equal to 2.8 Å and 2.5 Å respectively. The hydrogen bonds in those cases correspond to the standard *asymmetric hydrogen bond*, as shown schematically in Figure 3.1.2. The proton is localized

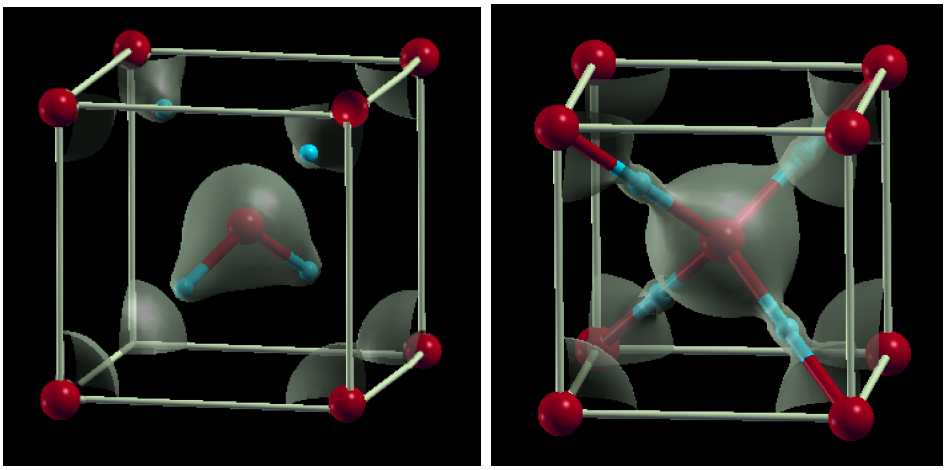

Figure 3.1.3: Electronic density computed from density functional theory calculations on: (left panel) a configuration of ice VII (i.e constituted of water molecules linked by hydrogen bonds); (right panel) a configuration of ice X (i.e. where the hydrogen nuclei lie midway between their two neighboring oxygen atoms).

near one oxygen and its free energy landscape can thus be represented by an asymmetric single well potential (see left panel in Figure 3.1.4).

At intermediate X-X' distances, a curious phenomenon can occur. Indeed, instead of only one equilibrium position, the proton can have two equivalent equilibrium positions: one near the hydrogen bond donor X and one near the hydrogen bond acceptor X'. In this case, proton hopping from one site to the other can occur. The free energy landscape of the proton can thus be seen as a symmetric double well potential (see center panel in Figure 3.1.4), where the two wells correspond to the two equilibrium positions. Hence, the proton can form a covalent bond with X and a hydrogen bond with X', or conversely, a covalent bond with X' and a hydrogen bond with X. This situation corresponds to what we will call *disordered hydrogen bonds* in the following. This occurs in the disordered phase VII of ice for example, where the oxygen-oxygen distance is close to 2.4 Å and the hydrogen can be found on both sides of the hydrogen bond. Hydrogen hopping over the potential barrier obviously depends on thermal fluctuations but can also be driven by quantum tunneling through the barrier.

Finally, at even smaller X-X' distances, the hydrogen nucleus is no longer covalently

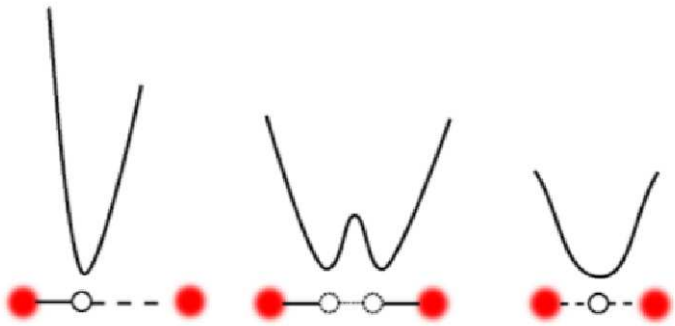

Figure 3.1.4: Cartoon depicting the free energy landscape of the proton in a hydrogen bond in different situations (ice VIII, ice VII and ice X). Figure from reference [106].

bonded to X or X', nor does it form an *actual* hydrogen bond with any of the two: the proton lies midway between X and X'. This constitutes what we will denote in the following a *symmetric hydrogen bond*; the distinction between the donor and the acceptor of the hydrogen bond is no longer appropriate. In this case, the proton free energy landscape is a symmetric single well potential (see right panel in Figure 3.1.4). Symmetric hydrogen bonds are the signature of the phase X of ice, where the oxygen-oxygen distance is approximately equal to or shorter than 2.3 Å. However, these symmetric hydrogen bonds are not a peculiarity of high pressure ice only, and can be found in other materials that are of geological interest and might play an important role in water transport in the Earth mantle, such as aluminium oxide hydroxide [107].

Another way of describing the different behaviors of hydrogen bonds is to look at the proton distribution function along the hydrogen bond direction (see Figure 3.1.5). From this point of view, asymmetric hydrogen bonds correspond to a proton localized on one side of the hydrogen bond: the distribution function would thus be unimodal and centered near the donor X. On the other hand, in the case of disordered hydrogen bonds, proton hopping results in a bimodal distribution, i.e. with two peaks corresponding to the two equilibrium sites of the proton. Finally, the proton distribution is unimodal again in the case of symmetric hydrogen bonds, i.e. when the proton lies midway between the hydrogen bond donor and acceptor. However, in this case, the distribution has its maximum at the center of the X-X' bond.

In order to present a simple, homogeneous description of hydrogen bonds for different X-X' distances, we represent the effective potential energy of the proton by a double well potential, where the distance between the two wells and the barrier height can vary. In Figure 3.1.5, three different situations are represented that correspond to asymmetric, disordered and symmetric hydrogen bonds. Indeed, for large X-X' distances, the distance between the two wells and the barrier are usually large enough that the proton distribution is centered in one well only. On the other hand, when the X-X' distance decreases, the two wells get closer to each other while the barrier height also decreases. In this case, the thermal energy is responsible for the proton's delocalization over the two wells, leading to a bimodal distribution function. Finally, when the X-X' distance is even shorter, the potential barrier can actually collapse, leading to a single well potential. This description was also presented by Benoit and coworkers [108] (see section 3.1.3 for more details). This picture is a classical one i.e. only thermal fluctuations are responsible for the proton's delocalization; if one considers the proton as a quantum particle, then several intermediate situations can occur. In particular, quantum tunneling can delocalize the proton over the two wells even if thermal fluctuations are negligible. Moreover, the zero-point motion of the proton can lead to a unimodal distribution function even though the potential is still a double well with a non-zero barrier. These "strange" quantum features will be addressed in more detail in the following sections: first, we will present theoretical studies of a quantum proton in a double well potential in sections 3.1.3 and 3.2 and then we will study proton tunneling and hydrogen bond symmetrization in a real system, namely ice under high pressure (section 3.3).

3.1.3 Previous theoretical studies of hydrogen bond symmetrization

In 1972, Holzapfel studied the linear motion of a proton between two oxygens [109]. He developed a model that correctly describes the experimental data for the equation of state of ice VII [110]. In his model, the hydrogen is subjected to two equivalent Morse potentials,

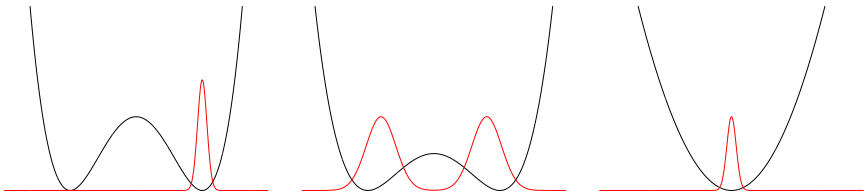

Figure 3.1.5: Schematic representation of the mean field potential energy landscapes of the protons in asymmetric (left), disordered (center) and symmetric (right) hydrogen bonds.

leading to a symmetric double well potential V_H:

$$V_H(r,R) = V_{\mathrm{OH}}\left[1 - \mathrm{e}^{-\alpha(r-a_0)} - \mathrm{e}^{-\alpha(R-r-a_0)}\right]^2 \tag{3.1.1}$$

where r is the O-H covalent bond length, R is the O-O distance, a_0 is the O-H covalent bond equilibrium length and V_{OH} is the corresponding covalent bond energy. From this potential, Holzapfel derived a critical oxygen-oxygen distance below which the equilibrium position of the proton is in the center of the hydrogen bond, and above which there are two equivalent equilibrium positions. For ice VII, the critical O-O bond length that would correspond to a transition to symmetric ice X is $R = 2.41$ Å. However, the proton is considered a classical particle in this work.

Stillinger and Schweizer [111–113] were among the first to emphasize the importance of quantum effects such as proton tunneling in the phase transitions of high pressure ice. They considered the many-body eigenfunctions of a system containing N water molecules and assumed a one-dimensional linear motion of the protons along the O-O segments. Based on a mean-field approximation for the proton potential that relies on a description of independent protons, they predicted the symmetrization of hydrogen bonds in ice VII. They also predicted that the importance of the quantum nature of hydrogen in this transition should result in a significant isotope effect when hydrogen is replaced by deuterium. In comparison with previous works, Schweizer and Stillinger were able to present a theory that includes both short and long-range interactions based on the concentrations of different hydrogen bond types as order parameters. Their work was also the first to include a two-state description of proton tunneling.

More recently, in 1998, Johannsen introduced an alternative model based on a double Morse potential (DMP) in order to analyze the correlation between the O-O distance and the proton stretching frequency [114]. The standard DMP consists in the sum of two Morse potentials centered on the two sites near each oxygen and forming a symmetric double well potential:

$$U_{DMP}(r) = u_M(r) + u_M(R-r) \tag{3.1.2}$$

where u_M is a Morse function, r is the O-H distance and R is the O-O distance. This DMP model has already been used to predict the behavior of hydrogen bonds in various materials [115]. However, for a more general description of hydrogen bonds, non-symmetric potentials have to be considered. Introducing an asymmetry in the proton potential has considerable consequences on the nature of its quantum states: the degeneracy between some low-energy levels is lifted leading to more localized states. Johannsen improved such a potential by replacing the Morse function u_M:

$$u_M(r) = u_0\left[\mathrm{e}^{-2a(r-r_0)} - 2\mathrm{e}^{-a(r-r_0)}\right] \tag{3.1.3}$$

by the following expression:

$$u(r) = u_0 \left[\frac{a\left(\mathrm{e}^{-b(r-r_0)} - 1\right) + b\left(\mathrm{e}^{a(r-r_0)} - 1\right)}{a + b\mathrm{e}^{a(r-r_0)}} - 1 \right] \tag{3.1.4}$$

where a and b control the shape of the attractive and repulsive parts of the potential, r_0 is the equilibrium O-H distance and u_0 a parameter controlling the depth of the potential. An asymmetry factor c is then introduced and the complete proton potential is: $U(r) = cu(r) + c^{-1}u(R - r)$ (see e.g. Figure 4.1.1). This type of model, that includes both symmetric and non-symmetric situations, allows for a correct description of transitions frequencies (i.e. energy differences between eigenstates) for several different compounds such as OH:$LiNbO_3$ for example. We will also use this model to study a one-dimensional chain of oxygen and hydrogen atoms in section 5.3.2.

Finally, *ab initio* path-integral molecular dynamics were also performed on ice at 100 K [108,116]. From these simulations, free energy profiles and proton distribution functions were extracted: the double-well picture presented above (see section 3.1.2) stands in the VII-X transition of ice. Depending on the barrier height, several characteristics of hydrogen bonds in ice VIII, VII or X can be recovered.

3.2 Study of a one-dimensional phenomenological model

3.2.1 Introduction of a Landau-like potential model

In order to present a consistent and simple description of the transition from disordered hydrogen bonds to symmetric hydrogen bonds, we use here a mean-field, one-dimensional approach for the proton potential. The potential we introduce is a symmetric double well potential similar to the potentials studied previously [111–114]; the barrier height and the positions of the two wells depend on the pressure. The expression of the potential is inspired by the Landau model of second-order phase transitions. Here, however, the role of temperature is replaced by pressure. Landau-like potentials have already been used to study the symmetrization of hydrogen bonds in high-pressure ice [117,118]. The potential can thus be written in the form:

$$V(x) = ax^4 + b\,(P - P_c)\,x^2 + V_0 \tag{3.2.1}$$

where x is the proton position along the O-O segment relative to its midpoint. a, b and P_c are fitting parameters, which are chosen as to reproduce the potential energy of protons in ice VII at approximately 50 GPa. Indeed, for each position x of the proton, the energy of a simulation box containing 54 water molecules in the ice VII configuration is minimized using the density functional theory. This gives an indication of the effective potential energy felt by the protons in ice at $T = 0$ K.[2] Here, we choose $P_c = 100$ GPa as the transition pressure from ice VII to ice X obtained from classical simulations i.e. simulations where the quantum nature of nuclei are not taken into account [119–122]. Indeed, this corresponds to the pressure at which the potential barrier disappears and $V(x)$ becomes a single well potential. By definition, the two minima of the potential are at $x_{\mathrm{eq}} = \pm\sqrt{\frac{b}{2a}\,(P_c - P)}$. For pressures below P_c, the barrier height is $\Delta V = \frac{b^2}{4a}\,(P_c - P)^2$. As pressure increases towards P_c, the two minima move closer to each other and the barrier height decreases. At $P = P_c$, $\Delta V = 0$.

[2] We choose $a = 7.2\,\mathrm{eV.\AA^{-4}}$, $b = 0.04\,\mathrm{eV.\AA^{-2}.GPa^{-1}}$ so that $V(x)$ correctly reproduces the proton effective potential energy computed in ice VII at 50 GPa approximately (see Appendix 3.A).

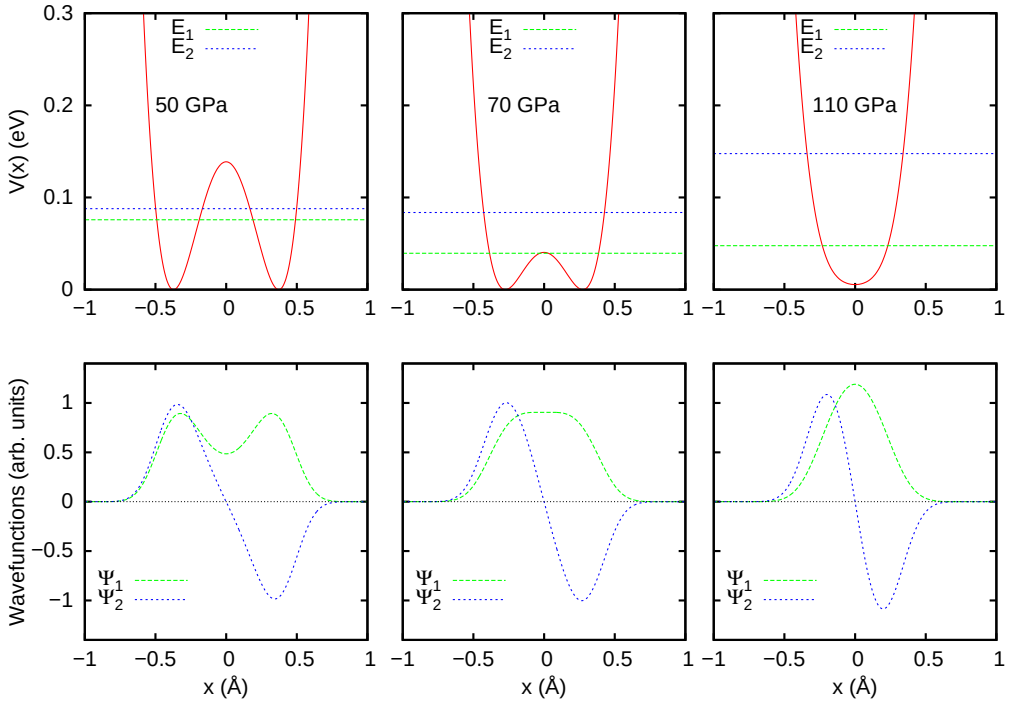

Figure 3.2.1: (top) Potential $V(x)$ at different pressures (50, 70 and 110 GPa) with the ground-state energy E_1 and the energy of the first excited state E_2. (bottom) Wave functions of the ground-state, $\Psi_1(x)$, and the first excited state, $\Psi_2(x)$.

From a classical point of view, the transition from asymmetric hydrogen bonds to symmetric hydrogen bonds occurs when the barrier disappears, at $P = P_c$. From a quantum point of view, this problem reduces to a time-independent Schrödinger equation for a proton in one dimension: a finite differences method turns it into an eigenproblem which is easily solved by standard linear algebra procedures. We can thus obtain the eigenenergies E_n and eigenfunctions $\Psi_n(x)$ of the system at $T = 0$ K. Typical eigenstates are shown in Figure 3.2.1 below the classical transition pressure, at 50 and 70 GPa and above the classical transition, at 110 GPa. Unsurprisingly, at low pressures (at 50 GPa), the two lowest energy states are almost degenerate and the ground-state wavefunction has two maxima near the bottom of the two wells, and a local minimum at $x = 0$. On the contrary, above the classical transition pressure (at 110 GPa), the ground-state wavefunction is centered around $x = 0$ where it is maximum. However, the ground-state wavefunction, $\Psi_1(x)$, undergoes a topological change when its local minimum at $x = 0$ becomes a maximum around 70 GPa, with no further modification at pressures above 70 GPa. This phenomenon is the signature of a quantum phase transition undergone by the system [123–125]. Indeed, a quantum phase transition is marked by a fundamental change of the topology of the ground state of the system. Hence, strictly speaking, quantum phase transitions occur at $T = 0$ K since they refer to singularities in the ground state [126]. Here, we are interested in the consequences that such a quantum phase transition can have even at finite temperature and we attempt to go beyond the $T = 0$ K description. In the following, we will study proton tunneling and its consequences on the VII-X transition from a more quantitative point of view (section 3.2.2) and then we will analyze the effect of thermal fluctuations this transition (section 3.2.3). In particular, we will see that the

main characteristics of the symmetrization transition of hydrogen bonds in ice are only slightly affected by thermal fluctuations. Therefore, we will refer to this transition as a "quantum-driven phase transition" at room temperature.

3.2.2 Quantum tunneling in a one-dimensional model

Below the transition, the proton is subject to quantum tunneling. In order to quantify proton hopping through the barrier, several approaches are possible: we will first present a semiclassical viewpoint, the WKB approximation, and then a more general approach based on the system's eigenfunctions. At the semiclassical level (within the WKB approximation), the transmission factor through the barrier is (see chapter VI in reference [127]):

$$\Gamma_{\mathrm{WKB}} = \exp\left[-2\int_{x_1}^{x_2}\sqrt{\frac{2m}{\hbar^2}\left(V(x)-E_1\right)}\,\mathrm{d}x\right] \tag{3.2.2}$$

where x_1 and x_2 correspond to $V(x_1) = V(x_2) = E_1$ and E_1 is the ground-state energy i.e. the zero-point energy. The top panel of Figure 3.2.2 shows Γ_{WKB} increasing as pressure increases until it reaches its final value, $\Gamma_{\mathrm{WKB}} = 1$ when $E_1 \geq V(0)$ i.e. when the zero-point energy is higher than the barrier height.

Another approach, based on the eigenfunctions of the system, consists in a simple quantum picture in terms of the ground-state and the first excited state. When the barrier is relatively high, these two states, $\Psi_1(x)$ and $\Psi_2(x)$, are almost degenerate (see top panel in Figure 3.2.4). We can then define two states, Ψ_{left} and Ψ_{right}, which correspond to a proton localized in the left and the right well respectively:

$$\Psi_{\mathrm{left}}(x) = \frac{\Psi_1(x)+\Psi_2(x)}{2}, \quad \Psi_{\mathrm{right}}(x) = \frac{\Psi_1(x)-\Psi_2(x)}{2}. \tag{3.2.3}$$

If our system is initially in the left well, i.e. in state Ψ_{left}, then the wave function at time t is:

$$\Psi(x,t) = \frac{\mathrm{e}^{-iE_1t/\hbar}}{2}\left(\Psi_1(x)+\Psi_2(x)\mathrm{e}^{-i\omega_{12}t}\right) \tag{3.2.4}$$

where we have defined

$$\omega_{12} \equiv \frac{E_2-E_1}{\hbar}. \tag{3.2.5}$$

Therefore, our system oscillates between the states Ψ_{left} and Ψ_{right} with a period $2\pi/\omega_{12}$: this phenomenon is called *coherent tunneling* [128]. The tunneling or hopping rate of the proton between the two wells is then given by

$$\Gamma_{12} \equiv \omega_{12} = \frac{E_2-E_1}{\hbar}. \tag{3.2.6}$$

In this case, Γ_{12} is also called the tunneling splitting and usually depends on the mass of the particle, on the height of the barrier and on the distance between the two wells.

Moreover, since Ψ_1 and Ψ_2 are eigenstates of the system, they are solutions to the time-independent Schrödinger equation:

$$\Psi_1'' + \frac{2m}{\hbar^2}(E_1-V)\Psi_1 = 0 \tag{3.2.7}$$

$$\Psi_2'' + \frac{2m}{\hbar^2}(E_2-V)\Psi_2 = 0 \tag{3.2.8}$$

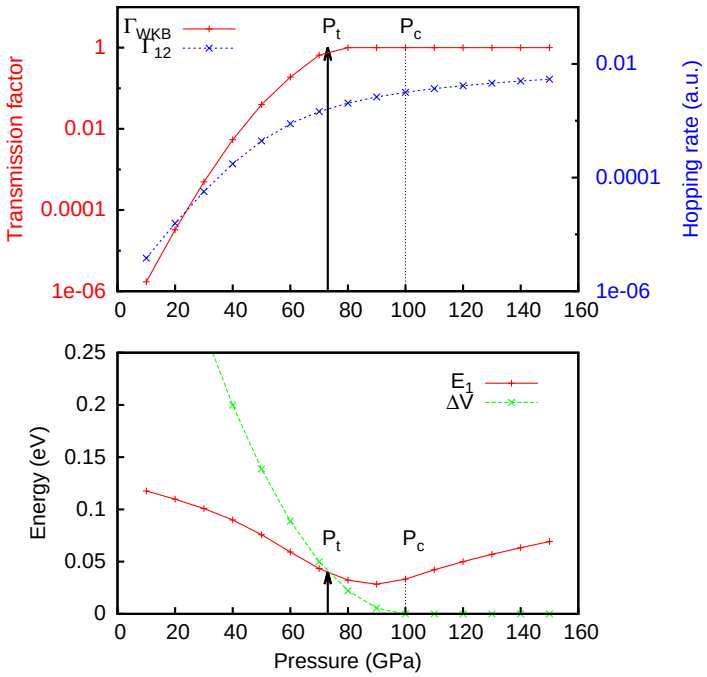

Figure 3.2.2: (top) Transmission factor Γ_{WKB} in the semiclassical WKB approximation and quantum hopping rate Γ_{12} as functions of pressure. (bottom) Zero-point energy E_1 and barrier height ΔV as a function of pressure. P_c indicates the classical transition pressure (above which $\Delta V = 0$) and P_t indicates the quantum critical pressure (where $\Delta V = E_1$).

Thus, equation (3.2.7)$\times\Psi_2-$ equation (3.2.8)$\times\Psi_1$ leads to:

$$\Psi_1''\Psi_2 - \Psi_2''\Psi_1 + \frac{2m}{\hbar^2}(E_1 - E_2)\Psi_1\Psi_2 = 0. \tag{3.2.9}$$

Integrating this equation over half the real space, we get:

$$\Psi_1'(0)\Psi_2(0) - \Psi_2'(0)\Psi_1(0) = \frac{2m}{\hbar^2}(E_2 - E_1)\int_{-\infty}^{0}\Psi_1(x)\Psi_2(x)\,\mathrm{d}x. \tag{3.2.10}$$

Since Ψ_2 is antisymmetric, $\Psi_2(0) = 0$ and we obtain the following expression for the hopping rate:

$$\Gamma_{12} = -\frac{\hbar}{2m}\frac{\Psi_2'(0)\Psi_1(0)}{\int_{-\infty}^{0}\Psi_1(x)\Psi_2(x)\,\mathrm{d}x}. \tag{3.2.11}$$

The numerator in equation (3.2.11) can be interpreted in terms of a current through the barrier at $x = 0$ [129]:

$$J(0) = -\frac{\hbar}{m}\Psi_2'(0)\Psi_1(0). \tag{3.2.12}$$

The top panel of Figure 3.2.2 also shows the evolution of the hopping rate Γ_{12} with pressure. The behaviors of the semiclassical Γ_{WKB} and of the quantum hopping rate Γ_{12} are very similar: they both increase as pressure increases. Above the critical pressure where E_1 equals the barrier height i.e. for $P > P_t$, while Γ_{WKB} does not evolve anymore, Γ_{12} continues to increase but with a slope much less important than for $P < P_t$. Hence, both approaches yield similar results regarding the evolution of proton hopping as pressure increases.

The lower panel in Figure 3.2.2 shows the evolution of the zero-point energy of the system, E_1, as well as that of the potential barrier height ΔV when pressure increases. Three regimes can be distinguished:

1. regime (I) i.e. $P \leq P_t$: $\Delta V \neq 0$ and $E_1 \leq \Delta V$
2. regime (II) i.e. $P_t \leq P \leq P_c$: $\Delta V \neq 0$ and $E_1 \geq \Delta V$
3. regime (III) i.e. $P \geq P_c$: $\Delta V = 0$

where P_t is a critical pressure (close to 70 GPa). In regime (I), the onset of proton tunneling leads to the proton hopping from one well to the other: therefore, Γ_{WKB} and Γ_{12} increase rapidly, while the barrier height decreases. However, the zero-point energy E_1 remains lower than the barrier, resulting in a wavefunction with two maxima and a local minimum at $x = 0$. In regime (II), the zero-point energy E_1 is higher than the barrier ΔV, leading to a maximum of the density at $x = 0$: the proton is mostly localized around the center of the O-O segment, even though the barrier has not yet disappeared ($\Delta V \neq 0$). Quantum tunneling is responsible for the delocalization of the proton over the two potential wells in regime (I), but the transition to symmetric hydrogen bonds occurs when the zero-point energy reaches the barrier height. The increase in Γ_{12} is then slowed down because tunneling does not occur anymore in regime (II) and thus Γ_{12} is no longer an indicator of proton hopping. At the semiclassical level, Γ_{WKB} has reached its maximum value and does not evolve anymore. In regime (III), the barrier has disappeared (i.e. $\Delta V = 0$) and the proton confinement is only due to the contraction of the O-O distance. Therefore, the quantum phase transition occurs when the zero-point energy reaches the height of the barrier, at which point the ground-state wavefunction displays a topological change. In the following section, we will discuss how thermal fluctuations affect proton tunneling as well as the symmetrization transition.

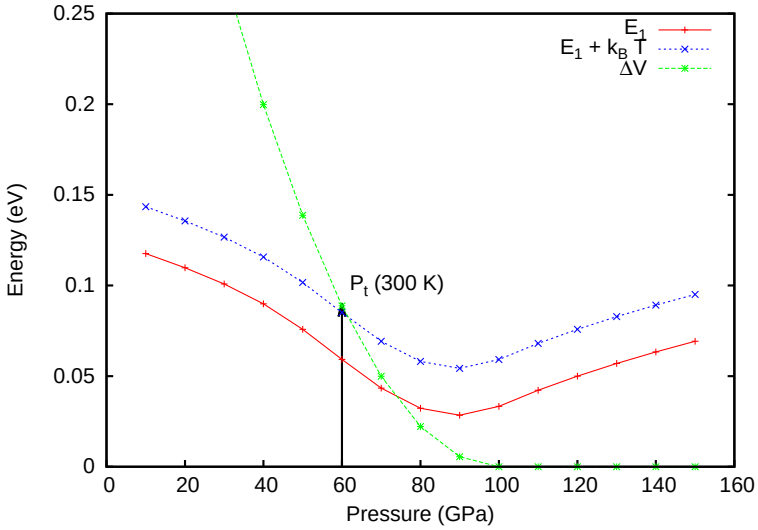

Figure 3.2.3: Zero-point energy, E_1, shifted zero-point energy at $T = 300$ K, $E_1 + k_BT$, and barrier height ΔV as functions of pressure. P_t indicates the transition pressure from asymmetric to symmetric hydrogen bonds at ambient temperature.

3.2.3 Thermal fluctuations contribution

The previous analysis was done at $T = 0$ K but can be extended to finite temperature through simple arguments. The thermal energy associated with a temperature of 300 K is approximately $k_BT \sim 26$ meV. In ice VII, this corresponds to half the barrier height at the quantum transition point (approximately 54 meV at 65 GPa), i.e.

$$k_BT = \frac{\Delta V}{2}\bigg|_{P=P_t} = \frac{E_1}{2}\bigg|_{P=P_t}. \tag{3.2.13}$$

A simple approximation consists in adding the thermal energy to the ground-state energy i.e.

$$E|_{T\neq 0} \approx E_1|_{T=0} + k_BT. \tag{3.2.14}$$

The transition pressure is still determined by the point where the energy is equal to the barrier height: thus, it is reduced from 70 GPa to approximately 60 GPa (see Figure 3.2.3). This is in agreement with experimental values found via infrared and Raman experiments and with numerical studies that do take into account the quantum nature of hydrogens (via PIMD [116] and via QTB [4]).

Furthermore, even at high temperatures, the contribution from zero-point motion - which is a purely quantum effect - is far from negligible. Indeed, it induces a massive change in the value of the transition pressure (P_t is about 40% smaller than P_c); this effect is even dominant compared to thermal fluctuations (which contribute for 5% approximately). This confirms that quantum-driven phase transitions do occur in real systems, even at room temperature, and reinforces the importance of correctly treating nuclear quantum effects.

In order to further understand the mechanism of the transition and in particular the role of thermal fluctuations, we look at the evolution of the eigenstates from a very high barrier potential (top panel in Figure 3.2.4) to a single well potential (lower panel in Figure 3.2.4). At low pressures, the states 1 and 2 are degenerate as are the states 3 and 4. Hence, the combination of states $\Psi_1 + \Psi_2$ and $\Psi_3 + \Psi_4$ correspond to localized states in each well (see equation (3.2.3)). Therefore, the transition rate $\Gamma_{13} = (E_3 - E_1/)\hbar = \Delta E_{13}/\hbar$

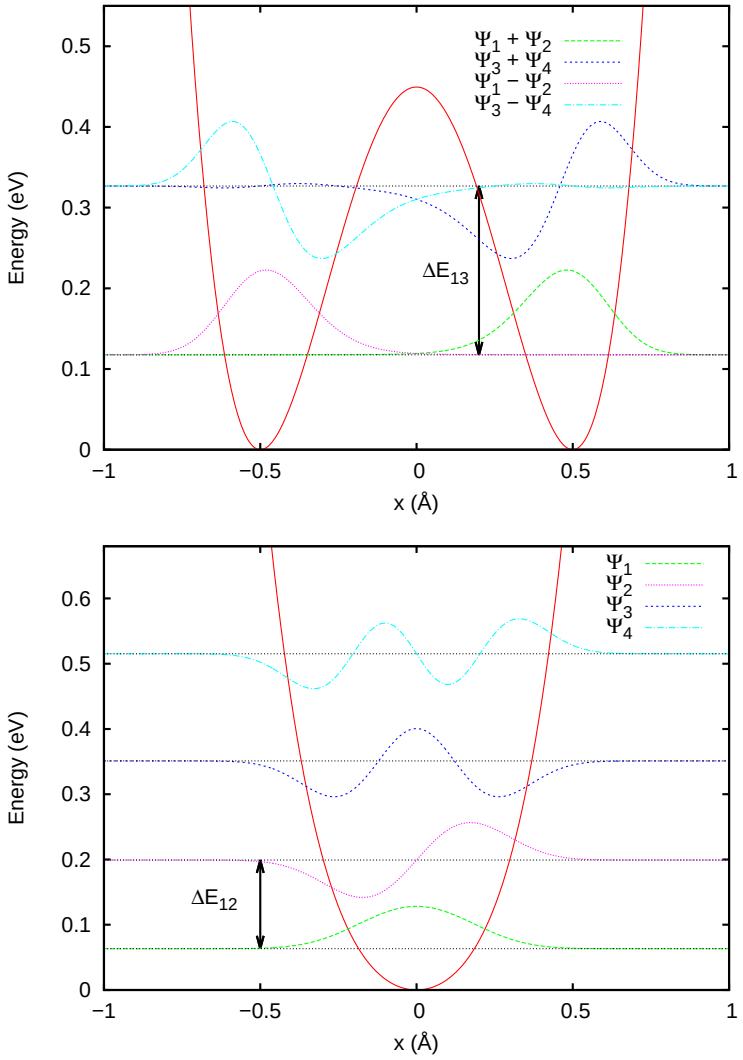

Figure 3.2.4: Potential $V(x)$ at 10 GPa (top) and 140 GPa (bottom) with corresponding eigenstates Ψ_i $(i = 1, 4)$. The eigenstates have been shifted according to their eigenenergies. $\Delta E_{13} = \hbar\Gamma_{13}$ and $\Delta E_{12} = \hbar\Gamma_{12}$ indicate the energy differences from state 1 to states 3 and 2 respectively (Γ_{ij} is the transition rate between state i and state j).

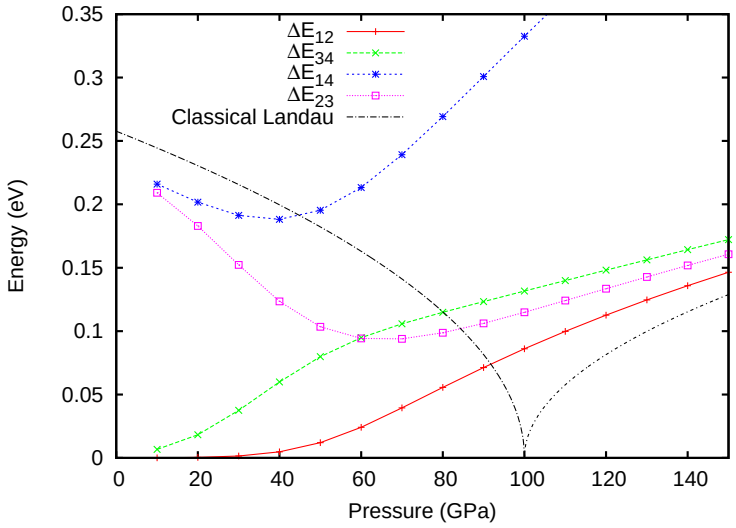

Figure 3.2.5: Energy differences $\Delta E_{ij} = E_j - E_i$ $(i, j = 1, 4)$ between the eigenstates Ψ_i and Ψ_j as functions of pressure. The black lines show the evolution of the energies $\hbar\omega_0^{(\mathrm{LP})}$ and $\hbar\omega_0^{(\mathrm{HP})}$ as derived from the classical Landau theory of second-order phase transitions (equations (3.2.15) and (3.2.16)).

represents the oscillation frequency at the bottom of the well. As pressure increases, the degeneracies between states 3 and 4 and then 1 and 2 are lifted: the combinations of states $\Psi_1 + \Psi_2$ and $\Psi_3 + \Psi_4$ are no longer localized states but are more complicated and Γ_{13} decreases. On the other hand, at high pressures, the eigenstates 1 and 2 correspond to the two lowest-energy states of the single-well potential and Γ_{12} is now the transition rate that represents the oscillation frequency in the potential. Figure 3.2.5 shows the evolution of the energy differences between the eigenstates with increasing pressure. As expected, ΔE_{13} decreases (as does ΔE_{24}) with increasing pressure as the system approaches the transition. On the other hand, ΔE_{12} (as ΔE_{34}) increases with increasing pressure. Furthermore, below the transition i.e. for $P < P_c$, the harmonic frequency at the bottom of each well is:

$$\omega_0^{(\mathrm{LP})} = 2\sqrt{\frac{b(P_c - P)}{m}} \tag{3.2.15}$$

while above the transition, the harmonic frequency is:

$$\omega_0^{(\mathrm{HP})} = \sqrt{\frac{2b(P - P_c)}{m}} \tag{3.2.16}$$

where LP and HP stand for "low pressure" and "high pressure" respectively. The evolution of these harmonic frequencies are also shown in Figure 3.2.5 (black lines). Hence, ω_0^2 is linear with pressure below and above the transition at $P = P_c$ which corresponds to the classical Landau theory of second-order phase transitions. More formally, we can define the classical susceptibility χ as the proportionality coefficient between the displacement of the atom, δx, and the force needed to displace it from its equilibrium position, δF:

$$\delta x = -\chi \delta F \Rightarrow \chi^{-1} = -\left.\frac{\mathrm{d}F}{\mathrm{d}x}\right|_{x_{\mathrm{eq}}} = \left.\frac{\mathrm{d}^2V}{\mathrm{d}x^2}\right|_{x_{\mathrm{eq}}}. \tag{3.2.17}$$

In the harmonic approximation, the inverse susceptibility is simply proportional to the square of the frequency, $\chi^{-1} = m\omega_0^2$. For a double well potential, we obtain:

$$\chi^{-1} = \begin{cases} 4b\,(P_c - P)\,, & \text{for } P \leq P_c \\ 2b\,(P - P_c)\,, & \text{for } P \geq P_c \end{cases} \tag{3.2.18}$$

In the classical Landau theory, the transition is accompanied by a soft mode, whose behavior is related to $\sqrt{\chi^{-1}}$. Hence, below and above the transition, we expect a mode ω_0 such that ω_0^2 is linear with pressure. Equation (3.2.18) also indicates that the proportionality coefficient below the transition is twice that above the transition.

The classical Landau theory can be adapted to the quantum transition, as we have seen that the transition rate Γ_{13} decreases with pressure below the transition while Γ_{12} increases above the transition, indicating the presence of a soft-mode at the transition. In order to generalize these results, we compute the quantum susceptibility from linear response theory. We consider a time-dependent perturbation $f(t)$ to our system with Hamiltonian:

$$H = H_0 - f(t)x = \frac{p^2}{2m} + V(x) - f(t)x \tag{3.2.19}$$

where $V(x)$ is the double well potential given in equation (3.2.1). The dynamical response function is

$$\chi(t) = \frac{i}{\hbar}\theta(t)\langle[\hat{x}(t), \hat{x}]\rangle \tag{3.2.20}$$

where $\theta(t)$ is the Heaviside function and the position operator $\hat{x}(t)$ is

$$\hat{x}(t) = \mathrm{e}^{iH_0 t/\hbar}\,\hat{x}\,\mathrm{e}^{-iH_0 t/\hbar}. \tag{3.2.21}$$

$[\hat{x}(t), \hat{x}]$ indicates the commutator of $\hat{x}(t)$ and $\hat{x}$ i.e. $[\hat{x}(t), \hat{x}] = \hat{x}(t)\hat{x} - \hat{x}\hat{x}(t)$. We introduce the density matrix of the system $\hat{\rho}(T)$ at temperature T which can be expressed in terms of the eigenstates of the system $\{\Psi_n, E_n\}$:

$$\hat{\rho}(T) = \sum_n \frac{\mathrm{e}^{-\beta E_n}}{Z}|\Psi_n\rangle\langle\Psi_n|, \tag{3.2.22}$$

$Z = \sum_n \mathrm{e}^{-\beta E_n}$ is the partition function and $\beta = (k_B T)^{-1}$ is the inverse temperature. Thus, equation (3.2.20) can be rewritten as:

$$\begin{aligned}
\chi(t) &= \frac{i}{\hbar}\theta(t)\,\mathrm{Tr}\left\{\hat{\rho}(T)\,[\hat{x}(t), \hat{x}]\right\} \\
&= \frac{i}{\hbar}\theta(t)\sum_m \langle\Psi_m|\hat{\rho}(T)\,[\hat{x}(t), \hat{x}]\,|\Psi_m\rangle \\
&= \frac{i}{\hbar}\theta(t)\sum_n \frac{\mathrm{e}^{-\beta E_n}}{Z}\langle\Psi_n|\,[\hat{x}(t), \hat{x}]\,|\Psi_n\rangle \\
&= \frac{i}{\hbar}\theta(t)\sum_n\sum_m \frac{\mathrm{e}^{-\beta E_n}}{Z}\left[\langle\Psi_n|\hat{x}(t)|\Psi_m\rangle\langle\Psi_m|\hat{x}|\Psi_n\rangle - \langle\Psi_n|\hat{x}|\Psi_m\rangle\langle\Psi_m|\hat{x}(t)|\Psi_n\rangle\right] \\
&= \frac{i}{\hbar}\theta(t)\sum_n\sum_m \frac{\mathrm{e}^{-\beta E_n}}{Z}\left[\mathrm{e}^{i(E_n - E_m)t/\hbar} - \mathrm{e}^{-i(E_n - E_m)t/\hbar}\right]|\langle\Psi_n|\hat{x}|\Psi_m\rangle|^2 \\
&= -\frac{2}{\hbar}\theta(t)\sum_n\sum_m \frac{\mathrm{e}^{-\beta E_n}}{Z}\sin(\omega_{nm}t)\,|\langle\Psi_n|\hat{x}|\Psi_m\rangle|^2
\end{aligned}$$

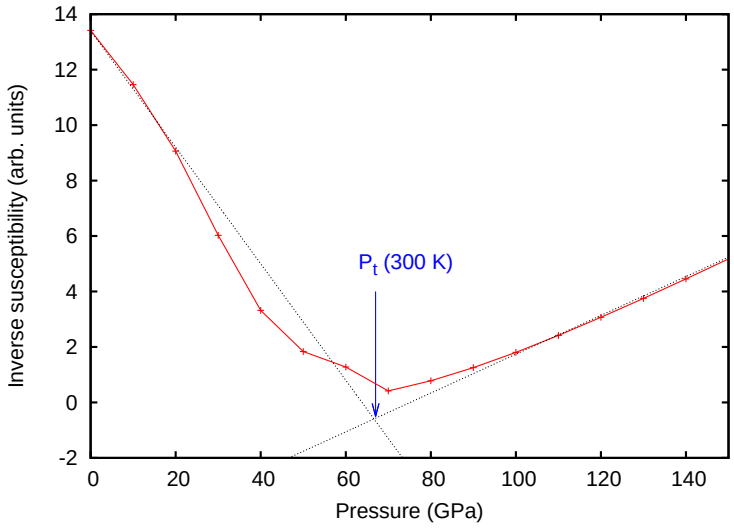

Figure 3.2.6: Inverse quantum susceptibility $\tilde{\chi}^{-1}$ at room temperature as a function of pressure (see equation (3.2.24)). The transition to symmetric hydrogen bonds at $T = 300$ K is indicated by the arrow at approximately 65 GPa and corresponds to the minimum of $\tilde{\chi}^{-1}$.

with

$$\omega_{nm} \equiv \frac{E_n - E_m}{\hbar}. \tag{3.2.23}$$

If we denote $x_{nm} = \langle \Psi_n | \hat{x} | \Psi_m \rangle$, then

$$\begin{aligned} \tilde{\chi}(\omega) &= -\frac{2}{\hbar} \sum_n \sum_m \frac{\mathrm{e}^{-\beta E_n}}{Z} |x_{nm}|^2 \int_0^\infty \sin(\omega_{nm} t)\, \mathrm{e}^{-i\omega t}\, \mathrm{d}t \\ &= \frac{2}{\hbar} \sum_n \sum_{m \neq n} \frac{\mathrm{e}^{-\beta E_n}}{Z} |x_{nm}|^2 \frac{\omega_{nm}}{\omega^2 - \omega_{nm}^2}. \end{aligned}$$

By definition, the static susceptibility is $\tilde{\chi} = \lim_{\omega \to 0} \tilde{\chi}(\omega)$; thus,

$$\tilde{\chi} = -\frac{2}{\hbar} \sum_n \sum_{m \neq n} \frac{\mathrm{e}^{-\beta E_n}}{Z} \frac{|\langle \Psi_n | \hat{x} | \Psi_m \rangle|^2}{\omega_{nm}}. \tag{3.2.24}$$

Above the transition, only the first two states are thermally accessible (i.e. occupied and thus relevant): hence, $\tilde{\chi}^{-1} \propto (E_2 - E_1)/|x_{12}|^2$ (i.e. the red line in Figure 3.2.5). Below the transition, when the first two states are degenerate, we have: $\tilde{\chi}^{-1} \propto (E_3 - E_2)/|x_{23}|^2$ (i.e. the purple curve in Figure 3.2.5). Figure 3.2.6 shows the evolution of $\tilde{\chi}^{-1}$ with pressure. We can clearly see that the susceptibility displays a minimum at the transition. Moreover, $\tilde{\chi}^{-1}$ is linear with pressure well below and above the transition, thus displaying the same behavior as the square of the O-H stretching mode frequency in ice, which softens at the transition. Indeed, the increase in proton tunneling below the transition pressure translates into an increase of $\tilde{\chi}$, which in turn, corresponds to a decrease of the frequency of the associated vibration mode. After the transition, the contraction of the potential leads to a gradual confinement of the proton, diminishing its fluctuations and implying a hardening of its vibrations.

3.3 The VII-X transition in high pressure ice

3.3.1 Introduction and previous studies

While the phase diagram of water is extremely complex (more than 16 phases have been found up to now! [130–133]), under very high pressure, only a few phases of ice exist. In particular, above 20 GPa and at room temperature, the most stable phase of ice is the phase VII, which consists in a molecular phase with a cubic structure and disordered hydrogen bonds. However, as pressure increases up to 100 GPa, the oxygen-oxygen distance decreases and the molecular phase VII, where the protons tunnel between covalent and hydrogen bonds, transforms into the non-molecular phase X, where the protons lie midway between the oxygens in a symmetric configuration.

This structural transition was first predicted theoretically in 1972 by Holzapfel [109]. He determined a critical O-O distance below which the proton is localized at the O-O midpoint and which corresponds to a pressure of 50 GPa. However, Holzapfel already mentioned that the zero-point energy of the protons most probably shifts the transition to lower pressures and that quantum effects might also be responsible for an isotope effect when H is replaced by D. The importance of nuclear quantum effects was further emphasized by Stillinger and Schweizer's theoretical work (see section 3.1.3) [111, 113].

The experimental and theoretical quest for the transition to symmetric hydrogen bonds encounters two main difficulties: performing Raman or infrared spectroscopy in this pressure range (between 30 and 100 GPa) is quite difficult because of the low-intensity (for Raman scattering) and broad (for infrared spectroscopy) peaks associated with hydrogen; on the other hand, taking nuclear quantum effects into account in simulations is also quite a challenge (see chapter 1). Hence, the first Raman and Brillouin scattering experiments found a transition near 45-50 GPa [134–136]. This transition pressure, near 45 GPa, was also confirmed by *ab initio* molecular dynamics simulations that used the LDA approximation with a gradient correction (see Appendix 2.B.4) as well as a variational Gaussian wavefunction approach [117, 118]. However, these studies were contradicted by other experiments, such as synchrotron X-ray diffraction [137], other Raman scattering experiments [138–140] and neutron diffraction measurements [141], which suggested a transition above 60-70 GPa.

Finally, in 1996, more precise infrared measurements allowed a better determination of the ice VII-ice X transition [142–144]. Figure 3.3.1 shows the evolution with pressure of the mode frequencies obtained by infrared spectroscopy. The clear decrease of the O-H stretching mode frequency is accompanied by an enormous broadening of the peak [142, 143]. Meanwhile, the O-H bending mode frequency does not vary significantly with pressure but disappears above 50 GPa. Finally, they observed a new mode in the high-pressure phase (ν_T) in the low-frequency region of the spectrum. Hence, the softening of the O-H stretching mode was associated with the transition from ice VII to ice X between 60 and 65 GPa. Moreover, several anomalies in these spectra were interpreted as evidence for proton tunneling in the 25-45 GPa range i.e. in phase VII [144]. Further experiments (infrared [145, 146] and Raman [147, 148] spectroscopy, X-ray diffraction [149]) confirmed this transition pressure and aimed at better understanding the complexity of the spectra of high-pressure ice. In particular, the O-H stretching mode softens at the transition but, because of its coupling to other modes, a cascading series of Fermi resonances was observed. The expected isotope effect on deuterated ice was also confirmed: the transition pressure is shifted to $80 - 90$ GPa for deuterated ice [146].

On the theoretical side, standard *ab initio* simulations were performed but as long as no

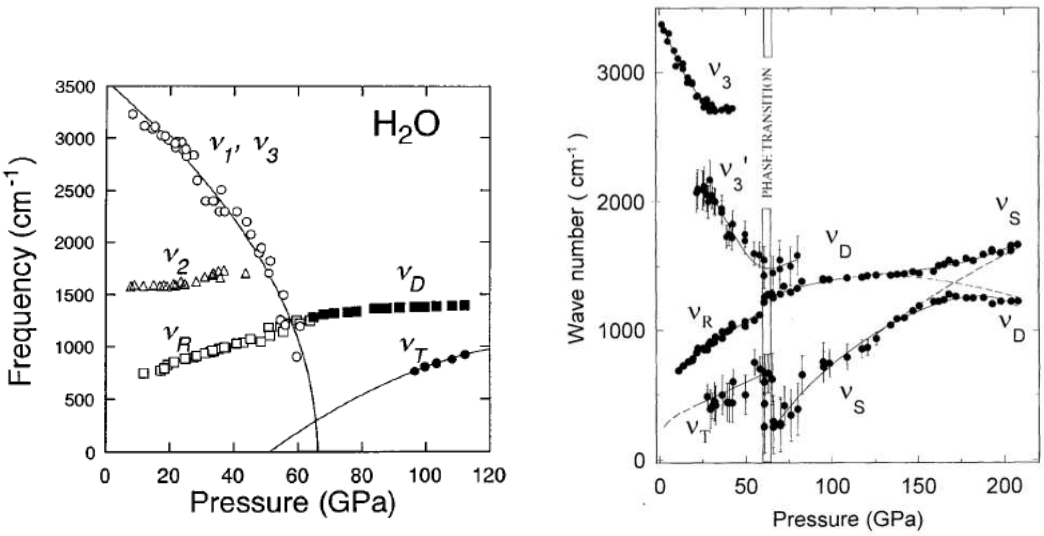

Figure 3.3.1: Evolution with pressure of measured peak frequencies via infrared spectroscopy. Left panel: results from Aoki and coworkers [142]; ν_1 and ν_3 are the symmetric and antisymmetric O-H stretching frequencies (due to the large width of the peaks, these two modes overlap); ν_2 is the O-H bending mode frequency; ν_T is a new mode which appears in the phase X above the transition; ν_R and ν_D are the librational and distortional lattice mode frequencies respectively. Right panel: results from Goncharov and coworkers [144]; ν_3, ν_3' and ν_S are the O-H stretching mode frequencies; ν_T is the translational mode frequency; ν_R' and ν_D' correspond to the rotational and deformation modes.

nuclear quantum effects were included, there was a gap of 30 GPa approximately between the numerically predicted transition pressure, ~ 90 GPa at ambient temperature, and the experimental one, ~ 60 GPa [119–122, 150]. However, the importance of zero-point effects and proton tunneling was clearly demonstrated by a path-integral molecular dynamics (PIMD) study from Benoit and coworkers [108, 116]. They were able to determine from the proton distribution function that proton tunneling occurs in ice VII which transforms into ice X around 72 GPa at 100 K (see Figure 3.3.2). Their work relied on the analysis from a structural point of view of the evolution of the hydrogen bonds with pressure. In the following, we compare our results that are obtained via QTB simulations with their PIMD calculations and complete the analysis of the phase transition from ice VII to ice X by analyzing the vibrational properties [4]. All computational details are in Appendix 3.B.

3.3.2 Structural properties of high-pressure ice

We first compare results from QTB molecular dynamics simulations to previous PIMD calculations [116] in order to validate our use of semiclassical proton dynamics. Figure 3.3.3 shows the contour plots of the average proton distribution $P(x, R_{OO'})$ as a function of the proton position relative to the bond midpoint $x = R_{OH} - R_{O'H}$ and the corresponding O-O distance, $R_{OO'}$. One should note that the distribution function P is averaged over one trajectory with no configurational averaging. Indeed, in the case of a double-well potential, one needs to average over trajectories with different initial conditions in order to obtain the expected symmetric probability distribution function. Here, we are interested in the probability for a proton of crossing the barrier at some point along its trajectory. At low

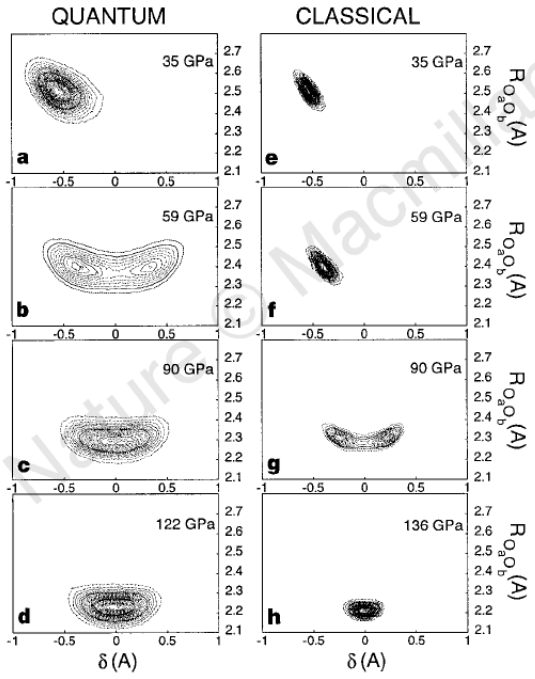

Figure 3.3.2: Average proton distribution function $P(\delta, R_{\mathrm{OO'}})$ as a function of the proton position relative to the bond midpoint $\delta = R_{\mathrm{OH}} - R_{\mathrm{O'H}}$ and the corresponding O-O distance $R_{\mathrm{OO'}}$ for quantum (left panels) and classical (right panels) simulations at $T = 100$ K and different pressures. Figure from reference [116]. *δ corresponds to x in the text.*

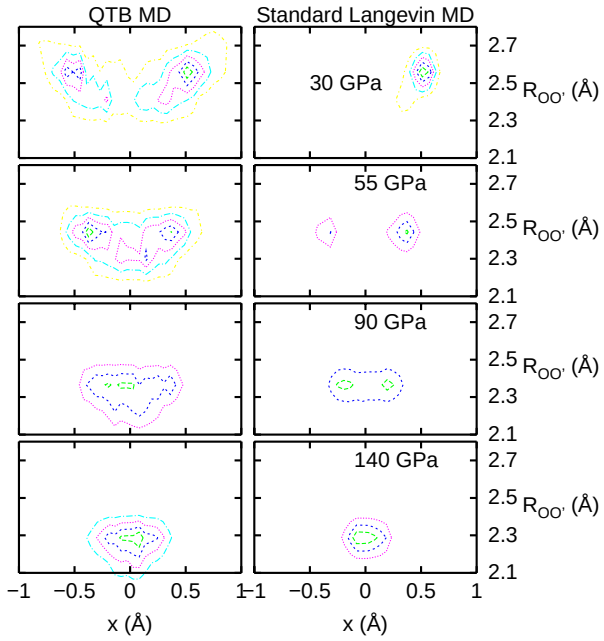

Figure 3.3.3: Contour plots of the average proton distribution function $P(x, R_{\mathrm{OO'}})$ as a function of the proton position relative to the bond midpoint, $x = R_{\mathrm{OH}} - R_{\mathrm{O'H}}$, and the corresponding O-O distance, $R_{\mathrm{OO'}}$ (no configurational average was performed), from QTB (left panels) and standard *ab initio* (right panels) molecular dynamics simulations.

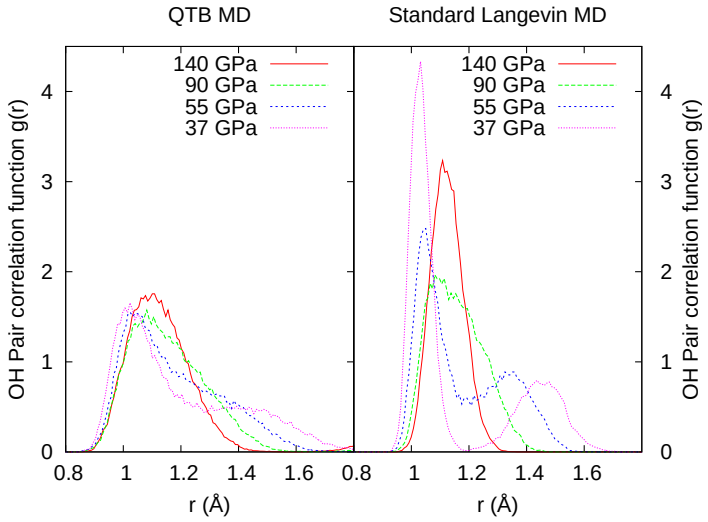

Figure 3.3.4: Oxygen-hydrogen pair correlation functions $g(r)$ as a function of the O-H distance, from QTB (left panel) and standard *ab initio* (right panel) molecular dynamics simulations.

pressure ($P \sim 30$ GPa), the proton is localized on one site in the classical frame, which shows explicitly that it never hops from one well to the other. Indeed, thermal fluctuations are not important enough at this pressure to induce a delocalization of the classical proton. In contrast, the proton is delocalized over two sites within the QTB framework, meaning that during its trajectory, the proton passes from one well to the other. Thus, the zero-point energy is properly accounted for in the QTB simulations allowing the proton to jump back and forth through the energy barrier at pressures as low as 30 GPa. When pressure is increased, the energy barrier is lowered thus allowing even the classical proton to hop between the two sites, as revealed by the probability distribution function at 55 GPa in the classical simulation. At 140 GPa, both methods show a unimodal distribution centered at $x = 0$, corresponding to ice X, while at 90 GPa, only the QTB distribution is unimodal. The distribution functions provided by QTB simulations are similar to those from *ab initio* PIMD calculations [116]: the onset of proton tunneling occurs however at lower pressure in our simulations mainly because of the higher temperature (300 K instead of 90 K in reference [116]).

An easier way to analyze the oxygen-hydrogen distances is to look at the O-H pair correlation functions $g(r)$ (see Figure 3.3.4). In both standard *ab initio* (without NQE) and QTB MD cases, the low-pressure results consist of two peaks, denoting two different bond lengths: short (~ 1.1 Å) for covalent O-H bonds and long (~ 1.4 Å) for compressed hydrogen H-O bonds. In the classical *ab initio* simulations, for $P \leq 40$ GPa, the proton never switches between the two bonds as the two peaks are well defined with $g(r) = 0$ between them. As the pressure increases, the two peaks merge progressively, until the proton is localized in the middle of the bond. In contrast, with the QTB method, the peaks are broader, thus revealing looser bonds, and merge at lower pressure.

Finally, we can consider that the proton position relative to the bond midpoint, x, is a good order parameter or reaction coordinate for the symmetrization transition (x corresponds to δ in reference [108]). As long as the hydrogen bonds are asymmetric, the average value of x is non-zero; at the transition and above, the hydrogen bonds are symmetric and x is equal to zero on average. Figure 3.3.5 shows the average probability

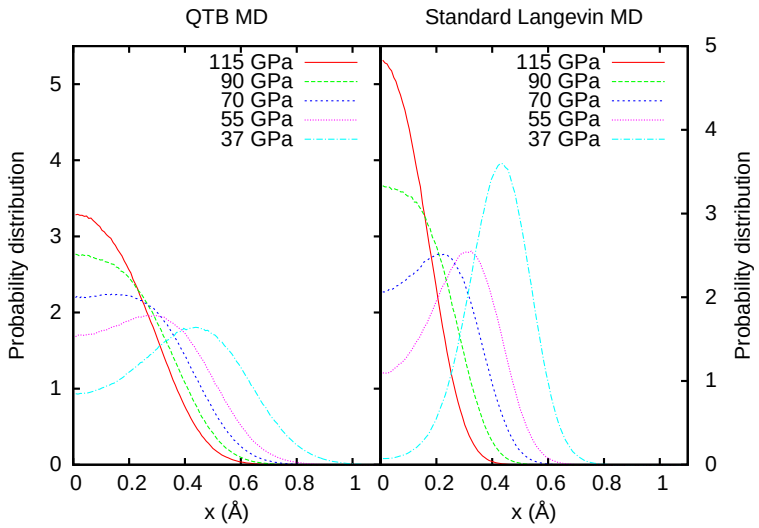

Figure 3.3.5: Probability distribution of the proton position relative to the bond midpoint $x = R_{\mathrm{OH}} - R_{\mathrm{O'H}}$ at different pressures, from QTB (left panel) and standard *ab initio* (right panel) molecular dynamics simulations.

distribution of $|x|$. Clearly, NQE tend to broaden the distributions and the transition to ice X occurs at lower pressure than in the classical framework, between 55 and 72 GPa. These results (as well as previous theoretical studies [106, 116, 151]) point out that NQE are significant and must be included for an accurate description of the symmetrization transition in ice. However, in both cases, proton tunneling tends to blur the transition in which the transformation of the two-peak probability distribution into a single peak is continuous.

3.3.3 Vibrational properties of high-pressure ice

In contrast to the progressive change of O-H distribution functions, infrared and Raman scattering experiments results display a relatively precise transition pressure at approximately 65 GPa. Indeed, as explained in section 3.3.1, the transition from ice VII to ice X is marked by a strong softening of the O-H stretching mode (see Figure 3.3.1) [142–148]. Moreover, the analysis of a one-dimensional phenomenological model in section 3.2.3 showed that, at room temperature, the inverse susceptibility displays a minimum that is related to a mode softening at the transition.

Thus, vibrational properties, which are naturally computed from the semiclassical atomic trajectories, at variance with PIMD, are a clue to identify the transition precisely. The simulated spectra are calculated through the Fourier transform of the nucleus autocorrelation function at different pressures (see also section 2.3.2 for more details on the computation of vibrational spectra):

$$I(\omega) \propto \sum_j \left| \int x_j(t) \mathrm{e}^{i\omega t} \, \mathrm{d}t \right|^2 \tag{3.3.1}$$

where

$$x_j(t) = \mathbf{r}_j(t) \cdot \mathbf{u}_j, \quad \mathbf{u}_j = \frac{\mathbf{OO}}{\|\mathbf{OO}\|^2}. \tag{3.3.2}$$

$x_j(t)$ is the relative position of hydrogen j on the O-O direction i.e. it is the projection of the hydrogen position vector $\mathbf{r}_j$ at time t along the direction vector $\mathbf{u}_j$.

The top panel of Figure 3.3.6 shows the proton vibrational spectrum $I(\omega)$ obtained from QTB simulations in ice VII at approximately 20 GPa. The various peaks in the spectrum can be identified by comparing our results to infrared and Raman measured frequencies (see Figure 3.3.1) [145,146,148]. Indeed, our spectra are in very good agreement with experimental measurements. Hence, at high frequency, near 3000 cm^{-1}, we have the O-H stretching mode: the antisymmetric and symmetric vibrations, ν_3 and ν_1 are undistinguishable in our spectrum due to the large width of the corresponding peak. At lower frequency, we can distinguish the O-H bending mode ν_2 around 1600 cm^{-1}, the rotational vibrations of the water molecule ν_R and ν''_R near 1200 and 850 cm^{-1} respectively and the translational mode ν_T at 350 cm^{-1} approximately. The lower panel of Figure 3.3.6 shows the proton vibrational spectra $I(\omega)$ for different pressures. We can already see that the high-frequency peak, corresponding to the O-H stretching mode, broadens as pressure increases and that its frequency decreases up to 70 GPa approximately.

The mode frequencies are then extracted from these spectra and shown in Figure 3.3.7 (each peak of $I(\omega)$ is fitted with a Lorentzian function in order to extract the frequency and the width of each mode). First, we can see that the QTB-MD results are in excellent agreement with both infrared and Raman measured frequencies (indicated by black dots) [145, 146, 148]. One of the most noticeable features of these spectra is that, as pressure approaches 65 GPa, the O-H stretching mode undergoes a significant softening, as already pointed out by scattering experiments. The O-H stretching mode presents a clear minimum at the VII-X transition, near 65 GPa. Struzhkin and coworkers [145] explained that, as pressure increases to the transition pressure, the stretching mode couples to the lower-frequency modes which results in a large number (or a cascade) of Fermi resonances between the softening stretching mode and the rotational mode, the bending mode and their combinations. In their work, they also calculated the transverse (TO) and longitudinal (LO) frequencies from their reflectivity spectra and found that the LO mode has a minimum at the transition (illustrated by the open triangles in Figure 3.3.7). This LO mode is in very good agreement with our high-frequency peak, at any pressure. We also computed the oxygen T_{2g} vibrational mode (see section 2.3.2 for more details). This mode is related to the cuprite-like structure of ice X and is Raman-active only in the symmetric phase X (hence, we show our results only above the transition). The frequencies computed from the QTB simulations are in excellent agreement with Raman measurements on high-pressure ice by Goncharov and coworkers [148] and Bove and coworkers [152].

Finally, Figure 3.3.8 shows the O-H stretching mode frequencies obtained in high-pressure ice from QTB simulations and from standard Langevin molecular dynamics i.e. simulations that exclude any NQE. Clearly, NQE play a role and modify the O-H stretching mode frequency. Moreover, the transition pressure P_t indicated by the minimum of the O-H frequency is lower when NQE are included via the QTB. This confirms that NQE play an important role in the VII-X transition in high-pressure ice.

3.3.4 Conclusion

Below the transition, in phase VII, the hydrogen bonds are asymmetric and disordered: proton tunneling occurs and is responsible for the blurring of the distribution functions below the transition; this leads to a "grey zone" (between 30 and 60 GPa approximately) where the protons are delocalized over their two equilibrium sites. The analysis of a one-dimensional Landau-like model of second-order phase transitions (see section 3.2) shows

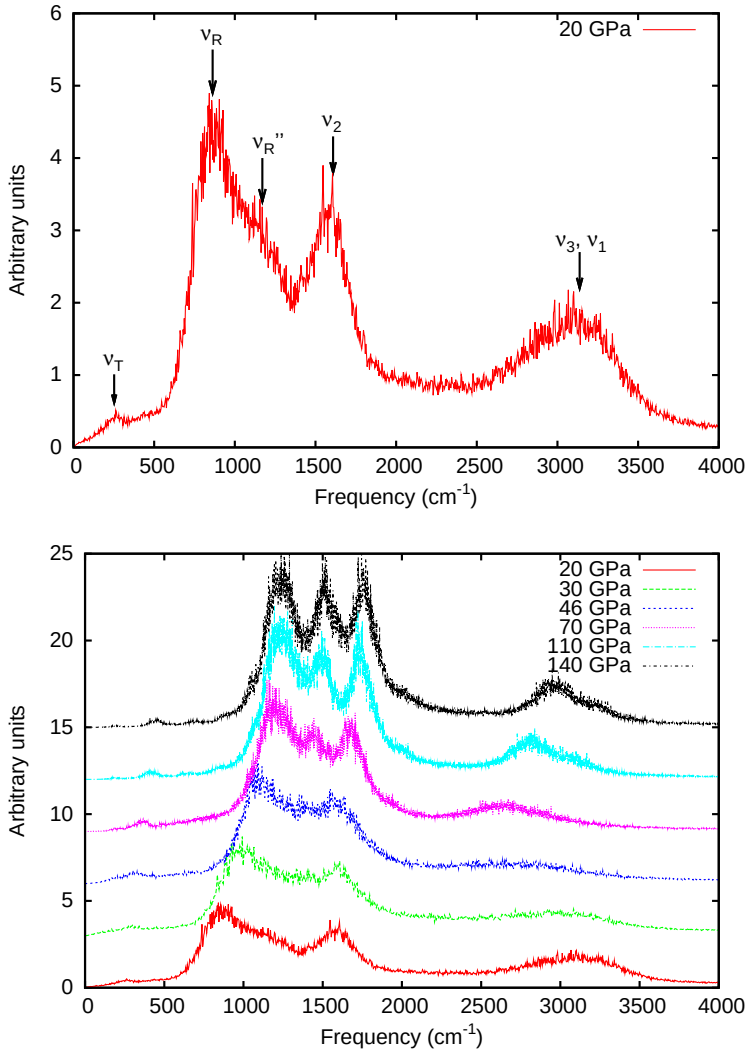

Figure 3.3.6: Proton vibrational spectrum in ice computed through equation (3.3.1) from QTB molecular dynamics simulations. Top panel: the proton spectrum is shown at 20 GPa approximately (the following mode frequencies are also indicated: the O-H stretching modes ν_1 and ν_3, the translational mode ν_T, the O-H bending mode ν_2 and the H_2O rotational modes ν_R and ν_R''). Lower panel: the proton spectra are shown for various pressures from 20 to 140 GPa.

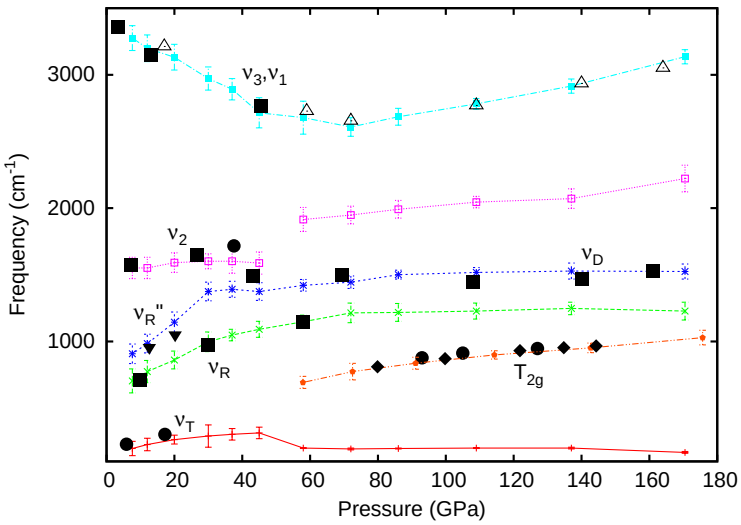

Figure 3.3.7: Vibrational frequencies and widths obtained with QTB at ambient temperature up to 180 GPa. Selected infrared (inverted triangles [146] and solid squares [145]) and Raman (solid circles [148] and solid diamonds [152]) experimental data are shown: ν_T is the translational vibration, ν_R and ν''_R are rotational vibrations of the H_2O molecule, ν_2 is the O-H bending vibration, ν_1 and ν_3 are the symmetric and antisymmetric O-H stretching vibrations, ν_D is a deformational mode and T_{2g} is an oxygen vibration mode. The open triangles are the highest LO frequency estimated in reference [145]. The softening of the O-H stretching mode indicates the transition from phase VII to phase X of ice.

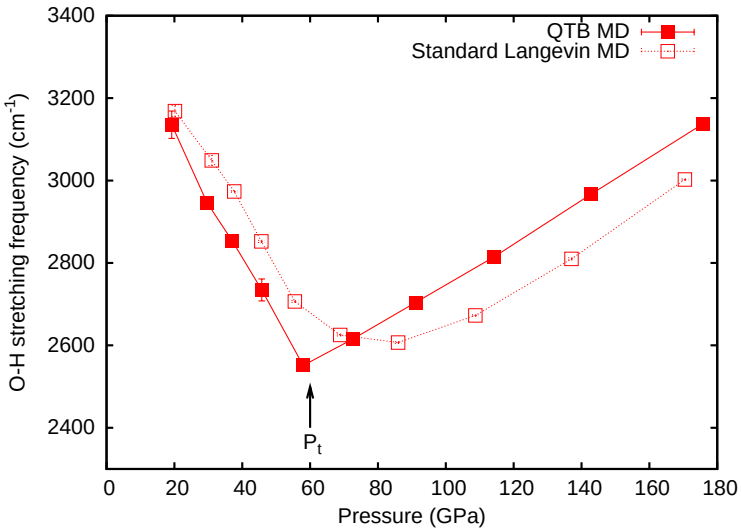

Figure 3.3.8: O-H stretching mode frequencies computed from QTB and standard Langevin molecular dynamics in high-pressure ice. The transition from ice VII to ice X is indicated by the minimum of the curve.

that the zero-point energy is the driving force of this transition: when the zero-point energy equals the potential barrier height, the proton distribution changes from a bimodal function to a unimodal one, with a maximum at the O-O midpoint. Furthermore, the transition to ice X is marked by a strong softening of the O-H stretching mode, as predicted by the study of the inverse susceptibility. The determination of a precise transition pressure is thus much easier through the analysis of the vibrational properties of the system.

Appendix

3.A Effective proton potential energy calculations

There are several different methods to obtain the potential energy surface of the protons. One could use for example metadynamics in order to get the free energy landscape. Here, we briefly describe the calculation of the potential energy at $T = 0$ K. In most cases, we reduce the problem to only one dimension; however, it is easily generalized to two or more dimensions. Assuming that x is the proton coordinate e.g. the proton position relative to the O-O midpoint, for each value of x, we let the atomic structure relax i.e. we minimize its energy while keeping x constant. The effective potential $V(x)$ that we obtain can then be viewed as a mean-field approximation for the potential energy landscape seen by the protons. This method implies that x is the relevant order parameter. Moreover, by reducing the problem to one degree of freedom (i.e. only one effective proton), we make several approximations. First, we simplify the inherent complexity of the atomic environment of the protons. This can, however, be repaired by taking into account the 3-dimensional position of the proton, $\mathbf{r}$, instead of x. Second, for each value of the order parameter, we move all protons coherently along their hydrogen bonds. A coherent motion of all protons, while possible, would actually be relatively rare and we would rather expect all protons to move independently from each other. Finally, by optimizing the atomic structure at $T = 0$ K, we neglect all dynamical fluctuations of the atomic positions and their consequences on the effective potential seen by the protons. In passing, we note that the exchange-correlation functional might also influence the potential [153]. Hence, we will use the PBE functional for all density functional theory studies on ice since it is known to provide a good description of hydrogen bonds (see Appendix 2.B.4). In AlOOH however, we will use the BLYP functional since it gives potential barriers approximately 15% higher than PBE (knowing that GGA tends to underestimate energy barriers, we used the functional that gave us the highest barrier).

We will compare the proton potentials in high-pressure pure and salty ices, as well as in high-pressure ice with an external homogeneous electric field. For the latter, we compute the potential felt individually by each proton instead of averaging over all the protons in the system:

$$V_p(\mathbf{r}) = -\int \mathbf{f}_p(\mathbf{r}') \cdot \mathrm{d}\mathbf{r}' \tag{3.A.1}$$

where $\mathbf{f}_p$ are the interatomic forces and $\mathrm{d}\mathbf{r}'$ are the displacements of each proton along the O-O segment. Hence, in high-pressure ice, if we average V_p over all the protons, we obtain the same potential $V(x)$ computed in the manner described above (i.e. through the total energy of the system). We will use $V_p(\mathbf{r})$ instead of $V(x)$ in high-pressure ice under an external electric field because if the electric field $\mathbf{E}$ is aligned along the $\mathbf{z}$ axis, then half the protons "feel" a positive effective electric field E_{eff} while the other half "feel" a negative effective electric field $-E_{\text{eff}}$ (since the O-H$\cdots$O bonds are aligned along the

(111) directions). Hence, if we averaged over all the protons, the effects of the electric field would cancel each other out and we would not be able to see anything.

3.B Computational details

The simulations were performed on a cell containing 54 water molecules. They were initially arranged in the phase VII geometry. We checked that simulations starting from the phase X gave the same results. The electronic structure is treated by the density functional theory (see Appendix 2.B) within the generalized gradient approximation (GGA) with a PBE functional [99]. We used ultrasoft pseudopotentials as available in the Quantum Espresso code. The electronic wave functions were expanded in plane waves up to a kinetic cutoff of 30 Ry (we checked the convergence of the total energy and forces). In order to check if van der Waals contributions to the functional are important in our system, we compared the energies obtained after structural relaxation of the simulation cell (see Table 1 in reference [4]) where van der Waals contributions are included within the DFT-D approximation [154]. We found that the relative difference in energies is approximately 0.1%. We also checked the effect of van der Waals contributions on the phonon frequencies: the relative shift of the phonon frequencies that is due to the van der Waals contributions never exceeds 10^{-4} and is thus negligible in our high-pressure study of ice.

We ran constant-volume simulations at room temperature ($T = 300$ K) using standard Langevin and QTB molecular dynamics (see section 2.3.1). We chose a damping coefficient of 333 cm^{-1} (approximately 10 THz). We also ran simulations with a damping coefficient of 3.33 cm^{-1}: the simulation results differ only in the width of the vibrational spectra. The simulations were run for a total time of approximately 29 ps with a 0.484 fs time step. The lattice parameter was varied from 18 to 14.5 bohrs, thus spanning a pressure range from 12 to 180 GPa (the pressure was computed through the stress theorem [155]).

Chapter 4

Towards lower symmetry: the effect of the environment on nuclear quantum effects

Contents

4.1 Introduction

In the previous chapter, we have analyzed the VII-X phase transition of high-pressure ice and described its mechanism which involves the quantum nature of protons. However, when dealing with other systems, namely salty ices (i.e. a LiCl or a NaCl molecule has been introduced into the ice structure) and the high-pressure δ phase of aluminium oxide hydroxide (AlOOH), we were confronted with more complicated atomic environments for

the hydrogen bonds. This in turn had consequences on the evolution of the O-H$\cdots$O bonds under pressure that were different than in the case of pure high-pressure ice. The following chapter will thus focus on protons that are confined in more complex atomic environments.

4.1.1 The effect of the atomic environment on the proton potential

The previous chapter focused on a double well picture for the proton effective potential (see section 3.2). This potential, however, represents a particular high-symmetry case as it is symmetric with respect to $x = 0$ i.e. the midpoint of the oxygen-oxygen distance. This assumption is verified in *pure* high-pressure ice where the system is constituted of water molecules only. The atomic environment of a hydrogen atom is indeed the same on both sides of the double well. However, this might not always be true in more complex crystals with lower symmetry or if this symmetry is broken by the presence of impurities. In 1998, Johannsen already predicted that a model potential for protons in hydrogen bonds should include an asymmetric case in order to correctly describe experimental hydrogen bonds in various systems [114]. Indeed, while coherent tunneling of protons has been observed experimentally in molecular crystals [128], in many cases, protons are localized [156] and this localization can sometimes be explained by an asymmetric proton potential. Several reasons can be invoked for the asymmetry of the potential. First, there are hydrogen bonds between chemically distinct donor and acceptor species, or the local environment of the hydrogen bond might not be symmetric. Another reason for the asymmetry of the potential is the coupling of hydrogen bond donor and acceptor to lattice vibrations, leading to a time-dependent proton effective potential. Indeed, in many systems, the displacements of protons are accompanied by a rearrangement of the surrounding electronic density leading to small readjustments of the atomic equilibrium positions. This coupling to the protons' environment usually renders the two wells of the potential inequivalent [128]. Finally, Johannsen remarked that the idea of a universal potential for the description of hydrogen bonds, even if appealing, might not be completely satisfactory. One should therefore be careful that each double well potential, with its adapted set of parameters, is valid only for a limited range of the bond length R. However, if the universality of the proton potential is unattainable at the moment, these potentials are useful to understand the mechanisms of proton localization and delocalization in several materials as well as for the study of isotope effects when protons are replaced by deuterium. As we will see in the next section, the shape of the potential can influence the properties of protons as introducing even a small asymmetry in the potential can lead to dramatic changes of the proton wavefunctions.

4.1.2 The consequences of an asymmetric potential on proton tunneling and hydrogen bond symmetrization: a one-dimensional study

We use in the following the same Landau-like potential that we used to model hydrogen bonds in high-pressure ice (see equation (3.2.1) in section 3.2.1). In the symmetric double well potential and in the case of a high barrier ($P = 10$ GPa) shown in the top panel of Figure 4.1.1, the low-energy states are almost degenerate ($E_1 \simeq E_2$, $E_3 \simeq E_4$ etc): each state is delocalized with an equal probability in each well. As explained in section 3.2.2, these states lead to coherent tunneling of protons through the barrier: the tunneling splitting $\Gamma_{12} = (E_2 - E_1)/\hbar$ then evaluates the proton hopping rate.

In order to introduce asymmetric potentials, we study the case of an asymmetric

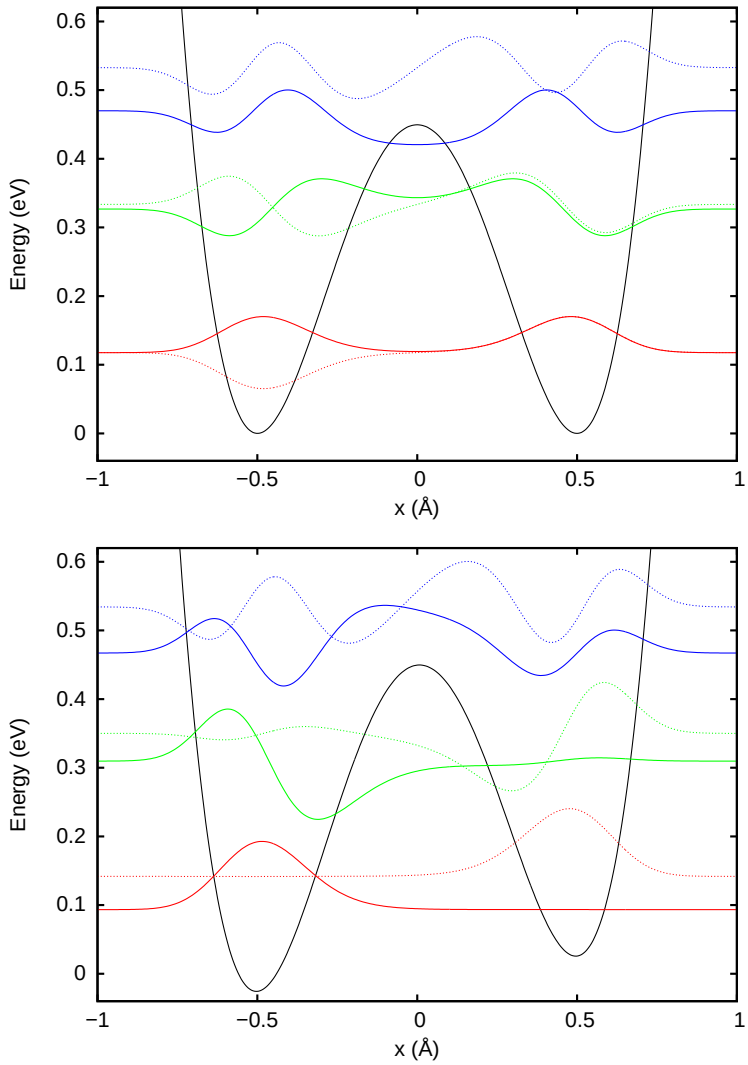

Figure 4.1.1: Symmetric ($E = 0$ - top panel) and asymmetric ($E = 0.014$ V.Å^{-1} - lower panel) double well potential (see equation (4.1.1)) and corresponding proton wave functions, calculated numerically. The baselines of the wave functions have been shifted to represent the energy levels. In both cases, $P = 10$ GPa i.e. we are considering the situation of a high barrier.

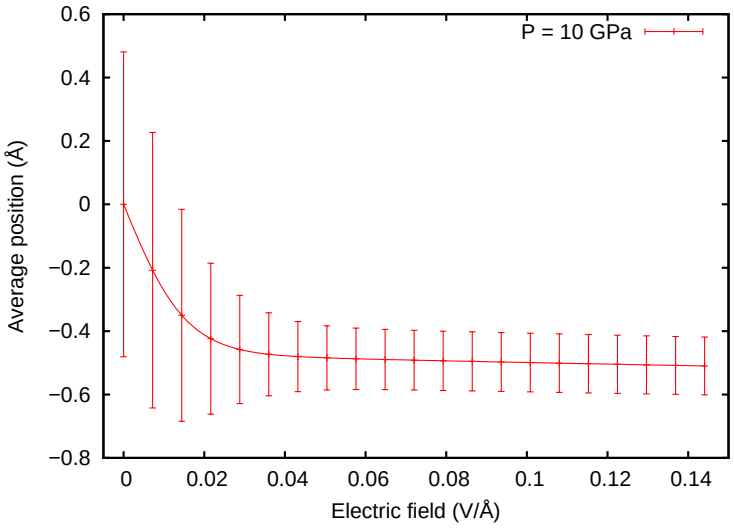

Figure 4.1.2: Average position $\langle x \rangle$ (see equation (4.1.2)) as a function of the electric field E in the potential $V(x)$ (see equation (4.1.1)) at $P = 10$ GPa and $T = 300$ K. The vertical bars correspond to the standard deviation σ_x (see equation (4.1.3)).

Landau-like potential:

$$V(x) = ax^4 + b\,(P - P_c)\,x^2 + Ex + V_0 \tag{4.1.1}$$

where we have included a linear term. E is a homogeneous electric field while x is the proton position along the oxygen-oxygen segment, P is the pressure. We use the same parameters (a, b and P_c) as in section 3.2.1 in order to represent the potential energy calculated in ice VII. As shown in the lower panel of Figure 4.1.1, the quantum states are considerably modified when the potential becomes non-symmetric. The lower-energy states are localized in a single well and the degeneracy is lifted. The higher-energy states, whose energies are close to the barrier height, have a non-zero probability in both wells indicating *incoherent tunneling* of protons through the barrier. As expected, for a small asymmetry of the potential as depicted in Figure 4.1.1, the wave functions above the barrier are not significantly affected by the asymmetry and are close to the corresponding wave functions in the symmetric potential. Since Γ_{12} or Γ_{WKB} (as defined in section 3.2.2) cannot be used to quantify proton tunneling in an asymmetric potential, we compare the average position $\langle x \rangle$ of the proton in the potential and its standard deviation σ_x. Indeed, at finite temperature T, we have:

$$\langle x \rangle = \mathrm{Tr}\{\hat{\rho}(T)\hat{x}\} = \frac{1}{Z}\sum_n \mathrm{e}^{-\beta E_n}\langle \Psi_n | x | \Psi_n \rangle \tag{4.1.2}$$

where $\hat{\rho}(T)$ is the density matrix defined in equation (3.2.22), Z is the partition function, $\beta = (k_B T)^{-1}$ is the inverse temperature and $\{\Psi_n, E_n\}$ are the eigenfunctions and eigenenergies of the system. Similarly, we compute the standard deviation of x i.e.

$$\sigma_x = \sqrt{\langle x^2 \rangle - \langle x \rangle^2}, \quad \text{and} \quad \langle x^2 \rangle = \mathrm{Tr}\{\hat{\rho}(T)\hat{x}^2\}. \tag{4.1.3}$$

Figure 4.1.2 shows the average position $\langle x \rangle$ and its standard deviation at a given pressure ($P = 10$ GPa) as a function of the electric field E i.e. as the asymmetry of the potential $V(x)$ increases. When $E = 0$ i.e. in the case of a symmetric potential, $\langle x \rangle = 0$

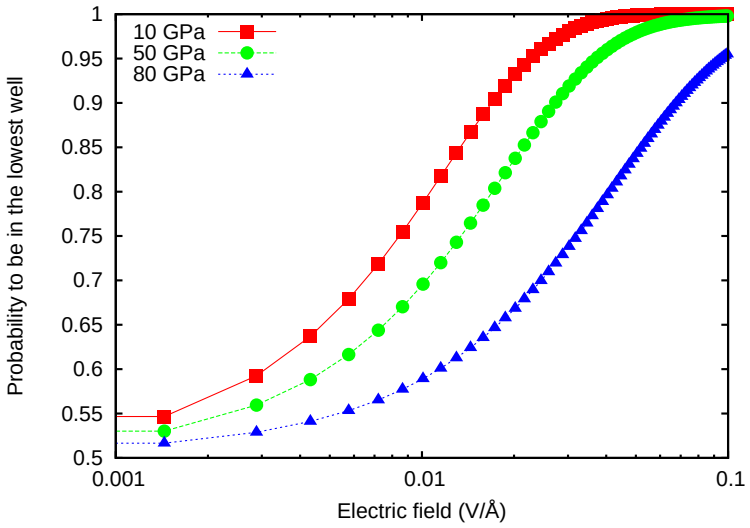

Figure 4.1.3: Probability for the proton to be in the lowest well (P_{low} in equation (4.1.4)) of the double well potential (equation (4.1.1)) as a function of the electric field E for different values of the pressure.

which indicates that the particle has an equal probability to be in the left or the right well.[1] As the asymmetry of the potential increases, the average position decreases and converges towards the position of the lowest well, near -0.5 Å. Similarly, the delocalization of the proton as indicated by its standard deviation σ_x is maximum when the potential is symmetric at $E = 0$. As the asymmetry of the potential increases, σ_x decreases and the potential is more and more localized in the lowest well of the potential. Another way to quantify the localization of the proton is to compute the probability to be in the lowest well:

$$P_{\text{low}} = \int_{-\infty}^{0} \rho(x,T)\,\mathrm{d}x \tag{4.1.4}$$

where $\rho(x,T)$ is the probability density at room temperature i.e.

$$\rho(x,T) = \frac{1}{Z}\sum_n \mathrm{e}^{-\beta E_n}|\Psi_n(x)|^2. \tag{4.1.5}$$

Figure 4.1.3 shows that P_{low} evolves rapidly with increasing E from 0.5 (corresponding to the quantum tunneling regime where the proton has equal probability to be in each well) to 1 (corresponding to a proton localized in the lowest well). Hence, within this simplified model, even a small electric field compared with local fields present in condensed matter at a nanometric scale, drastically reduces the proton tunneling rate between the two potential wells. In this case, the proton's equilibrium position is equivalent to the equilibrium position of its classical counterpart: this means that even a small electric field is sufficient to suppress much of the quantum nature of protons in ice !

The asymmetry of the proton potential can thus be responsible for the localization of protons and for the disappearance of proton hopping. However, the transition from phase VII, with disordered and asymmetric hydrogen bonds, to phase X, with symmetric hydrogen bonds, is driven by the zero-point energy (ZPE) of the system. The transition

[1] $\langle x\rangle = 0$ also corresponds to the case where the proton density has a maximum at $x = 0$. Here, $P = 10$ GPa and the density has two maxima, one in each well.

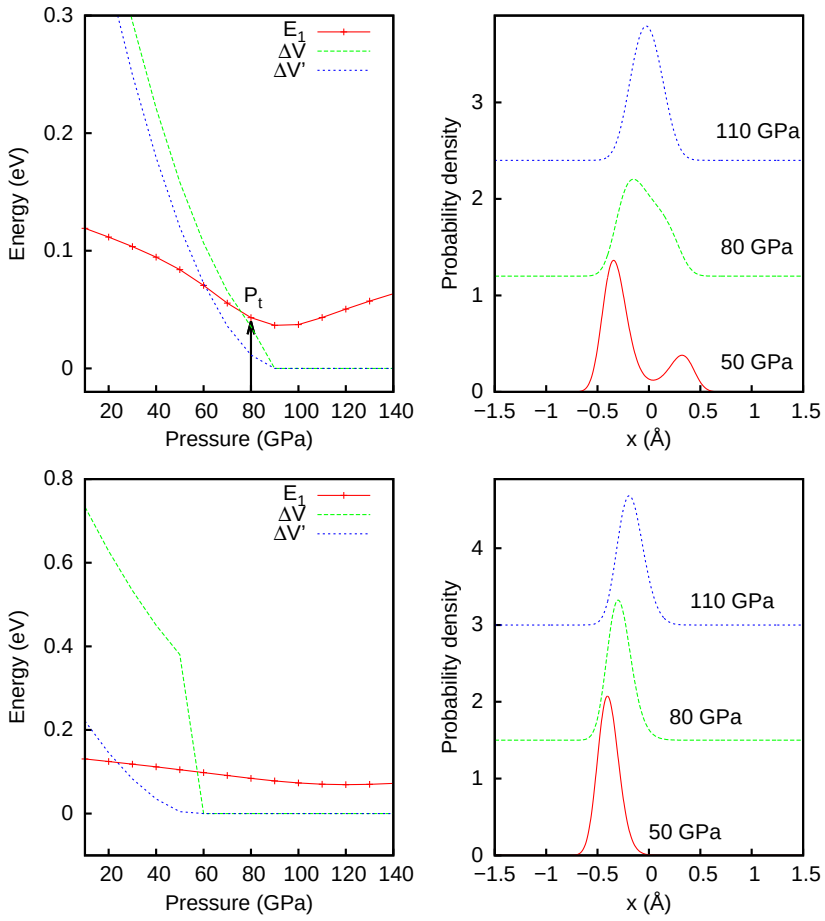

Figure 4.1.4: Left panels: Evolution of zero-point energy E_1 and barrier heights ΔV and $\Delta V'$ as functions of pressure for two different values of E (top panel: $E = 0.014$ V.Å^{-1}, lower panel: $E = 0.14$ V.Å^{-1}). P_t indicates the quantum transition pressure (i.e. $\Delta V = E_1$). Right panels: Probability density $\rho(x, T)$ at room temperature and different pressures for $E = 0.014$ V.Å^{-1} (top panel) and $E = 0.14$ V.Å^{-1} (lower panel).

actually occurs when the ZPE equals the barrier height and coincides with a topological change of the proton's wavefunction (see section 3.2). When the potential is asymmetric, instead of one energy barrier, we are now faced with two different barriers that we will denote ΔV and $\Delta V'$, with $\Delta V > \Delta V'$. The left panels in Figure 4.1.4 show the evolution of the ZPE, ΔV and $\Delta V'$ with pressure in two asymmetric cases. From a classical point of view, the transition should occur when the two wells merge into a single one. In the first case (top left panel), the electric field is sufficiently small so that the ZPE equals ΔV at a lower pressure ($P_t \simeq 80$ GPa) than the classical transition pressure ($P_c \simeq 90$ GPa). The ZPE tends to lower the transition pressure and at the transition, the proton density changes from a two-maxima distribution to a single-maximum function (see top right panel in Figure 4.1.4). In the second case, the asymmetry of the potential is much more important; as shown in the lower left panel in Figure 4.1.4, the double-well potential becomes a single-well potential before the ZPE actually levels with the barriers. Moreover, as shown in the lower right panel of Figure 4.1.4, the density does not undergo any topological change: at any pressure, the density has a single maximum which is off-centered with respect to the center of the potential. As pressure increases, the position of this maximum is shifted towards the center of the potential; however, even at high pressure, the density is not symmetric with respect to $x = 0$. Hence, the term "symmetrization transition" may not be appropriate when the potential is strongly asymmetric: we will use the term "pseudo-symmetrization" instead in these cases since the proton distribution function will remain asymmetric and off-centered above the transition pressure in these cases. In particular, when the asymmetry is important, there is no modification of the nature of the proton density; in this case, no transition takes place in the system. Moreover, as in pure ice, a rigorous way to take into account the excited states at finite temperature is to consider the inverse susceptibility χ^{-1} as a function of pressure (see equation (3.2.24)). The minimum of χ^{-1} indicates the transition from asymmetric hydrogen bonds to symmetric O-H bonds. Figure 4.1.5 shows the evolution of χ^{-1} as a function of pressure for different values of the electric field E. As E increases, χ^{-1} is shifted towards higher pressures, which is consistent with the top panel in Figure 4.1.4 where proton tunneling is reduced. Hence, the soft mode accompanying the transition is shifted towards higher frequencies for a given pressure.

Finally, we note in passing that we have studied here a Landau-like potential with an additional linear term. At a given pressure, the system undergoes a first-order phase transition as the electric field E is varied. Indeed, the potential first derivative $V'(x)$ has three real roots if

$$\Delta = 8ab^3 (P_c - P)^3 - 27a^2E^2 > 0. \tag{4.1.6}$$

In this case i.e. if $\Delta > 0$, then the potential $V(x)$ has two minima and a maximum. For $E \neq 0$, one of the minima corresponds to a metastable state. However, when E reaches a critical value so that $\Delta = 0$, this metastable state disappears and the potential has only one minimum. The critical value E at which the first-order transition occurs is

$$E = \left[\frac{8b^3}{27a} (P_c - P)^3\right]^{1/2}. \tag{4.1.7}$$

In the following, we will discuss two different situations in which the proton effective potential is asymmetric. First, we will show how small impurities in high-pressure ice can affect the tunneling properties of protons (section 4.2). Then, we will study the symmetrization of hydrogen bonds in a more complex system, the δ phase of aluminium oxide hydroxide (section 4.3).

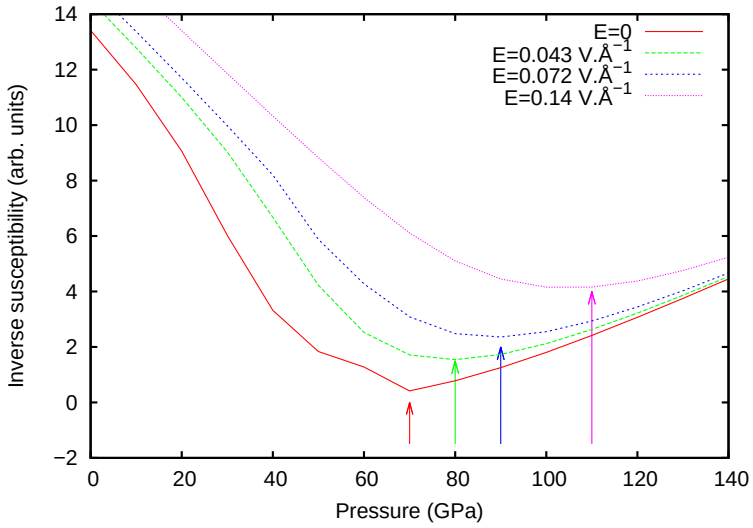

Figure 4.1.5: Inverse quantum susceptibility χ^{-1} at room temperature as a function of pressure (see equation (3.2.24)) for different values of the electric field E. The arrows indicate the minimum of the curve.

4.2 The VII-X transition in salty ices under high-pressure

4.2.1 Why are salty ices important ?

Ices under very high pressure are present in many planets. Indeed, the recent Voyager, Galileo and Cassini-Huygens missions have greatly improved our knowledge of ice-rich planetary bodies, both for planets within our solar system [157–160] and extra-solar planets [161, 162]. However, while pure high-pressure ice has been extensively studied both experimentally and theoretically, natural ices are usually "dirty" in the sense that they unavoidably contain impurities such as salt. The incorporation of impurities into the ice structure may be due to interactions between the ice and subsurface oceans, or between the ice and surrounding silicate or metallic materials that may be present in the planet's interior. The effect of ionic defects in high-pressure ice has only been recently investigated [5, 152, 163–171]. Indeed, it was thought for a long time that, upon cooling a salty solution, water would expel the salt ions and form pure ice on the one hand and salt hydrate on the other hand. Only recently experiments showed that one could indeed introduce a large amount of salt into the ice structure by forming first an amorphous phase of the salt solution and then recrystallizing it under pressure [165]. The consequences of the presence of salt ions in the ice structure are varied and can be quite massive, even for small salt concentrations. For instance, Klotz and coworkers showed through neutron scattering experiments that in LiCl-ice, the displacement factors of the oxygens are five times larger than in pure ice and the transition from the phase VII to the ordered phase VIII does not occur upon cooling [165]. Moreover, Raman spectroscopy on NaCl-ice showed that there is a systematic increase of the O-H stretching frequencies at any pressure up to 27 GPa [163]. Finally, it was shown by Bove and coworkers in 2015 that, for LiCl salt concentrations as low as 2 mol%, the transition pressure from phase VII to phase X is shifted from 60 GPa to 90 GPa approximately [152].

In the following, we will focus on this particular property of salty ices and determine whether the up-shift of VII-X transition pressure is due to local steric effects and if this

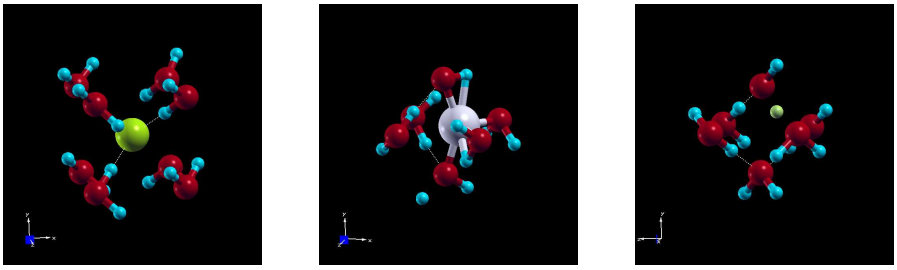

Figure 4.2.1: Atomic structure showing: (left panel) the substitutional site occupied by the anion Cl^- (or the cation Na^+); (center panel) the octahedral interstitial site occupied by the cation Li^+; (right panel) the interstitial site occupied by the cation D^+ (or the cation H^+). The red balls are oxygen atoms and the light blue balls are hydrogen atoms.

Ice types	Compositions	Initial cation sites
H-ices	$HCl{:}53H_2O$	interstitial
	$DCl{:}53H_2O$ deuterated cation	interstitial
Li-ices	$LiCl{:}53H_2O$	interstitial
	$LiCl{:}53D_2O$ deuterated	interstitial
Na-ices	$NaCl{:}53H_2O$	interstitial
	$NaCl{:}52H_2O$	substitutional

Table 4.1: List of studied systems. The anion is always chlorine replacing a water molecule at an oxygen site.

effect is generalizable to other salty ices (section 4.2.2). Then, we will confirm that the experimental results are indeed well reproduced by our QTB simulations and we will question the resilience of NQE in those systems (section 4.2.3). Finally, we will attempt to explain the behavior of protons in salty ices by comparing our results to those obtained with a model system consisting of pure ice under an external electric field (section 4.2.4).

4.2.2 A local steric effect or a long-range effect ?

In order to determine which effects are specific to the cation and which are generalizable to other ices containing ionic impurities, we study several salty ices with different cations: LiCl-ice, NaCl-ice, HCl-ice and its deuterated version DCl-ice. We compare simulations that include or not the quantum nature of nuclei (QTB-MD versus standard Langevin MD) to distinguish between NQE and classical thermal effects. The technical details of these simulations are described in Appendix 4.A. We study different types of salt in order to distinguish local steric effects from more general, long-range effects. Indeed, the different cations studied here (Na^+, Li^+, H^+ and D^+) have different sizes and behave differently: Na^+ is most likely to occupy a substitutional site (replacing a water molecule as shown in the left panel of Figure 4.2.1), Li^+, H^+, and D^+ will occupy interstitial sites. For example, Li^+ can be found in an octahedral site, surrounded by six water molecules, while H^+ and D^+ will be found on a oxygen-oxygen segment that is not already occupied by a hydrogen (see center and right panels of Figure 4.2.1). For clarity, we will denote by (S) an ice structure with a cation occupying a substitutional site and (I) an ice structure with a cation occupying an interstitial site. A summary of the studied systems is given in Table 4.1.

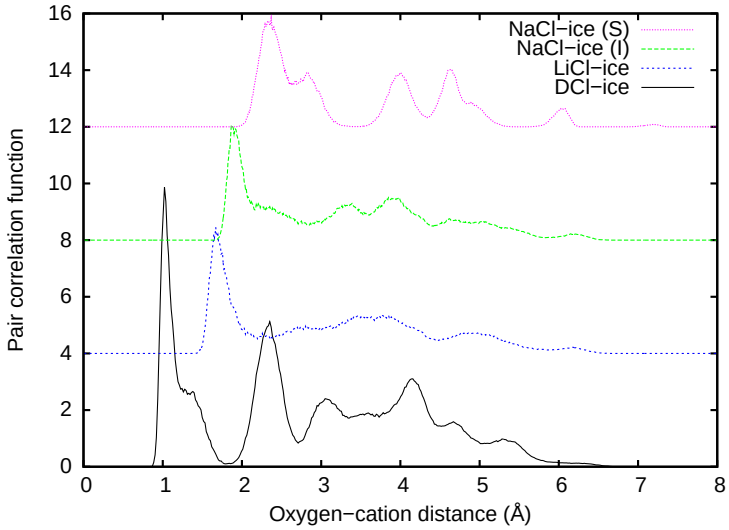

Figure 4.2.2: Pair correlation function of the cation-oxygen distance for different salty ices at approximately 50 GPa, averaged over QTB molecular dynamics trajectories.

A detailed study of the ice structure during the simulations shows that the cation can behave quite differently depending on its type and size. Unsurprisingly, the anion Cl^- remains in its initial site (substitutional). On the other hand, the trajectories of the cation differ significantly depending on whether it is H^+, D^+, Li^+ or Na^+. Figure 4.2.2 shows the pair correlation function of the cation-oxygen distance averaged over the QTB simulations at approximately 50 GPa (i.e. in the ice VII structure). The distances between the cation and the oxygen atoms are completely different depending on the cation considered: the distance between D and its first oxygen neighbors is approximately 1 and 1.3 Å, while the same distances are approximately 1.8 Å for LiCl-ice (I), 1.9 Å for NaCl-ice (I) and 2.2 Å for NaCl-ice (S). Finally, the dynamics of the cation are very different depending on the pressure and the type of cation introduced into ice. Indeed, the trajectories of the cations during our simulations are different depending on the pressure and the type of cation as are the characteristic times of their displacements.

Moreover, while the behavior of the cations varies depending on the type and size of cation introduced, the oxygen lattice is also locally modified by the presence of the impurity. Figure 4.2.3 shows the average oxygen-oxygen distance (corresponding to the O-H$\cdots$O bonds) in different salty ices compared to pure ice. We can clearly see that, even though the O-O distances near the cation are slightly larger than that of pure ice at the same pressure, the majority of O-O distances (representing 94% of the hydrogen bonds in our system) are unaffected by the presence of salt. Hence, the introduction of salt in ice results in a local distortion of the ice lattice, in agreement with previous calculations [165]. In particular, the O-O distances are slightly larger near the cation than in the rest of the system.

4.2.3 The ice VII - ice X transition in salty ices

We have seen in the previous section that the introduction of salt into high-pressure ice affected the local atomic structure near the cation and that the detailed properties of the lattice distortion depended on the type of cation introduced. Since the atomic environment is likely to affect the behavior of hydrogen bonds (see section 4.1), we investigate the VII-

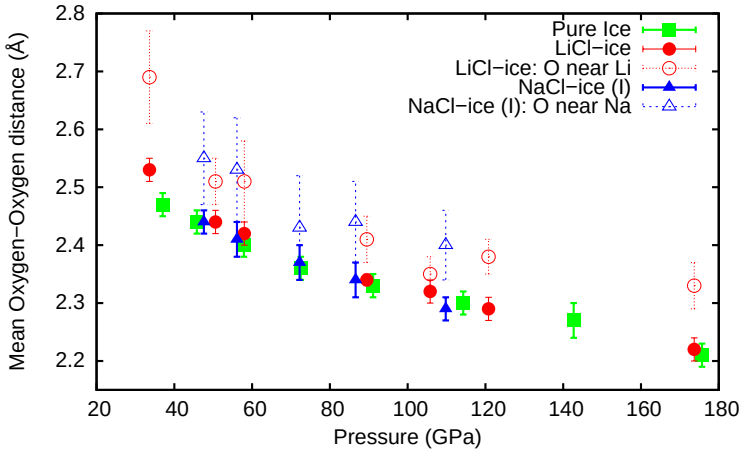

Figure 4.2.3: Average oxygen-oxygen distance (corresponding to the O-H$\cdots$O bonds) in pure ice (squares), in NaCl-ices (triangles), and in LiCl-ices (circles). Open symbols correspond to the average O-O distance near the cation.

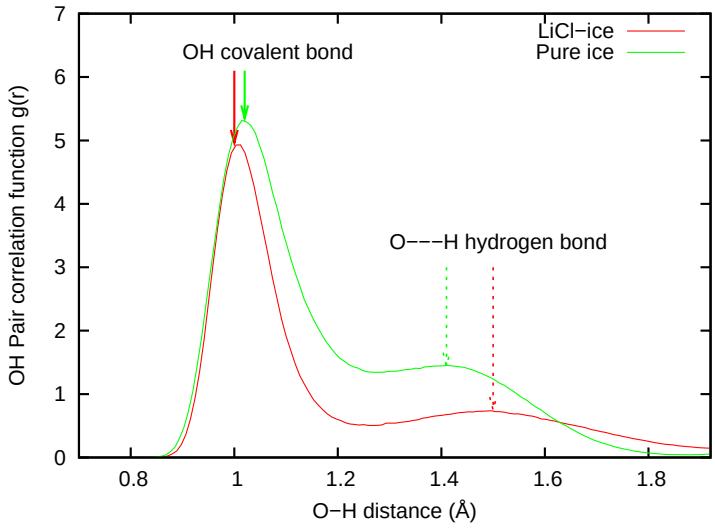

Figure 4.2.4: Pair correlation function of the oxygen-hydrogen distance in ice VII at approximately 35 GPa in pure ice (green) and in LiCl-ice (red) averaged over QTB molecular dynamics trajectories.

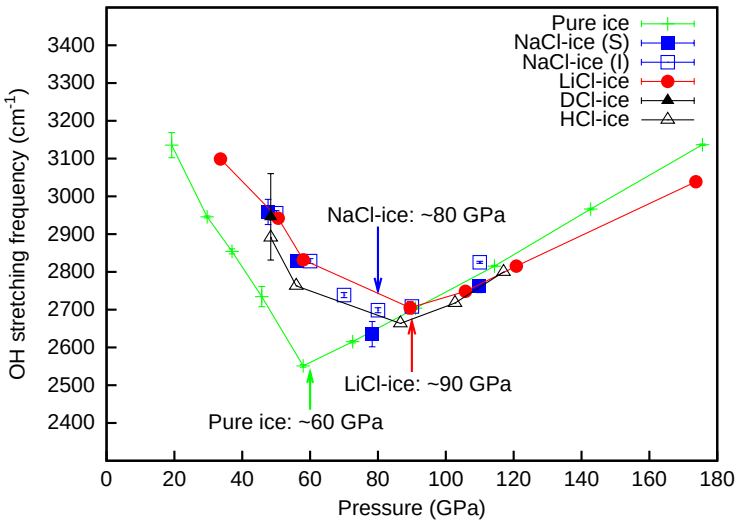

Figure 4.2.5: O-H stretching mode frequency as a function of pressure obtained from QTB simulations in pure ice (green), NaCl-ices (blue: (I) - solid squares , (S) - open squares), LiCl-ice (red), HCl-ice (black solid triangles) and DCl-ice (black open triangles). The transition pressure to ice X is indicated by the minimum of the curve.

X transition in salty ices by looking at the O-H pair correlation function (PCF) and then the O-H stretching vibration. The analysis of the oxygen-hydrogen PCF (see Figure 4.2.4) shows that, upon the introduction of salt (LiCl in the presented case), the two O-H distances are impacted: the first peak of the PCF, corresponding to the covalent O-H bond, is shifted to shorter distances while the second peak, corresponding to the hydrogen bond H$\cdots$O, is shifted to larger distances with respect to pure ice. Moreover, the proton disorder, as indicated by the height of the PCF between the two peaks, is much lower in salty ice than in pure ice. Hence, proton hopping is clearly reduced in ice VII in the presence of salt.

However, we have seen in section 3.3 that to determine a precise transition pressure from ice VII to ice X, one has to analyze the vibrational spectrum of ice. Indeed, the transition to phase X is marked by a strong softening of the O-H stretching mode: the frequency of this mode displays a minimum at the transition pressure (see Figure 3.3.7). The pressure evolution of the O-H stretching mode is displayed in Figure 4.2.5 for pure and salty ices. While in pure ice, the transition pressure predicted by QTB is around 60 GPa, in all salty ices studied here, the VII to X transition occurs at a higher pressure than in pure ice, at approximately 90 GPa. Hence, the results from QTB simulations are in very good agreement with experimental measurements. Indeed, recent experiments on both LiCl-ice [152] and NaCl-ice [5] showed that the T_{2g} oxygen vibrational mode, which is characteristic of the cuprite-like structure of ice X, appears around 90 GPa in the Raman spectra of salty ices. Moreover, the transition pressure P_t is independent of the actual position of the cation Na^+, whether interstitial or substitutional. Finally, the similarities between the different salty ices studied here indicate that the shift of P_t does not depend significantly on the type or size of the ionic impurity (at least in the concentration range studied here and within our statistical uncertainty).

Hence, the presence of small quantities of ionic impurities in ice shifts the transition pressure by about $20 - 30$ GPa with respect to pure ice. This shift is roughly the same pressure shift as observed when quantum effects are neglected in pure ice (see section

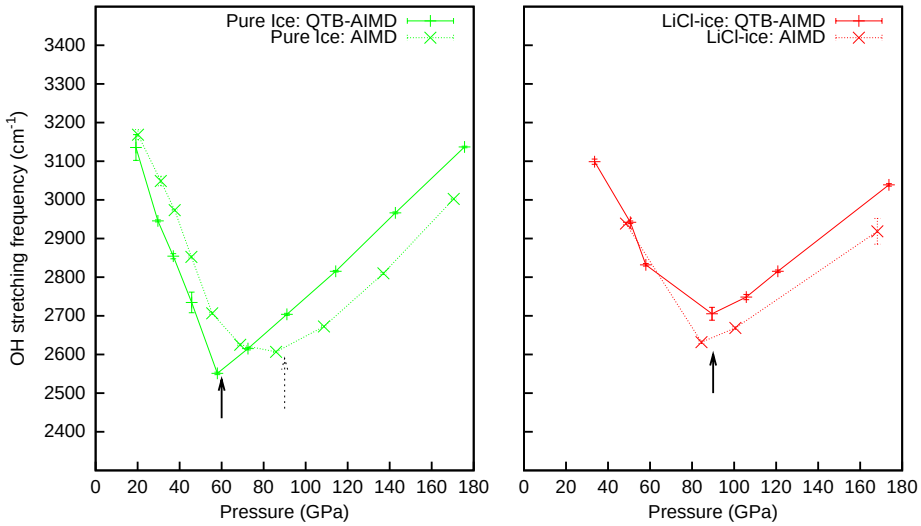

Figure 4.2.6: O-H stretching mode frequency as a function of pressure obtained from QTB (solid lines) and standard Langevin (dotted lines) simulations in pure ice (left panel) and LiCl-ice (right panel). The transition pressure to ice X is indicated by the minimum of the curve.

3.3.1) [4, 116, 119, 122]. Indeed, what is even more surprising is that standard Langevin simulations, where protons are treated as classical particles, yield the same transition pressure in salty ices as QTB simulations, while they yielded different P_t in pure ice (see Figure 4.2.6). Therefore, NQE are lifted in the O-H spectrum of high-pressure ice in the presence of salt and, as we have seen just previously, the hopping rate of protons is decreased in salty ices. This raises the fundamental question of the resilience of NQE in the presence of salt.

4.2.4 Influence of the ion-induced electric field on the quantum properties of protons

More insight on the role of NQE or their absence in salty ices can be obtained by computing the proton effective potential energy, at $T = 0$ K, where the protons' positions are constrained along the O-O segment (see Appendix 3.A for more details). Figure 4.2.7 shows the obtained effective potential energy in the different salty ices as well as that in pure ice. One of the major differences between the potential in salty ices and the one in pure ice is that the double well potential becomes asymmetric in the presence of salt: the well at $r = d_{\mathrm{OH}}/d_{\mathrm{OO}} \simeq 0.62$ has a higher energy than the well at $r \simeq 0.36$. Moreover, the potentials for LiCl-ices, NaCl-ices and HCl-ices are very similar, indicating that the presence of an ionic impurity implies a general effect on the protons in ice, independently of the type or size of the cation. Now, we have seen in the previous section (section 4.1.2) that a small asymmetry in the proton potential is likely to modify dramatically its wavefunction and thus the quantum effects associated with it. In particular, we have seen that even a small asymmetry in the potential results in a rapid decrease of the proton tunneling rate and an increase of the transition pressure to ice X, which can also be seen as a disappearance of NQE in salty ices.

The question that remains is the origin of such an asymmetry in the proton's potential. Indeed, steric or geometrical effects may explain the asymmetry of the mean proton

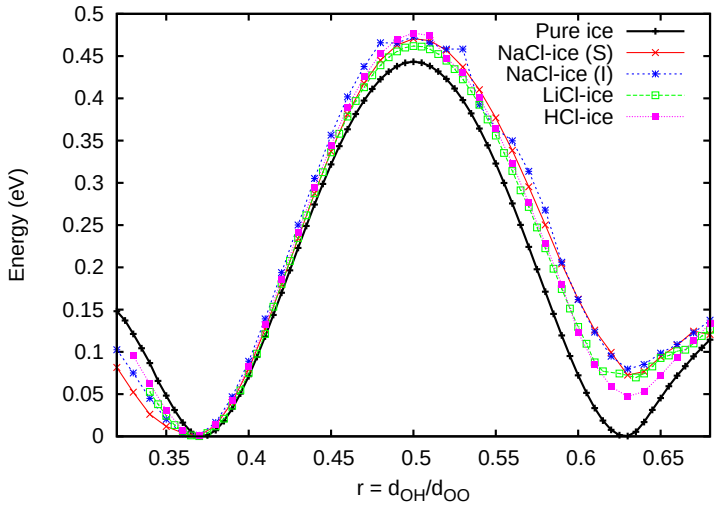

Figure 4.2.7: Proton potential energy obtained in pure ice (black curve) and in several different salty ices (colored curves) at approximately 10 GPa.

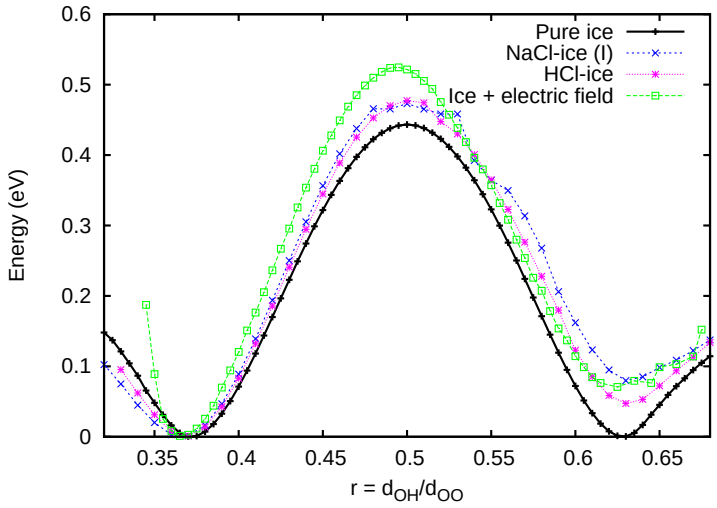

Figure 4.2.8: Hydrogen potential energy obtained in pure ice (black curve), in several different salty ices (NaCl-ice (I) and HCl-ice) and in pure ice under an external uniform electric field ($E = 0.05$ V/Å), at approximately 10 GPa.

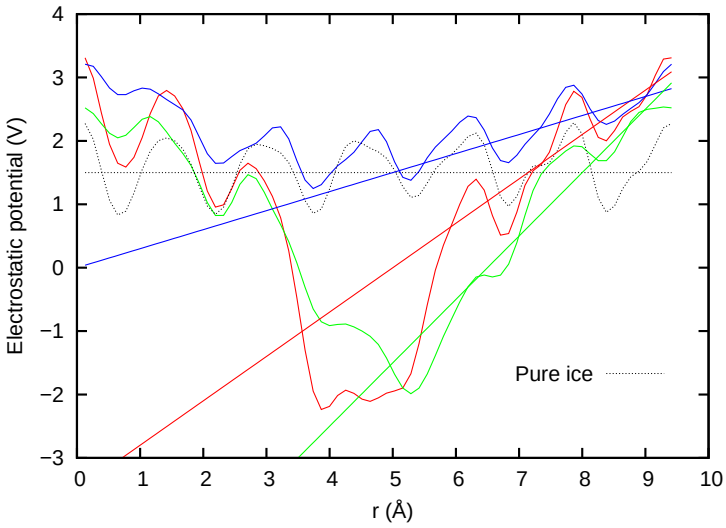

Figure 4.2.9: Macroscopic electrostatic potential along several (1,1,1) directions in LiCl-ice (colored curves) and in pure ice (black curve). The lines represent the average gradient of the potential i.e. the corresponding electric field.

potential for the hydrogen atoms that are nearest-neighbors of the cation but not for the majority of them. Therefore, even though natural, the explanation for the asymmetry of the hydrogen potential that relies on local distortions caused by steric effects near the cation is not satisfactory. In particular, since steric effects are completely different in LiCl-ice (I) and HCl-ice for example, they cannot be held responsible for the modification of the proton potential which is almost the same in these two ices. Furthermore, the oxygen-oxygen distance, which is a critical parameter for the behavior of hydrogen bonds (see section 3.2 and reference [108]), is little affected by the presence of the salt, at least for the concentrations studied here. The asymmetric potential studied in section 4.1.2 consists in a Landau-like double well potential with an external electric field (see equation (4.1.1)). The Landau-like potential without any external electric field ($E = 0$) was used to model the VII-X transition in pure high-pressure ice (see section 3.2). Hence, the potential in equation (4.1.1) would correspond to pure high-pressure ice under an external homogeneous electric field E. Thus, we focus on the effect of such a field on the O-H$\cdots$O bonds. We compute the effective potential energy of the protons in the presence of an external electric field in the same way as for pure high-pressure ice and for salty ices (see Appendix 3.A). The resulting potentials are shown on Figure 4.2.8: the presence of a uniform external field (here, $\mathbf{E}$ is parallel to the $\mathbf{c}$ axis) has for consequence that the proton potential becomes asymmetric. We can therefore make a parallel between the effect of a homogeneous electric field on the O-H$\cdots$O bonds in pure high-pressure ice and the O-H$\cdots$O bonds in salty ices that are far from the ionic impurity i.e. that are not affected by the geometrical distortion near the cation.

Indeed, as it is incorporated into the ice structure, salt is dissociated into its cation and its anion, that then occupy different sites in the ice structure, leading to a dipole electric field in ice. We derive the electric potential $V_{\text{elec}}(\mathbf{r})$ from total energy calculations on a relaxed configuration of pure and salty ice using density functional theory (see Appendix 2.B). We can then average this potential macroscopically i.e.

$$V_{\text{macro}}(\mathbf{r}) = \frac{1}{\Omega}\int_{\Omega} V_{\text{elec}}(\mathbf{r}')\,\mathrm{d}\mathbf{r}' \tag{4.2.1}$$

where Ω is the primitive cell volume i.e. each value of the potential is averaged over a cubic box of volume $\Omega = a^3$ (a being the primitive cell lattice parameter). Figure 4.2.9 shows the macroscopically averaged electrostatic potential $V_{\text{macro}}(\mathbf{r})$ in LiCl-ice, plotted along several (1,1,1) directions i.e. $\mathbf{r} = \mathbf{r}_0 + \frac{r}{\sqrt{3}}(1,1,1)$ for different $\mathbf{r}_0$. The average electric field is then estimated from the gradient of the potential. We can see that, as expected, in pure ice, the potential is constant meaning that there is no electric field in pure ice. In salty ice, however, the gradient of the potential is non-zero: the large dip in the potential corresponds to the position of the impurity but the slope of the potential indicates that there is indeed a non-zero electric field in salty ice. The intensity of the electric field depends on the position in the system since it derives from the electric dipole created by the dissociation of the salt into the cation and the anion. However, the intensity of the electric field is in the $0.2 - 1$ V/Å range. Therefore, even though local steric effects most likely affect the potential energy of protons near the cation, the asymmetry of the potential of the majority of protons that are far from the impurity can be explained by the long-range electric field induced by the salt dissociation [172].[2] We note in passing that recent Raman spectroscopy experiments also suggested that the electric field induced by the ions dissociation is responsible for the lengthening of the H$\cdots$O hydrogen bonds and the concomitant shortening of the O-H covalent bonds in salty ices [173].

In salty ices, apart from local geometrical distortions of the oxygen lattice, the main effect on the protons is the asymmetry of their effective potential energy, which can be explained by the long-range electric field induced by the salt dissociation. The major consequence of such an asymmetry in the protons' potential is that nuclear quantum effects, in particular proton hopping, are drastically reduced. This then impacts the actual transition pressure from ice VII to ice X which is shifted by approximately $20 - 30$ GPa, a non-negligible effect even for small salt concentrations !

4.3 Aluminium oxide hydroxide under high-pressure

4.3.1 Introduction

In the previous section, we showed that the tunneling properties of protons are dramatically affected by the presence of ionic impurities in ice because it affects the proton potential. However, the symmetrization transition still occurs albeit at higher pressures. Indeed, in high-pressure ice, whether pure or salty, the O-H$\cdots$O bonds are symmetric with respect to the O-O midpoint. Hence, we now investigate what happens if the O-O midpoint no longer is an inversion center for the hydrogen bonds. This could occur for hydrogen bonds in more complex minerals, with various environments. Indeed, in high-pressure ice, the elastic properties and in a more general way, the global structure, are determined by the hydrogen bonds. This is not always the case since in other hydrous minerals, such as aluminium oxide hydroxide (AlOOH), the elastic properties could be determined by other interatomic bonds than hydrogen bonds (see Figure 4.3.1). Finally, even though hydrous minerals under pressure have been studied extensively since they are believed to play a crucial role in the transport of water in the Earth mantle, nuclear quantum effects have not been considered in AlOOH so far in contrast to other hydrous minerals such as $Mg(OH)_2$

[2] The main differences between salty ices and simulations performed on pure ice with an external electric field are in the repulsive part of the potential, which is however not essential to the tunneling properties of protons (mainly dependent on the height and width of the barrier). These differences are most likely due to the higher complexity of the actual electric field present in salty ice than our model with a uniform electric field. In particular, the dipole electric field intensity varies depending on the proton's position.

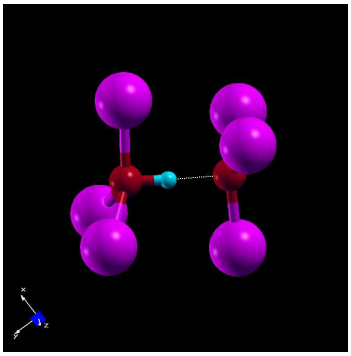

Figure 4.3.1: Schematic representation of the O-H$\cdots$O bonds in δ-AlOOH at low pressure ($P = 0$ GPa).

and $Ca(OH)_2$ [174–176].

In this section, we will study the hydrogen bonds in AlOOH, and more precisely, in its delta phase. δ-AlOOH has been synthesized for the first time in 2000 at 21 GPa and 1000°C [177] and is a polymorph of the more known diaspore (α-AlOOH) and boehmite (γ-AlOOH). It has been shown to be stable in a wide range of pressure and temperature [178–180] and its structure is relatively well known [107, 177–184]. However previous studies suggested that under increasing pressure, δ-AlOOH undergoes a symmetrization transition similar to the ice VII - ice X transition. In particular, recent synchrotron X-ray diffraction measurements indicated that there is a phase transition between 6.1 and 8.2 GPa, which is characterized by a modification of the compression properties of δ-AlOOH [107]. However, this technique was unable to characterize precisely the post-transition phase and also to determine whether proton hopping does actually occur in δ-AlOOH. On the other hand, theoretical calculations predicted that δ-AlOOH undergoes a second-order phase transition from an asymmetric (hydrogen off-centered - HOC) to a symmetric (hydrogen centered - HC) structure at about 30 GPa [182, 185]. Moreover, *ab initio* phonon dispersion curves computed at 0 K showed that the vibrational modes involving protons are subject to strong modifications near the transition [186]. However, these studies included neither thermal nor quantum effects, which would be likely to reduce the transition pressure as is the case in high-pressure ice (see section 3.3). Hence, the actual position of the hydrogen atoms in δ-AlOOH is still a matter of debate since there are inconsistencies between experimental and theoretical results. The importance of NQE in this system is also unknown: however, neutron scattering experiments on δ-AlOOH and its deuterated version δ-AlOOD yield isotope effects that indicate that NQE do play a role [187].

Finally, it has been shown that in the low-pressure phase α of AlOOH, namely diaspore, hydrogen bonds do not symmetrize up to at least 110 GPa [188, 189]. Therefore, in the following, we will study the evolution of hydrogen bonds under increasing pressure in δ-AlOOH: first, we will analyze the protons' effective potential from a one-dimensional perspective (section 4.3.2) and then we will focus on the structural and vibrational properties of δ-AlOOH by including both thermal and NQE in our simulations (section 4.3.3).

4.3.2 The one-dimensional proton potential in AlOOH

In order to get more insight on the behavior of protons in δ-AlOOH, we compute the proton's effective potential energy $V(x)$ where x is the proton transfer coordinate (see

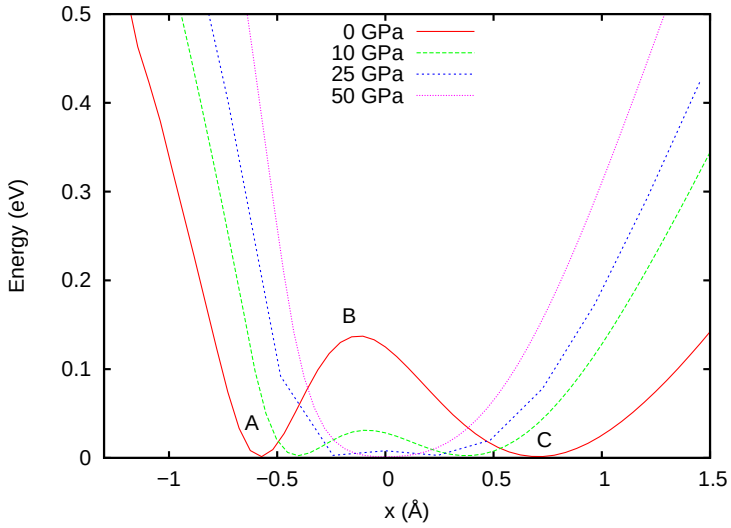

Figure 4.3.2: Effective proton potential energy $V(x)$ in δ-AlOOH for different pressures. $x = \mathrm{d_{H\cdots O}} - \mathrm{d_{O\text{-}H}}$ is the proton transfer coordinate i.e. the relative position of the proton with respect to its two neighboring oxygen atoms.

Appendix 3.A). Figure 4.3.2 shows the resulting potential $V(x)$ in δ-AlOOH at different pressures. First, we note that at low pressure, $V(x)$ is a double-well similar to the protons' potential in high-pressure ice (Figure 3.2.1). As pressure is increased, the potential barrier collapses and the distance between the two wells decreases up to 30 GPa where $V(x)$ becomes a single-well potential. Hence, from a purely classical point of view and without taking into account any thermal fluctuations, the symmetrization of hydrogen bonds should occur at 30 GPa. This is indeed the transition pressure from the HOC to the HC structure found previously by Tsuchiya and coworkers both from structural relaxations of their simulation cells and from phonon calculations at $T = 0$ K [182, 186].

However, we can see that the potential $V(x)$ is an asymmetric double-well; indeed, $V(x)$ is not symmetric with respect to the O-O midpoint. At 0 GPa for example, the two wells are centered at approximately -0.5 Å (point A on the figure) and 0.6 Å (point C on the figure). These two equilibrium positions have the same energy because in both cases, the O-H$\cdots$O bonds have the same structure if we consider the first neighbors of each hydrogen atom. However, the shapes of the two wells differ. Moreover, the barrier is approximately 0.15 eV high, which is about the same height as the barrier in high-pressure ice at approximately 50 GPa, and is located close to the midpoint of the O-O distance ($x = -0.1$ Å - point B on the figure). The asymmetry of the potential can be explained by the surrounding Al and O atoms around the constrained O-H$\cdots$O bonds; in particular, when the proton lies in well A, the nearest oxygen atoms that are not part of the O-H$\cdots$O bonds are close enough to alter the proton's potential energy landscape for small proton displacements from the equilibrium. This situation is therefore different from the pure ice one because of the asymmetry of the potential; it is also different from the potential in salty ices, where a long-range dipole electric field rendered the two equilibrium positions non-equivalent (see Figure 4.2.8).

In order to determine the behavior of protons in the potentials shown in Figure 4.3.2, we solve the corresponding time-independent Schrödinger equation for the potentials and compute the corresponding eigenfunctions and eigenenergies $\{\Psi_n, E_n\}$. Figure 4.3.3 shows the evolution of the ground-state density $|\Psi_1(x)|^2$ and the zero-point energy E_1 as pressure

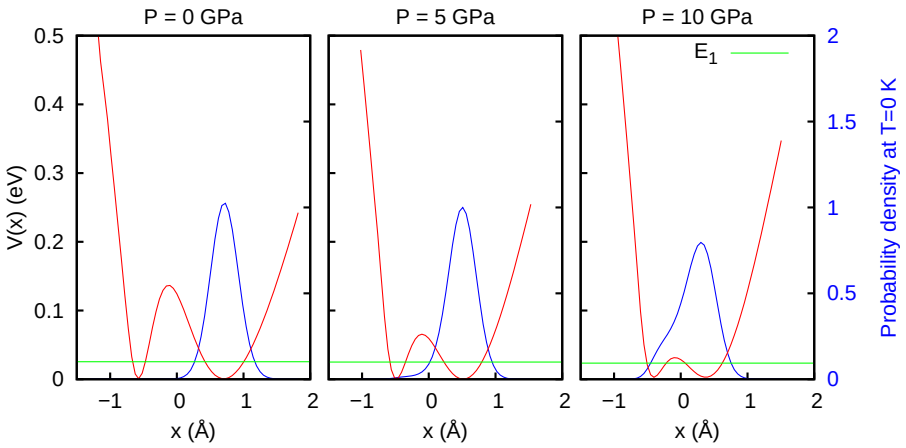

Figure 4.3.3: Evolution under compression of the effective proton potential in δ-AlOOH with the corresponding ground-state density $|\Psi_1(x)|^2$ and zero-point energy E_1 (at $T = 0$ K).

is increased. At low pressure, the proton's ground-state is localized in the right well (it has only one maximum), indicating asymmetric hydrogen bonds and localized protons which is consistent with the HOC structure found by Tsuchiya and coworkers [182]. Hence, the asymmetry of the potential strongly inhibits proton tunneling at 0 K, even though both wells have the same energy. This is clearly different from the case of high-pressure ice, where for the same barrier height, proton hopping occurs in a symmetric potential and the ground-state density displays two maxima. As pressure increases, the ground-state remains localized in the same well until the zero-point energy equals the barrier height, between 10 and 15 GPa. Hence, in contrast to the VII-X transition in high-pressure ice, the notion of quantum phase transition, as defined by a topological change of the wavefunction, does not hold in the case of δ-AlOOH since the shape of the ground-state density does not display any profound modification at the transition (as described in section 4.1.2 and Figure 4.1.4).

At finite temperature, the proton density $\rho(x, T)$ is given in equation (4.1.5) and the corresponding expectation value of the energy is:

$$\langle E \rangle = \frac{1}{Z} \sum_n E_n \mathrm{e}^{-\beta E_n} \tag{4.3.1}$$

where Z is the partition function and β is the inverse temperature. Figure 4.3.4 shows the evolutions under compression of $\rho(x, T)$ and $\langle E \rangle$ at room temperature. At low pressure, the contribution of excited states to the density $\rho(x, T)$ makes it asymmetric and delocalized over the two wells: $\rho(x, T)$ has two maxima, one in each well. Proton hopping is thus possible due to the inclusion of thermal effects. At higher pressures, thermal fluctuations further delocalize the proton over the two wells (the two peaks of the density get closer) and, when the energy $\langle E \rangle$ equals the barrier height, the density displays only one maximum near the center of the potential (the two peaks have merged). Hence, when thermal fluctuations are included, AlOOH undergoes a phase transition from asymmetric hydrogen bonds (where proton hopping occurs) to a phase δ' characterized by only one maximum in the proton density. This phase transition is marked by a topological change of the proton density (similar to that observed in the lower panel of Figure 4.1.4) and the transition pressure derived from this one-dimensional analysis is approximately 10 GPa, which is in

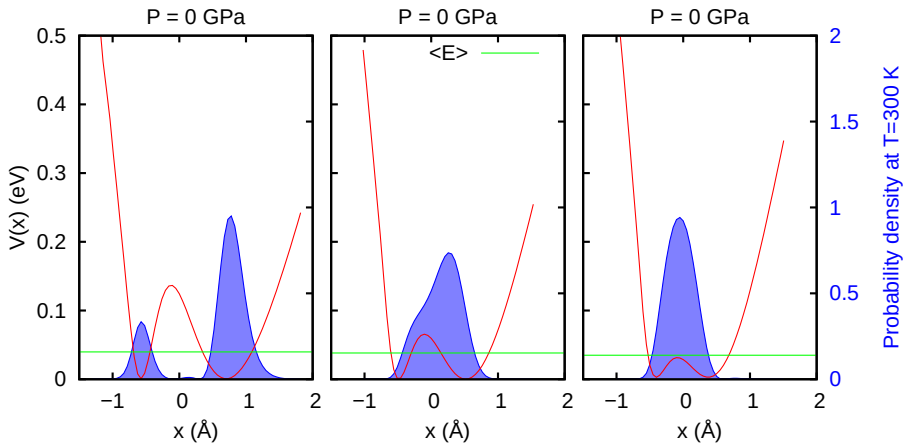

Figure 4.3.4: Evolution under compression of the effective proton potential in δ-AlOOH with the corresponding proton density $\rho(x,T)$ (equation (4.1.5)) and energy $\langle E \rangle$ at $T = 300$ K (equation (4.3.1)).

agreement with experimental predictions [107].[3]

However, because the proton effective potential is asymmetric, the probability density is not symmetric with respect to the O-O midpoint. At low pressure, even though proton hopping tends to delocalize the protons over their two equilibrium sites, they are more localized in one well than the other (as shown by the two peaks of the density in the left panel of Figure 4.3.4). Hence, the probability for the proton to be in well A or well C is not 0.5 as in pure high-pressure ice. Furthermore, above the transition pressure, although the proton density displays only one maximum, this maximum is not centered at the O-O midpoint. Hence, we will refer to the hydrogen bonds in the post-transition phase as *pseudo-symmetric* bonds instead of symmetric (or HC), as suggested previously in section 4.1.2. We will now investigate this pseudo-symmetrization transition in δ-AlOOH via QTB MD simulations.

4.3.3 QTB simulations on δ-AlOOH

We run QTB MD simulations, as well as standard *ab initio* Langevin dynamics simulations on δ-AlOOH at several pressures between 0 and 30 GPa (see computational details in Appendix 4.A). We first analyze the structural properties, in particular the O-H interatomic distances; then, we focus on the vibrational spectra.

Structural properties

In order to analyze the evolution of hydrogen bonds upon increasing pressure, we compute the O-H pair correlation functions (PCF) averaged over the QTB or the standard Langevin MD trajectories (see Figure 4.3.5). At low pressure, the PCF displays two peaks indicating two distinct bond lengths, consistent with the HOC structure: around 1.05 Å

[3]There is a still a small discrepancy between our transition pressure and the experimental one found by Kuribayashi and coworkers ($\simeq$ 8 GPa). Several reasons could be invoked since thermal and zero-point energy effects are very sensitive to the barrier height which, in turn, depends on the actual exchange-correlation functional [153], as well as on the different approximations made when computing the proton potential $V(x)$.

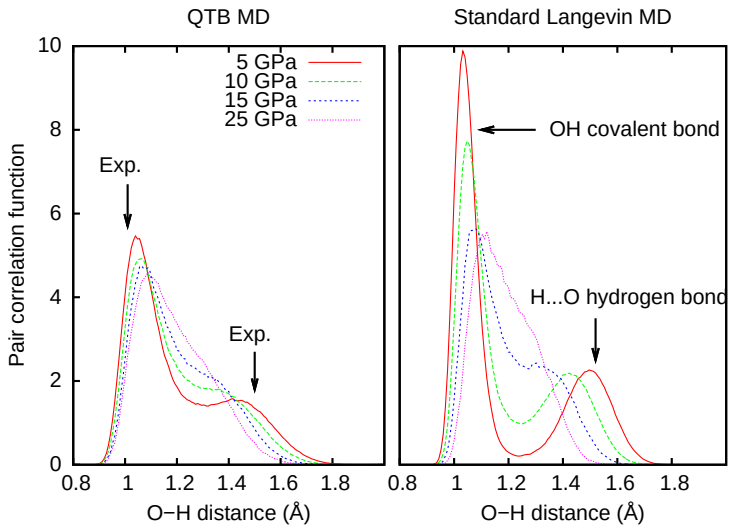

Figure 4.3.5: Pair correlation functions of the O-H distance obtained via QTB (left panel) and standard Langevin (right panel) simulations, in δ-AlOOH for different pressures, at room temperature. The black arrows in the left panel indicate neutron scattering measurements of O-D distances by Sano-Furukawa and coworkers [190].

for the covalent O-H bonds and around 1.5 Å for hydrogen bonds.[4] Upon compression, there is a dilatation of the O-H covalent bond and a concomitant contraction of the hydrogen bond length. As pressure further increases, the two peaks merge until they become hardly distinguishable: at these pressures, the covalent and the hydrogen bond cannot be differentiated anymore. However, the PCF from QTB are different from those obtained via standard Langevin MD: the peaks are broader when NQE are taken into account and they merge at a lower pressure, even though the positions of the peaks are similar. Moreover, the minimum of the PCF between the two peaks is much higher when NQE are taken into account, suggesting that either disorder or proton tunneling occurs at low pressure. Thus, our QTB simulations show that the PCF undergoes a major modification between 10 and 15 GPa: below this pressure, the PCF displays two maxima while above this pressure, the PCF has only one maximum. Hence, δ-AlOOH undergoes a phase transition at $10-15$ GPa as already suggested by the one-dimensional analysis in section 4.3.2. Furthermore, in the post-transition phase, the PCF is not centered at the midpoint of the O-O distance (as it should be in the HC structure of Tsuchiya and coworkers [182]), but its maximum is slightly off-centered. Hence, the term "symmetric hydrogen bonds" is not appropriate here and the analysis of the PCF suggests a pseudo-symmetrization of hydrogen bonds between 10 and 15 GPa. Below the transition, hydrogen bonds are subject to thermal disorder and proton hopping occurs. Above the transition, the hydrogen atoms are slightly off-centered with respect to the midpoint of the O-O distance.

The usual relevant proton transfer coordinate in symmetrization transitions is $x = d_{H\cdots O} - d_{O\text{-}H}$ where $d_{H\cdots O}$ and $d_{O\text{-}H}$ are the O-H distances between a given proton H and its two nearest-neighbor oxygen atoms. Figure 4.3.6 shows the probability distribution

[4] These distances are in agreement with experimental measurements on δ-AlOOD obtained through neutron scattering around 5 GPa (indicated by black arrows in the left panel of Figure 4.3.5) [190]. Indeed, the positions of the two peaks are almost the same whether we include NQE or not. Hence, the distances for hydrogen (O-H) and deuterium (O-D) are expected to be similar, even though quantum effects are weaker for deuterium than for hydrogen.

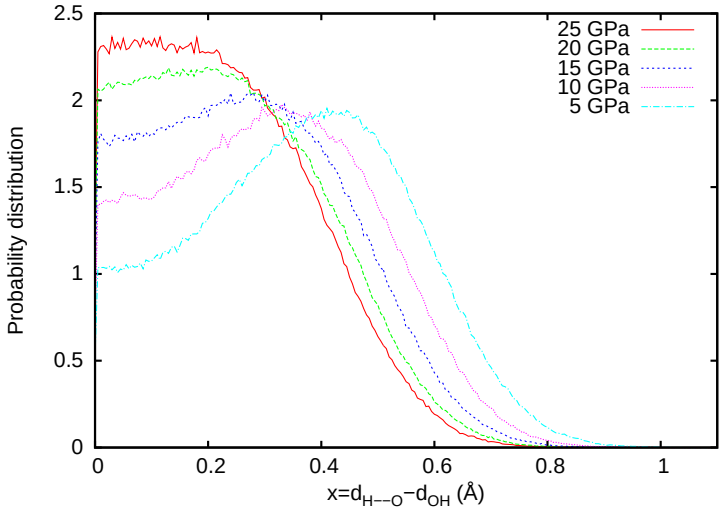

Figure 4.3.6: Probability distribution of the proton position relative to the bond midpoint $x = \mathrm{d_{H\cdots O}} - \mathrm{d_{O\text{-}H}}$ at different pressures in δ-AlOOH from QTB molecular dynamics simulations.

$P(x)$ in δ-AlOOH obtained from QTB simulations. In contrast with high-pressure ice (see Figure 3.3.5), the probability distribution of x does not display a maximum at $x = 0$ at the transition i.e. between 10 and 15 GPa. On the contrary, even in the post-transition phase, the maximum of the probability distribution of x is centered at a finite value of x. This is consistent with slightly off-centered protons above the transition and the fact that this transition should be considered as a pseudo-symmetrization. However, similarly to the VII-X transition in high-pressure ice, the structural properties do not yield a precise transition pressure. Hence, we turn to the vibrational spectra of δ-AlOOH in the following paragraph.

Vibrational spectra of δ-AlOOH

The vibrational spectra can be computed directly from the atomic trajectories (see section 2.3.2) but they are rather complex in δ-AlOOH. Hence, we conduct a preliminary vibrational mode analysis via the dynamical matrix (see section 2.B.5) at 0 K and without any quantum or anharmonic effects, which is described in Appendix 4.B. This approach allows us to choose a basis of eigenvectors that is a key to the interpretation of the hydrogen vibrational spectra (see section 2.3.2). Figure 4.3.7 shows the evolution of the frequencies of the O-H stretching and bending modes with pressure. At low pressure, we distinguish two stretching modes at approximately 2800 and 2100 cm^{-1} and two bending modes around 1400 cm^{-1} (in the $(\mathbf{a}, \mathbf{b})$ plane) and 1200 cm^{-1} (in the $\mathbf{c}$ direction). These results are in very good agreement with Raman measurements at ambient pressure [178].[5] Upon compression, the O-H stretching modes soften gradually, their frequencies dropping to approximately 1800 and 2500 cm^{-1}. Moreover, the width of the high-frequency mode increases, which implies that these two peaks merge at the transition and are no longer distinguishable. In contrast, the bending mode frequencies increase slightly with pressure.

[5] Due to the large widths of the peaks in the calculated spectrum, we could distinguish only two high-frequency O-H stretching modes, while Ohtani and coworkers observed four broad bands. Tsuchiya and coworkers [186] suggested that the presence of these multiple bands, instead of two sharp peaks is due to hydrogen disorder at low pressure, which is consistent with our results on the O-H pair correlation.

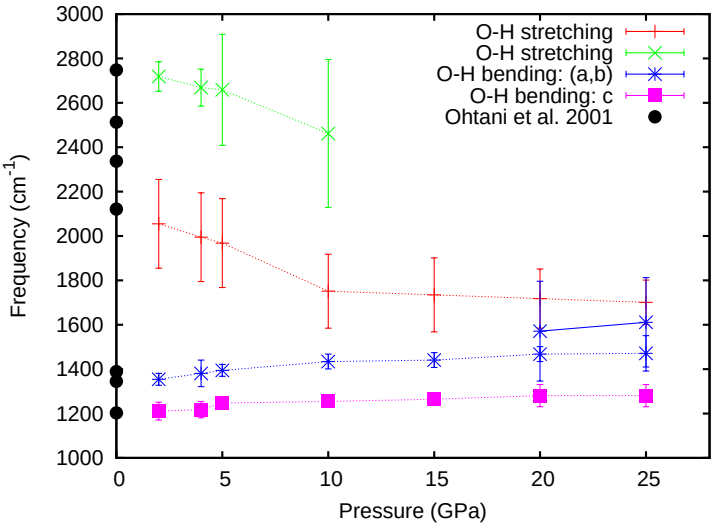

Figure 4.3.7: Pressure evolution of the hydrogen vibrational mode frequencies in δ-AlOOH, obtained from QTB simulations at $T = 300$ K. The vertical bars indicate the widths of the peaks in the spectrum and the black dots correspond to Raman spectroscopy data from Ohtani and coworkers [178].

Above the critical pressure ($P_t \sim 10$ GPa), the O-H stretching mode frequency ($\simeq 1800$ cm^{-1}) does not vary appreciably with pressure, at least up to 25 GPa, while the bending mode frequencies increase continuously. The second O-H bending mode in the $(\mathbf{a}, \mathbf{b})$ plane becomes distinguishable only above 20 GPa. The previous trends agree with those found by Tsuchiya and coworkers [186]. The softening of the O-H stretching mode up to about 10 GPa, where bending and stretching modes mix up, is consistent with a phase transition as also suggested by the modification of the O-H PCF. Hence, δ-AlOOH undergoes a transition from phase δ with asymmetric hydrogen bonds (and where proton hopping occurs), to a phase δ', with pseudo-symmetric hydrogen bonds, which occurs around 10 GPa according to the analysis of the simulated vibrational spectra.

4.3.4 Comparison between δ-AlOOH and α-AlOOH

We have mentioned in the introduction that no symmetrization transition was observed in diaspore i.e. in the phase α of aluminium oxide hydroxide at least up to 110 GPa [188, 189]. For the sake of comparison, we also ran QTB MD simulations on α-AlOOH at several pressures up to 30 GPa approximately. Figure 4.3.9 shows the contour plots of the distribution functions of the proton's position along the O-O direction i.e. $P(r_{\text{parallel}}, r_{\text{ortho}})$ where

$$r_{\text{parallel}} = \overrightarrow{OH} \cdot \vec{u}, \quad r_{\text{ortho}} = \overrightarrow{OH} \cdot \vec{v}, \quad \vec{u} = \frac{\overrightarrow{OO}}{|\overrightarrow{OO}|}, \quad \vec{u} \cdot \vec{v} = 0 \tag{4.3.2}$$

and $(\vec{u}, \vec{v})$ are two orthogonal unit vectors in the plane that contains the two nearest neighbors (O) of each proton and its nearest Al (see Figure 4.3.8). We can clearly see that at low pressure, in δ-AlOOH, the proton's distribution displays two peaks indicating proton hopping along the O-H$\cdots$O bonds. On the contrary, in α-AlOOH at low pressure, the proton's distribution displays a single maximum. Moreover, this peak is off-centered with respect to the O-O direction meaning that the angle between the O-H covalent bond

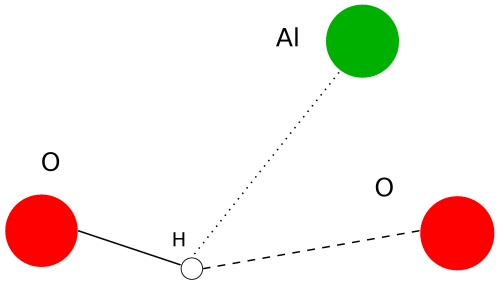

Figure 4.3.8: Schematic representation of a proton, its two nearest oxygen atoms and its nearest aluminium.

and the O-O direction is non-zero ($r_{\text{ortho}} = 0$ would correspond to a linear hydrogen bond). Furthermore, no proton hopping occurs in diaspore at low pressure, even though NQE are included via the QTB. As pressure is increased up to 25 GPa approximately, we see that in δ-AlOOH, the proton's distribution has a single maximum as already discussed in the previous sections, meaning that we are now in the δ' phase with pseudo-symmetric bonds (again, we can see that the distribution is slightly biased which confirms the analysis of the PCF above). On the other hand, the distribution in diaspore remains unchanged by increasing pressure: the protons are localized on one side of the O-H$\cdots$O bonds and no proton hopping or pseudo-symmetrization occurs. This analysis shows that in the case of δ-AlOOH, the reduction of the proton's effective potential to one dimension, along the O-O direction, is consistent with the fact that the distribution is almost symmetric with respect to $r_{\text{ortho}} = 0$ i.e. in the direction orthogonal to O-O. In α-AlOOH, the situation is more complex. Therefore, we compute the two-dimensional effective proton potential $V(r_{\text{parallel}}, r_{\text{ortho}})$ (see left panel of Figure 4.3.10). We can see that the potential is no longer a double well as in high-pressure ice or in δ-AlOOH but displays a single minimum slightly off-centered with respect to the O-O direction and corresponding to the proton's equilibrium position. We can also see the influence of the Al atom nearby that affects the potential and renders it asymmetric. Hence, even though the structures of the two phases are similar (see right panel in Figure 4.3.10 and Figure 4.3.1), the effective potential felt by the protons is very deeply affected by their atomic environment with different consequences regarding proton hopping and hydrogen bond pseudo-symmetrization.

4.4 Conclusion

We have seen in this chapter that the environment of the protons can have a major impact on their behavior and in particular on their quantum properties. Indeed, in high-pressure ice, the structure is highly symmetric and the oxygen-oxygen midpoint represents an inversion center for the hydrogen bonds. Hence, the proton's effective potential landscape is a symmetric double well: proton hopping occurs when the barrier is low enough and the two equilibrium positions are close enough (as in phase VII of high-pressure ice). In this scenario, the system undergoes a structural transition from asymmetric hydrogen bonds (phase VII) to symmetric bonds (phase X) when the energy of the system equals the barrier height. This transition is *quantum-driven* since the zero-point energy contribution is much larger than the thermal fluctuations at room temperature. Furthermore, the VII-X transition is accompanied by a topological change of the proton's density, going from a bimodal distribution to a unimodal one that is centered at the O-O midpoint. This picture is strongly challenged when the material has a more complex structure than ice. First,

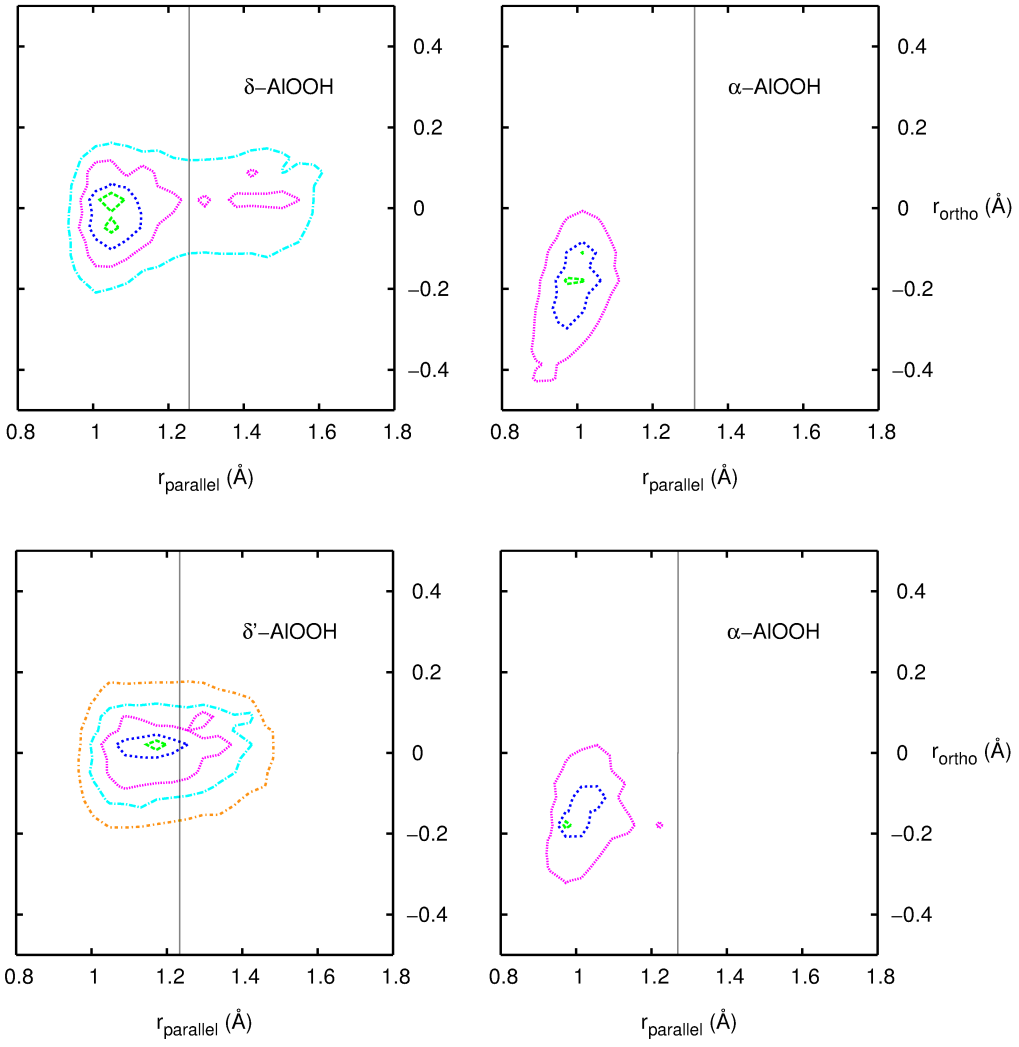

Figure 4.3.9: Contour plots of the proton distribution functions $P(r_{\text{parallel}}, r_{\text{ortho}})$ where r_{parallel} is the proton's position along the O-O direction and r_{ortho} is its position in the the direction orthogonal to O-O (see equations (4.3.2)): (top panels) at 5 GPa and (lower panels) at 25 GPa, obtained from QTB MD simulations at room temperature in δ-AlOOH (left column) and α-AlOOH (right column). The grey vertical lines indicate the perpendicular bisectors of the O-O segment.

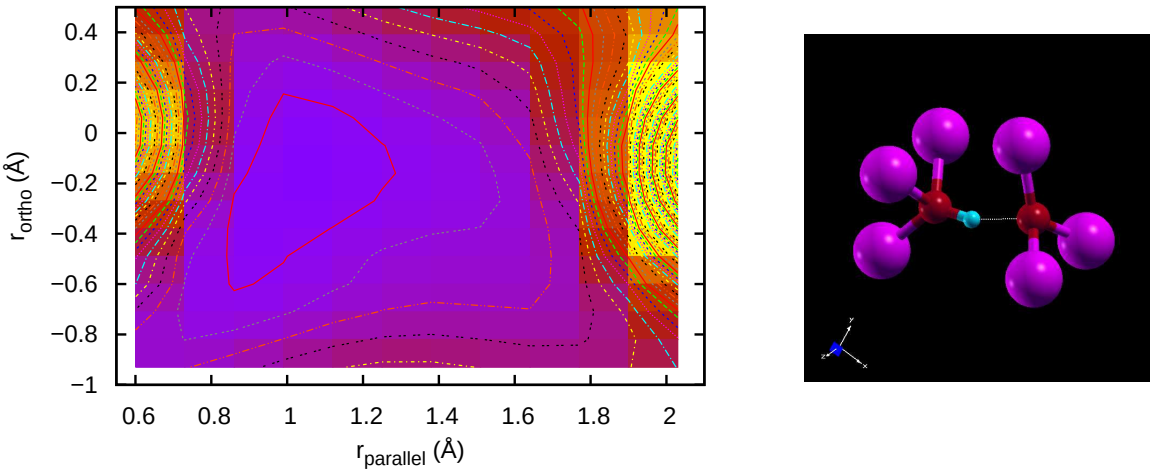

Figure 4.3.10: Left panel: Contour plots of the effective proton potential $V(r_{\text{parallel}}, r_{\text{ortho}})$ in α-AlOOH at 10 GPa. Right panel: Schematic representation of a hydrogen bond in α-AlOOH.

we have seen that a small concentration of ionic impurities in high-pressure ice yields a long-range electric field that affects the protons' potential and renders it asymmetric (see section 4.2). Consequently, proton hopping is drastically reduced, the protons are more localized than in pure ice and nuclear quantum effects are lifted ! This also affects the VII-X transition in salty ices which is shifted to higher pressures, even for small salt concentrations. Finally, we studied a more complex mineral, aluminium oxide hydroxide. Under high pressure, two phases are metastable, phase α, also called diaspore, and phase δ. The structures of these two phases are similar; however, the protons behave very differently in each phase. In phase δ, the proton's potential is an asymmetric double well potential: thus, at finite temperature, proton hopping occurs. On the contrary, in phase α, the proton's potential consists in a highly asymmetric single-well localized near the nearest neighbor oxygen atom. Hence, protons are trapped in their equilibrium position and nuclear quantum effects seem negligible. Moreover, in the case of δ-AlOOH, the hydrogen bond is not symmetric with respect to the O-O midpoint. Under increasing pressure, δ-AlOOH undergoes a pseudo-symmetrization transition to a phase δ' with pseudo-symmetric hydrogen bonds: the proton's density transforms from a bimodal to a unimodal distribution, however, it remains asymmetric and is not centered at the O-O midpoint. In α-AlOOH, in contrast with the δ-δ' transition, no pseudo-symmetrization is seen in our pressure range since the distribution is already unimodal at low pressure.

To summarize, we showed in this chapter a few examples where nuclear quantum effects have different consequences on the properties of hydrogen-containing systems. The atomic environment and the complexity of the material are important ingredients that can affect the proton's effective potential, rendering the standard double-well picture unsuited in these cases. However, even though the proton's energy landscape are more complex, quantum effects can still play an important role in the localization or delocalization of protons.

Appendix

4.A Computational details

Salty ices We run QTB and standard Langevin molecular dynamics (see chapter 2) on salty ices. In both cases, the atomic forces are computed within the density functional theory (see Appendix 2.B), via the generalized gradient approximation [99], as implemented in the Quantum Espresso package [89]. Simulations run over a time length of about 25 ps with a 0.484 fs integration time step. Our simulation cell contains 53 or 54 water molecules and one LiCl, NaCl, HCl or DCl pair, corresponding to a concentration of about 2% mol (see table 4.1). The initial configurations correspond to those described in reference [165] for LiCl-ice. The most likely position for the cation Cl^- is an oxygen substitutional lattice site, where it replaces a water molecule (see left panel in Figure 4.2.1). Cl^- is thus surrounded by 8 water molecules. The site occupied by the anion depends on its size: Na^+ can occupy either a substitutional site as Cl^- (denoted substitutional NaCl-ice) or an interstitial site, as does initially Li^+, H^+ and D^+. This interstitial site is the center of the unit cell face (see center panel in Figure 4.2.1) and is octahedrally coordinated by oxygen atoms. The initial distance between the anion and the cation is between 4.6 and 4.8 Å.

Aluminium oxide hydroxide, δ-AlOOH As for salty ices, we run both QTB and standard Langevin molecular dynamics simulations on δ-AlOOH at different pressures. The atomic forces are computed within the DFT, via the GGA, through the Becke-Lee-Yang-Parr (BLYP) functional [191, 192]. The interaction between the ionic cores and the valence electrons is described through ultra-soft pseudopotentials with non-linear core corrections. The Kohn-Sham orbitals are expanded in plane-waves with 50 Ry energy cutoff. The simulation cell is a $2 \times 2 \times 3$ supercell containing 24 AlOOH units. The corresponding Brillouin zone is sampled by a $2 \times 2 \times 2$ Monkhorst-Pack grid with a $1 \times 1 \times 1$ offset (i.e. half a grid step in each direction). The simulations are run at ambient temperature ($T = 300$ K) and the time length of each simulation is approximately 29 ps with a 0.484 fs integration time step. The instantaneous pressures are computed via the stress theorem [155] (the kinetic contribution to the pressure is negligible with respect to the fluctuations of the pressure).

In order to check that the computational ingredients of our simulations are correct, we compared the equations of state obtained via QTB MD and standard Langevin dynamics simulations to previous experimental and theoretical results. Previous synchrotron X-ray experiments showed a change of compressibility of δ-AlOOH near 10 GPa [187]. Similarly, theoretical calculations by Tsuchiya and coworkers performed in the asymmetric $P2_1nm$ structure and in the symmetric, hydrogen-centered Pnnm structure yielded two distinct bulk moduli [182, 185]. Hence, we compare the equations of state that we obtained via QTB and standard Langevin MD to these previous calculations (see Figure 4.A.1). Up

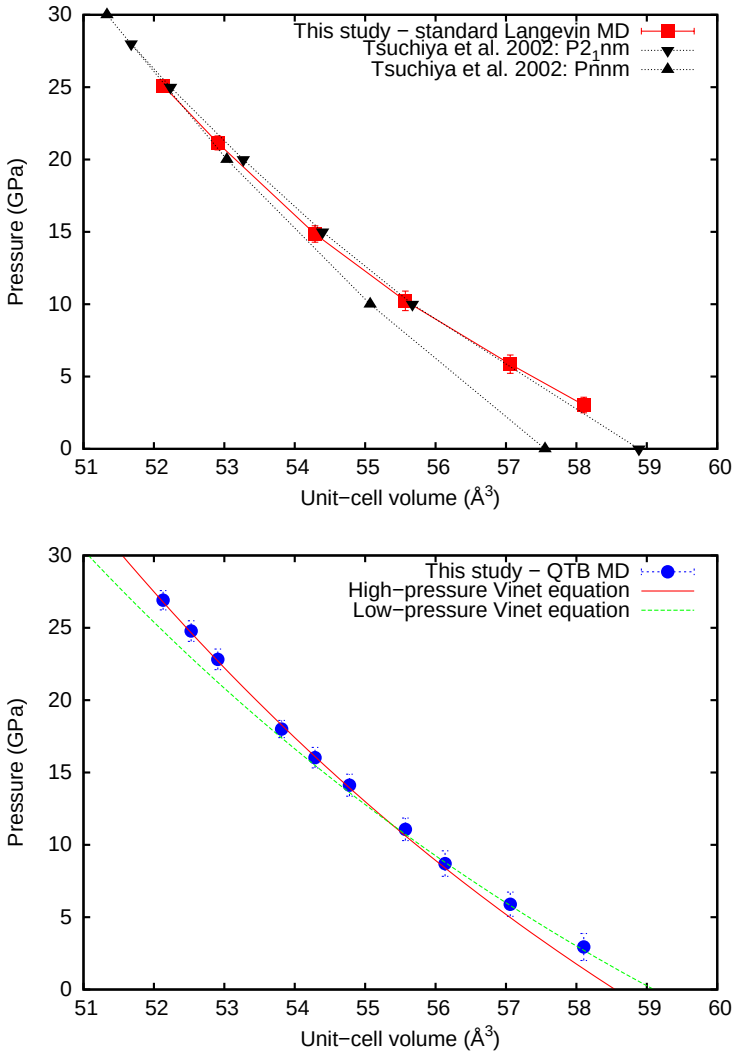

Figure 4.A.1: Equation of state of δ-AlOOH from standard Langevin molecular dynamics (top panel: squares) and from Quantum Thermal Bath molecular dynamics (lower panel: circles). The (P, V) values computed by Tsuchiya and coworkers at $T = 0$ K in the P2$_1$nm (top panel: inverted triangles) and the Pnnm (top panel: triangles) are also shown [182]. In the lower panel, the QTB data has been fitted with two distinct Vinet equations [193]: in the low-pressure (LP) structure, $V_{\mathrm{LP}} = 59.1$ Å^3, $B_{\mathrm{LP}} = 154.2$ GPa and in the high-pressure (HP) structure, $V_{\mathrm{HP}} = 58.5$ Å^3, $B_{\mathrm{HP}} = 183.4$ GPa; in both structures, $B'_{\mathrm{HP}} = B'_{\mathrm{LP}} = 4$.

to 25 GPa, our results from standard Langevin MD are in very good agreement with those from Tsuchiya and coworkers [182] (see top panel in Figure 4.A.1). This confirms that the above computational ingredients are consistent within the standard Langevin MD frame. Then, we fitted the (P, V) points computed from our QTB simulations with two distinct Vinet equations of state [193], one adapted to the low-pressure structure and the other to the high-pressure structure (see lower panel in Figure 4.A.1), as done in previous studies [182, 187]. Within this procedure, the two equations of state cross between 10 and 15 GPa; accordingly, the bulk modulus changes from 154 ± 2 GPa at low pressure to 183 ± 2 GPa at high pressure. These values are in good agreement with previous calculations [182, 185]. The small discrepancies with the experiments [187] are mainly due to the GGA functional, which slightly overestimates the cell parameters with respect to the experimental values. Our dynamical simulations are therefore consistent with a change of compressibility in δ-AlOOH with an increase of the bulk modulus by about 20% between 10 and 15 GPa at T = 300 K, which is compatible with a phase transition towards stiffer O-H$\cdots$O bonds as indicated by experiments.

4.B Dynamical matrix analysis in δ-AlOOH

In order to determine which phonon modes are relevant to the hydrogen bond pseudo-symmetrization in δ-AlOOH, we calculate the dynamical matrix via the density functional perturbation theory [100], within the harmonic approximation at 0 K. From the dynamical matrix, the phonon frequencies and eigenvectors are computed at pressures well below and above the transition pressure and far enough from it to avoid strong non-linear effects connected with mode mixing at the transition. In the asymmetric hydrogen bond configuration ($P2_1nm$ or HOC 1) [186], the vibration modes consist in two high-frequency O-H stretching modes (around 2670 - 2710 cm^{-1} at 0 GPa), and four O-H$\cdots$O bending modes (between 1100 and 1350 cm^{-1}). The two low-frequency bending modes are vibrations in the $\mathbf{c}$ direction, while the two high-frequency bending modes are vibrations in the $(\mathbf{a}, \mathbf{b})$ plane (which contains the O-H$\cdots$O bonds). When pressure increases, the O-H stretching mode frequencies decrease abruptly, while the bending mode frequencies increase slightly. Finally, in the high-pressure symmetric phase (Pnnm or HC) [186], there are two bending modes in the $(\mathbf{a}, \mathbf{b})$ plane (around 1600 - 1700 cm^{-1} at 50 GPa), which harden gradually, while two stretching modes and the two remaining bending modes in the $\mathbf{c}$ direction vibrate in the 1300 - 1400 cm^{-1} range.

As already suggested by Tsuchiya and coworkers [182, 186], this is consistent with the fact that the transition from the HOC to the HC structure in δ-AlOOH is a second-order phase transition, characterized by a strong softening of the O-H stretching modes. Moreover, at the transition pressure P_c, there is an important mixing of the bending and stretching modes. Hence, we cannot simply rely on the description of the vibrational properties of δ-AlOOH directly via the dynamical matrix approach close to the HOC - HC transition. This is why we turn to the study of the atomic trajectories in order to take into account the inherent anharmonicity of the system, as well as thermal and quantum effects.

Nevertheless, the dynamical matrix approach allows us to choose a basis of eigenvectors - the phonon directions $\mathbf{u}_j$, $j \in [1, 5]$ - that is a key to the interpretation of the hydrogen vibrational spectra. A schematic representation of the eigenvectors on top of the local atomic structure of δ-AlOOH is shown in Figure 4.B.1. In the $P2_1nm$ configuration, $\mathbf{u}_1$ is parallel to the O-O direction, while $\mathbf{u}_2$ is orthogonal to $\mathbf{u}_1$ in the $(\mathbf{a}, \mathbf{b})$ plane. In the Pnnm configuration, the O-H stretching mode eigenvector $\mathbf{u}_3$ forms a small angle with the

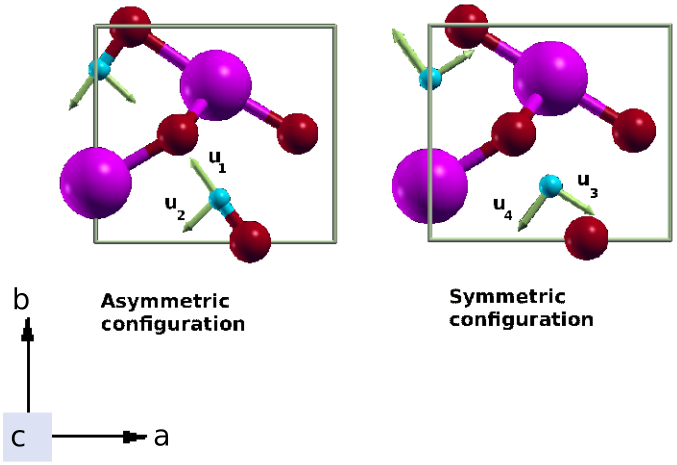

Figure 4.B.1: Schematic representation of the atomic structure of δ-AlOOH, from asymmetric (left) to symmetric (right) hydrogen bonds. Color code: H in light blue, O in red, Al in violet. The eigenvectors $\mathbf{u}_j$ $(j = 1, \dots 4)$ for the stretching $(j = 1, 3)$ and bending $(j = 2, 4)$ modes in the $(\mathbf{a}, \mathbf{b})$ plane are indicated for the hydrogen-off-centered (HOC) and hydrogen-centered (HC) structures, respectively. $\mathbf{u}_5$, not represented, is normal to the plane. The crystallographic conventions used here are the same as in reference [186].

O-O direction, and $\mathbf{u}_4$ is orthogonal to $\mathbf{u}_3$ in the $(\mathbf{a}, \mathbf{b})$ plane. In both configurations, $\mathbf{u}_5$ is parallel to the $\mathbf{c}$ direction. As it can be seen in Figure 4.B.1, the eigenvectors from the two phases are quite similar: in particular, and apart from an irrelevant sign, $\mathbf{u}_1 \approx \mathbf{u}_3$ and $\mathbf{u}_2 \approx \mathbf{u}_4$. Therefore, the use of these eigenvectors to obtain mode-specific density of states (see equation (2.3.11)) appears to be reliable in both phases. At the transition, the O-H modes can mix and become a linear combination of harmonic ones; apart from the modes here reported, there are no others involving proton displacements in the harmonic case. Therefore, the $\mathbf{u}_j$ vectors form a minimal basis set to analyze the behavior with pressure of modes involving protons.

Chapter 5

Retrospective on the Quantum Thermal Bath method: model systems

Contents

5.1 Introduction

We have shown in chapter 2 that the QTB is an exact method in the harmonic approximation. Then, in chapters 3 and 4, we have used the QTB method straightforwardly on various hydrogen-bonded systems (high-pressure ice and aluminium oxide hydroxide) and we have seen that it yields correct results that are in agreement with experimental measurements. In particular, the O-H stretching mode frequencies are correctly described in both phase VII and phase X of ice. However, especially at the transition, the system is quite anharmonic; yet, the QTB still yields interesting results in this case. In the following, we will investigate the reliability and the limits of the QTB method for anharmonic systems, by using simple models in which the anharmonicity can easily be tuned. First, we will attempt to point out from a theoretical point of view where difficulties arise from when trying to describe quantum probability distributions with classical trajectories. Then, we will focus on a specific pitfall of the QTB method, the zero-point energy leakage. By studying two models with few degrees of freedom, we will be able to compare results from QTB simulations with exact quantum calculations and thus attempt to define the range of applicability of the QTB. Finally, we have seen in the two previous chapters (3 and 4) that the QTB simulations allowed us to construct one-dimensional models that capture the essence of the behavior of protons in the real three-dimensional system. In particular, the double well potential has been extensively used to study the hydrogen bond symmetrization, hence, we will analyze the results obtained from QTB in such a potential.

5.2 Computing quantum probabilities from classical-like trajectories: the limits of the Ehrenfest theorem

In order to understand the limits of the QTB in an anharmonic system, we first remind that this method is based on the Ehrenfest theorem, as do other semi-classical methods (see section 1.3.2). It states that the average values of the quantum operators $\hat{x}$ and $\hat{p}$, namely position and momentum, obey classical-like equations of motion:

$$\frac{\mathrm{d}\langle\hat{x}\rangle}{\mathrm{d}t} = \frac{\langle\hat{p}\rangle}{m}, \quad \frac{\mathrm{d}\langle\hat{p}\rangle}{\mathrm{d}t} = -\langle\frac{\partial V(\hat{x})}{\partial x}\rangle \tag{5.2.1}$$

where $\langle\hat{A}\rangle = \langle\Psi|\hat{A}|\Psi\rangle$ is the expectation value of any operator $\hat{A}$ and Ψ is the wavefunction of the system. $\langle\hat{x}\rangle$ can be considered as the center of mass of the wavefunction Ψ and the time-dependent function $\langle\hat{x}\rangle(t)$ is the trajectory of the center of mass. The equation of motion of the center of mass is thus:

$$m\frac{\mathrm{d}^2\langle\hat{x}\rangle}{\mathrm{d}t^2} = -\langle\frac{\partial V(\hat{x})}{\partial x}\rangle. \tag{5.2.2}$$

Equation (5.2.2) is similar to the Newton's equation of classical dynamics if we identify $\langle\hat{x}\rangle$ with the position of the classical particle. However, the force $f = -\partial V/\partial x$ (in the right hand side of equation (5.2.2)) is averaged over the entire wavefunction ($\langle\Psi|f|\Psi\rangle$) whereas it would simply be evaluated at the position of the center of mass in a purely classical picture:

$$f_{\text{class}} = -\left.\frac{\partial V}{\partial x}\right|_{x=\langle\hat{x}\rangle} \neq -\langle\frac{\partial V}{\partial x}\rangle = f_{\text{quant}} \tag{5.2.3}$$

If the wavefunction Ψ is relatively localized, then this difference is negligible and the center of mass has a classical motion. In particular, in a harmonic oscillator $V(x) = m\omega^2x^2/2$, the force $-\partial V/\partial x = -m\omega^2x$ is linear, and the ground-state wavefunction is Gaussian. In this case, $f_{\text{class}} = f_{\text{quant}}$ and the motion of the center of mass is classical. The idea of the QTB method is to mimick the spatial expansion of the wavefunction Ψ via a stochastic motion. The time average of the force to which the particle is subjected along the stochastic dynamics thus reproduces the expectation value of the quantum force operator. Using this procedure, the QTB yields the correct quantum distributions of position and momentum, in a harmonic potential as seen previously in section 2.2.2, but also in realistic anharmonic systems as seen in chapters 3 and 4. We will discuss more particularly the case of a double-well potential in the following section.

However, while the classical picture stands for the expectation values of $\hat{p}$ and $\hat{x}$, these two operators do not commute and $[\hat{x},\hat{p}] = i\hbar$; hence, if we look at higher order expectation values, we obtain:

$$\frac{1}{2m}\frac{\mathrm{d}\langle\hat{p}^2\rangle}{\mathrm{d}t} = -\langle\frac{\hat{p}}{m}\frac{\partial V(\hat{x})}{\partial x}\rangle + \frac{\hbar}{2mi}\langle\frac{\partial^2 V(\hat{x})}{\partial x^2}\rangle \tag{5.2.4}$$

$$\frac{1}{2}m\frac{\mathrm{d}\langle\hat{x}^2\rangle}{\mathrm{d}t} = \langle\hat{p}\hat{x}\rangle + \frac{i\hbar}{2} \tag{5.2.5}$$

The classical analogue of equation (5.2.4) concerns the left hand side and the first term of the right hand side of the equation and corresponds to the fact that the variation of kinetic energy is the work done by the force $f = -\partial V/\partial x$ (see equation (2.2.1)). However, the second term of the right hand side is purely quantum since it arises from the non-commutativity of $\hat{p}$ and $\hat{x}$. In the case of a harmonic oscillator, with frequency ω, equation

(5.2.4) becomes:

$$\frac{1}{2m}\frac{\mathrm{d}\langle\hat{p}^2\rangle}{\mathrm{d}t} = -\omega^2\langle\hat{p}\hat{x}\rangle + \frac{\hbar\omega^2}{2i} \tag{5.2.6}$$

and the second term of the right hand side, the quantum term, is an imaginary constant term. As Ben-Nun and Levine describe in reference [194], the problem that arises from the quantum term can now be "fixed" by shifting the actions of the modes and therefore correctly taking into account the zero-point energy while computing classical trajectories. We also note that in the case of a harmonic oscillator, according to equations (5.2.4) and (5.2.5), we have:

$$\frac{1}{2m}\frac{\mathrm{d}\langle\hat{p}^2\rangle}{\mathrm{d}t} + \frac{1}{2}m\omega^2\frac{\mathrm{d}\langle\hat{x}^2\rangle}{\mathrm{d}t} = 0 \tag{5.2.7}$$

so that the average total energy is constant. Finally, in the case of a harmonic oscillator, since the expectation value $\langle p^n\rangle$ for $n \geq 3$ can be expressed in terms of $\langle p\rangle$ and $\langle p^2\rangle$ only, the "fix" in reference [194] that ensures that the binary terms $\langle p^2\rangle$, $\langle x^2\rangle$, and $\langle xp + px\rangle$ are correctly given by classical trajectories, is correct at all orders. The QTB method also takes care of this aspect since the zero-point energy is included in the expression of the random force (see equation (2.2.3)). In particular, for the harmonic oscillator, we can define an effective temperature T_{eff} from the energy of the system so that:

$$k_B T_{\text{eff}} = \hbar\omega\left[\frac{1}{2} + \frac{1}{\mathrm{e}^{\hbar\omega/k_B T} - 1}\right] \tag{5.2.8}$$

where T is the classical temperature (the temperature of the bath). The effective temperature T_{eff} takes into account both the zero-point energy of the oscillator, $\hbar\omega/2$, and the Bose-Einstein distribution at the physical temperature T. The QTB simulation in the harmonic oscillator is therefore equivalent in this particular case to a classical MD simulation at the temperature T_{eff}.

In contrast, in a real anharmonic system, the QTB introduces a distribution of effective temperatures $T_{\text{eff}}(\omega)$ since each vibrational mode has a different energy and the balance between the QTB pumping and damping ensures that no equipartition of the energy occurs. The quantum term in equation (5.2.4) is not constant and depends on the operators $\hat{x}$ and $\hat{p}$. The analogy between the expectation values of these quantum operators and the position and momentum of the center of mass of Ψ is thus not correct anymore. Hence, in anharmonic systems, another problem arises, namely the zero-point energy leakage (ZPEL), which we will discuss in the following section 5.3.

5.3 The zero-point energy leakage

We have thus seen that using classical-like equations of motion to compute atomic trajectories of quantum particles has some limits for anharmonic systems, especially concerning the high-order expectation values of $\hat{x}^n$ and $\hat{p}^n$. We however know, from chapters 3 and 4, that the QTB nevertheless yields quite satisfactory results in real anharmonic systems. To overcome this apparent contradiction, we now focus specifically on the zero-point energy leakage (ZPEL), because it can lead to dramatic consequences for the structure of the system, as we will show below.

In a classical MD simulation, equipartition of the energy occurs: if each degree of freedom has a different initial energy, energy transfers will occur due to non-linear mode couplings and each degree of freedom will end up with the same average energy. If we define the effective temperature from the average kinetic energy $E_k^{(j)}$ of each degree of freedom

j i.e. $k_B T_{\text{eff}}^{(j)} = 2E_k^{(j)}$, then in a classical simulation, $T_{\text{eff}} = T$ where T is the temperature of the bath. In a quantum system, this is not true anymore since the quantum energy distribution is non-uniform and depends on the frequency of the vibrational modes. In particular, high-frequency modes have more energy than low-frequency ones. During a QTB simulation, there is a balance between QTB pumping and damping on the one hand, which tries to enforce the quantum energy distribution, and energy transfers between the vibrational modes on the other, which tend to drag the system towards an equipartition of the energy. If the second phenomenon turns out not to be negligible, ZPEL occurs i.e. part of the energy of the high-frequency modes is transferred into the low-frequency ones. As a consequence, low-frequency modes end up with too much kinetic energy which can then destroy the structure of the system e.g. if the effective temperature of the low-frequency modes is higher than the melting temperature of the system.

ZPEL has been observed in several systems (water clusters and liquid water, Lennard-Jones systems...) [195–198] and it has been recently pointed out by Bedoya-Martinez and coworkers to appear in QTB simulations [197]. Several solutions to the ZPEL problem in the case of the QTB have also been suggested: Bedoya-Martinez and coworkers tried to modify the noise power spectrum in order to reinforce the quantum bath pumping and thus obtain an energy distribution that is closer to the correct quantum one. This however remains a rather ad-hoc solution that has to be adapted individually for each system. In contrast, Ganeshan and coworkers proposed a deterministic approach to suppress the ZPEL which however requires the knowledge of the vibration normal coordinates prior to the simulation [196].

In the following section, we investigate the conditions leading to ZPEL for a better understanding of the validity of the QTB method. To that purpose, we will study two different models in which we can easily compare the QTB to exact calculations. First, we will use a simple model consisting of two coupled harmonic oscillators (section 5.3.1) that will allow us to control the anharmonicity easily. Then, we will analyze a one-dimensional chain of atoms (section 5.3.2) in which the mode couplings are introduced via realistic interatomic potentials. We note that the study of the ZPEL within the QTB, and more generally, the development and the critical analysis of the QTB method, is part of a collaboration with Fabien Brieuc and Hichem Dammak of Ecole Centrale Paris and with Marc Hayoun from Ecole Polytechnique. The results of this study are to be published (a manuscript of the submitted paper is given in the Publications section 5.5).

5.3.1 Coupled harmonic oscillators

We consider two coupled one-dimensional harmonic oscillators, with frequencies ν_1 and ν_2. Thanks to the small number of parameters, this system provides a clear illustration of the ZPEL within the QTB method and allows for the analysis of the conditions leading to this phenomenon. In particular, we can easily tune the non-linear coupling between the two oscillators and compare the QTB results with the exact numerical solution of the corresponding time-independent Schrödinger equation. The system is described by the Hamiltonian H:

$$H = \frac{1}{2}m\dot{x}_1^2 + \frac{1}{2}m\omega_1^2 x_1^2 + \frac{1}{2}m\dot{x}_2^2 + \frac{1}{2}m\omega_2^2 x_2^2 + \mathcal{C}_3(x_1 - x_2)^3 + \mathcal{C}_4(x_1 - x_2)^4 \qquad (5.3.1)$$

where $\omega_i = 2\pi\nu_i$ is the angular frequency of each oscillator, x_1 and x_2 are the coordinates of the two oscillators, m is their mass and $\mathcal{C}_3$ and $\mathcal{C}_4$ are two anharmonic coupling constants.

Friction coefficient	$\gamma = 4 \times 10^{-4}\,\omega_1$
Cut-off frequency	$\Omega_{\text{cut}} = 2\omega_1$
Time step	$\delta t = 0.05\omega_1^{-1}$
Total number of time steps	10^7
Number of independent trajectories	~ 30
Ratio of frequencies	$\Omega \in [0.05 - 0.8]$
Cubic coupling constant	$c_3 \in [0 - 25 \times 10^{-4}]$
Quartic coupling constant	$c_4 \in [0 - 40 \times 10^{-4}]$
Temperature	$k_B T = 0.03\,h\nu_1$

Table 5.1: Technical and numerical details concerning the QTB simulations on the two coupled harmonic oscillators (equation (5.3.2)).

H can be written in a dimensionless form, $\tilde{H} = H/\hbar\omega_1$, so that:

$$\tilde{H} = \frac{\dot{q}_1^2}{2} + \frac{q_1^2}{2} + \frac{\dot{q}_2^2}{2} + \Omega^2\frac{q_2^2}{2} + c_3(q_1 - q_2)^3 + c_4(q_1 - q_2)^4 \tag{5.3.2}$$

where we introduced the following variables:

$$\Omega = \frac{\nu_2}{\nu_1} = \frac{\omega_2}{\omega_1} \tag{5.3.3}$$

$$\xi = \sqrt{\frac{\hbar}{m\omega_1}}, \quad q_i = \frac{x_i}{\xi} \tag{5.3.4}$$

$$c_3 = \frac{\mathcal{C}_3\xi^3}{\hbar\omega_1}, \quad c_4 = \frac{\mathcal{C}_4\xi^4}{\hbar\omega_1} \tag{5.3.5}$$

$$t^* = \omega_1 t, \quad \dot{q}_i = \frac{\mathrm{d}q_i}{\mathrm{d}t^*} \tag{5.3.6}$$

q_1 and q_2 are the reduced positions of the two oscillators and Ω is the ratio of their frequencies (we choose $\nu_1 > \nu_2$). We study the evolution of the energies ϵ_1 and ϵ_2 of the two oscillators with a cubic or a quartic coupling governed by the dimensionless parameters c_3 and c_4 that are:

$$\epsilon_1 = \left\langle \frac{\dot{q}_1^2}{2} \right\rangle + \left\langle \frac{q_1^2}{2} \right\rangle, \quad \epsilon_2 = \left\langle \frac{\dot{q}_2^2}{2} \right\rangle + \Omega^2 \left\langle \frac{q_2^2}{2} \right\rangle. \tag{5.3.7}$$

The numerical details of the QTB simulations are given in Table 5.1: the temperature is set to $k_B T = 0.03\,h\nu_1$ (e.g. $T \sim 60$ K if $\nu_1 = 40$ THz) so that the thermal energy contribution to the energies of the oscillators is negligible with respect to their zero-point energies and the parameters c_3 and c_4 are chosen so that a large range of coupling energies is covered. The exact quantum calculation shows that the energies of the oscillators are almost independent of the anharmonic coupling intensities in the range of coupling values studied here and are equal to their zero-point energies; hence, in reduced units, $\epsilon_1^{\text{exact}} = 0.5$ and $\epsilon_2^{\text{exact}} = \Omega/2$. Figure 5.3.1 shows the average energies obtained from QTB simulations with a damping term $\gamma = 4 \times 10^{-4}$ in two distinct cases: $\Omega = 0.5$ with only a cubic coupling ($c_3 \neq 0$, $c_4 = 0$) and $\Omega = 0.25$ with only a quartic coupling ($c_3 = 0$, $c_4 \neq 0$). The average coupling energy is $\epsilon_c = \langle c_n(q_1 - q_2)^n \rangle$ with $n = 3$ for the cubic case and $n = 4$ for the quartic case. As expected, in the uncoupled case i.e. $c_3 = 0$ and $c_4 = 0$, the QTB gives the expected quantum energies for the two oscillators, corresponding to their zero-point energies, i.e. $\epsilon_i^{\text{QTB}} = \epsilon_i^{\text{exact}}$ for $i = 1, 2$. In contrast, when the coupling constants c_3 or c_4

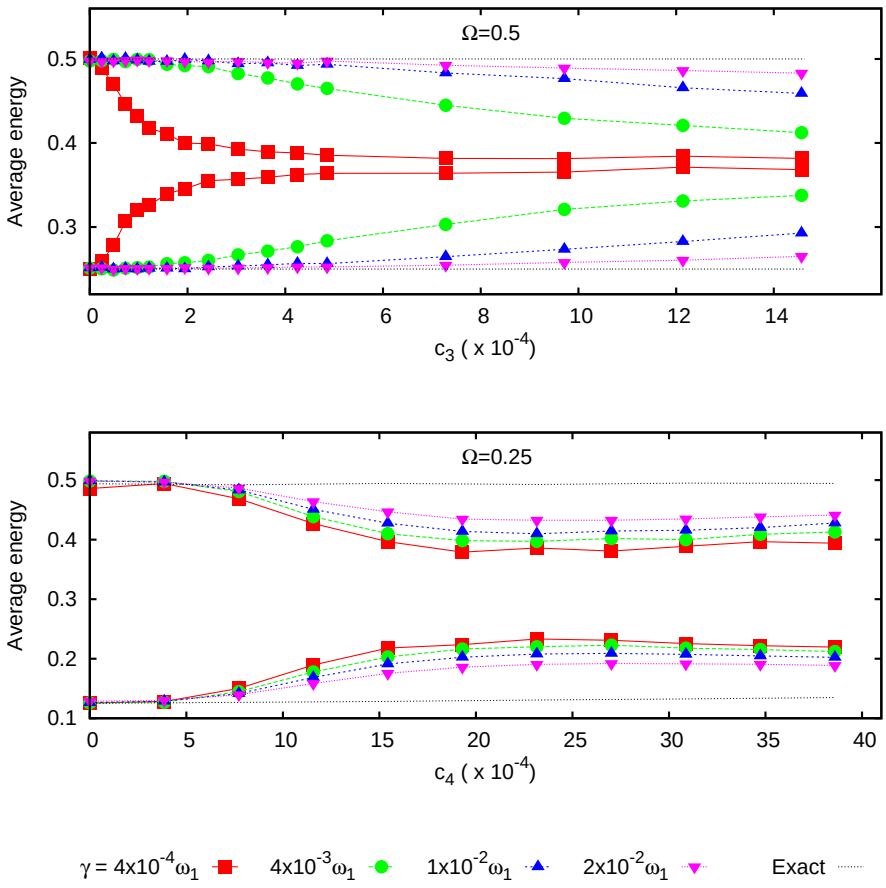

Figure 5.3.1: Average energies, ϵ_1 and ϵ_2, of the two oscillators and average coupling energy ϵ_c computed with the QTB as a function of the intensity of the coupling constants c_3 and c_4. The damping term is $\gamma = 4 \times 10^{-4}$. Top panel: cubic coupling ($c_3 \neq 0$, $c_4 = 0$) with $\Omega = 0.5$. Lower panel: quartic coupling ($c_4 \neq 0$, $c_3 = 0$) with $\Omega = 0.25$. By symmetry, $\epsilon_c = 0$ in the cubic case.

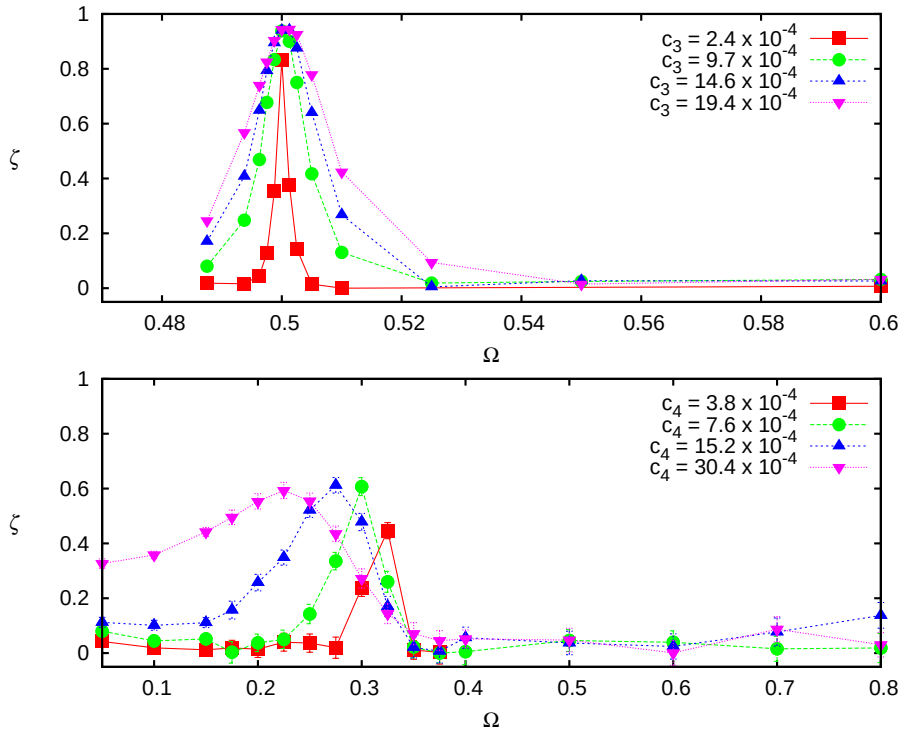

Figure 5.3.2: Zero-point energy leakage quantified through the deviation factor ζ (equation (5.3.8)) as a function of the ratio of frequencies Ω. Top panel: cubic coupling ($c_3 \neq 0$, $c_4 = 0$). Lower panel: quartic coupling ($c_4 \neq 0$, $c_3 = 0$). The damping term is $\gamma = 4{\times}10^{-4}$.

are increased, the energies obtained from QTB diverge from the exact results: part of the energy of oscillator 1 is transferred into oscillator 2, hence, ZPEL occurs.

In the following, we investigate how ZPEL depends on the coupling constants c_3 and c_4 and on the frequency ratio Ω. To quantify the ZPEL, we adopt the following deviation factor ζ:

$$\zeta = \frac{\Delta\epsilon^{\text{exact}} - \Delta\epsilon^{\text{QTB}}}{\Delta\epsilon^{\text{exact}}} = \frac{(\epsilon_1^{\text{exact}} - \epsilon_2^{\text{exact}}) - (\epsilon_1^{\text{QTB}} - \epsilon_2^{\text{QTB}})}{\epsilon_1^{\text{exact}} - \epsilon_2^{\text{exact}}} \tag{5.3.8}$$

Within this definition, there is no leakage when $\zeta = 0$ i.e. when $\epsilon_{1,2}^{\text{QTB}} = \epsilon_{1,2}^{\text{exact}}$. In contrast, the leakage is maximum when $\zeta = 1$ i.e. when the system has reached an equipartition of the energy: $\epsilon_1^{\text{QTB}} = \epsilon_2^{\text{QTB}}$. In Figure 5.3.2, ζ is shown as a function of Ω for different values of c_3 and c_4. We can see that the ZPEL strongly depends on the ratio of frequencies and is present only for certain values of Ω. In the cubic case, it occurs only near $\Omega = 0.5$ (top panel of Figure 5.3.2). Indeed, cubic terms in the potential are known to be responsible for frequency doubling or the second harmonic generation (2ω). This is further confirmed by the analysis of the vibrational spectrum of the two oscillators computed from QTB trajectories in the cubic case, with $c_3 = 2.4 \times 10^{-4}$ for example (top left panel of Figure 5.3.3): harmonics at $2\omega_2$, $\omega_1 - \omega_2$, and $\omega_1 + \omega_2$ are visible. Therefore, at $\Omega = 0.5$, there is a resonance between the couple of modes $(\omega_1; 2\omega_2)$ and $(\omega_2; \omega_1 - \omega_2)$. Similarly, the quartic terms are responsible for the generation of modes with frequency 3ω; ZPEL is indeed observed near the resonance at $\Omega = 1/3$ (lower panel of Figure 5.3.2). However, while increasing quartic coupling, significant ZPEL occurs for a range of small Ω values, in contrast with the cubic coupling case. The lower panel of Figure 5.3.3 shows that, in the case of $\Omega = 0.2$ and $c_4 = 15.2 \times 10^{-4}$, many other modes than ω_1 and ω_2 also appear

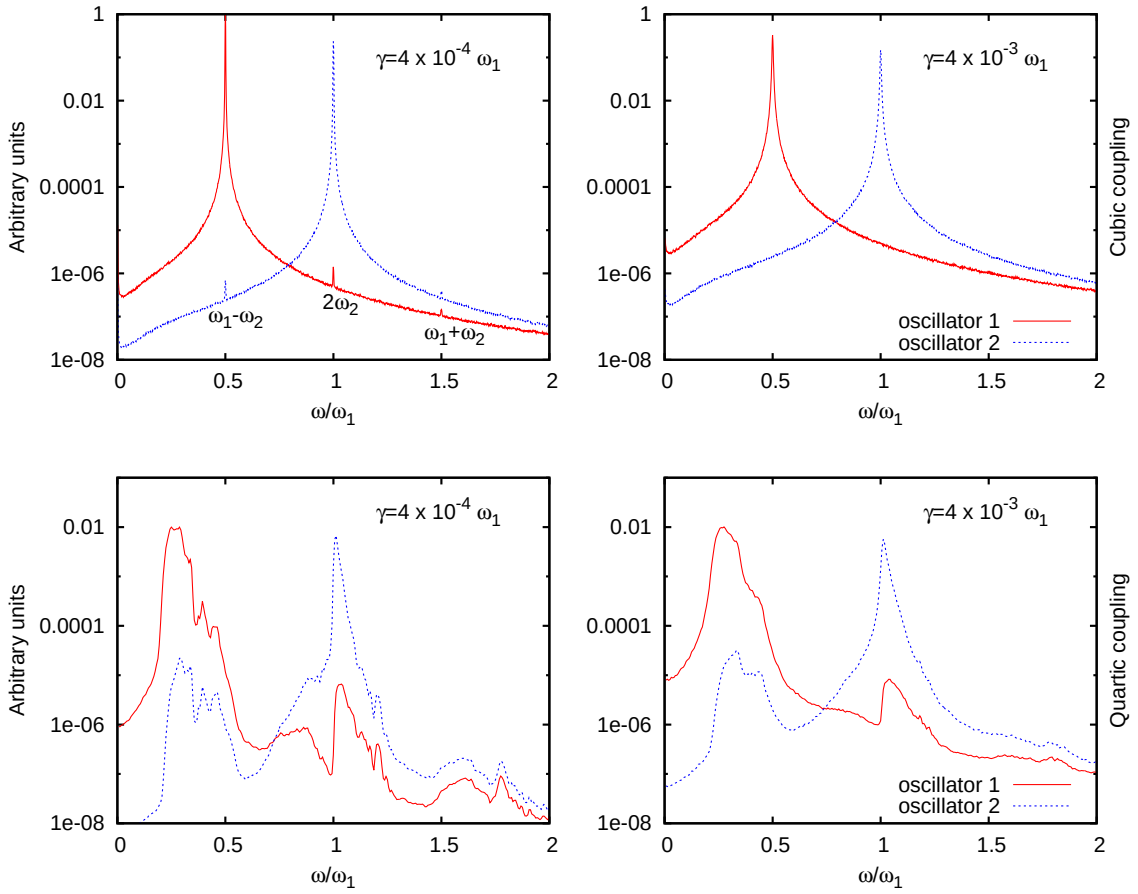

Figure 5.3.3: Vibrational spectra (in logarithmic scale) of oscillators 1 (in red) and 2 (in blue) obtained from QTB-MD simulations in the case of a cubic coupling (top panels) with $\Omega = 0.5$ and $c_3 = 2.4 \times 10^{-4}$, and in the case of a quartic coupling (lower panels) with $\Omega = 0.2$ and $c_4 = 15.2 \times 10^{-4}$. The spectra are computed with two different values of the friction coefficient: $\gamma = 4 \times 10^{-4}\omega_1$ and $\gamma = 4 \times 10^{-3}\omega_1$.

in the spectrum. Therefore, the quartic coupling case is quite different from the cubic case where the anharmonicity introduced satellite peaks in addition to the normal modes ω_1 and ω_2. Here, a large range of frequencies are excited due to mode mixing and mode coupling. Hence, multiple resonances are likely to occur leading to a significant ZPEL for values of $\Omega < 1/3$.

Influence of the friction coefficient γ

The damping coefficient is now varied from $4 \times 10^{-4}\omega_1$ to $2 \times 10^{-2}\omega_1$. We focus on the frequency range where the ZPEL is important: $\Omega = 0.5$ for cubic coupling and $\Omega = 0.25$ for quartic coupling. Figure 5.3.4 shows that ZPEL strongly depends on γ: increasing γ can limit the leakage and even practically remove it in the case of the cubic coupling. In particular, for $c_3 = 2.4 \times 10^{-4}$, a value of γ equal to $4 \times 10^{-3}\omega_1$ is sufficient to remove the ZPEL ($\zeta = 0.08$). The top right panel of Figure 5.3.3 shows the vibrational spectra obtained in this case with the larger γ: while the ZPEL has been suppressed, the peaks corresponding to the resonances ($2\omega_2$, $\omega_1 - \omega_2$ and $\omega_1 + \omega_2$) have also disappeared. This further illustrates the relation between the mode resonances and the ZPEL. Moreover, increasing γ also leads to a broadening of the peaks of the oscillators in the spectra, consistently with the fact that the full width at half maximum in the case of a harmonic oscillator is equal to γ in a Langevin dynamics. The case of the quartic coupling is more complicated: even for large values of γ, the ZPEL is reduced but not completely suppressed (Figure 5.3.4). The lower right panel of Figure 5.3.3 also shows that increasing γ in the case of a quartic coupling with $\Omega = 0.2$ and $c_4 = 15.2 \times 10^{-4}$ is not sufficient to suppress all of the resonances between the different modes.

Furthermore, we can estimate the characteristic time t_{tr} of the energy transfer between the two oscillators by running NVE calculations in which only one of the oscillators (e.g. oscillator 1) is excited at $t = 0$. t_{tr} can then be roughly estimated by calculating the typical activation time of the second oscillator (e.g. oscillator 2). Figure 5.3.5 shows the evolution of the energies of the two oscillators with time. As the energy of oscillator 1 decreases, the energy of oscillator 2 increases as $\exp(t/t_{tr})$ and we can estimate t_{tr} for each value of the coupling constant. Figure 5.3.6 shows the evolution of t_{tr} for $\Omega = 0.5$ as a function of the cubic coupling constant c_3 ($c_4 = 0$ here). As expected, the characteristic time of energy transfer is directly related to the intensity of the coupling and in particular, t_{tr} is inversely proportional to c_3. To remove the ZPEL, we need to choose a value for the damping γ that is greater than the typical transfer frequency $\nu_{\mathrm{ZPEL}} = t_{tr}^{-1}$, in order to hinder the energy transfer between the two oscillators. For example, we can see in Figure 5.3.6 that for $c_3 = 4 \times 10^{-4}$, $t_{tr} \sim 400\omega_1^{-1}$ thus $\nu_{\mathrm{ZPEL}} \sim 2.4 \times 10^{-3}\,\omega_1$. Accordingly, Figure 5.3.4 shows that for $\gamma = 4 \times 10^{-4}\,\omega_1$ i.e. for $\gamma < \nu_{\mathrm{ZPEL}}$, ZPEL occurs while for $\gamma = 4 \times 10^{-3}\,\omega_1$ i.e. for $\gamma > \nu_{\mathrm{ZPEL}}$, ZPEL is largely reduced.

In conclusion, this simple model raises several important issues: the role of resonances and the possibility to remove or at least significantly reduce the effects of ZPEL by increasing γ. We now address these issues on a more complex model in the following section.

5.3.2 One-dimensional chain of atoms

We consider a one-dimensional chain of atoms, consisting of 3 oxygen atoms interspaced with 3 hydrogen atoms, with periodic boundary conditions. The interactions between the atoms are described by two interatomic potentials. On the one hand, the O-H interaction is a Morse-type potential derived by Johannsen for hydrogen-bonded systems [114] and

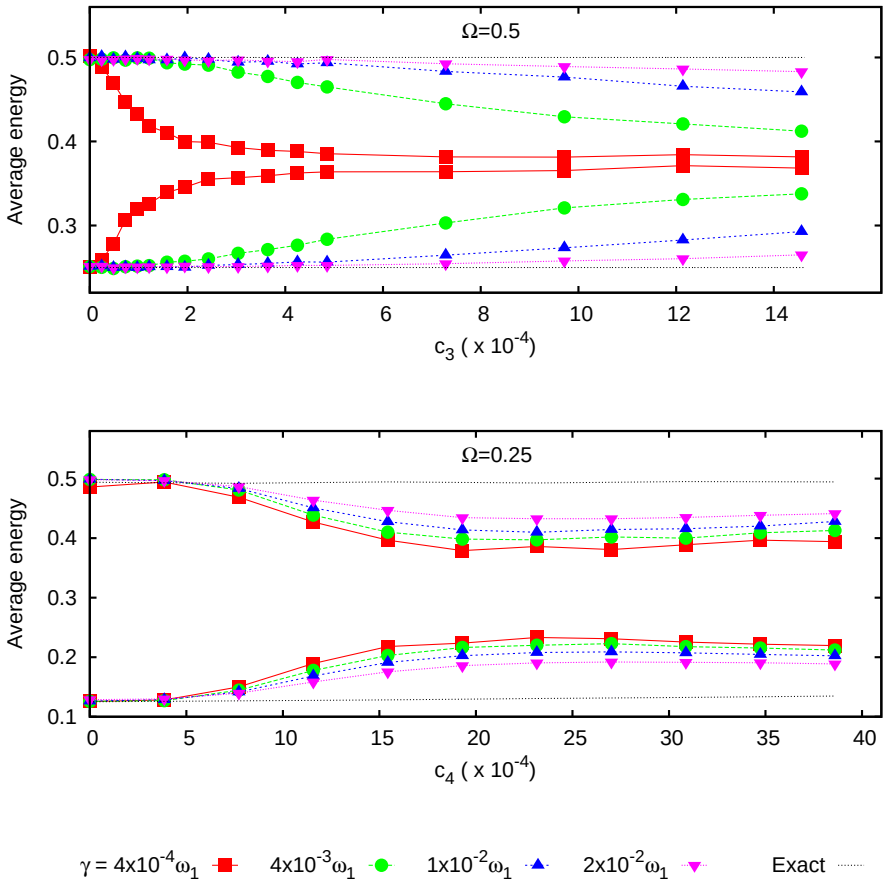

Figure 5.3.4: Effect of the damping coefficient γ (given in ω_1 unit) on the energies of the two oscillators (equation (5.3.7)) as a function of the coupling constants. Top panel: cubic coupling ($c_3 \neq 0$, $c_4 = 0$) and $\Omega = 0.5$. Lower panel: quartic coupling ($c_4 \neq 0$, $c_3 = 0$) and $\Omega = 0.25$. The solid line and symbols represent the results obtained from QTB-MD and the grey dashed lines represent the exact results.

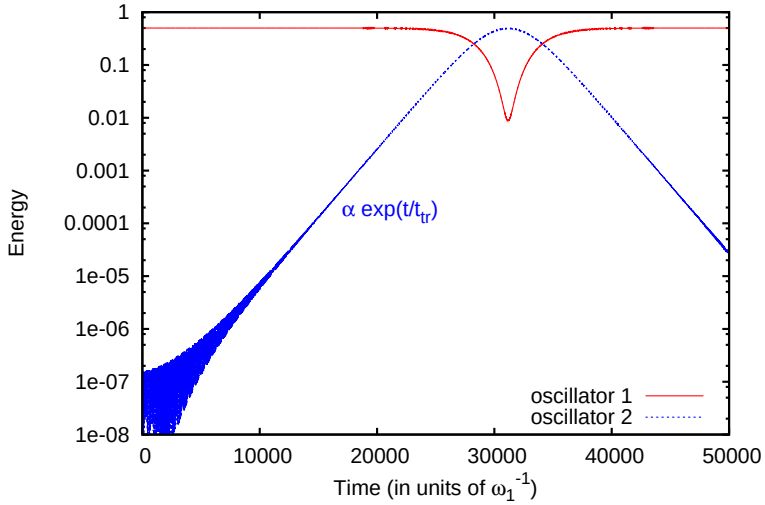

Figure 5.3.5: Energies of oscillator 1 (in red) and oscillator 2 (in blue) as functions of time during a NVE simulation in which only oscillator 1 is excited at $t = 0$. The evolution of the energy of oscillator 2 is proportional to $\exp(t/t_{tr})$ where t_{tr} is the characteristic time of energy transfer between the two oscillators. Here, $\Omega = 0.5$, $c_3 = 1.0 \times 10^{-4}$ and $c_4 = 0$.

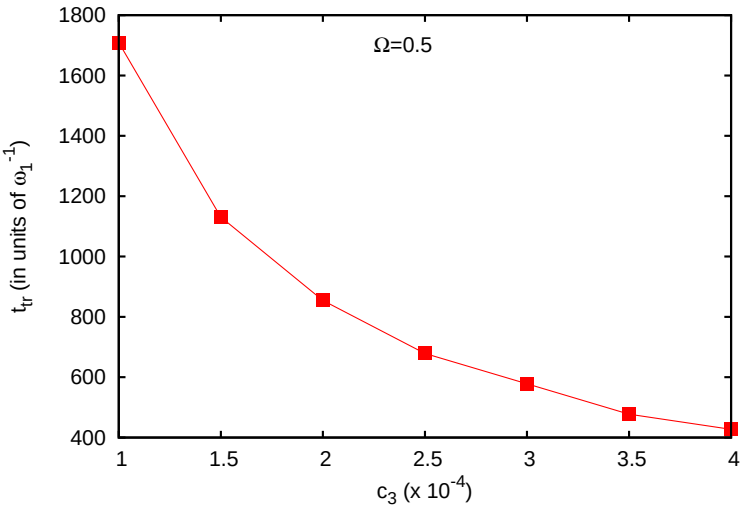

Figure 5.3.6: Energy transfer time between the two oscillators t_{tr} (in units of ω_1^{-1}) as a function of the cubic coupling constant c_3. Here, $\Omega = 0.5$ and $c_4 = 0$. t_{tr} is estimated from the evolution of the energy of oscillator 2 during NVE simulations in which only oscillator 1 is initially excited.

already discussed in section 3.1.3:

$$V_{\mathrm{OH}}(r) = \frac{u_0}{a + b\mathrm{e}^{a(r-r_0)}} \left[a \left(\mathrm{e}^{-b(r-r_0)} - 1 \right) + b \left(\mathrm{e}^{a(r-r_0)} - 1 \right) \right] - u_0 \tag{5.3.9}$$

where r is the O-H distance, u_0 is the height of the potential barrier, r_0 the equilibrium O-H distance, and a and b are two parameters. The values of the parameters are set so that: $r_0 = 0.96$ Å (which corresponds to the length of the covalent bond in the OH^- ion), $a \simeq 7.11$ Å^{-1}, $b \simeq 2.00$ Å^{-1} and $u_0 = 2.73$ eV so that the O-H stretching frequency (ν_{OH}) in the harmonic approximation of the potential V_{OH} given in equation (5.3.9) approximately equals 100 THz. On the other hand, the O-O interaction is described by a standard Morse potential:

$$V_{\mathrm{OO}}(R) = C_0 \left(1 - \mathrm{e}^{-\alpha_0 (R-R_0)} \right)^2 - C_0 \tag{5.3.10}$$

where C_0 and α_0 are the depth and the width of the potential respectively and R_0 the O-O equilibrium distance. The parameters are the following: $C_0 = 3.81$ eV, $R_0 = 2.88$ Å and α_0 varies so that the value of the O-O frequency (ν_{OO}) lies between 10 and 60 THz. The simulations are run with a 0.1 fs time step and the total simulation time is about 3 ns. The QTB results are averaged over 12 trajectories.

The potential energy of an hydrogen atom is given by $V_{\mathrm{OH}}(r) + V_{\mathrm{OH}}(R-r)$ which is a double-well potential. We can thus define short "covalent" O-H bond (~ 1 Å) and longer "hydrogen bonds" H$\cdots$O (~ 1.9 Å). Although this model cannot represent a real ice cluster or any other real physical system, it is characterized by realistic O-H frequencies and mode couplings; it is thus useful to assess the effects of ZPEL in real hydrogen-bonded systems. A normal mode analysis of the system yields one low-frequency, ν_2, corresponding to the O-O lattice mode, and two very similar high-frequencies, ν_1, corresponding to the O-H stretching modes. In analogy with the previous model, the O-H stretching modes roughly play the role of the high-frequency oscillator (ν_1) while the O-O lattice mode corresponds to the low-frequency oscillator (ν_2). In the following, we will show the influence of the parameter $\Omega = \nu_2/\nu_1$ and the friction coefficient γ on ZPEL at $T = 600$ K. The frequency ν_2 is varied through the parameter α_0 while the frequency ν_1 is almost constant since ν_{OH} is fixed at 100 THz. The results from QTB are compared with those obtained from PIMD simulations, using a Trotter number $P = 20$ which ensures a good convergence of all the physical quantities in all cases studied here. For each QTB simulation, we checked that the total energy of the system, as well as the kinetic and potential energies, are in good agreement with the reference values given by PIMD.

In order to evaluate the leakage, we compare the kinetic energy of the light atoms, significantly involved in the high-frequency modes, to that of the heavier atoms, mainly involved in the low-frequency modes. Thus, the effective temperatures T_{H} and T_{O} of H and O atoms are computed:

$$\frac{k_B T_{\mathrm{H}}}{2} = \frac{1}{N_{\mathrm{H}}} \sum_{i=1}^{N_{\mathrm{H}}} \langle E_k^{(i)} \rangle, \quad \frac{k_B T_{\mathrm{O}}}{2} = \frac{1}{N_{\mathrm{O}}} \sum_{i=1}^{N_{\mathrm{O}}} \langle E_k^{(i)} \rangle \tag{5.3.11}$$

where N_{H} and N_{O} are the number of H and O atoms respectively (here, $N_{\mathrm{H}} = N_{\mathrm{O}} = 3$), and $\langle E_k^{(i)} \rangle$ is the average kinetic energy of atom i. In a classical system, equipartition ensures that the kinetic energy is equally distributed among all degrees of freedom: they all have the same temperature and $T_{\mathrm{H}}^{(\mathrm{class})} = T_{\mathrm{O}}^{(\mathrm{class})}$. This is not true in the quantum case: high-frequency modes have more kinetic energy and $T_{\mathrm{H}} \neq T_{\mathrm{O}}$. As high-frequency mode eigenvectors have approximately 95% projection on the displacements of hydrogen atoms, the kinetic energy of hydrogens is higher than the oxygen counterpart and $T_{\mathrm{H}} > T_{\mathrm{O}}$. This

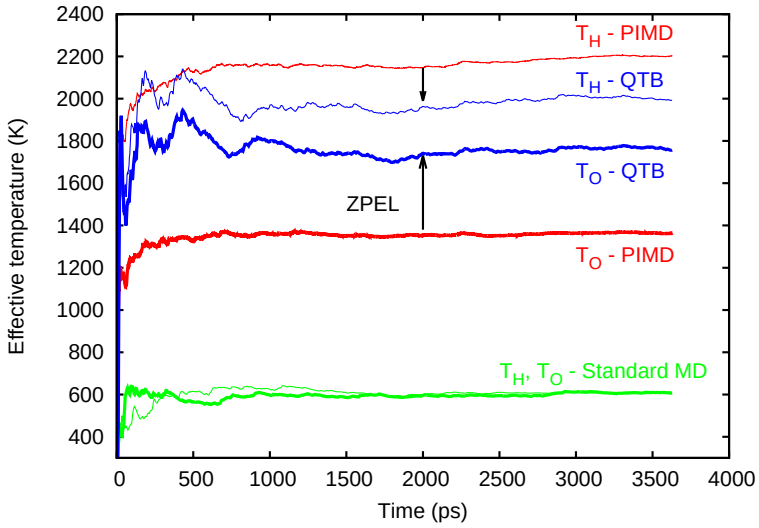

Figure 5.3.7: Effective temperatures T_{O} and T_{H} of oxygen and hydrogen atoms (equation (5.3.11)) calculated through classical MD, QTB and PIMD simulations at $T = 600K$. Here $\Omega = 0.5$. The arrows indicate the temperature shifts due to zero-point energy leakage (ZPEL).

occurs in both QTB and PIMD, which serves as a reference here. From Figure 5.3.7, one sees that, as expected, the leakage makes the effective temperature of light atoms decrease and that of heavier atoms increase with respect to the PIMD reference values. In this case, the ZPEL can be quantified through the deviation factor:

$$\zeta = \frac{(T_{\mathrm{H}} - T_{\mathrm{O}})^{\mathrm{PIMD}} - (T_{\mathrm{H}} - T_{\mathrm{O}})^{\mathrm{QTB}}}{(T_{\mathrm{H}} - T_{\mathrm{O}})^{\mathrm{PIMD}}}. \tag{5.3.12}$$

$\zeta = 0$ if there is no leakage and $0 < \zeta < 1$ if leakage occurs. Its dependence on Ω is shown in Figure 5.3.8. Similarly to the coupled harmonic oscillators' model (section 5.3.1), ZPEL occurs mostly for $\Omega \sim 0.5$. We can also see that ZPEL can be substantially decreased by increasing γ when $\Omega \sim 1/2$, similarly to the case of two coupled oscillators. However, significant ZPEL is also observed for $\Omega < 0.2$ which corresponds to a highly anharmonic regime where a structural transition occurs and is therefore a different physical situation than the other values of Ω that will not be discussed in detail here.

Figure 5.3.9 shows the distributions of interatomic distances, d_{OH} and d_{OO} for the case $\Omega = 0.5$ computed from QTB, PIMD and standard MD simulations. One can see that the d_{OH} distribution is almost not affected by ZPEL while the d_{OO} distribution is more sensitive to ZPEL: the QTB distribution is too broad, which is consistent with the excess of kinetic energy for the oxygen that comes from the ZPEL. However, when ZPEL is suppressed by increasing γ, the d_{OO} distribution from QTB coincides with the PIMD distribution.

We have seen in the case of the two coupled harmonic oscillators that increasing γ has consequences on the vibrational spectrum of the system; in particular, the peaks are broadened and the peaks corresponding to the mode resonances disappear when γ is large enough to remove the ZPEL (see Figure 5.3.3). Figure 5.3.10 shows the vibrational spectrum of the one-dimensional chain of atoms for $\Omega = 0.5$ and for two different values of γ. For $\gamma = 0.2$ THz, ZPEL occurs while for $\gamma = 10$ THz, ZPEL is almost fully removed (see Figures 5.3.8). As expected, increasing the friction coefficient γ leads to broader peaks.

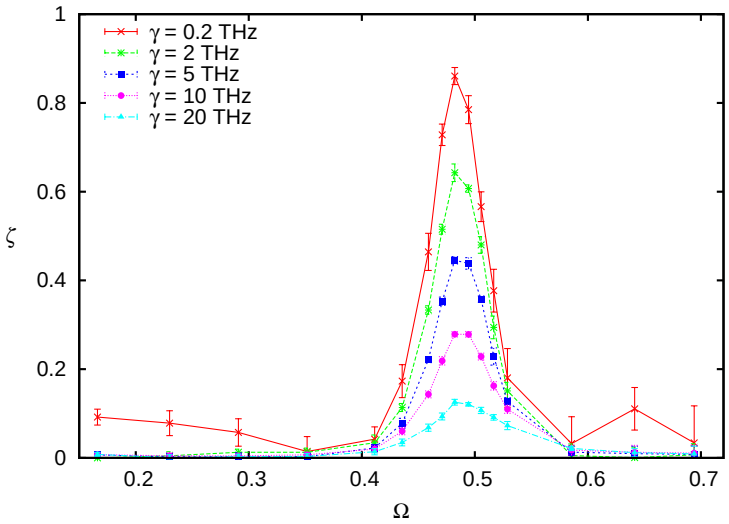

Figure 5.3.8: Zero-point energy leakage quantified by the deviation factor ζ using the definition (5.3.12) as a function of the frequency ratio Ω.

However, the positions of these peaks hence the corresponding mode frequencies are not modified by the large value of γ. Thus, even with a large damping term, the vibrational spectrum still yields useful information about the mode frequencies whenever the peaks in the vibrational spectrum are separated by more than γ.

In conclusion, in a system containing different chemical elements, the kinetic energy repartition between them can be used as an indicator of ZPEL. More generally, in a real system, a diagonalization of the dynamical matrix prior to the simulation could give access to the normal mode frequencies ω_i in the harmonic approximation. One could thus compute the corresponding approximate effective temperatures $\hbar\omega_i/2k_B$. If they are quite different from the QTB kinetic energies then it would be an indication that ZPEL occurs. As in the case of two coupled harmonic oscillators, the ZPEL is intrinsically related to resonances between vibrational modes. Similarly, increasing the friction coefficient allows to suppress the ZPEL. However, when the system is highly anharmonic, values of γ higher than the vibrational frequencies of the system are required to counterbalance the leakage. In this case, the quantum structural properties are well reproduced but the information obtained by looking at dynamical properties should be used with caution.

5.3.3 Conclusion

We have attempted in this section to perform a quantitative study of ZPEL in QTB simulations. We first found that ZPEL is intrinsically related to the coupling between vibrational modes; therefore, this is hardly avoidable in practice, since in realistic systems many modes can resonate. However, we also found that by increasing the damping term γ, one can significantly reduce the ZPEL and even in some cases, remove it entirely. This is due to the fact that by increasing the damping term, one reinforces the QTB pumping rate with respect to the equilibration rate of the system, which is caused by the non-linear couplings between vibrational modes. This in turn drags the system towards the correct quantum energy distribution imposed by the QTB. However, it is commonly accepted that increasing the damping term in Langevin simulations helps reaching the thermal equilibrium while biasing the system, in particular its vibrational spectrum. Here, we come to the conclusion that the damping should be increased in QTB simulations in order to avoid

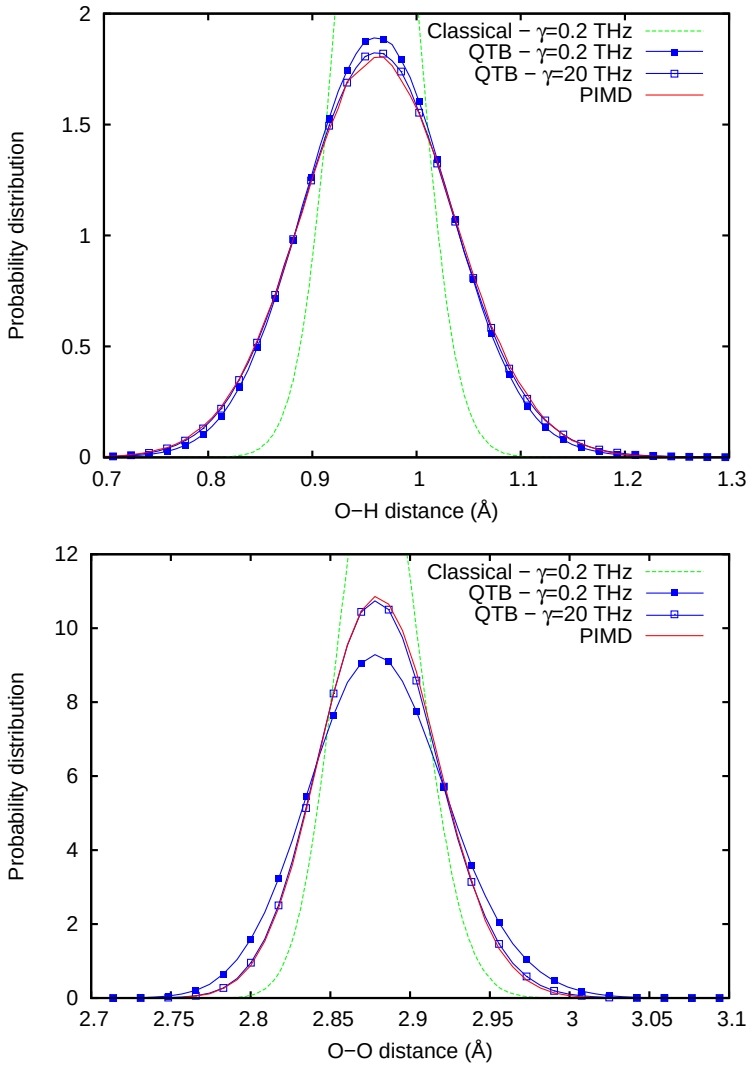

Figure 5.3.9: Probability distribution of the O-H distance (top panel) and the O-O distance (lower panel) computed from classical MD, PIMD and QTB, for different values of the friction coefficient γ (0.2 and 20 THz) and for $\Omega = 0.5$.

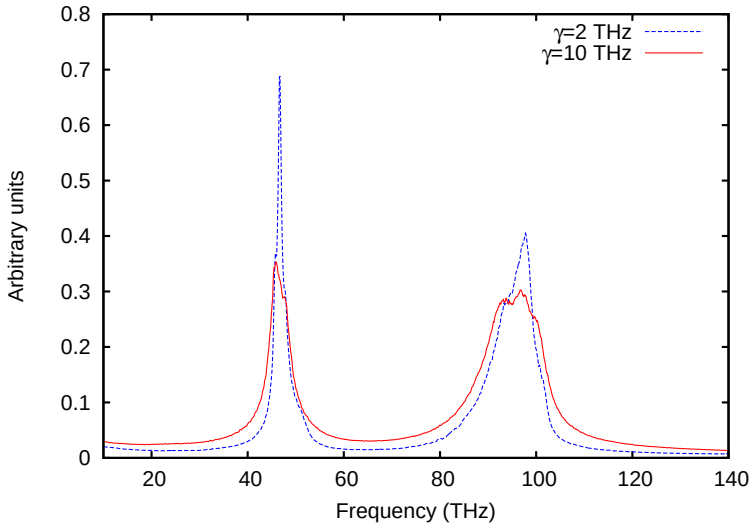

Figure 5.3.10: Vibrational spectrum obtained from QTB simulations for $\Omega = 0.5$ and two different values of the damping coefficient: $\gamma = 0.2$ THz (dashed line) and $\gamma = 10$ THz (full line).

the ZPEL. The effects of a large damping should then be carefully studied on both structural and dynamical properties in each specific case. Our results tend to show that the QTB is a relatively robust method and yields excellent results as long as one keeps in mind the physics of the problem. This is particularly well illustrated in the case of the phase transitions of $BaTiO_3$ (BTO). QTB simulations performed with a small damping lead to a completely wrong phase diagram. In contrast, with a larger damping, one recovers the correct sequence of phase transitions at the correct transition temperatures (see the submitted paper on ZPEL in Publications section 5.5). On the other hand, damping usually broadens vibrational peaks making it difficult and sometimes impossible to distinguish between different vibrational modes. However, the mode frequencies are often not dramatically altered allowing the study of high-frequency O-H vibrational modes for example as seen previously. This also justifies our Landau-like approach to phase transitions and enables the direct comparison of the QTB spectra with spectroscopic measurements, something which is usually hardly attainable by other methods (see chapter 1).

5.4 The QTB and the double well potential

We have just seen that in weakly anharmonic systems, the QTB could yield quite good results, as long as the ZPEL is avoided by choosing an appropriate damping term. However, we have seen in chapters 3 and 4 that the QTB simulations allowed us to construct a model that accounts for hydrogen bonds in various systems, by means of a one-dimensional double well potential. This kind of potential is highly anharmonic, especially if the barrier is sufficiently small that proton tunneling can occur, such as is the case in ice VII. In the following, we will analyze the results obtained from QTB simulations on a one-dimensional double well potential in order to assess the performance of the QTB in an unfavorable case. We consider the following symmetric double well potential:

$$V(x) = V_0 \left[\left(\frac{x}{x_0} \right)^2 - 1 \right]^2 \tag{5.4.1}$$

	"High-barrier" $V_0 = 2.7211$ eV, $x_0 = 0.21$ Å	"Low-barrier" $V_0 = 0.54422$ eV, $x_0 = 0.13$ Å
Exact solution	$E_{\text{tot}} = 0.68$ eV	$E_{\text{tot}} = 0.37$ eV
QTB result	$E_{\text{tot}} = 0.68$ eV	$E_{\text{tot}} = 0.40$ eV
Classical result	$E_{\text{tot}} = 0.26$ eV	$E_{\text{tot}} = 0.26$ eV

Table 5.1: Energies obtained from the numerical solution of the time-independent Schrödinger equation, the Quantum Thermal Bath method and classical molecular dynamics, using the double well potential given in equation (5.4.1).

where V_0 is the height of the barrier at $x = 0$ and $\pm x_0$ are the positions of the two wells. We compare results from classical molecular dynamics (using a Langevin thermostat), to QTB molecular dynamics and to the numerical solution of the time-independent Schrödinger equation. Simulations are performed at $T \sim 300$ K with a damping term $\gamma = 10$ THz and a cutoff frequency $\nu_{\text{cut}} \sim 6600$ THz. First, we look at the energies given by the QTB for two different potentials (see table 5.1). As expected, classical molecular dynamics yields a total energy equal to $k_B T$ i.e. the thermal energy is correctly obtained with a Langevin thermostat (in particular, it is independent of the potential). Moreover, energy equipartition occurs meaning that the average potential energy is equal to the average kinetic energy. The quantum energy on the other hand is given by :

$$\langle E \rangle = \text{Tr}[\rho H] \tag{5.4.2}$$

where H is the Hamiltonian of the system (with eigenstates Ψ_n and eigenenergies E_n) and ρ the density matrix i.e.

$$\rho = \frac{1}{Z} \sum_n \mathrm{e}^{-\beta E_n} |\Psi_n\rangle\langle\Psi_n| . \tag{5.4.3}$$

$Z = \sum_n \exp(-\beta E_n)$ is the partition function and $\beta = (k_B T)^{-1}$ is the inverse temperature. Hence, the average total energy is:

$$\langle E \rangle = \frac{1}{Z} \sum_n \mathrm{e}^{-\beta E_n} E_n. \tag{5.4.4}$$

In both the high-barrier case ($V_0 = 2.7211$ eV) and the low-barrier case ($V_0 = 0.54422$ eV), the quantum energy $\langle E \rangle$ is almost equal to the zero-point energy. In the high-barrier case, the QTB result is in good agreement with the exact total energy. Additional QTB simulations at $T \sim 0$ K yield the same total energy as at ambient temperature which confirms that the QTB correctly accounts for the zero-point energy of the system. Moreover, the average potential energy and average kinetic energy correspond to the potential and kinetic part of the quantum energy as well. In the low-barrier case, the QTB overestimates the total energy of the system with respect to the quantum result. In particular, the average kinetic energy is overestimated while the average potential energy is slightly underestimated. Hence, in the case of a high-barrier potential, the two wells can be approximated by two quasi-harmonic potentials and the QTB yields the correct energies. On the contrary, in the low-barrier potential, the system is much more anharmonic and the QTB fails to retrieve the quantum results.

We now focus on the structural properties of the system. Depending on the parameters of the potential, the QTB yields position distribution functions that can be in good agreement with the exact quantum one (see top panel of Figure 5.4.1): in the high-barrier case, the QTB distribution displays two peaks that are almost the same as the quantum

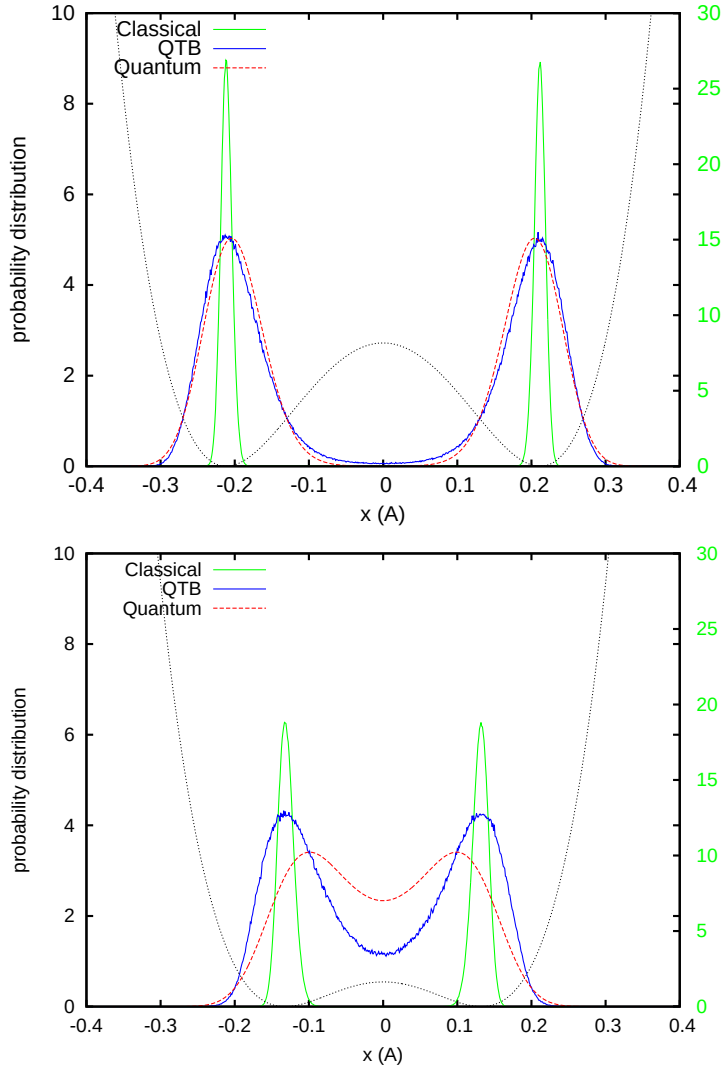

Figure 5.4.1: Probability distribution in a double well potential (equation (5.4.1)) ($V_0 = 0.1\,\text{Ha} \simeq 2.72$ eV and $x_0 = 0.21$ Å for the top panel and $V_0 = 0.02\,\text{Ha} \simeq 0.54$ eV and $x_0 = 0.13$ Å for the lower panel). The exact quantum results are in red, the classical results are in green and the QTB results are in blue ($T = 300$ K).

density, while the classical distribution is much narrower.[1] In the low-barrier case however (see lower panel of Figure 5.4.1), the QTB distribution is not equal to the quantum one: the positions of the two peaks are not close enough, and the value of the density between the two peaks is too low; we note that the QTB still gives better results than the classical simulation as far as the position distribution is concerned. Indeed, part of the spatial delocalization inherent to the quantum nature of the particle is captured by the QTB. This is also consistent with the fact that the QTB energies slightly depart from the exact one in this case (see table 5.1). Concerning the vibrational properties of the system, the same trend is observed. In the high-barrier potential, the QTB spectrum displays a high-frequency peak corresponding to the vibration of the particle in the bottom of the well. The QTB frequency ($\nu_{\mathrm{QTB}} \sim 320$ THz) is lower than its classical counterpart ($\nu_{\mathrm{classical}} \sim 340$ THz) and the QTB peak is broader than the classical one[2]; this indicates that the QTB accounts for part of the anharmonicity of the system better than the classical simulation. In contrast, in a low-barrier potential, proton tunneling occurs. This purely quantum effect is partly reproduced by the QTB: the distribution has a non-zero value at the top of the barrier. However, the QTB trajectories associated to proton hopping events are non-physical: the QTB introduces a hopping frequency which can be more important by a few orders of magnitude than the correct quantum tunneling frequency.

To summarize, the double well potential is a clear illustration of the limits of the QTB. In the case of a high barrier, for which proton tunneling is negligible and the two wells can be considered as two independent quasi-harmonic potentials, the QTB yields relatively good results: the energies correspond to the quantum ones meaning that the zero-point energy of the system is well reproduced, and both the structural and (high-frequency) dynamical properties are correctly described by the QTB. However, in the case of a low-barrier potential and significant proton tunneling, the QTB shows some downsides. Indeed, in order to take into account quantum tunneling, the QTB overestimates the kinetic energy of the particle: hence, the energy deviates from the exact result (still being closer to it than purely classical simulations) while the dynamics of this process is not realistic. On the other hand, the position distribution still yields interesting information: tunneling is indicated by a non-zero value at the top of the barrier potential and the spatial delocalization of the particle is partly taken into account. If we now look back at the QTB results on high-pressure ice for example, proton tunneling was correctly described by the QTB as the distribution functions were in agreement with the PIMD distributions. This is also partly due to the fact that ice is a real system, with many degrees of freedom and that the reduction of the proton's motion to only one-dimension is quite restrictive. Furthermore, the high-frequency O-H stretching mode frequencies are also well described by the QTB and in agreement with spectroscopic measurements. This is because the corresponding vibrations are weakly anharmonic - such as the oscillation at the bottom of wells - and thus well accounted for by the QTB. In contrast, we do not expect the low-frequency dynamics of proton transfer along the hydrogen bonds or proton hopping to be correctly reproduced by the QTB.

[1] The distributions have been averaged over several independent trajectories in order to recover symmetric distributions.

[2] As a comparison, the transition frequency ν_{quantum} obtained from the energy differences between the ground state and the first excited state is approximately 300 THz.

5.5 Conclusion

The QTB is an approximate method that relies on the quantum fluctuation-dissipation theorem which is exact in the linear response theory framework [2]. Hence, the QTB yields the correct energies, distribution probabilities and vibrational spectra in the case of a harmonic oscillator (see section 2.2.2). However, we have seen in previous chapters (3 and 4) that the QTB also gives good results in real anharmonic systems, such as ice VII or δ-AlOOH. Here, we tried to carry out a critical analysis of the QTB method and analyze its limitations. In particular, the QTB is prone to ZPEL where part of the energy of high-frequency modes leaks into low-frequency modes with potential dramatic consequences for the structure of the system. This problem is inherent to any semiclassical method i.e. where the expectation values of the quantum operators $\hat{x}$ and $\hat{p}$ are replaced by classical variables, that have classical trajectories during which equipartition of the energy tends to occur. The ZPEL is a damaging problem, however, it can be handled to a certain degree by choosing a sufficiently large damping coefficient. Another problem of the QTB concerns its results in anharmonic systems. We can say that in a weakly anharmonic system, e.g. a double well with a large barrier, the QTB correctly reproduces the position distributions as well as the high-frequency vibrational spectra. In contrast, in a highly anharmonic system e.g. in a low-barrier double well potential in which proton tunneling is quite strong, the QTB yields acceptable distance distributions, as in ice VII for example. The frequencies of proton tunneling on the other hand are incorrect because the QTB trajectories associated with proton tunneling do not have any physical significance. However, from the information obtained via QTB simulations, we can construct models that are able to capture the essence of the physical phenomena studied (such as the Landau-like potential in high-pressure ice) and from these models, one can compute quantities such as proton tunneling frequencies directly from purely quantum calculations.

Conclusion and perspectives

Studying nuclear quantum effects (NQE) is a challenging task, both from a computational and a theoretical point of view. In particular, the development of simulation methods that are able to treat NQE is still an active field of research today. The Quantum Thermal Bath (QTB) was introduced by Dammak and coworkers recently [1] and constituted an original approach in which the quantum delocalization of a particle is mimicked by means of a stochastic motion. The QTB is similar to the Langevin thermostat except that the random force is not a white noise but has a specific power spectrum given by the quantum fluctuation-dissipation theorem [2]. This implies that the QTB method is a little bit trickier to handle than standard Langevin dynamics as it involves the use of a frequency cut-off in the generation of the stochastic force in order to avoid exciting non-physical vibrations in the system. The QTB had then been successfully applied to the study of the quantum isotope effect in lithium hydride and lithium deuteride [199]. Thus, at the beginning of this thesis, the QTB appeared as a promising method to include NQE in molecular dynamics simulations, even though we did not have much experience using it: it had the tremendous advantage of presenting no additional computational cost compared to standard molecular dynamics and of being relatively easy to implement since its formulation is general (and not system-dependent). Hence, we implemented the QTB in the Quantum Espresso package [89], aiming at studying materials that contain hydrogen atoms and thus gain more insight into the mechanisms of NQE.

We started with one of the prototypical systems in which quantum effects play a role, the high-pressure phases of ice. We focused on the symmetrization transition from the proton-disordered phase VII to the symmetric phase X that has been detected experimentally at about 60 GPa at room temperature, whereas simulations without any NQE predict a transition pressure of 100 GPa. Benoit and coworkers [116] were the first to report that NQE were responsible for the downshift of the transition pressure. Thus, we compared QTB and standard molecular dynamics simulations with the intention of distinguishing quantum from classical (thermal) effects. We found that the QTB yields the correct transition pressure as well as the correct protons distribution functions, in agreement with PIMD results. A new achievement was that the vibrational spectra computed from QTB simulations are fully consistent with experimental measurements [4]. This confirmed that the QTB is able to satisfactorily reproduce structural and dynamical properties in several real anharmonic systems, even though its formalism is based on the linear response theory. Moreover, the QTB results allowed us to devise an efficient Landau-like approach to analyze the mechanism of the transition. The effective potential landscape of the protons can be modeled by a double-well potential, in which the barrier height and the distance between the two wells depend on the pressure. We ran purely quantum calculations on a one-dimensional model effectively avoiding the approximations inherent to the QTB method and pointing out the role of the zero-point energy in the symmetrization of hydrogen bonds.

The QTB allowed us to take care of NQE in the symmetrization of hydrogen bonds in high-pressure ice, hence we performed the same analysis on salty ices. By comparing QTB to simulations without any NQE, we came across an unexpected result, namely the disappearance of NQE ! In particular, we found that proton hopping is less important in salty ice than in pure ice but more spectacularly, the VII-X transition pressure is up-shifted by approximately 30 GPa [5]. Again, the QTB simulations enabled us to set up a model system to understand the mechanism by which NQE are lifted in salty ice: we considered pure ice under an external electric field and showed that even a small electric field, such as the one due to the dissociation of salt in ice, can make the proton's effective potential landscape asymmetric. Since NQE are very sensitive to the symmetry of the potential, the consequences of a small electric field can be quite important and can explain the disappearance of NQE in this case. This example also showed that the environment of the hydrogen bonds is of paramount importance. The question that naturally arises after this study is what happens to NQE in crystals in which the atomic structure has a lower symmetry than in ice. Thus, we studied the high-pressure phases of aluminium oxide hydroxyde (δ and α). The QTB simulations showed the important role of thermal fluctuations as well as quantum effects in proton disorder and proton hopping. More interestingly, the small differences between the structures of δ and α are important enough so that in one case, a pseudo-symmetrization of hydrogen bonds occurs near 10 GPa (the δ-δ' transition [6]), while in the other case, no such transition is observed up to at least 50 GPa (in α-AlOOH).

In parallel, using the QTB which is an approximate method prompted us to study in more detail the validity and the range of applicability of this method, in particular for anharmonic systems. To this purpose, we used simple models with few degrees of freedom, in which we could compare the QTB results to exact quantum calculations. We found that, even though the QTB has several drawbacks, such as zero-point energy leakage or yielding incorrect results in anharmonic systems, these problems can be handled to a certain degree so that, once the leakage has been reduced below a physically relevant value, the QTB is a relatively robust method that can provide very good results.

In conclusion, two main points emerge from the work presented in this thesis. On the one hand, we showed through the different systems studied here that NQE have a complex role and can impact the system's properties in various and sometimes counterintuitive ways. They are extremely sensitive to many parameters, such as the symmetry of the atomic environment, and must thus be handled with care. On the other hand, concerning the QTB method in itself, we clearly established that if one is interested in studying quantum effects in hydrogen-containing solids, then the QTB is a useful and efficient method: it can give valuable information about the complex role of quantum effects and their importance with respect to classical thermal fluctuations. In particular, it gives access to the system's structural and dynamical properties as long as one is aware of the inherent limitations of the QTB and keeps a critical eye on the results. However, if one wants to study biological matter or liquids for example, i.e. materials that are highly anharmonic and with weak interatomic bonds, then the QTB in its present form and implementation does not represent a suitable framework and one needs to turn towards more robust alternative methods.

Bibliography

[1] H. Dammak, Y. Chalopin, M. Laroche, M. Hayoun, and J.-J. Greffet, "Quantum thermal bath for molecular dynamics simulation," Physical Review Letters **103**, 190601 (2009).

[2] H. B. Callen and T. A. Welton, "Irreversibility and generalized noise," Physical Review **83**, 34 (1951).

[3] F. Brieuc, Y. Bronstein, H. Dammak, P. Depondt, F. Finocchi, and M. Hayoun, "Zero-point energy leakage in Quantum Thermal Bath molecular dynamics simulations," (in preparation).

[4] Y. Bronstein, P. Depondt, F. Finocchi, and A. M. Saitta, "Quantum-driven phase transition in ice described via an efficient Langevin approach," Physical Review B **89**, 214101 (2014).

[5] Y. Bronstein, P. Depondt, L. E. Bove, R. Gaal, A. M. Saitta, and F. Finocchi, "Quantum versus classical protons in pure and salty ice under pressure," Physical Review B **93**, 024104 (2016).

[6] Y. Bronstein, P. Depondt, and F. Finocchi, "Nuclear quantum effects in the hydrogen bond symmetrization phase transition of δ-AlOOH," (submitted).

[7] R. P. Bell, *The proton in chemistry* (Cornell University Press, 1973), 2nd ed.

[8] G. A. Jeffrey and W. Saenger, *Hydrogen bonding in biological structures* (Springer-Verlag Berlin, 1991).

[9] C. H. Collie, J. B. Hasted, and D. M. Ritson, "The dielectric properties of water and heavy water," Proceedings of the Physical Society of London **60**, 145–160 (1948).

[10] N. N. Greenwood and A. Earnshaw, *Chemistry of the Elements* (Butterworth Heinemann, Oxford, 1997), 2nd ed.

[11] G. F. Reiter, J. Mayers, and P. Platzman, "Direct observation of tunneling in KDP using neutron Compton scattering," Physical Review Letters **89**, 135505 (2002).

[12] M. Benoit and D. Marx, "The shapes of protons in hydrogen bonds depend on the bond length," Journal of Chemical Physics and Physical Chemistry **6**, 1738–1741 (2005).

[13] W. H. Miller, "Including quantum effects in the dynamics of complex (i.e., large) molecular systems," The Journal of Chemical Physics **125**, 132305 (2006).

[14] C. J. T. de Grotthuss, "Sur la décomposition de l'eau et des corps qu'elle tient en dissolution à l'aide de l'électricité galvanique [Upon the decomposition of water, and of the bodies which it holds in solution, by means of galvanic electricity]," Annales de Chimie **58**, 54–73 (1806).

[15] B. J. Alder and T. E. Wainwright, "Studies in molecular dynamics. I. General method," The Journal of Chemical Physics **31**, 459–466 (1959).

[16] B. J. Berne and D. Thirumalai, "On the simulation of quantum systems: path integral methods," Annual Review of Physical Chemistry **37**, 401–424 (1986).

[17] W. H. Miller, "Quantum dynamics of complex molecular systems," Proceedings of the National Academy of Sciences **102**, 6660–6664 (2005).

[18] A. Witt, S. D. Ivanov, M. Shiga, H. Forbert, and D. Marx, "On the applicability of centroid and ring polymer path integral molecular dynamics for vibrational spectroscopy," The Journal of Chemical Physics **130**, 194510 (2009).

[19] A. G. Császár, C. Fábri, T. Szidarovszky, E. Mátyus, T. Furtenbacher, and G. Czakó, "The fourth age of quantum chemistry: molecules in motion," Physical Chemistry and Chemical Physics **14**, 1085–1106 (2012).

[20] J. Cao and G. A. Voth, "The formulation of quantum statistical mechanics based on the feynman path centroid density. I. Equilibrium properties," The Journal of Chemical Physics **100**, 5093 (1994).

[21] J. Cao and G. A. Voth, "The formulation of quantum statistical mechanics based on the feynman path centroid density. II. Dynamical properties," The Journal of Chemical Physics **100**, 5106 (1994).

[22] J. Cao and G. A. Voth, "The formulation of quantum statistical mechanics based on the feynman path centroid density. III. Phase space formalism and analysis of centroid molecular dynamics," The Journal of Chemical Physics **101**, 6157 (1994).

[23] J. Cao and G. A. Voth, "The formulation of quantum statistical mechanics based on the feynman path centroid density. IV. Algorithms for centroid molecular dynamics," The Journal of Chemical Physics **101**, 6168 (1994).

[24] D. Marx, M. E. Tuckerman, J. Hutter, and M. Parrinello, "The nature of the hydrated excess proton in water," Nature **397**, 601–604 (1999).

[25] T. D. Hone, P. J. Rossky, and G. A. Voth, "A comparative study of imaginary time path integral based methods for quantum dynamics," The Journal of Chemical Physics **124**, 154103 (2006).

[26] I. R. Craig and D. E. Manolopoulos, "Quantum statistics and classical mechanics: real time correlation functions from ring polymer molecular dynamics," The Journal of Chemical Physics **121**, 3368 (2004).

[27] B. J. Braams and D. E. Manolopoulos, "On the short-time limit of ring polymer molecular dynamics," The Journal of Chemical Physics **125**, 124105 (2006).

[28] R. P. Feynman and A. R. Hibbs, *Quantum Mechanics and path integrals* (New York: McGraw-Hill, 1965).

[29] M. Parrinello and A. Rahman, "Study of an F center in molten KCl," The Journal of Chemical Physics **80**, 860 (1984).

[30] B. J. Berne and G. D. Harp, *On the Calculation of Time Correlation Functions* (John Wiley & Sons, Inc., 1970), pp. 63–227.

[31] G. J. Martyna, "Adiabatic path integral molecular dynamics methods. I. Theory," The Journal of Chemical Physics **104**, 2018–2027 (1996).

[32] J. Cao and G. J. Martyna, "Adiabatic path integral molecular dynamics methods. II. Algorithms," The Journal of Chemical Physics **104**, 2028–2035 (1996).

[33] D. Marx, M. E. Tuckerman, and G. J. Martyna, "Quantum dynamics via adiabatic ab initio centroid molecular dynamics," Computer Physics Communications **118**, 166 (1999).

[34] I. R. Craig and D. E. Manolopoulos, "Chemical reaction rates from ring polymer molecular dynamics," The Journal of Chemical Physics **122**, 084106 (2005).

[35] T. F. Miller and D. E. Manolopoulos, "Quantum diffusion in liquid *para*-hydrogen from ring-polymer molecular dynamics," The Journal of Chemical Physics **122**, 184503 (2005).

[36] I. R. Craig and D. E. Manolopoulos, "A refined ring polymer molecular dynamics theory of chemical reaction rates," The Journal of Chemical Physics **123**, 034102 (2005).

[37] T. F. Miller and D. E. Manolopoulos, "Quantum diffusion in liquid water from ring polymer molecular dynamics," The Journal of Chemical Physics **123**, 154504 (2005).

[38] I. R. Craig and D. E. Manolopoulos, "Inelastic neutron scattering from liquid *para*-hydrogen by ring polymer molecular dynamics," Chemical Physics **322**, 236–246 (2006).

[39] W. Hu and G. C. Schatz, "Theories of reactive scattering," The Journal of Chemical Physics **125**, 132301 (2006).

[40] E. Sim and N. Makri, "Path integral simulation of charge transfer dynamics in photosynthetic reaction centers," The Journal of Physical Chemistry B **101**, 5446–5458 (1997).

[41] N. Makri, "Quantum dissipative dynamics: A numerically exact methodology," The Journal of Physical Chemistry A **102**, 4414–4427 (1998).

[42] M. Beck, A. Jäckle, G. Worth, and H.-D. Meyer, "The multiconfiguration time-dependent Hartree (MCTDH) method: a highly efficient algorithm for propagating wavepackets," Physics Reports **324**, 1–105 (2000).

[43] H.-D. Meyer and A. G. Worth, "Quantum molecular dynamics: propagating wavepackets and density operators using the multiconfiguration time-dependent Hartree method," Theoretical Chemistry Accounts **109**, 251–267 (2003).

[44] J. M. Bowman, "Self-consistent field energies and wavefunctions for coupled oscillators," The Journal of Chemical Physics **68**, 608 (1978).

[45] J. M. Bowman, "Application of SCF-SI theory to vibrational motion in polyatomic molecules," The Journal of Physical Chemistry **83**, 905 (1979).

[46] E. J. Heller, "Time-dependent approach to semiclassical dynamics," The Journal of Chemical Physics **62**, 1544 (1975).

[47] V. Buch, "Exploration of multidimensional variational Gaussian wave packets as a simulation tool," The Journal of Chemical Physics **117**, 4738 (2002).

[48] P. A. Frantsuzov and V. A. Mandelshtam, "Equilibrium properties of quantum water clusters by the variational Gaussian wavepacket method," The Journal of Chemical Physics **128**, 094304 (2008).

[49] W. H. Miller, "Classical S matrix: Numerical application to inelastic collisions," The Journal of Chemical Physics **53**, 3578–3587 (1970).

[50] W. H. Miller, "Comment on: Semiclassical time evolution without root searches," The Journal of Chemical Physics **95**, 9428–9430 (1991).

[51] E. J. Heller, "Cellular dynamics: A new semiclassical approach to time-dependent quantum mechanics," The Journal of Chemical Physics **94**, 2723–2729 (1991).

[52] E. J. Heller, "Reply to Comment on: Semiclassical time evolution without root searches: Comments and perspective," The Journal of Chemical Physics **95**, 9431–9432 (1991).

[53] K. G. Kay, "Integral expressions for the semiclassical time-dependent propagator," The Journal of Chemical Physics **100**, 4377–4392 (1994).

[54] K. G. Kay, "Numerical study of semiclassical initial value methods for dynamics," The Journal of Chemical Physics **100**, 4432–4445 (1994).

[55] W. H. Miller, "The semiclassical initial value representation: A practical way for adding quantum effects to classical molecular dynamics simulations," The Journal of Physical Chemistry A **105**, 2942–2955 (2001).

[56] K. W. Ford and J. A. Wheeler, "Semiclassical description of scattering," Annals of Physics **7**, 259–286 (1959).

[57] R. B. Bernstein, *Quantum effects in elastic molecular scattering* (John Wiley & Sons, Inc., 1966), p. 75.

[58] W. H. Miller, *Classical-limit quantum mechanics and the theory of molecular collisions* (John Wiley & Sons, Inc., 1974), pp. 69–177.

[59] R. Marcus, "Extension of the WKB method to wave functions and transition probability amplitudes (S-matrix) for inelastic or reactive collisions," Chemical Physics Letters **7**, 525–532 (1970).

[60] R. A. Marcus, "Theory of semiclassical transition probabilities (S matrix) for inelastic and reactive collisions," The Journal of Chemical Physics **54**, 3965–3979 (1971).

[61] J. H. Van Vleck, "The correspondence principle in the statistical interpretation of quantum mechanics," Proceedings of the National Academy of Sciences **14**, 178–188 (1928).

[62] X. Sun and W. H. Miller, "Mixed semiclassical–classical approaches to the dynamics of complex molecular systems," The Journal of Chemical Physics **106**, 916–927 (1997).

[63] H. Wang, X. Sun, and W. H. Miller, "Semiclassical approximations for the calculation of thermal rate constants for chemical reactions in complex molecular systems," The Journal of Chemical Physics **108**, 9726 (1998).

[64] E. Pollak and J.-L. Liao, "A new quantum transition state theory," The Journal of Chemical Physics **108**, 2733–2743 (1998).

[65] J. A. Poulsen, G. Nyman, and P. J. Rossky, "Practical evaluation of condensed phase quantum correlation functions: A feynman–kleinert variational linearized path integral method," The Journal of Chemical Physics **119**, 12179–12193 (2003).

[66] Q. Shi and E. Geva, "Semiclassical theory of vibrational energy relaxation in the condensed phase," The Journal of Physical Chemistry A **107**, 9059–9069 (2003).

[67] Q. Shi and E. Geva, "Vibrational energy relaxation in liquid oxygen from a semiclassical molecular dynamics simulation," The Journal of Physical Chemistry A **107**, 9070–9078 (2003).

[68] P. Frantsuzov, A. Neumaier, and V. A. Mandelshtam, "Gaussian resolutions for equilibrium density matrices," Chemical Physics Letters **381**, 117–122 (2003).

[69] P. A. Frantsuzov and V. A. Mandelshtam, "Quantum statistical mechanics with gaussians: Equilibrium properties of van der waals clusters," The Journal of Chemical Physics **121**, 9247–9256 (2004).

[70] M. F. Herman and E. Kluk, "A semiclasical justification for the use of non-spreading wavepackets in dynamics calculations," Chemical Physics **91**, 27–34 (1984).

[71] J. Shao and N. Makri, "Forward-Backward semiclassical dynamics without prefactors," The Journal of Physical Chemistry A **103**, 7753–7756 (1999).

[72] J. Shao and N. Makri, "Forward-Backward semiclassical dynamics with linear scaling," The Journal of Physical Chemistry A **103**, 9479–9486 (1999).

[73] J. Liu and W. H. Miller, "Using the thermal Gaussian approximation for the Boltzmann operator in semiclassical initial value time correlation functions," The Journal of Chemical Physics **125**, 224104 (2006).

[74] J. Liu and W. H. Miller, "An approach for generating trajectory-based dynamics which conserves the canonical distribution in the phase space formulation of quantum mechanics. II. Thermal correlation functions," The Journal of Chemical Physics **134**, 104102 (2011).

[75] J. Liu, "Path integral Liouville dynamics for thermal equilibrium systems," The Journal of Chemical Physics **140**, 224107 (2014).

[76] A. Schmid, "On a quasiclassical Langevin equation," Journal of Low Temperature Physics **49**, 609–626 (1982).

[77] J.-S. Wang, "Quantum thermal transport from classical molecular dynamics," Physical Review Letters **99**, 160601 (2007).

[78] E. M. Heatwole and O. V. Prezhdo, "Second-order Langevin equation in quantized Hamilton dynamics," Journal of the Physical Society of Japan **77**, 044001 (2008).

[79] S. Buyukdagli, A. V. Savin, and B. B. Hu, "Computation of the temperature dependence of the heat capacity of complex molecular systems using random color noise," Physical Review E **78**, 066702 (2008).

[80] R. Kubo, "The fluctuation-dissipation theorem," Reports on Progress in Physics **29**, 255 (1966).

[81] M. Ceriotti, G. Bussi, and M. Parrinello, "Nuclear quantum effects in solids using a colored-noise thermostat," Physical Review Letters **103**, 030603 (2009).

[82] R. Brown, *The miscellaneous botanical works of Robert Brown: Volume 1.* (R. Hardwicke, London, 1866).

[83] A. Einstein, "Über die von der molekularkinetischen Theorie der Wärme geforderte Bewegung von in ruhenden Flüssigkeiten suspendierten Teilchen [On the movement of small particles suspended in a stationary liquid demanded by the molecular-kinetic theory of heart]," Annalen der Physik **322**, 549–560 (1905).

[84] P. Langevin, "Sur la théorie du mouvement brownien [On the theory of brownian motion]," Comptes Rendus de l'Académie des Sciences (Paris) **146**, 530–533 (1908).

[85] R. Kubo, M. Toda, and N. Hashitsume, *Statistical Physics II: Nonequilibrium statistical mechanics* (Springer, 1978).

[86] J.-L. Barrat and D. Rodney, "Portable implementation of a Quantum Thermal Bath for molecular dynamics simulations," Journal of Statistical Physics **144**, 679–689 (2011).

[87] A. A. Maradudin, T. Michel, A. R. McGurn, and E. R. Méndez, "Enhanced backscattering of light from a random grating," Annals of Physics **203**, 255–307 (1990).

[88] Y. Chalopin, H. Dammak, M. Laroche, M. Hayoun, and J.-J. Greffet, "Radiative heat transfer from a black body to dielectric nanoparticles," Physical Review B **84**, 224301 (2011).

[89] P. Giannozzi et al., "QUANTUM ESPRESSO: a modular and open-source software project for quantum simulations of materials," Journal of Physics: Condensed Matter **21**, 395502 (2009).

[90] G. J. Martyna, M. E. Tuckerman, D. J. Tobias, and M. L. Klein, "Explicit reversible integrators for extended system dynamics," Molecular Physics **87**, 5 (1996).

[91] S. W. Lovesey, *Theory of neutron scattering from condensed matter* (United Kingdom: Clarendon Press, 1984).

[92] M. Martinez, M.-P. Gaigeot, D. Borgis, and R. Vuilleumier, "Extracting effective normal modes from equilibrium dynamics at finite temperature," The Journal of Chemical Physics **125**, 144106 (2006).

[93] A. Scherrer, F. Agostini, D. Sebastiani, and E. K. U. Gross, "Nuclear velocity perturbation theory for vibrational circular dichroism: an approach based on the exact factorization of the electron-nuclear wave function," The Journal of Chemical Physics **143**, 074106 (2015).

[94] S. K. Min, F. Agostini, and E. K. U. Gross, "Coupled-trajectory quantum-classical approach to electronic decoherence in nonadiabatic processes," Physical Review Letters **115**, 073001 (2015).

[95] F. Agostini, A. Abedi, and E. K. U. Gross, "Classical nuclear motion coupled to electronic non-adiabatic transitions," The Journal of Chemical Physics **141**, 214101 (2014).

[96] M. Born and K. Huang, *Dynamical theory of crystal lattices* (Oxford: Clarendon Press, 1954).

[97] P. Hohemberg and W. Kohn, "Inhomogeneous electron gas," Physical Review **136**, B864 (1964).

[98] W. Kohn and L. J. Sham, "Self-consistent equations including exchange and correlation effects," Physical Review A **140**, 1133 (1965).

[99] J. P. Perdew, K. Burke, and M. Ernzerhof, "Generalized gradient approximation made simple," Physical Review Letters **77**, 3865 (1996).

[100] S. Baroni, S. de Gironcoli, A. D. Corso, and P. Giannozzi, "Phonons and related crystal properties from density-functional perturbation theory," Review of Modern Physics **73**, 515 (2001).

[101] V. R. Brill and A. Tippe, "Gitterparameter von Eis I bei tiefen Temperaturen [Lattice parameter of ice I at low temperatures]," Acta Crystallographica **23**, 343 (1967).

[102] P. V. Hobbs, *Ice physics* (Clarendon Press Oxford, 1974).

[103] E. Arunan et al., "Definition of the hydrogen bond (IUPAC recommendations 2011)," Pure and Applied Chemistry **83**, 1637–1641 (2011).

[104] L. Pauling, *The nature of the chemical bond and the structure of molecules and crystals* (Cornell University Press, 1960).

[105] E. D. Isaacs, A. Shukla, P. M. Platzman, D. R. Hamann, B. Barbiellini, and C. A. Tulk, "Covalency of the hydrogen bond in ice: a direct X-ray measurement," Physical Review Letters **82**, 600–603 (1999).

[106] L. Lin, J. A. Morrone, and R. Car, "Correlated tunneling in hydrogen bonds," Journal of Statistical Physics **145**, 365–384 (2011).

[107] T. Kuribayashi, A. Sano-Furukawa, and T. Nagase, "Observation of pressure-induced phase transition of δ-AlOOH by using single-crystal synchrotron X-ray diffraction method," Physics and Chemistry of Minerals **41**, 303–312 (2014).

[108] M. Benoit and D. Marx, "The role of quantum effects and ionic defects in high-density ice," Solid State Ionics **125**, 23–29 (1999).

[109] W. B. Holzapfel, "On the symmetry of hydrogen bonds in ice VII," The Journal of Chemical Physics **56**, 712 (1972).

[110] W. B. Holzapfel and H. G. Drickamer, "Effect of pressure on the volume of the high-pressure (VII) phase of H_2O and D_2O," The Journal of Chemical Physics **48**, 4798 (1968).

[111] F. H. Stillinger and K. S. Schweizer, "Ice under pressure: transition to symmetrical hydrogen bonds," The Journal of Physical Chemistry **87**, 4281–4288 (1983).

[112] K. S. Schweizer and F. H. Stillinger, "Phase transitions induced by proton tunneling in hydrogen-bonded crystals. ground-state theory," Physical Review B **29**, 350–360 (1984).

[113] K. S. Schweizer and F. H. Stillinger, "High pressure phase transitions and hydrogen-bond symmetry in ice polymorphs," The Journal of Chemical Physics **80**, 1230 (1984).

[114] P. G. Johannsen, "Vibrational states and optical transitions in hydrogen bonds," Journal of Physics: Condensed Matter **10**, 2241 (1998).

[115] M. Mackowiak, "Isotope effect on high-pressure behavior of hydrogen-bonded crystals," Physica B+C **145**, 320–328 (1987).

[116] M. Benoit, D. Marx, and M. Parrinello, "Tunnelling and zero-point motion in high-pressure ice," Nature **392**, 258 (1998).

[117] C. Lee, D. Vanderbilt, K. Laasonen, R. Car, and M. Parrinello, "*Ab initio* studies on high pressure phases of ice," Physical Review Letters **69**, 462 (1992).

[118] C. Lee, D. Vanderbilt, K. Laasonen, R. Car, and M. Parrinello, "*Ab initio* studies on the structural and dynamical properties of ice," Physical Review B **47**, 4863 (1993).

[119] M. Bernasconi, P. L. Silvestrelli, and M. Parrinello, "*Ab initio* infrared absorption study of the hydrogen-bond symmetrization in ice," Physical Review Letters **81**, 1235 (1998).

[120] R. Caracas, "Dynamical instabilities of ice X," Physical Review Letters **101**, 085502 (2008).

[121] X. Z. Lu, Y. Zhang, P. Zhao, and S. J. Fang, "Vibrational analysis of the hydrogen-bond symmetrization in ice," Journal of Physical Chemistry B **115**, 71 (2011).

[122] L. Tian, A. I. Kolesnikov, and J. Li, "Ab initio simulation of hydrogen bonding in ices under ultra-high pressure," The Journal of Chemical Physics **137**, 204507 (2012).

[123] S. L. Sondhi, S. M. Girvin, J. P. Carini, and D. Shahar, "Continuous quantum phase transitions," Review of Modern Physics **69**, 315 (1997).

[124] D. Schwandt, F. Alet, and S. Capponi, "Quantum Monte Carlo simulations of fidelity at magnetic quantum phase transitions," Physical Review Letters **103**, 170501 (2009).

[125] A. F. Albuquerque, F. Alet, C. Sire, and S. Capponi, "Quantum critical scaling of fidelity susceptibility," Physical Review B **81**, 064418 (2010).

[126] S. Sachdev, *Quantum Phase Transitions* (Cambridge University Press, 2011).

[127] A. Messiah, *Quantum Mechanics* (Dover Publications, Inc., 1958).

[128] T. Horsewill, M. Johnson, and H. P. Trommsdorff, "Proton tunnelling in intermolecular hydrogen bonds," Europhysics News **28**, 140–142 (1997).

[129] Y. Dakhnovskii, B. Bursulaya, and H. J. Kim, "Quantum tunneling in an anharmonic classical bath. Enhanced kinetic isotope effects in an Arrhenius region," The Journal of Chemical Physics **102**, 7838 (1995).

[130] V. F. Petrenko and R. W. Whitworth, *Physics of Ice* (Oxford University Press, 1999).

[131] C. G. Salzmann, P. G. Radaelli, E. Mayer, and J. L. Finney, "Ice XV: A new thermodynamically stable phase of ice," Physical Review Letters **103**, 105701 (2009).

[132] M. Benoit, M. Bernasconi, P. Focher, and M. Parrinello, "New high-pressure phase of ice," Physical Review Letters **76**, 2934–2936 (1996).

[133] B. Militzer and H. F. Wilson, "New phases of water ice predicted at megabar pressures," Physical Review Letters **105**, 195701 (2010).

[134] K. R. Hirsch and W. B. Holzapfel, "Symmetric hydrogen bonds in ice X," Physics Letters A **101**, 142–144 (1984).

[135] A. Polian and M. Grimsditch, "New high-pressure phase of H_2O: Ice X," Physical Review Letters **52**, 1312–1314 (1984).

[136] K. R. Hirsch and W. B. Holzapfel, "Effect of high pressure on the Raman spectra of ice VIII and evidence for ice X," The Journal of Chemical Physics **84**, 2771 (1986).

[137] R. J. Hemley, A. P. Jephcoat, H. K. Mao, C. S. Zha, L. W. Finger, and D. E. Cox, "Static compression of H_2O-ice to 128 GPa (1.28 Mbar)," Nature **330**, 737–740 (1987).

[138] P. Pruzan, J. C. Chervin, and B. Canny, "Determination of the D_2O ice VII-VIII transition line by Raman scattering up to 51 GPa," The Journal of Chemical Physics **97**, 718 (1992).

[139] P. Pruzan, J. C. Chervin, and B. Canny, "Stability domain of the ice VIII proton-ordered phase at very high pressure and low temperature," The Journal of Chemical Physics **99**, 9842 (1993).

[140] P. Pruzan, "Pressure effects on the hydrogen bond in ice up to 80 GPa," Journal of Molecular Structure **322**, 279–286 (1994).

[141] R. J. Nelmes, J. S. Loveday, R. M. Wilson, J. M. Besson, P. Pruzan, S. Klotz, G. Hamel, and S. Hull, "Neutron diffraction study of the structure of deuterated ice VIII to 10 GPa," Physical Review Letters **71**, 1192 (1993).

[142] K. Aoki, H. Yamawaki, M. Sakashita, and H. Fujihisa, "Infrared absorption study of the hydrogen-bond symmetrization in ice to 110 GPa," Physical Review B **54**, 15673 (1996).

[143] K. Aoki, H. Yamawaki, and M. Sakashita, "Observation of Fano interference in high-pressure ice VII," Physical Review Letters **76**, 784 (1996).

[144] A. F. Goncharov, V. V. Struzhkin, M. S. Somayazulu, R. J. Hemley, and H. K. Mao, "Compression of ice to 210 gigapascals: infrared evidence for a symmetric hydrogen-bonded phase," Science **273**, 218 (1996).

[145] V. V. Struzhkin, A. F. Goncharov, R. J. Hemley, and H. K. Mao, "Cascading Fermi resonances and the soft mode in dense ice," Physical Review Letters **78**, 4446 (1997).

[146] M. Song, H. Yamawaki, H. Fujihisa, M. Sakashita, and K. Aoki, "Infrared absorption study of Fermi resonance and hydrogen-bond symmetrization of ice up to 141 GPa," Physical Review B **60**, 12644 (1999).

[147] P. Pruzan, E. Wolanin, M. Gauthier, J. C. Chervin, B. Canny, D. Häusermann, and M. Hanfland, "Raman scattering and X-ray diffraction of ice in the Megabar range. Occurence of a symmetric disordered solid above 62 GPa," The Journal of Physical Chemistry B **101**, 6230–6233 (1997).

[148] A. F. Goncharov, V. V. Struzhkin, H. K. Mao, and R. J. Hemley, "Raman spectroscopy of dense H_2O and the transition to symmetric hydrogen bonds," Physical Review Letters **83**, 1998 (1999).

[149] P. Loubeyre, R. LeToullec, E. Wolanin, M. Hanfland, and D. Hausermann, "Modulated phases and proton centring in ice observed by x-ray diffraction up to 170 GPa," Nature **397**, 503 (1999).

[150] A. Putrino and M. Parrinello, "Anharmonic Raman spectra in high-pressure ice from *ab initio* simulations," Physical Review Letters **888**, 176401 (2002).

[151] J. A. Morrone, L. Lin, and R. Car, "Tunneling and delocalization effects in hydrogen bonded systems: a study in position and momentum space," The Journal of Chemical Physics **130**, 204511 (2009).

[152] L. E. Bove, R. Gaal, Z. Raza, A. A. Ludl, S. Klotz, A. M. Saitta, A. F. Goncharov, and P. Gillet, "Effect of salt on the H-bond symmetrization in ice," Proceedings of the National Academy of Sciences **112**, 8216 (2015).

[153] S. Nachimuthu, J. Gao, and D. Truhlar, "A benchmark test suite for proton transfer energies and its use to test electronic structure model chemistries," Chemical Physics **400**, 8–12 (2012).

[154] S. Grimme, J. Antony, S. Ehrlich, and H. Krieg, "Consistent and accurate *ab initio* parametrization of density functional dispersion correction (DFT-D) for the 94 elements H-Pu," The Journal of Chemical Physics **132**, 154104 (2010).

[155] O. H. Nielsen and R. M. Martin, "Quantum-mechanical theory of stress and force," Physical Review B **32**, 3792 (1985).

[156] V. A. Benderskii, D. E. Makarov, and C. A. Wight, *Chemical dynamics at low temperatures* (John Wiley & Sons, Inc., 1994).

[157] J. D. Anderson, G. Schubert, R. A. Jacobson, E. L. Lau, W. B. Moore, and W. L. Sjogren, "Europa's differentiated internal structure: inferences from four Galileo encounters," Science **281**, 2019–2022 (1998).

[158] K. K. Khurana, M. G. Kivelson, D. J. Stevenson, G. Schubert, C. T. Russell, R. J. Walker, and C. Polanskey, "Induced magnetic fiels as evidence for subsurface oceans in Europa and Callisto," Nature **395**, 777–780 (1998).

[159] N. Schilling, K. K. Khurana, and M. G. Kivelson, "Limits on an intrinsic dipole moment in Europa," Journal of Geophysical Research **109**, E05006 (2004).

[160] B. G. Bills, "Free and forced obliquities of the Galilean satellites of Jupiter," Icarus **175**, 233–247 (2005).

[161] J. J. Lissauer, "Extrasolar planets," Nature **419**, 355–358 (2002).

[162] M. Gillon, F. Pont, B.-O. Demory, F. Mallmann, M. Mayor, T. Mazeh, D. Queloz, A. Shporer, S. Udry, and C. Vuissoz, "Detection of transits of the nearby hot Neptune GJ 436 b," Astronomy and Astrophysics **472**, L13–L16 (2007).

[163] M. R. Frank, C. E. Runge, H. P. Scott, S. J. Maglio, J. Olson, V. B. Prakapenka, and G. Shen, "Experimental study of the NaCl-H_2O system up to 28 GPa: Implications for ice-rich planetary bodies," Physics of the Earth and Planetary Interiors **155**, 152–162 (2006).

[164] M. R. Frank, H. P. Scott, S. J. Maglio, V. B. Prakapenka, and G. Shen, "Temperature induced immiscibility in the NaCl-H_2O system at high pressure," Physics of the Earth and Planetary Interiors **170**, 107–114 (2008).

[165] S. Klotz, L. E. Bove, T. Straessle, T. C. Hansen, and A. M. Saitta, "The preparation and structure of salty ice VII under pressure," Nature Materials **8**, 405 (2009).

[166] L. E. Bove, S. Klotz, J. Philippe, and A. M. Saitta, "Pressure-induced polyamorphism in salty water," Physical Review Letters **106**, 125701 (2011).

[167] M. R. Frank, E. Aarestad, H. P. Scott, and V. B. Prakapenka, "A comparison of ice VII formed in the H_2O, NaCl-H_2O, and CH_3OH-H_2O systems: Implications for H_2O-rich planets," Physics of the Earth and Planetary Interiors **215**, 12–20 (2012).

[168] P. Valenti, R. J. Bodnar, and C. Schmidt, "Experimental determination of H_2O-NaCl liquidi to 25 mass% NaCl and 1.4 GPa: Application to the Jovian satellite Europa," Geochimica et Cosmochimica Acta **92**, 117–128 (2012).

[169] B. Journaux, I. Daniel, R. Caracas, G. Montagnac, and H. Cardon, "Influence of NaCl on ice VI and ice VII melting curves up to 6 GPa, implications for large icy moons," Icarus **226**, 355–363 (2013).

[170] G. N. Ruiz, L. E. Bove, H. R. Corti, and T. Loerting, "Pressure-induced transformations in LiCl-H_2O at 77 K," Physical Chemistry Chemical Physics **16**, 18553 (2014).

[171] A. A. Ludl, L. E. Bove, A. M. Saitta, M. Salanne, T. C. Hansen, C. L. Bull, R. Gaal, and S. Klotz, "Structural characterization of eutectic aqueous NaCl solutions under variable temperature and pressure conditions," Physical Chemistry Chemical Physics **17**, 14054–14063 (2015).

[172] J. Klimes, D. R. Bowler, and A. Michaelides, "Understanding the role of ions and water molecules in the NaCl dissolution process," The Journal of Chemical Physics **139**, 234702 (2013).

[173] Q. Zeng, T. Yan, K. Wang, Y. Gong, Y. Zhou, Y. Huang, C. Q. Sun, and B. Zou, "Compression icing of room-temperature NaX solutions (X = F, Cl, Br, I)," Physical Chemistry and Chemical Physics **18**, 14046–14054 (2016).

[174] S. Raugei, P. L. Silvestrelli, and M. Parrinello, "Pressure-induced frustration and disorder in $Mg(OH)_2$ and $Ca(OH)_2$," Physical Review Letters **83**, 2222–2225 (1999).

[175] M. M. and S. L., "High-pressure proton disorder in brucite," American Mineralogist **91**, 127–134 (2006).

[176] J. Horita, A. M. dos Santos, C. A. Tulk, B. C. Chakoumakos, and V. B. Polyakov, "High-pressure neutron diffraction study on H-D isotope effects in brucite," Physics and Chemistry of Minerals **37**, 741–749 (2010).

[177] A. Suzuki, E. Ohtani, and T. Kamada, "A new hydrous phase δ-AlOOH synthesized at 21 GPa and 1000 °C," Physics and Chemistry of Minerals **27**, 689–693 (2000).

[178] E. Ohtani, K. Litasov, A. Suzuki, and T. Kondo, "Stability field of new hydrous phase, δ-AlOOH, with implications for water transport into the deep mantle," Geophysical Research Letters **28**, 3991–3993 (2001).

[179] A. Sano, E. Ohtani, T. Kubo, and K. Funakoshi, "In situ X-ray observation of decomposition of hydrous aluminum silicate $AlSiO_3OH$ and aluminum oxide hydroxide d-AlOOH at high pressure and temperature," Journal of Physics and Chemistry of Solids **65**, 1547–1554 (2004).

[180] A. Sano, E. Ohtani, T. Kondo, N. Hirao, T. Sakai, N. Sata, Y. Ohishi, and T. Kikegawa, "Aluminous hydrous mineral δ-AlOOH as a carrier of hydrogen into the core-mantle boundary," Geophysical Research Letters **35**, L03303 (2008).

[181] C. B. Vanpeteghem, E. Ohtani, and T. Kondo, "Equation of state of the hydrous phase δ-AlOOH at room temperature up to 22.5 GPa," Geophysical Research Letters **29**, 1119–1121 (2002).

[182] J. Tsuchiya, T. Tsuchiya, S. Tsuneyuki, and T. Yamanaka, "First principles calculation of a high-pressure hydrous phase, δ-AlOOH," Geophysical Research Letters **29**, 1909 (2002).

[183] W. R. Panero and L. P. Stixrude, "Hydrogen incorporation in stishovite at high pressure and symmetric hydrogen bonding in δ-AlOOH," Earth and Planetary Science Letters **221**, 421–431 (2004).

[184] K. Komatsu, T. Kuribayashi, A. Sano, E. Ohtani, and Y. Kudoh, "Redetermination of the high-pressure modification of AlOOH from single-crystal synchrotron data," Acta Crystallographica Section E **62**, i216–i218 (2006).

[185] J. Tsuchiya and T. Tsuchiya, "Elastic properties of δ-AlOOH under pressure: First principles investigation," Physics of the Earth and Planetary Interiors **174**, 122–127 (2009).

[186] J. Tsuchiya, T. Tsuchiya, and R. M. Wentzcovitch, "Vibrational properties of δ-AlOOH under pressure," American Mineralogist **93**, 477–482 (2008).

[187] A. Sano-Furukawa, H. Kagi, T. Nagai, S. Nakano, S. Fukura, D. Ushijima, R. Iizuka, E. Ohtani, and T. Yagi, "Change in compressibility of δ-AlOOH and δ-AlOOD at high pressure: A study of isotope effect and hydrogen-bond symmetrization," American Mineralogist **94**, 1255–1261 (2009).

[188] B. Winkler, M. Hytha, C. Pickard, V. Milman, M. Warren, and M. Segall, "Theoretical investigation of bonding in diaspore," European Journal of Mineralogy **13**, 343–349 (2001).

[189] A. Friedrich, E. Haussühl, R. Boehler, W. Morgenroth, E. A. Juarez-Arellano, and B. Winkler, "Single-crystal structure refinement of diaspore at 50 GPa," American Mineralogist **92**, 1640–1644 (2007).

[190] A. Sano-Furukawa, K. Komatsu, C. B. Vanpeteghem, and E. Ohtani, "Neutron diffraction study of δ-AlOOD at high pressure and its implication for symmetrization of the hydrogen bond," American Mineralogist **93**, 1558–1567 (2008).

[191] A. D. Becke, "Density-functional exchange-energy approximation with correct asymptotic behavior," Physical Review A **38**, 3098–3100 (1988).

[192] C. Lee, W. Yang, and R. G. Parr, "Development of the Colle-Salvetti correlation-energy formula into a functional of the electron density," Physical Review B **37**, 785–789 (1988).

[193] P. Vinet, J. R. Smith, J. Ferrante, and J. H. Rose, "Temperature effects on the universal equation of state of solids," Physical Review B **35**, 1945–1953 (1987).

[194] M. Ben-Nun and R. D. Levine, "Conservation of zero-point energy in classical trajectory computations by a simple semiclassical correspondence," The Journal of Chemical Physics **101**, 8768 (1994).

[195] S. Habershon and D. E. Manolopoulos, "Zero point energy leakage in condensed phase dynamics: An assessment of quantum simulation methods for liquid water," The Journal of Chemical Physics **131**, 244518 (2009).

[196] S. Ganeshan, R. Ramirez, and M. V. Fernandez-Serra, "Simulation of quantum zero-point effects in water using a frequency-dependent thermostat," Physical Review B **87**, 134207 (2013).

[197] O. N. Bedoya-Martinez, J.-L. Barrat, and D. Rodney, "Computation of the thermal conductivity using methods based on classical and quantum molecular dynamics," Physical Review B **89**, 014303 (2014).

[198] J. Hernandez-Rojas, F. Calvo, and E. G. Noya, "Applicability of quantum thermal baths to complex many-body systems with various degrees of anharmonicity," Journal of Chemical Theory and Computation **11**, 861–870 (2015).

[199] H. Dammak, E. Antoshchenkova, M. Hayoun, and F. Finocchi, "Isotope effects in lithium hydride and lithium deuteride crystals by molecular dynamics simulations," Journal of Physics: Condensed Matter **24**, 435402 (2012).

Publications

The following works have been published:

- "Quantum-driven phase transition in ice described via an efficient Langevin approach", Yael Bronstein, Philippe Depondt, Fabio Finocchi and Antonino Marco Saitta, Physical Review B **89**, 214101, 2014.
- "Quantum versus classical protons in pure and salty ice under pressure", Yael Bronstein, Philippe Depondt, Livia E. Bove, Richard Gaal, Antonino Marco Saitta and Fabio Finocchi, Physical Review B **93**, 024104, 2016.
- "Zero-point energy leakage in Quantum Thermal Bath molecular dynamics simulations", Fabien Brieuc, Yael Bronstein, Hichem Dammak, Philippe Depondt, Fabio Finocchi and Marc Hayoun, Journal of Chemical Theory and Computation **12** (12), 5688, 2016.
- "Thermal and nuclear quantum effects in the hydrogen bond dynamical symmetrization phase transition of δ-AlOOH", Yael Bronstein, Philippe Depondt and Fabio Finocchi, accepted in European Journal of Mineralogy.